2013

Geomechanics and elastic anisotropy of the Bakken Formation, Williston Basin

Mehdi Ostadhassan
University of North Dakota, mehdi.ostadhassan@UND.edu

GEOMECHANICS AND ELASTIC ANISOTROPY OF THE BAKKEN FORMATION, WILLISTON BASIN

by

MEHDI OSTADHASSAN

Bachelor of Science, Petroleum University of Technology, Iran, 2005

Master of Science, IFP-School (Institute France du Petrole), France, 2008

A Dissertation

Submitted to the Graduate Faculty

of the

University of North Dakota

In partial fulfillment of the requirements

for the degree of

Doctor of Philosophy

Grand Forks, North Dakota

May

2013

This thesis, submitted by Mehdi Ostadhassan in partial fulfillment of the requirements for the Degree of Doctor of Philosophy from the University of North Dakota, has been read by the Faculty Advisory Committee under whom the work has been done, and is hereby approved.

_____
Dr. Richard LeFever

_____
Dr. Steve Benson

_____
Dr. William Gosnold

_____
Dr. Hossein Salehfar

_____
Dr. Irina Smoliakova

This thesis is being submitted by the appointed advisory committee as having met all of the requirements of the Graduate School at the University of North Dakota and is hereby approved.

_____
Dr. Wayne Swisher
Dean of the Graduate School

_____
April 24th 2013

Title	Geomechanics and Elastic Anisotropy of the Bakken Formation, Williston Basin
Department	Geology and Geological Engineering
Degree	Doctor of Philosophy

In presenting this dissertation in partial fulfillment of the requirements for a graduate degree from the University of North Dakota, I agree that the library of this University shall make it freely available for inspection. I further agree that permission for extensive copying for scholarly purposes may be granted by the professor who supervised my dissertation work or, in his absence, by the Chairperson of the department or the dean of the Graduate School. It is understood that any copying or publication or other use of this dissertation or part thereof for financial gain shall not be allowed without my written permission. It is also understood that due recognition shall be given to me and to the University of North Dakota in any scholarly use which may be made of any material in my dissertation.

Mehdi Ostadhassan
April 24th 2013

TABLE OF CONTENTS

LIST OF FIGURES

LIST OF TABLES

ACKNOWLEDGEMENTS

The author of this PhD dissertation would like to recognize a few people who made this thesis possible. First, I would like show my sincere appreciation to my advisor, Dr. Richard LeFever, for his guidance and support. I would also like to express my deep appreciation to the members of my committee, Prof. Steven A. Benson, Prof. Hossein Salehfar, Prof. William Gosnold, and Prof. Irina P. Smoliakova, who provided me with invaluable insights and support along the way, as well as Prof. Joseph Hartman, the chair of *Harold Hamm School of Geology and Geological Engineering*.

I would specially like to acknowledge the following individuals: Prof. Steven A. Benson, the chair of the *UND Petroleum Engineering Department*, Mr. Scott Johnson, Mrs. Katie Sagstuen, Mrs. Shanna Corbett, and Mrs. Cassandra Olson for all their help and support throughout this research. I'd also like to thank Dr. Gabriela Martinez from Schlumberger DCS who helped me through data processing and interpretation during my training at Schlumberger DCS. I would like to thank Messrs. Jonathan Lean (Hess Corp.) and Jack Breig (Whiting Petroleum Corp.) who provided me with the data. This research was made possible through U.S. DoE and NDIC financial supports for that I owe my gratitude.

Last but not least I have to show my gratitude to several individuals that have helped me in different ways. In particular, I'd like to thank my very best friend Hadi Jabbari, whom I spent most of my time and explored all of the U.S. with, for his invaluable comments and input; a very good friend of mine, Siavash Zamiran, for the fruitful discussions; and Darin Buri who was always there to help me.

Finally, I'd like to thank all my friends at the *UND Petroleum Engineering Department* and *Harold Hamm School of Geology and Geological Engineering*.

To My Parents

Who without their support, love and prayers I wouldn't have been able to become me

ABSTRACT

Many of the earth's rocks exhibit anisotropic characteristics. Anisotropy is particularly common in many sedimentary rocks, such as shales. Anisotropy is defined as the spatial alignment of mineral grains, layers, fractures and stresses which causes elastic wave velocity and other elastic properties to vary with direction. There are two types of anisotropy: intrinsic and stress-induced. Intrinsic anisotropy is caused by beddings, microstructures or aligned fractures formed during deposition. Stress-induced anisotropy is caused by strain associated with external stresses. Intrinsic anisotropy originates in the absence of external stresses, while stress-induced anisotropy results from tectonic and overburden stresses. The style of earth material alignment causes two simplified, but convenient models of anisotropy: vertically transverse isotropy (VTI), like shale, and horizontally transverse isotropy (HTI), like vertically fractured medium. These models have been used to describe how physical properties of rock vary in a medium. Identifying the anisotropy in a formation is important in reservoir characterization seismic data processing and oil-field development.

Deep shales are the most abundant yet least characterized sedimentary rocks in the Williston Basin of North Dakota. They are significant sources of hydrocarbon unconventional resources in this basin. This dissertation aims to fulfill an investigation of anisotropy in this rock type in several different facets through exploiting of field data. I seek to generate key information for better interplay of field in-situ stress and the existing

natural fracture systems for the purpose of drilling, well completion, perforating, hydraulic fracturing and defining reservoir properties.

In this study advanced sonic logging data has been processed and interpreted to calculate three independent shear moduli. These parameters then will be used to estimate Thomsen (1986) anisotropy parameters, elastic stiffness coefficients and principal stresses of deep shales in the Williston Basin. The parameters then will be used to generate shear radial profiles and slowness-frequency plots analyze formation anisotropy type and origin as well as reservoir quality.

The next step will be to evaluate direction and magnitude of the minimum and maximum anisotropic principal horizontal stresses as the governing element in geomechanical modeling. I will analyze wellbore stability and predict wellbore behavior under stress alteration caused by drilling. Elastic anisotropy of the formation will be included in the 3-D numerical models. In addition the effects of local geological features on the mode of anisotropy both in the far-field and around the borehole to get an in-depth insight of the fractures will be studied. Finally, by generating stress polygons for the reservoir, before and after production and pressure decline, I will try to study how reservoir depletion may cause future geological natural hazards such as faulting and induced seismic events in the region.

Chapter I

INTRODUCTION

Motivations

The Bakken Formation in the Williston Basin is an unconventional reservoir that has been one of the major producers of oil for almost 50 years. Recently with new advancements in horizontal drilling, hydraulic fracturing and Enhanced Oil Recovery (EOR) techniques, this formation is considered one of the most prolific oil shale layers in the U.S. All these have highly increased oil production from the Bakken reservoir, resulting in North Dakota becoming the second oil producer in the U.S. Innovative production technology in the Bakken has introduced new challenges to the oil industry involved with successful stimulation plans, field horizontal drilling operations and wellbore stability found specifically in shales. Considering that shales are also the main constituent of all the sedimentary basins around the world, I needed to address the problems encountered in tight shale oil layers while performing field operations. Geomechanical modeling, which plays a significant role for a successful field operation, is one of the major concerns. We need to characterize shales and their elastic parameters initially and input these characteristics in further modeling steps to improve geomechanical and wellbore stability analysis in horizontal, inclined and vertical wells. Additionally, I am calling for further studies to examine how production from this

reservoir can cause geologic hazards such as large scale induced seismic events in the region.

Organization of This Thesis

This thesis presents various subjects that will help to better characterize the Bakken Formation. I have tried to address problems encountered with geomechanical and geophysical modeling of the Bakken Formation and to improve the previous numerical models that have been developed. The main objective of this research is to include anisotropic behavior of the Bakken Formation in geomechanical modeling which has been neglected in many previous studies. Anisotropic behavior of the Bakken Formation is believed to originate from the presence of platy shaped clay minerals throughout this rock unit. Recent improvements in sonic logging have facilitated the measurement of anisotropy in the field. These measurements are used as input parameters in most of the models in this thesis. Anisotropic versus isotropic models have been created and compared.

Chapter 1 discusses different shale plays and how they are distributed geographically throughout the U.S. as well as their importance. A brief geological and operational history in the Williston Basin where the Bakken Formation extends is provided as well.

Chapter 2 is dedicated to well log data analysis and data preparation as the main input parameters for further chapter. Three wells have been chosen for this research in three different oil fields located in two different counties in North Dakota. Density, gamma ray, compressional and shear wave velocities, both slow and fast, along with anisotropic elastic moduli have been measured and analyzed through the Bakken Formation. Different types of cross-plots have been generated to distinguish the Bakken Formation

and its three different members. It has been observed how different properties, especially elastic moduli such as Young's modulus and Poisson's ratio, vary between the shaly Upper Bakken (UB) to the silty-limy Middle Bakken (MB) and the shaly Lower Bakken (LB).

Seismic Anisotropy and new improvements for formation characterization are discussed in Chapter 3. This chapter is divided into three main studies and two different wells are featured. The first is located on the crest of the Nesson Anticline, which is the region's primary geological structure. The second well, which is far from the Nesson Anticline, was chosen to see how geological structural features can improve the anisotropy of the Bakken as well as reservoir quality. It starts with a complete study of Thomsen (1986) anisotropy parameters and the differences between each well, plus the cause of this discrepancy. The second part discusses anisotropy origins and indications obtained from slowness-frequency plots also known as dispersion plots for each layer of the Bakken. This chapter closes with a section on shear radial profiling (SRP) analysis to know how it benefits formation evaluation specifically for recognition of permeable units (the Middle Bakken) from impermeable ones (the Upper and Lower Bakkens).

Chapter 4 demonstrates geomechanical modeling and stress analysis around the borehole and at the wellbore wall. In this chapter I have tried to point out how elastic anisotropy of the Bakken can cause a huge impact on numerical geomechanical modeling results and cause changes in stresses' magnitudes around the borehole. Wellbore stability through the Bakken Formation in shale units and the middle member is discussed thoroughly. 3D geomechanical models have been created and wellbore failures in vertical, horizontal and deviated wells including anisotropic properties of the Bakken have been studied. Stress

alteration around the borehole for various well deviation angles is also presented. Finally, I have run a geomechanical model including chemical, thermal and poro-elastic properties of shales in a vertical well to understand wellbore failures. Mohr-Coulomb failure criterion was used, as it is the most widely used criterion in the industry. Conclusions as well as suggestions for the future work are presented in Chapter 5.

U.S. Shale Plays

Significant activities are underway in the U.S. to explore and develop America's shale oil plays. The shale oil plays contain "fine grained, organic rich, sedimentary rocks." The shales are both the source of and the reservoir for oil. They are also defined by the extremely small pore sizes which make them relatively impermeable to fluid flow, unless natural or artificial fractures occur.

To gain a better understanding of the potential U.S. domestic shale oil resources, Energy Information Administration (EIA) commissioned INTEK, Inc. to develop an assessment of onshore Lower 48 States technically recoverable shale oil resources (EIA, 2010). This report estimates shale oil resources for the undeveloped portions of 20 shale plays that have been discovered. Eight of those shale plays are subdivided into 2 or 3 areas, resulting in a total of 29 separate resource assessments. The map in Figure 1 shows the location of the shale plays in the Lower 48 States.

According to the shale report's assessment there are 23.9 billion barrels of recoverable of shale oil in the onshore Lower 48 States. The largest shale oil formation is the Monterey/Santos play in southern California, which is estimated to hold 15.4 billion barrels or 64 percent of the total shale oil resources. The Monterey shale play is the

primary source rock for the conventional oil reservoirs found in the Santa Maria and San Joaquin Basins in southern California. The next largest shale oil plays are the Bakken and the Eagle Ford, which are assessed to hold approximately 3.6 billion barrels and 3.4 billion barrels of oil, respectively.

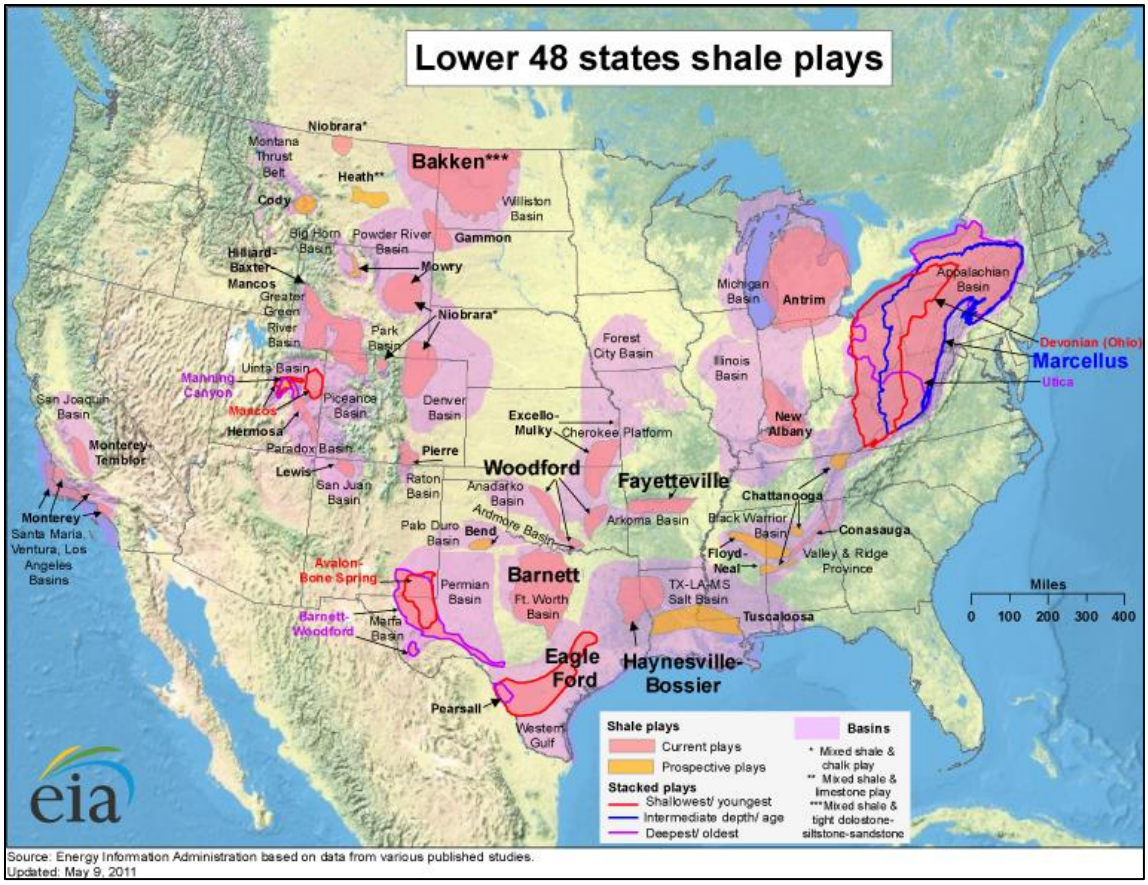

Figure 1 Map of major U.S. shale plays including the Bakken in Williston Basin, ND, (EIA, 2010).

Table 1 summarizes the amount of revocable resources in Billion Barrels of Oil (BBO) of major U.S. shale oil plays with the area of extension in square miles. The Estimated Ultimate Recovery (EUR) in Thousands Barrels (MBO) per well is denoted in the last column.

Table 1 Technically recoverable shale oil recourses summary in the U.S.

Play	Technically Recoverable Resource	Area (sq. miles)	Average EUR
	Oil (BBO)		Oil (MBO/well)
Eagle Ford	3.35	3,323	300
Total Gulf Coast	3.35	3,323	300
Avalon & Bone Springs	1.58	1,313	300
Total Southwest	1.58	1,313	300
Bakken	3.59	6,522	550
Total Rocky Mountain	3.59	6,522	550
Monterey/Santos	15.42	1,752	550
Total West Cost	15.42	1,752	550
Total Lower 48 U.S.	23.94	12,910	460

Bakken Shale Play Overview

The Bakken shale oil play is located within the Williston Basin in Montana and North Dakota and extends into the Canadian provinces of Manitoba and Saskatchewan. This oil field contains 3.6 billion barrels which would be the largest finding in U.S history (EIA, 2011). A net acreage area for Bakken is approximately 6,522 square miles in the U.S. The shale oil play has an average EUR of 550 MBO per well. In 2008, USGS conducted an assessment of the Bakken shale (Pollastro et al., 2008). The total undiscovered resource is estimated between 3,063 and 4,319 MMOE (Million Barrels of Oil Equivalent), with a mean at 3,645 MMBO (Million Barrels of Oil Equivalent) of total continuous resources (EIA, 2011). Figure 2 provides a representative type curve for the Middle Bakken and the Three Forks as the main reservoirs in the Bakken play for the West Williston and East Nesson regions. Figure 3 depicts the proved, probable and possible oil production per day in North Dakota. The amount of produced oil from 1970 until now is shown with the green curve.

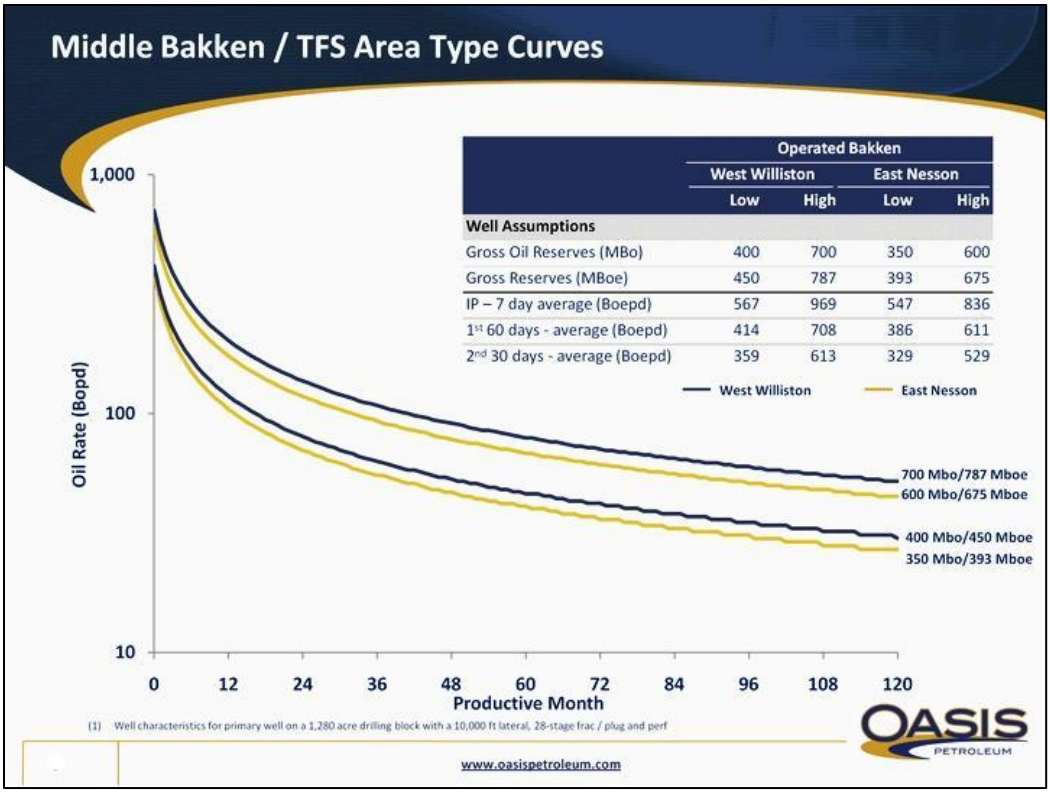

Figure 2 A representative type curve for Middle Bakken and Three Forks as the main reservoirs in the Bakken play for West Williston and East Nesson regions (courtesy of Oasis Petroleum).

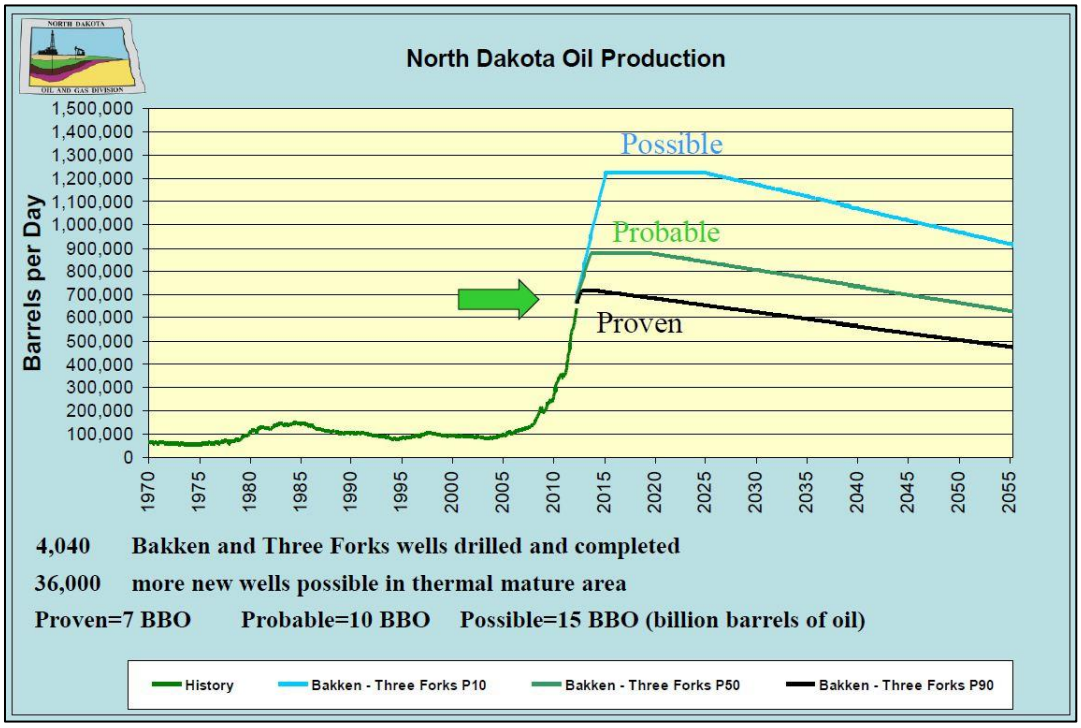

Figure 3 North Dakota oil production, proven, probable and possible barrels per day (courtesy of North Dakota Petroleum Council).

History of the Bakken Formation

USGS assessment (Pollastro et al., 2008) shows that the Upper Devonian-Lower Mississippian Bakken Formation (Pollastro et al., 2008) holds 3.6 billion barrels of technically recoverable oil, 1.85 trillion cubic feet of associated/dissolved gas, and 148 million barrels of natural gas liquids. The Bakken formation consists of three members: the Lower, Middle and Upper Bakken. The main constituent of the Upper and Lower Bakken are dark marine shales with high organic content, while mixed clastics and carbonates have formed the Middle Bakken. The Middle Bakken is considered to be the main producing interval. Oil production from the Bakken goes back to 1950 (Figure 4) when Antelope field discovery took place. The Bakken production and development history then continued by more vertical drilling when the first horizontal well was drilled in the beginning of 1990s. The Parshall Field discovery in 2006 (Nordeng, 2010, Durham, 2009) was a breakthrough in the Bakken production history and caused a skyrocket in the number of horizontal wells drilled in the region. Production from the low permeability Bakken has been significantly enhanced by technologies like horizontal drilling and new stimulation techniques, such as multi-stage hydraulic fracturing. The Bakken is characterized as a "resource play" or "self-sourced" where all the wells are productive, and the petroleum system, source, reservoir and seal are intermixed.

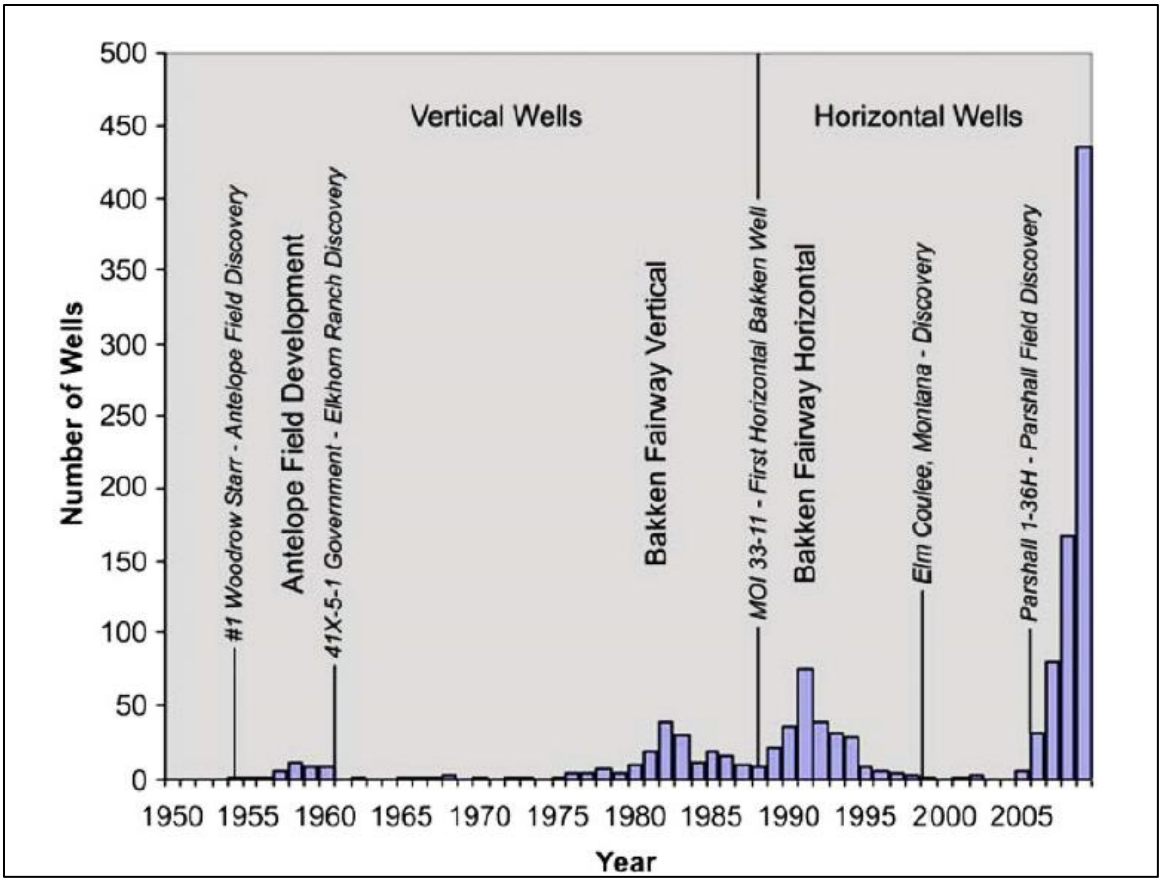

Figure 4 Historic distribution of the Bakken, significant discoveries and technologic advances in Williston Basin (Nordeng, 2010).

Geology of the Bakken Formation

Figure 5 represents how the Williston Basin (an intracrationic basin) occupies half of western North Dakota, portions of eastern Montana, northwestern South Dakota in the U.S. plus southeastern Saskatchewan and southwestern Manitoba in Canada. In North Dakota, the Williston Basin's deepest measurement is almost 14500ft and includes continuous sedimentation from the Cambrian through the Tertiary (Pitman etal., 2001). The middle member, a combination of clastics and carbonates, is sandwiched in between the two marine shales. This is due to the cyclical transgression and regression stages, resulting in the deposition of such sediments and evaporates.

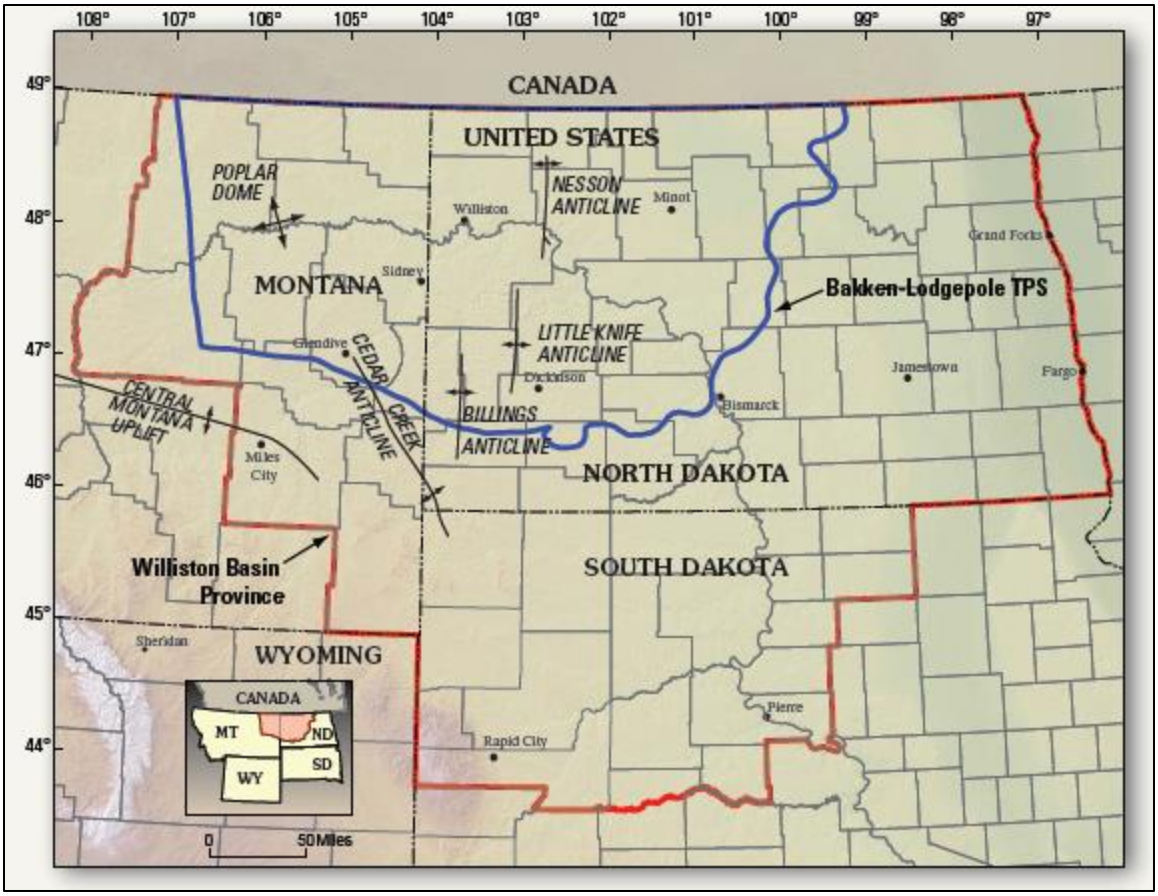

Figure 5 Williston Basin Province (in red), Bakken Lodgepole petroleum system (in blue), with major structural features (Pollastro et al, 2008)

The Bakken Formation as shown in Figure 6 conformably underlies the Mississippian Lodgepole Formation and overlies the Devonian Three Forks in the deeper part of the basin. The boundary between the Bakken and the Three Forks is unconformable along the flanks of the basin (Figure 7). Among the main constituents of the sediments of the Three Forks Formation, interbedded dolomitic and argillaceous shales and siltstones, silty and argillaceous dolomite, mudstones, and anhydrite (Karasinski, 2006) are found extensively. The major constituent sediments of the Lodgepole Formation are dark argillaceous limestones that are cherty and fossiliferous in the basin center. Along the margins of the basin these carbonates are interbedded with lighter colored peloidal,

fossiliferous, and occasionally oolitic limestone beds which are separated by darker colored shales and argillaceous limestones (Grover, 1996).

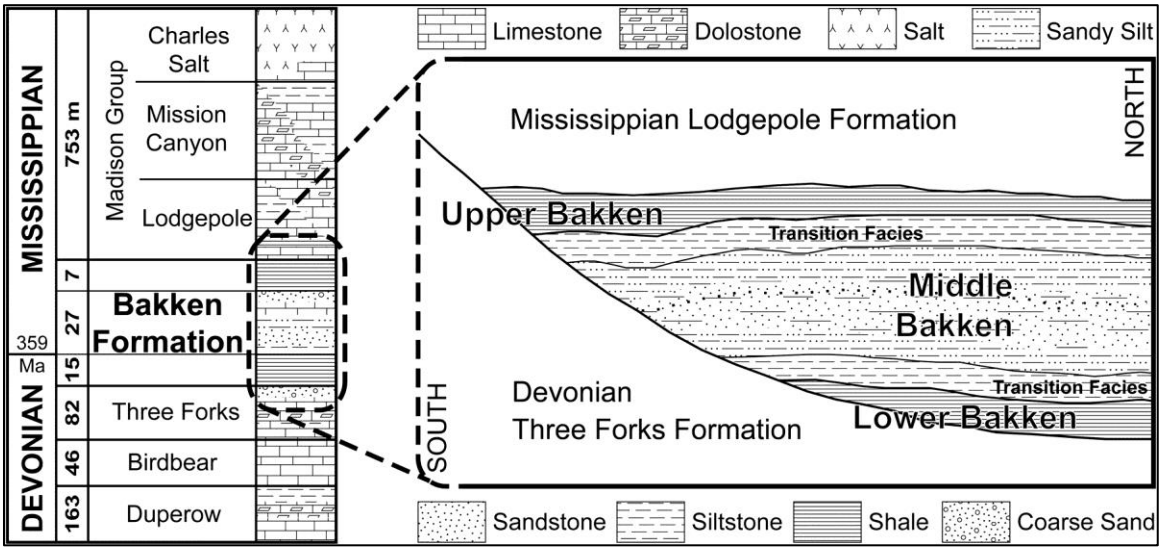

Figure 6 Williston Basin stratigraphic column with the Bakken Formation lithology shown on the right.

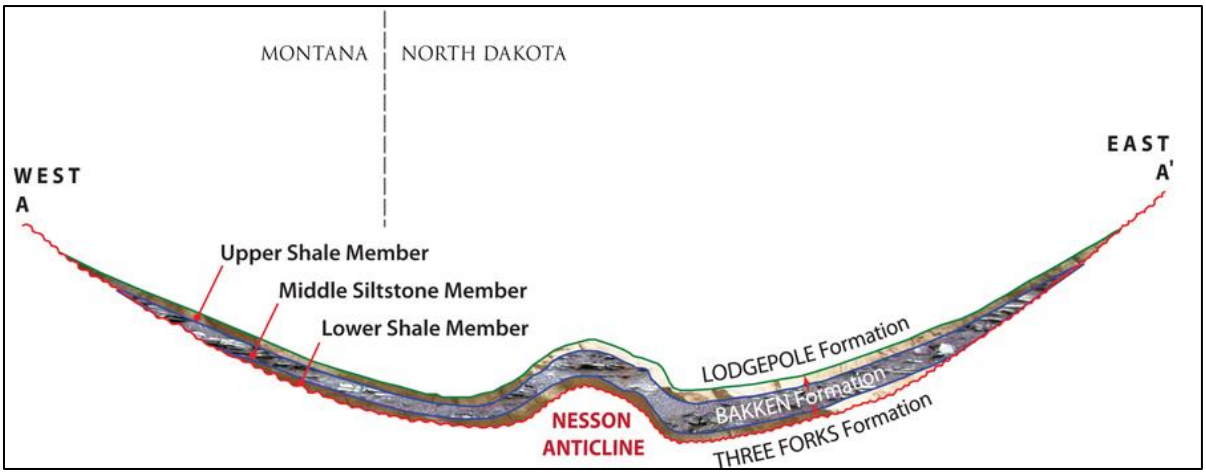

Figure 7 Cross-section of the Bakken through the basin from west to the east with Nesson Anticline in the center of the basin (courtesy of Energy and Environmental Research Center EERC).

The maximum thickness of the Bakken Formation in North Dakota is 160 ft (Figure 8 and 9) which has its well-defined depocenter just east of the north-south trend Nesson Anticline (LeFever, 2008). Considering the geological structures in the Williston Basin in

North Dakota, Nesson Anticline, Little-knife Aniticline and Billings Aniticline all trending north-south can be mentioned where Nesson Anticline (Figure 5) is the major one and plays a significant role in the productivity of the wells which will be discussed in Chapter 3. As previously discussed, the Bakken Formation is the result of sea level fluctuations. The Lower Bakken (dark-gray to brownish-black to black, fissile, slightly to highly organic rich shale which is locally calcareous at the base) is deposited in an offshore marine environment during periods of sea-level rise; the Middle Bakken was deposited in a coastal environment during a rapid sea-level drop and then followed by another sea-level rise during which the Upper Bakken dark-gray to brownish-black, slightly calcareous, organic-rich shales were deposited (Webster, 1982; LeFever et al.,1991; Smith, 1996 and Hayes, 1984).

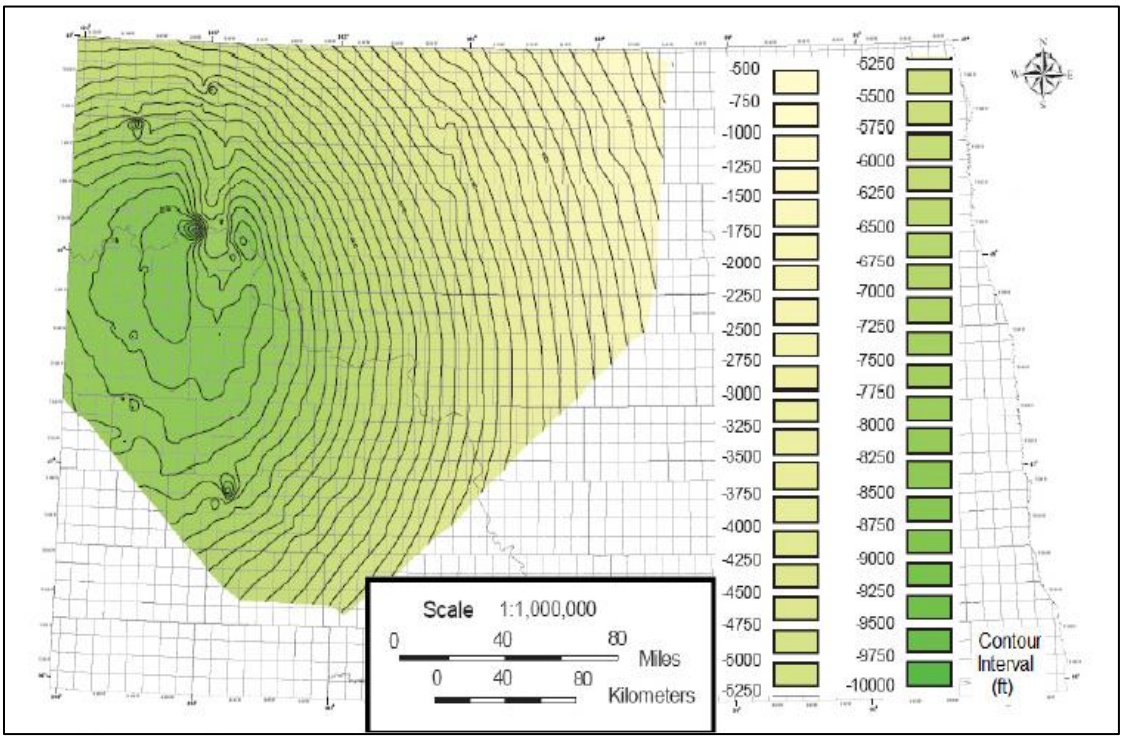

Figure 8 Structure contour map for top of the Bakken Formation (Lefever, 2008).

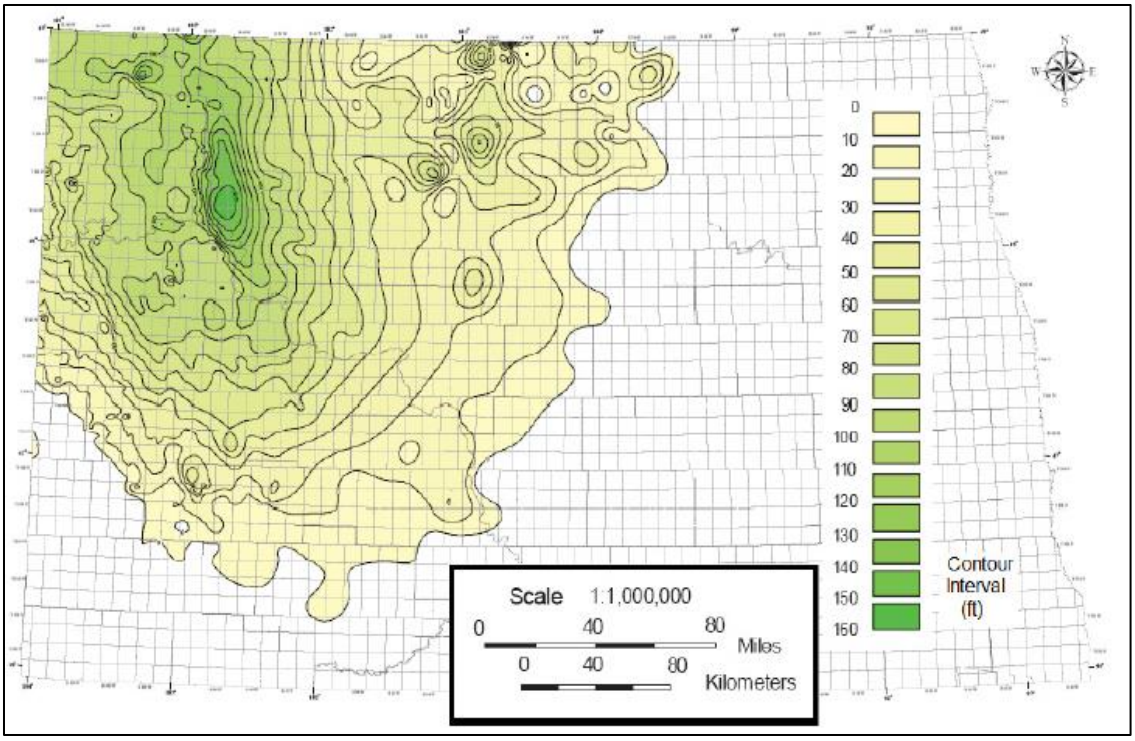

Figure 9 Isopach map of the Bakken Formation (Lefever, 2008).

Although both of the upper and lower members are shaly and look similar, detailed geological studies show that crystallized limestones and greenish-gray shale beds can be found in the lower member whereas they don't exist in the upper member (Pitman et al., 2001; LeFever, 2008). The Middle Bakken is highly heterogeneous and its lithology varies significantly in the region ranging from calcareous siltstones to sandstones dominated by quartz with minor amounts of feldspar, to dolostones, silty limestones, and occasionally oolitic limestone (Pitman et al., 2001; LeFever, 2008). It has been proved that the lithology of the middle member has a main effect on the productivity of the wells.

The Upper and Lower Bakken shales are both source and seals. Most oil generated was expelled into the Middle Bakken and did not migrate into the overlying Madison group

(Price and LeFever, 1994). The thermal maturity of shales varies widely and has an important influence on the reservoir quality of the Middle Bakken (Pitman et al., 2001). The very low permeability of the upper and lower shale members, which vary from 0.01 mD to 20 mD, serves as a very effective seal for the middle member reservoir. The middle member is believed to be the reservoir and has very low porosity (1% - 15%) and permeability (0 - 20 millidarcies), particularly for being a reservoir rock. The Bakken Formation and its members are easily recognizable on geophysical well logs because of their high gamma ray and resistivity signature response in upper and lower shale units (Figure 10).

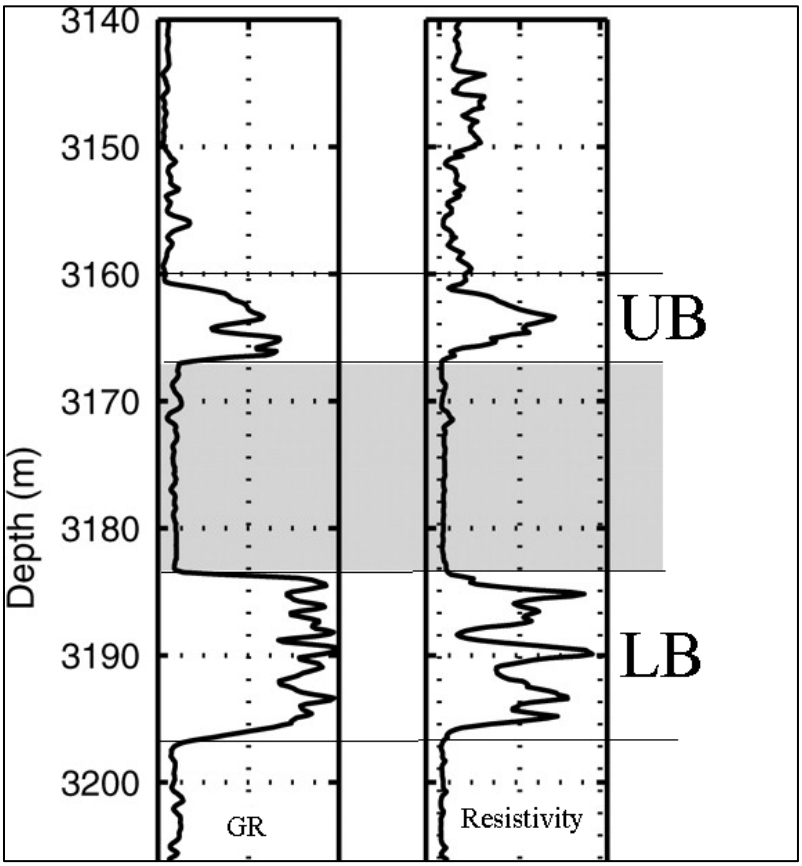

Figure 10 A typical Bakken gamma ray and resistivity log response (The gray area represents middle member).

Chapter II

GEOPHYSICAL WELL LOG ANALYSIS

Introduction

The geographic area in this study is located in Mountrail County and Divide County, North Dakota; the northern and eastern of the Nesson Anticline respectively. Figure 11 shows the well locations. Well 1 is Av-Wrigley located in Divide County, Well 2 is Ruland located on the crest of the Nesson Anticline in Mountrail County and Well 3 is Sikes State located to the east of the Nesson Anticline in Mountrail County. Av-Wrigley is located in the Forthun oil field, Sikes State is producing in Sanish field (one of the major oil fields in the Williston Basin) and Ruland is producing in the Manitou oil field.

Well log data was acquired by Sonic Scanner tool (MSIP) developed by Schlumberger which can provide axial, azimuthal and radial measurements, including shear wave propagation for both fast and slow shear waves. Sonic Scanner tool specifications will be discussed later in more detail in chapter 3.

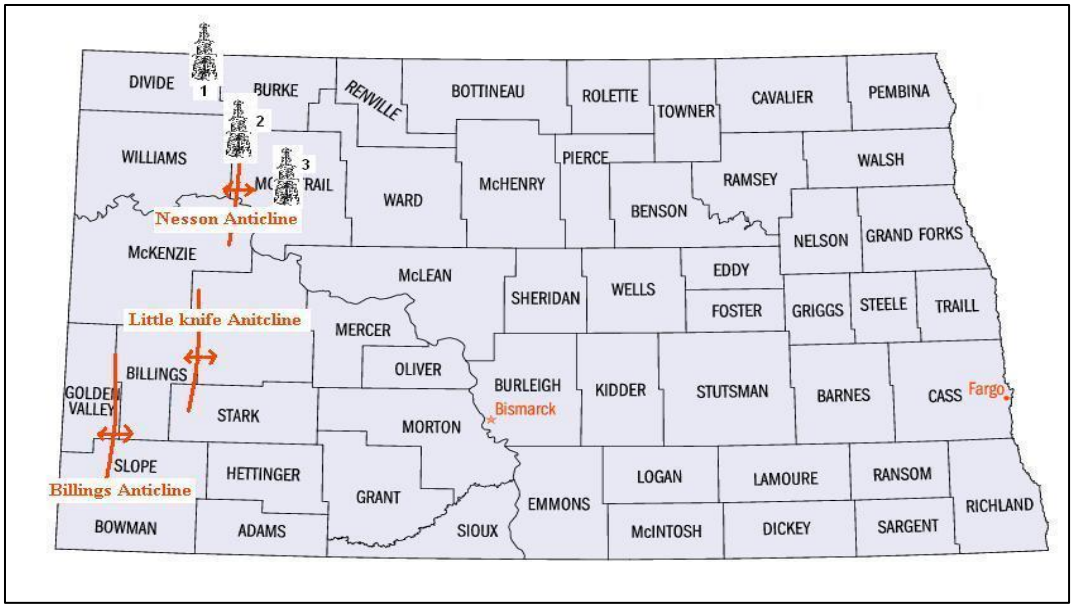

Figure 11 Geographic representation of wells understudy plus the major geologic features in the area.

Data Analysis

Well log data including depth and thickness, density, velocity for compressional wave, shear wave both fast and slow and Stoneley wave with V_p/V_s ratio were analyzed. Elastic moduli such as Young's modulus both in vertical and horizontal directions and Poisson's ratio in horizontal and vertical directions have been evaluated as well. The purpose of analyzing the well log data is to construct geomechanical models to study wellbore stability and the stresses around the borehole as well as the seismic anisotropy.

Figure 12 shows the well log data for Av-Wrigley well. The Bakken Formation can be identified in the log suite specifically from the gamma ray response. The Upper and Lower Bakken shales have very high gamma ray responses compared to the middle member and the LodgePole and the Three Forks Formations. Figure 13 represents well log suite for the Ruland well and Figure 14 depicts the same set of logs for the Sikes State well. Well log data analysis is performed using Hampson-Russell software. More

sophisticated data processing and interpretation was carried out at Schlumberger Data Consulting Services (DCS) in using GeoFrame software, Best DeltaT module.

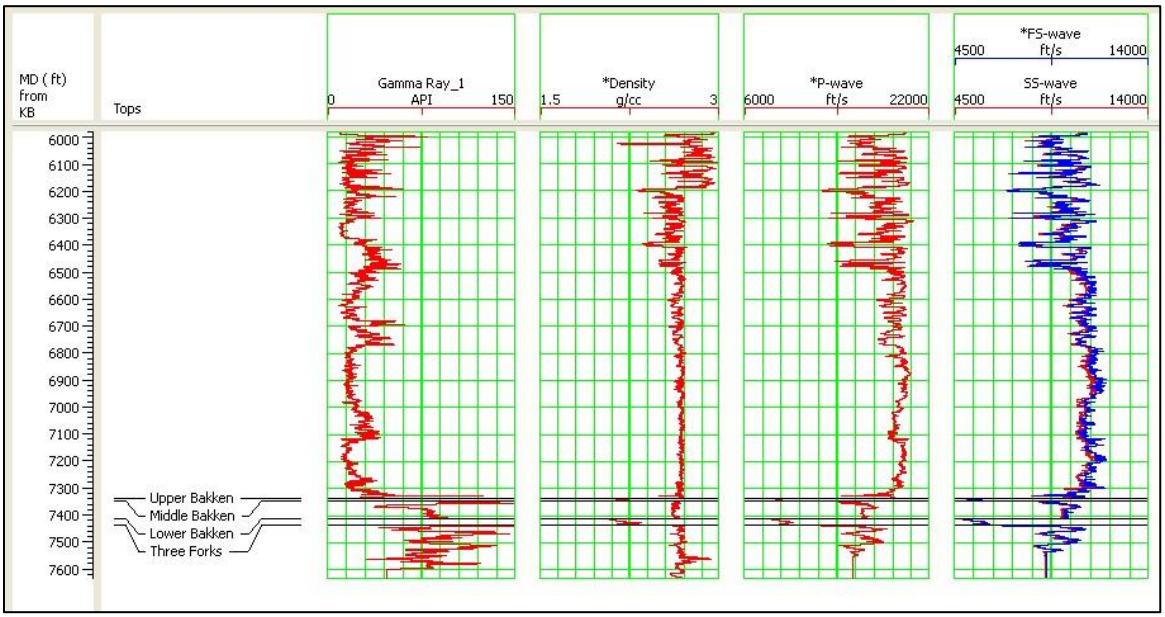

Figure 12 Av-Wrigley log suite, Gamma ray first track, Density second track, P-wave velocity third track, Shear wave velocity(fast and slow) fourth track.

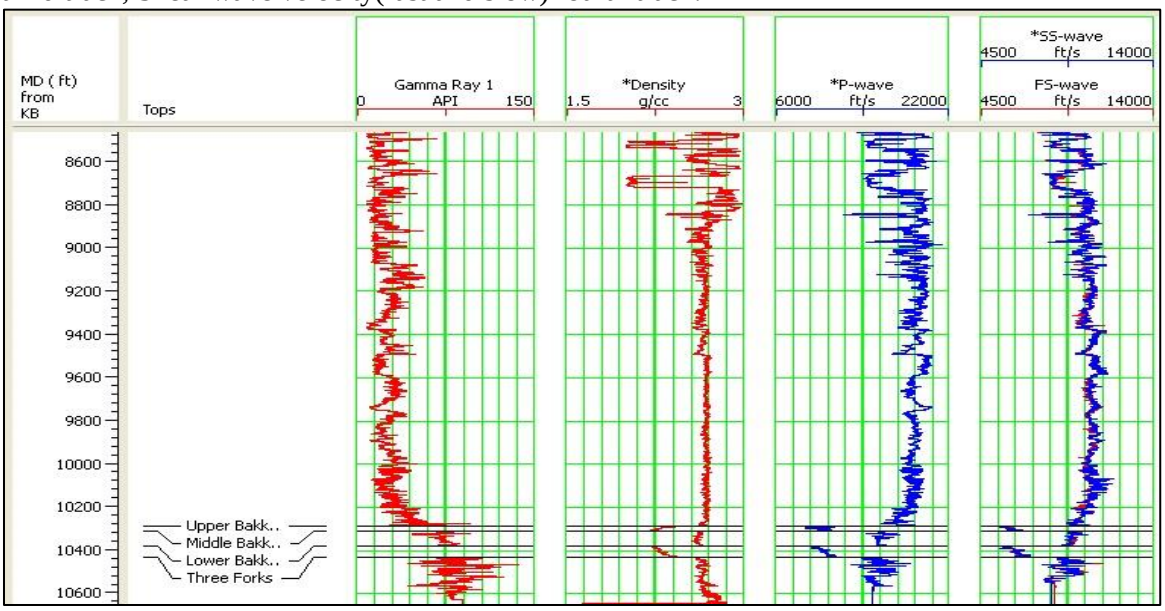

Figure 13 Ruland well log suite, Gamma ray first track, Density second track, P-wave velocity third track, Shear wave velocity (fast and slow) fourth track.

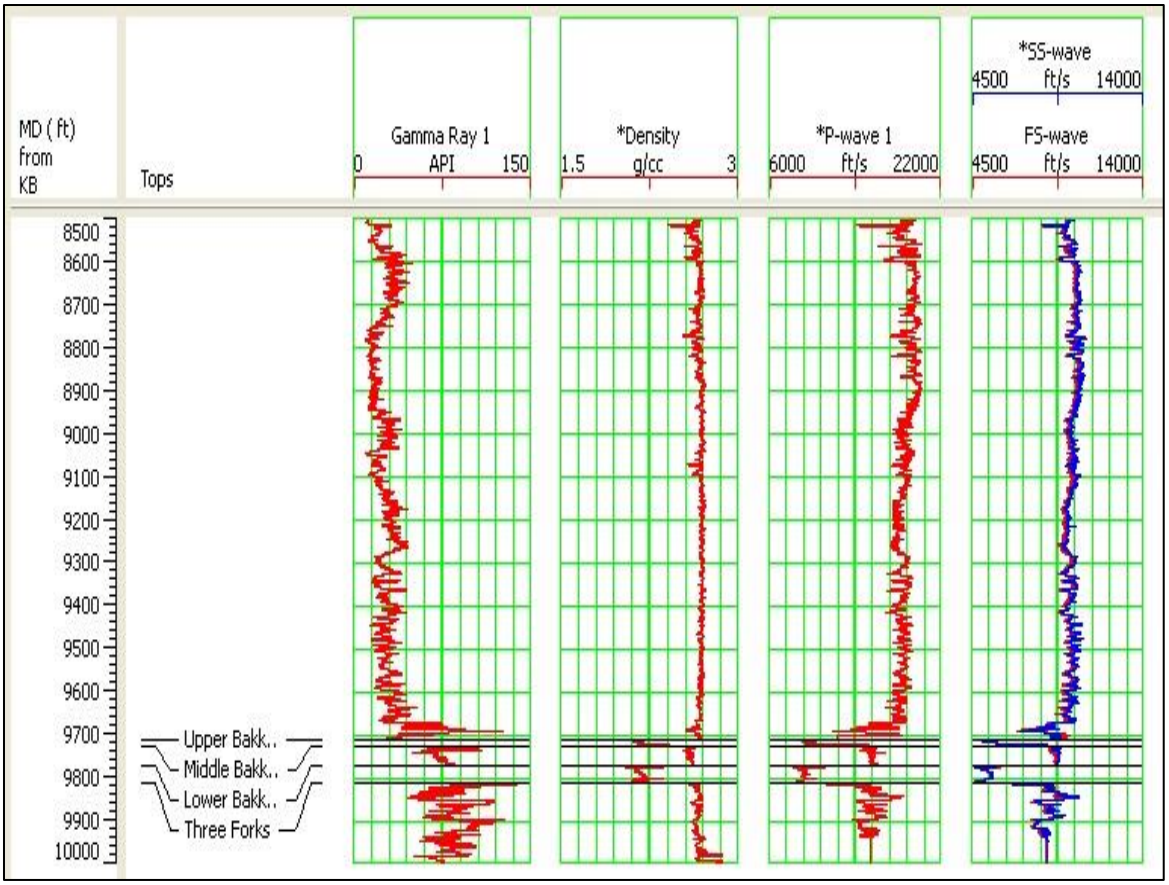

Figure 14 Sikes State log suite, Gamma ray first track, Density second track, P-wave velocity third track, Shear wave velocity (fast and slow) fourth track.

Depth and Thickness

Figure 15 is a summary of the depth and thickness of the Bakken interval in each of the wells. The Bakken Formation is at a depth of about 10000ft. It is deeper in the Sanish Field and shallower in the Forthun Field. The Sanish Field and the Manitou Filed are located in the center of the basin around the depocenter while the Forthun Field in the north is located around the margins of the basin. The average depth of the Bakken is about 10000ft in the Sanish Field and 7300ft in the Forthun Field (Table 2). The difference of the average depth between the two fields is about 2700ft.

Table 2 Depth and Thickness of the Bakken Formation.

Number	Well	Field	Bakken Top Depth (ft)	Thickness (ft)			
				Bakken	UB	MB	LB
1	Wrigley	Forthun	7311	99	12	65	22
2	Ruland	Sanish	10268	143	21	67	55
3	Sikes State	Sanish	9682	104	16	47	41

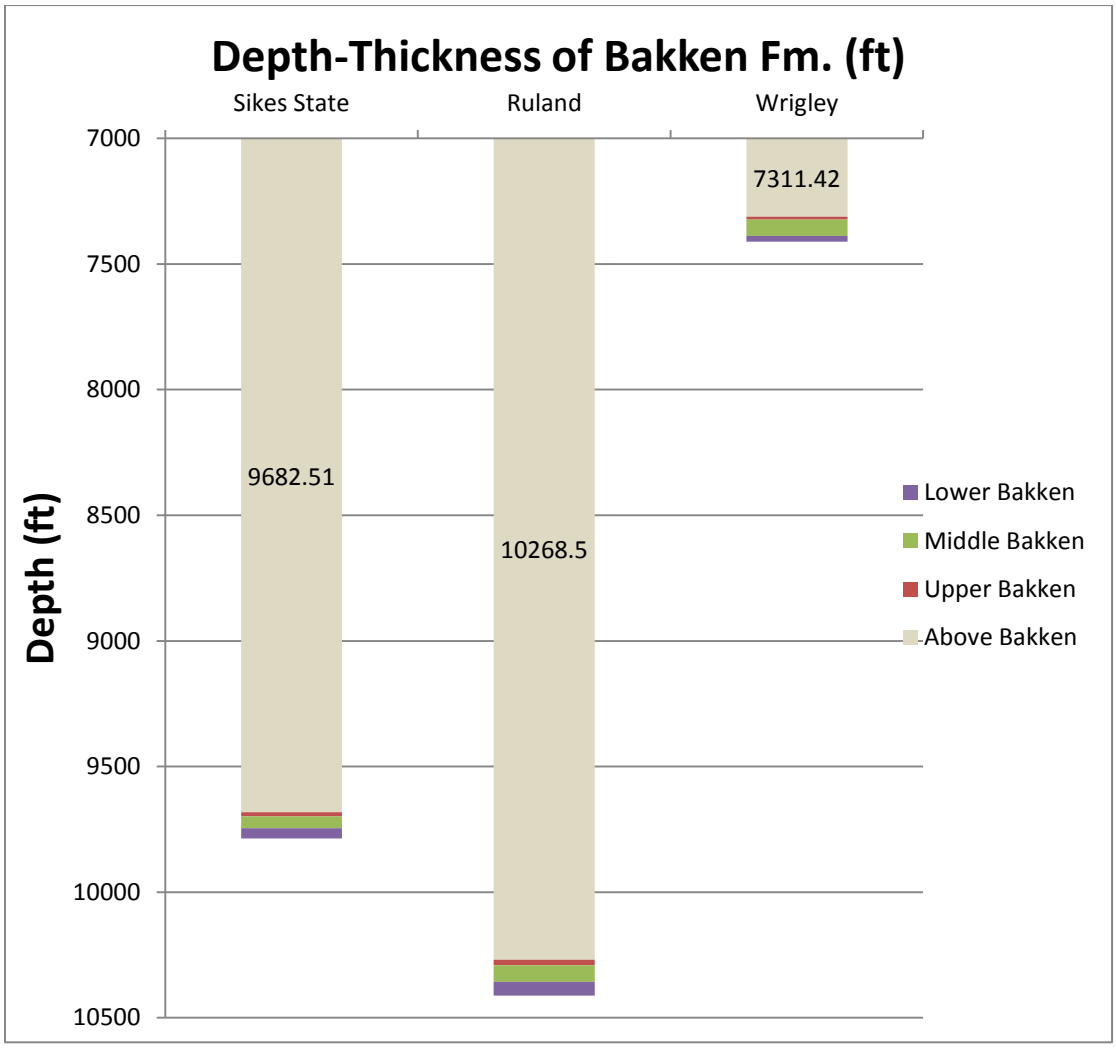

Figure 15 Thickness and depth of the Bakken Formation and the three members in the wells.

Density

Figure 16 shows the bulk density of the Upper, Middle and Lower Bakken at each of the wells. Figure 17 shows the average density values in the three members of the Bakken Formation. The density decreases dramatically at the Upper and Lower Bakken shales when compared to upper and lower Lodgepole and the Three Forks Formations. The density log shows that the Middle Bakken has lower density than the Lodgepole and the Three Forks due to the higher clay volume of this unit. Density values don't change enormously in these three wells. The average density is about 2.18 g/cm^3 for the Upper Bakken, 2.25 g/cm^{3}for the Lower Bakken and 2.62 g/cm3 for the Middle Bakken. The changes in densities are due to the change in the mineralogical composition of each unit.

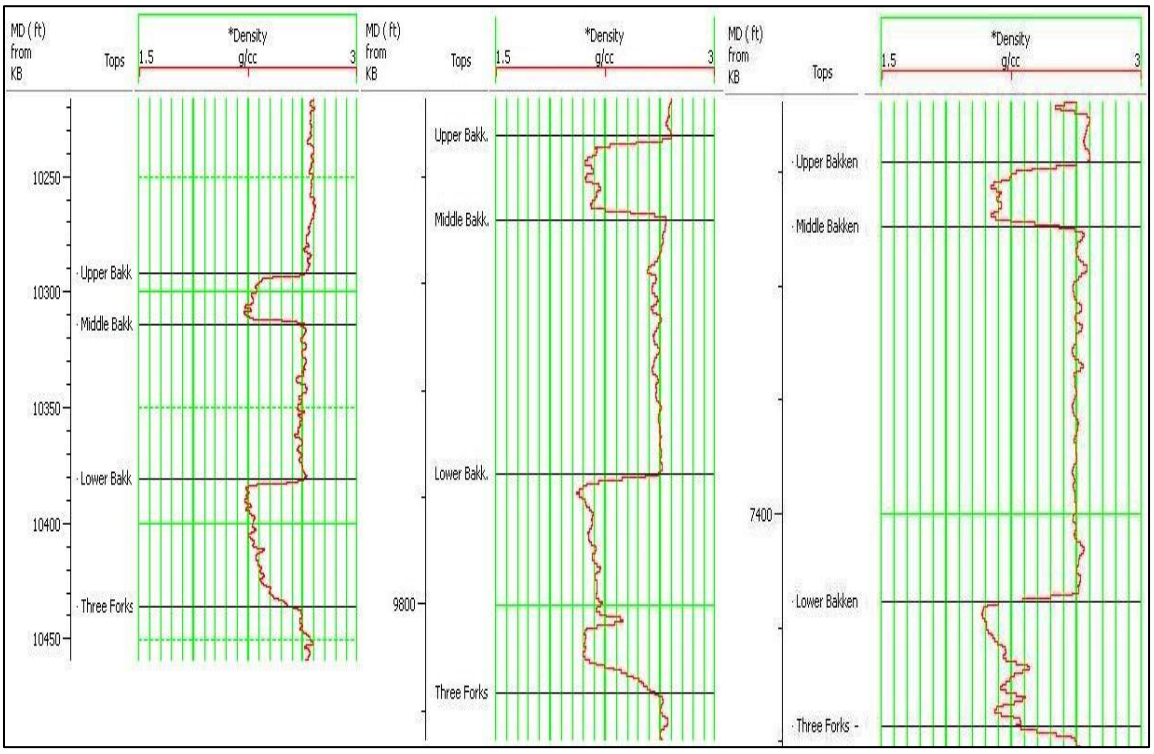

Figure 16 Density of the Bakken Formation through the wells, from left: Ruland, Sikes State and Wrigley.

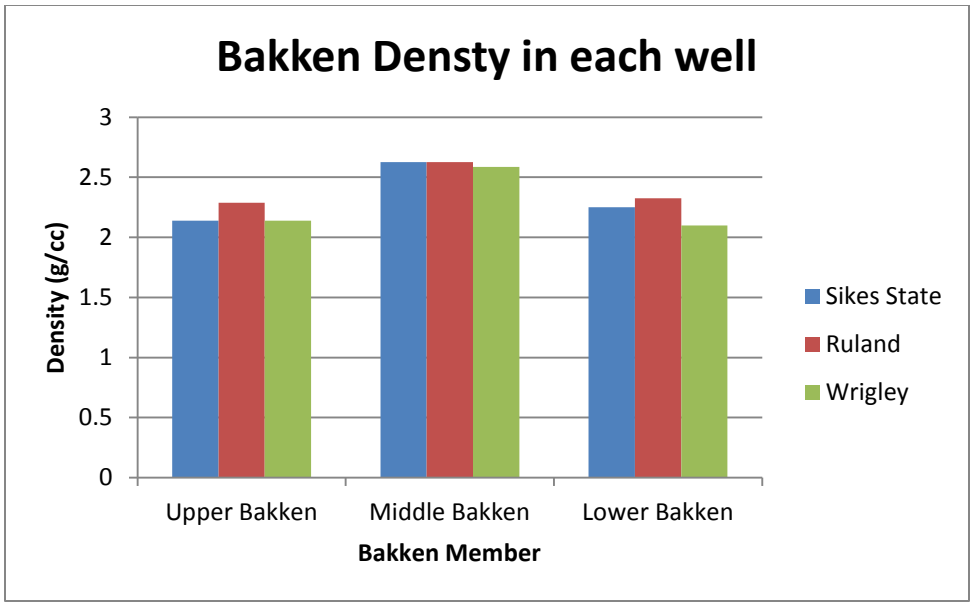

Figure 17 Bakken members average density variation in each well.

Velocity

Both the compressional (P) wave and shear (S) wave velocities (fast, slow and Stoneley) are plotted in Figure 18 and Figure 19. The average values are shown in Table 3. The Upper and Lower Bakken similarly have lower velocities compared to the middle member and Lodgepole-Three Forks. Velocity decreases sharply from the Lodgepole to the Upper Bakken both in P & S-wave velocities. Calculations show that the average velocity decline from Lodgepole to Lower Bakken for P wave velocity is almost 50% from 18000 ft/s to 9500 ft/s and S wave velocity drops 40% from 10500 ft/s to 6000 ft/s. There are also slight velocity variations within the middle member due to the interval lithology changes and heterogeneous nature of the Middle Bakken which can vary from siltstone to limestone, dolomite and sandstone with various clay volumes. The average P-wave velocity is about 9550 ft/s for the Upper and Lower Bakken and about 16000 ft/s for the Middle Bakken. The average fast shear-wave velocity is about 5550 ft/s for the Upper and Lower Bakken and around 9400 ft/s for the Middle Bakken. Due to

anisotropic behavior of upper and lower members (which will be discussed in the next chapter), the fast and slow shear waves' average velocities are expected to be similar. The slow shear wave average velocity in middle member is 9000ft/s which is 400ft/s less than the velocity value for the fast shear wave velocity. This change is due to the presence of vertical fractures in the Middle Bakken which will be addressed thoroughly in further chapters.

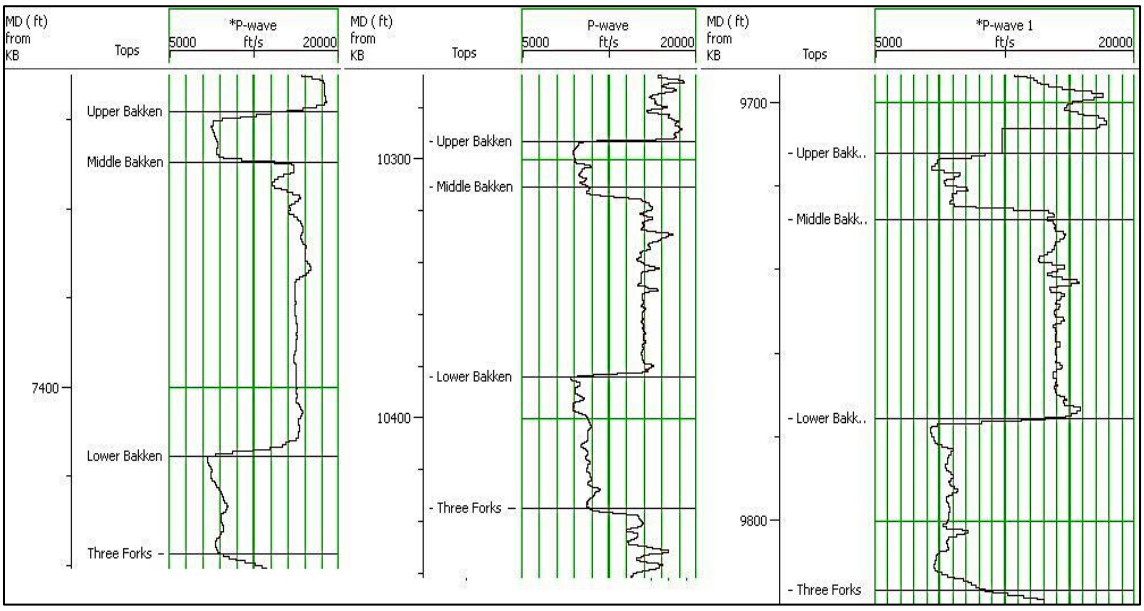

Figure 18 Compressional wave velocities (ft/s), for the wells, from left: Wrigley, Ruland and Sikes State.

Table 3 Average compressional and shear wave velocity (ft/s) values for each member of the Bakken Formation.

	P wave (ft/s)	Fast shear wave (ft/s)	Slow shear wave (ft/s)	Stoneley wave (ft/s)
Upper Bakken	9500	5500	5500	3812.5
Middle Bakken	15750	9375	9000	4000
Lower Bakken	9625	5625	5625	3812.5

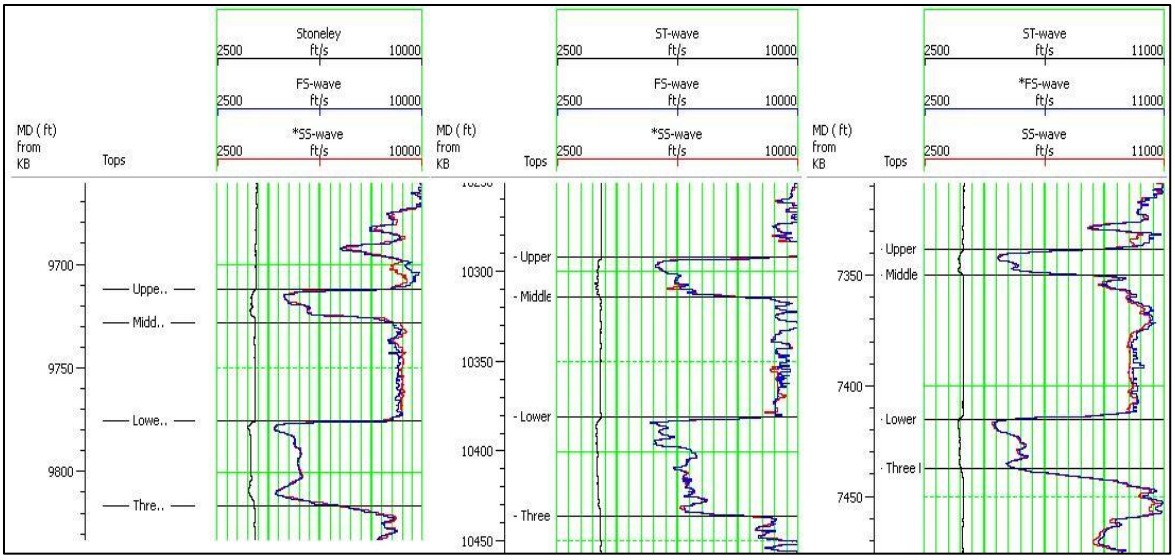

Figure 19 Shear (fast (blue), slow (red) and Stoneley (black)) wave velocities (ft/s), for each well, from left: Sikes State, Ruland and Wrigley.

One of the distinct features of the shear wave propagating through an anisotropic medium is splitting (birefringence) into two different components, which has been observed in both laboratory and in physical models (Cheadle et al., 1991) as well as in the field (Mueller, 1992). In a medium with vertically aligned fractures the near vertical propagated shear wave, fast shear (FS), will be polarized parallel to the fracture orientation and slow shear (SS) is polarized perpendicular to the fracture orientation which causes it to travel slower. The Sonic Scanner is an advanced acoustic logging tool capable of measuring the fast shear and slow shear velocities as well as the Stoneley wave velocity. Stoneley wave is the shear wave propagating in the horizontal direction. Looking closer at Figure 19, it was found that the fast and slow shear waves are overlapping in UB and LB while they show some level of splitting in MB. This phenomenon can be an evidence of the presence of vertical natural fractures.

V_p/V_s Ratio

V_p/V_s ratio is the ratio of P-wave and S-wave velocities. Studies show that there is a correlation between V_p/V_s ratio and lithology (Castagna, et. Al., 1985 and Tatham and McCormack, 1991). The typical V_p/V_s value is from 1.84 to 1.99 for limestone, from 1.78 to 1.84 for dolomite, from1.59 to1.76 for sandstone and from 1.70 to 3.00 for shale (Tatham and McCormack, 1991). The V_p/V_s value of shale is in a rather broader range, and is usually higher than the V_p/V_s value of sandstone, particularly in porous clastic sequences. Figure 20 shows the V_p/V_s ratio of the Bakken Formation in each well.

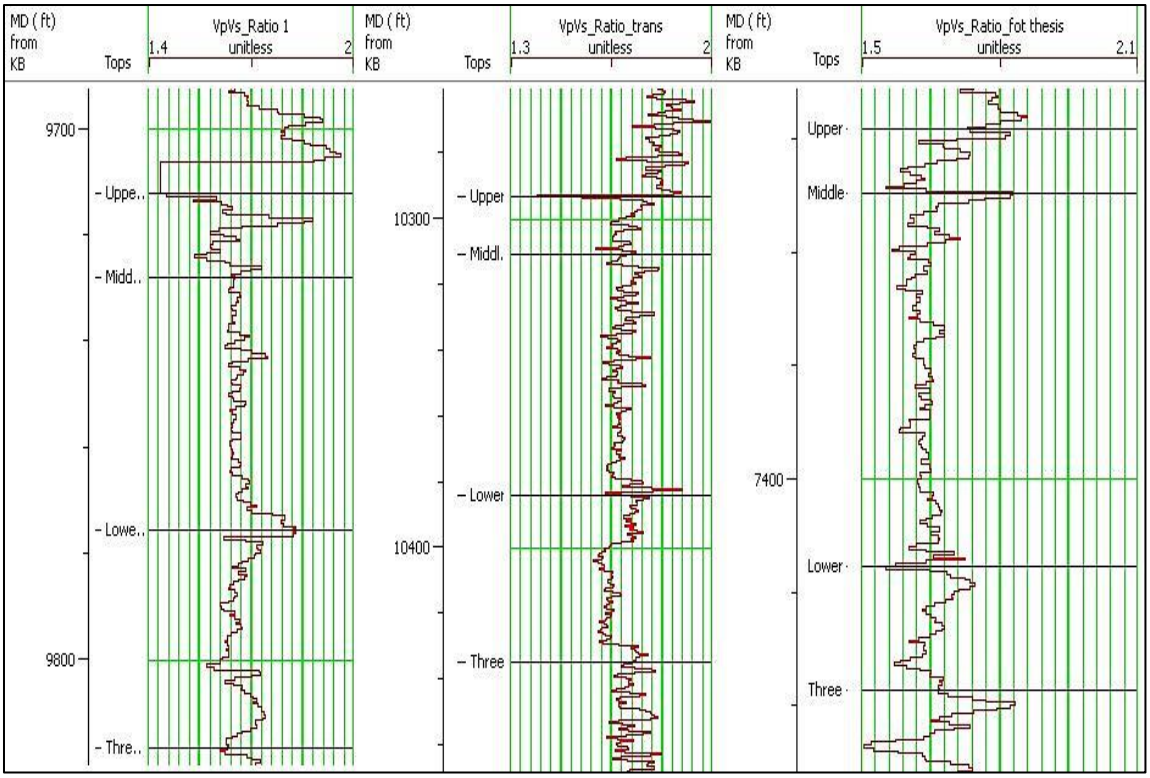

Figure 20 V_p/V_s ratio in three wells. From left to right: Sikes State, Ruland and Wrigley

Figure 20 illustrates that the V_p/V_s ratio of the Bakken Formation is quite lower than the V_p/V_s ratio of the Lodgepole Formation and the Three Forks which are mainly limestone and dolomite; therefore, they should show higher V_p/V_s ratio. The Upper and Lower

Bakken shales have slightly lower V_p/V_s ratios than the Middle Bakken, suggesting greater siliceous content. The V_p/V_s ratio of the Bakken Shale is about 1.64, which is quite low for clay-rich shales. This was interpreted mainly due to the high kerogen content of these rock units. Table 4 lists the laboratory ultrasonic velocities measured on the Bakken shale samples reported by Vernik and Liu (1997). The average V_p/V_s ratio of 13 dry samples is about 1.67, which is not much higher than the average V_p/V_s ratio that was observed in the log data. It was interesting to see that the oil saturated laboratory sample has the exact V_p/V_s value that was found in the log data.

Table 4 Laboratory ultrasonic measured velocities of the Bakken (from Vernik & Liu, 1997)

Type	V_p (Km/s)	V_s (Km/s)	V_p/V_s	Average of V_p/V_s
Dry	3.13	1.88	1.67	1.67
	3.02	1.76	1.72	
	3.41	2.02	1.65	
	3.38	2.12	1.59	
	3.18	1.93	1.65	
	3.62	2.22	1.63	
	3.36	2.06	1.63	
	3.46	2.00	1.73	
	3.51	2.03	1.73	
	3.29	1.86	1.77	
Brine Saturate	3.34	1.86	1.80	1.80
Oil Saturated	3.96	2.42	1.64	1.64

Young's modulus and Poisson's ratio

When a medium is elastically anisotropic it will show discrepancies in a physical property measured in each direction, whereas in an isotropic medium the measured value

stays the same in all directions. The Sonic Scanner estimates the velocities in both vertical and horizontal directions, thus it is capable of measuring dynamic Young's modulus and Poisson's ratio in both vertical and horizontal directions.

Figures 21-23 depict the dynamic anisotropic horizontal Young's modulus, vertical Young's modulus, vertical and horizontal Poisson's ratio, plus the isotropic shear, bulk and Young's modulus for the Bakken interval. These values are calculated from relationships introduced in chapter 4 (Mavko, et al, 1998) using compressional and shear wave velocities in horizontal and vertical directions with the measured density of the formation.

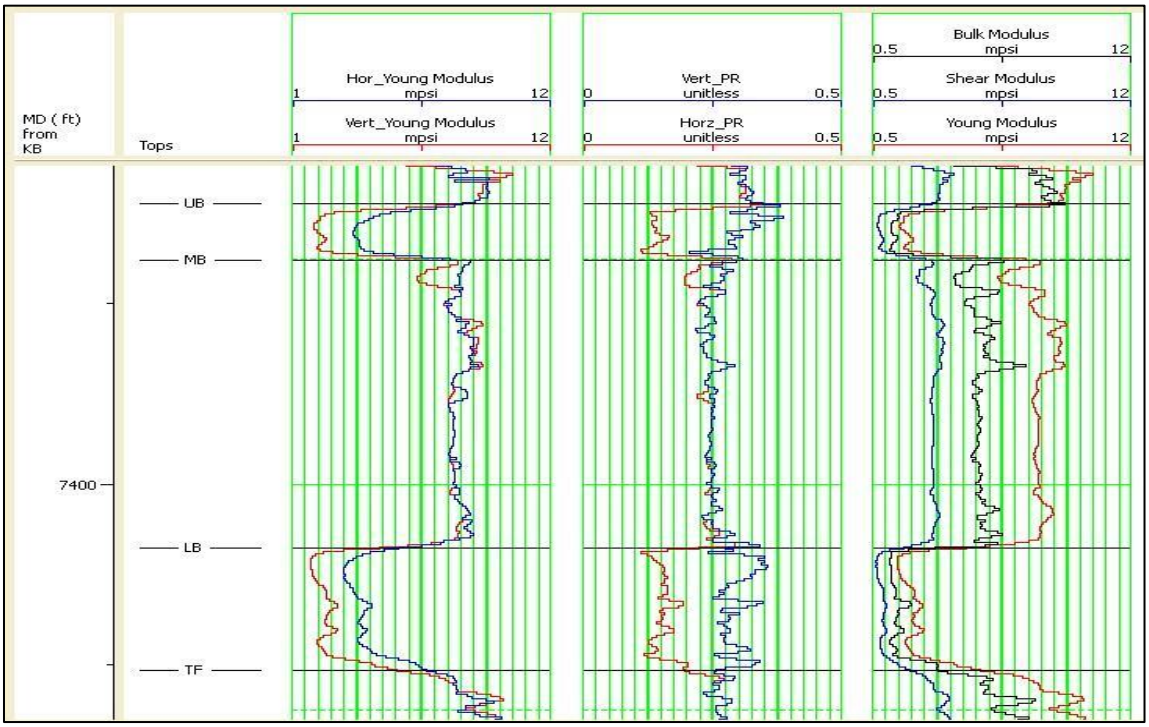

Figure 21 Elastic moduli through the Bakken Formation in the Wrigley well. The first track denotes anisotropic Young's modulus, the second track anisotropic Poisson's ratio, and the third track shows isotropic bulk, shear and Young's modulus.

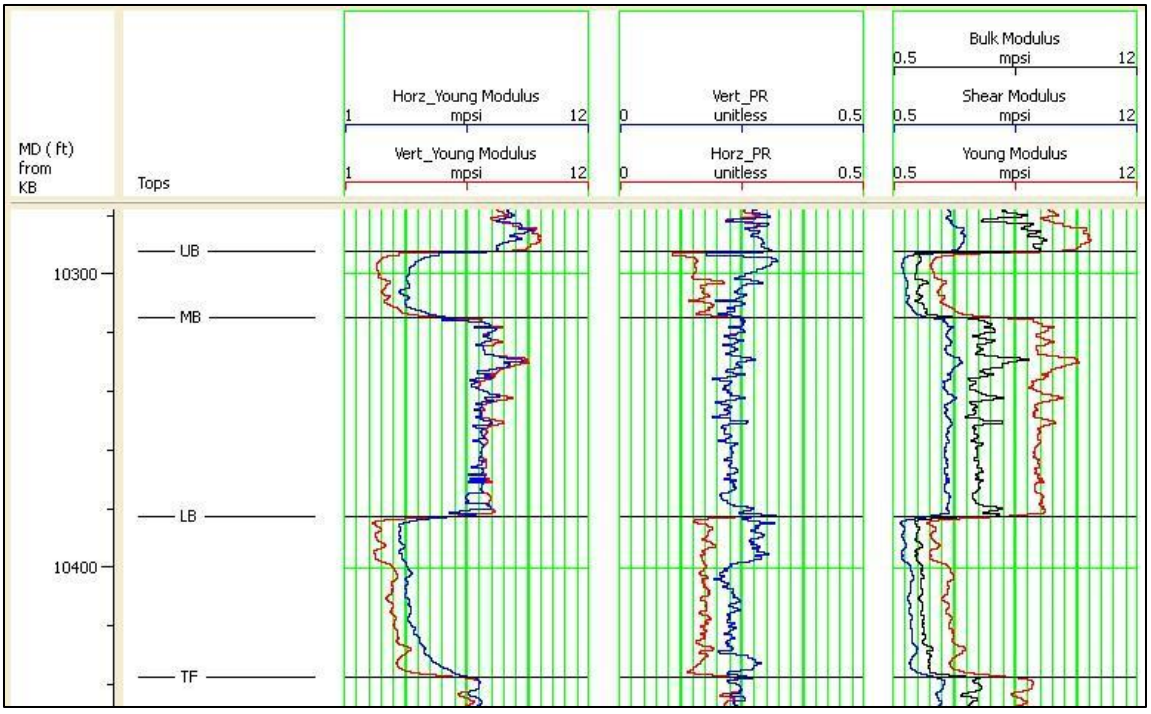

Figure 22 Elastic moduli through the Bakken Formation in the Ruland well. The first track denotes anisotropic Young's modulus, the second track anisotropic Poisson's ratio, and the third track shows isotropic bulk, shear and Young's modulus.

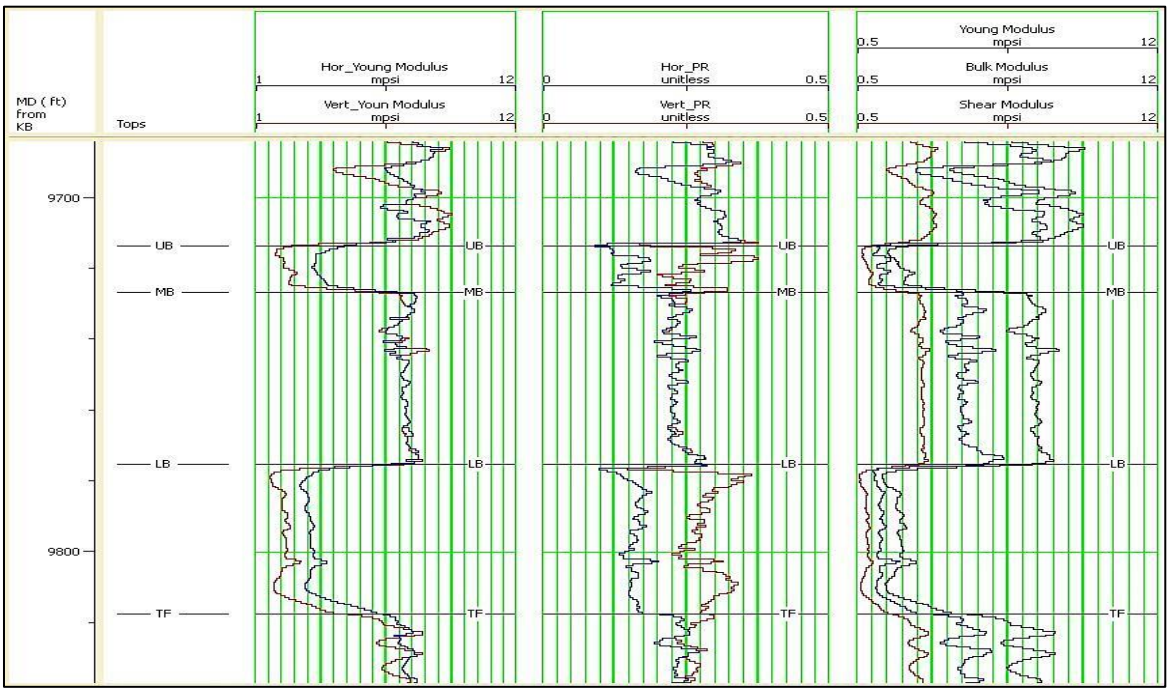

Figure 23 Elastic moduli through the Bakken Formation in the Sikes State well. The first track denotes anisotropic Young's modulus, the second track anisotropic Poisson's ratio, and the third track shows isotropic bulk, shear and Young's modulus.

From the logs it was seen that the Upper and Lower Bakken shales have lower moduli than the middle member, the Three Forks and the Lodgepole intervals. For the Lodgepole, Three Forks and the Middle Bakken, the vertical and horizontal moduli are quiet similar thus show elastic isotropy. It's noteworthy that horizontal and vertical Young's modulus may vary in some specific depths in middle member where the fractures exist. For the Upper and Lower Bakken shales, the vertical Young's modulus is much less than the horizontal Young's modulus. The average horizontal Young's modulus value is 3.75 Mpsi, which is 1.4 times the vertical value (2.65Mpsi). This is interpreted due to the anisotropic behavior of the Bakken Formation in lower and upper shale members. Shales, due to their laminated structure show different elastic properties in vertical and horizontal directions. This concept is discussed extensively in next chapter. It should also be noted that elastic properties, such as the Young's modulus and Poisson's ratio measured by the log, are considered to be the dynamic values and may not truly represent the elastic nature of the rocks.

The vertical and horizontal Poisson's ratio are almost similar in the Lodgepole, the Three Forks and the Middle Bakken. This could be a good indication of the isotropic behavior of these layers however slight dissimilarity can still be observed in two of the wells through middle member. This could be explained by the presence of natural vertical and sub-vertical fractures (see Chapter 4). There is a distinct contrast between the horizontal and vertical Poisson's ratio for the Upper and Lower Bakken shales. The vertical value is much greater than the horizontal value. It can be seen that the average vertical Poisson's ratio of both Upper and Lower Bakken shales is 0.24, which is 1.45 times the average horizontal Poisson's ratio (0.17).

Cross-Plots

Cross-plots are used in well log analysis to calculate from graphs or charts a result based on two or more forms of data. Input data include resistivity, acoustic, and nuclear logging measurements and, if available, core, test, and production data. Applications of specific cross-plot concepts allow recognition of log calibration problems, normalization of basic log measurements, and determination of lithologic reservoir characteristics in clastic and complex mineralogy (Fertl, 1981).

Figure 24 depicts density (g/cc) versus P-wave travel time cross-plot. A cross-plot of sonic travel time (velocity) and formation density can be used to identify the lithology. Two main data clusters could be identified within this cross-plot. By linking the clusters to the corresponding well log data it is revealed that the lithology of upper and lower members is completely distinctive from the lithology of middle member, the Lodgepole and the Three Forks Formations. Setting gamma ray as the color scale will help us to better identify major differences in the lithology of the formation. Figure 25 presents P-wave travel time versus density with gamma ray as the color scale. The Middle Bakken can easily be separated from the upper and lower members since it shows a very high gamma ray signature unlike the upper and lower shaly members.

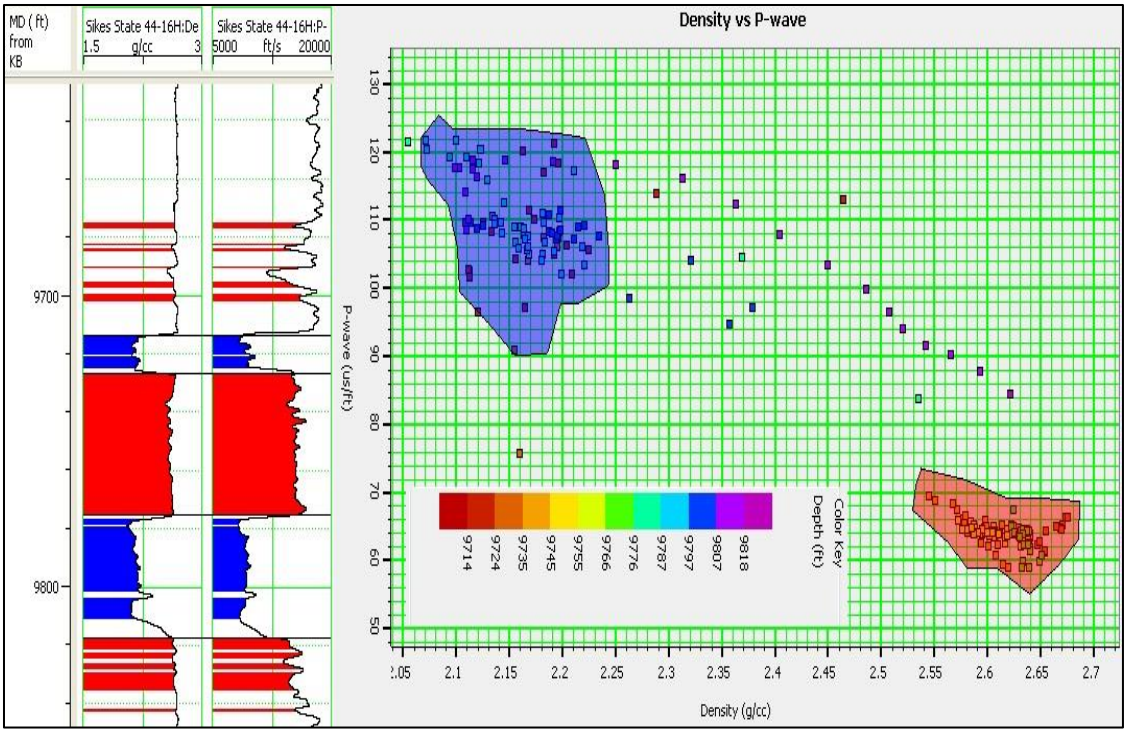

Figure 24 Density versus P-wave travel time cross-plot with depth (ft) as the color scale.

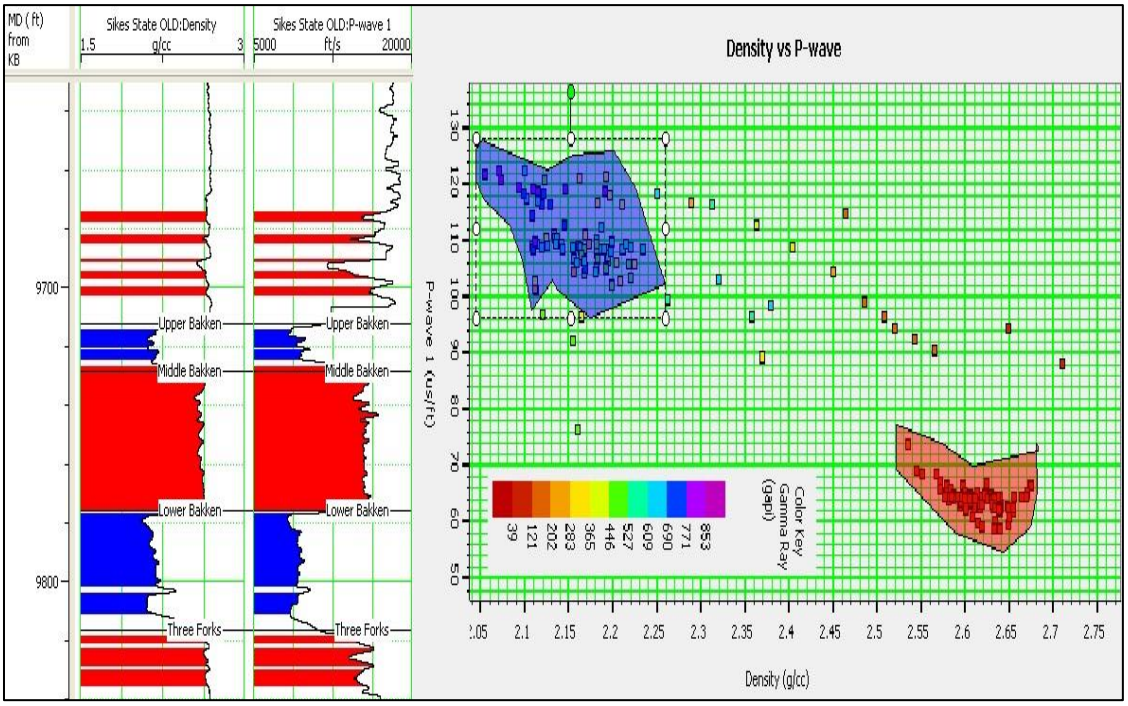

Figure 25 Density versus P-wave travel time cross-plot with gamma ray as the color scale.

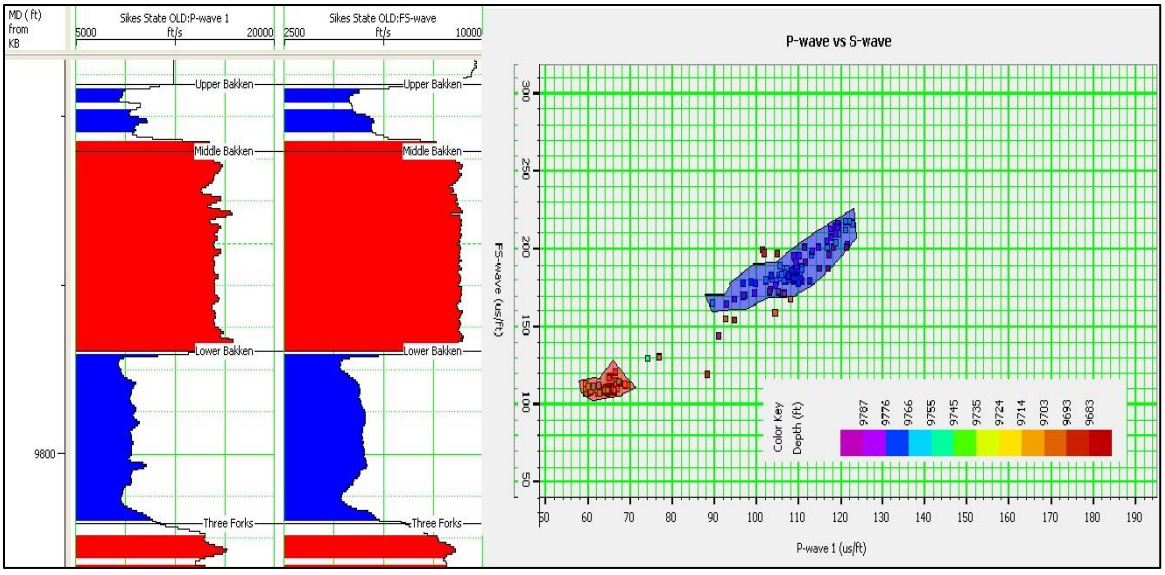

Figure 26 P-wave travel time versus S-wave travel timecross-plot where depth is the color scale.

A compressional wave travel time versus shear wave travel time cross-plot can be very applicable to identify lithology (Castagna, et al, 1984). Figure 26 shows a compressional and shear wave travel time cross-plot. Two very distinct and separate clusters can be seen. The blue cluster represents the shaly units of the Bakken Formation while the red unit with lower travel time is related to the middle member of the Bakken and the underlying Three Forks Formation.

Figure 27 shows vertical Young's modulus versus vertical Poisson's ratio and Figure 28 shows horizontal Young's modulus versus horizontal Poisson's ratio. Considering both, two main data groups can be identified: one is the Upper and Lower Bakken shales marked with red dots and the other one is representing Lodgepole (limestone), Three Forks (limestone) and Middle Bakken (sandstone, siltstone, dolomite and limestone) marked with the blue dots. These figures explain that from a mechanical point of view, the Upper and Lower Bakken shales are very different from the rest of the intervals.

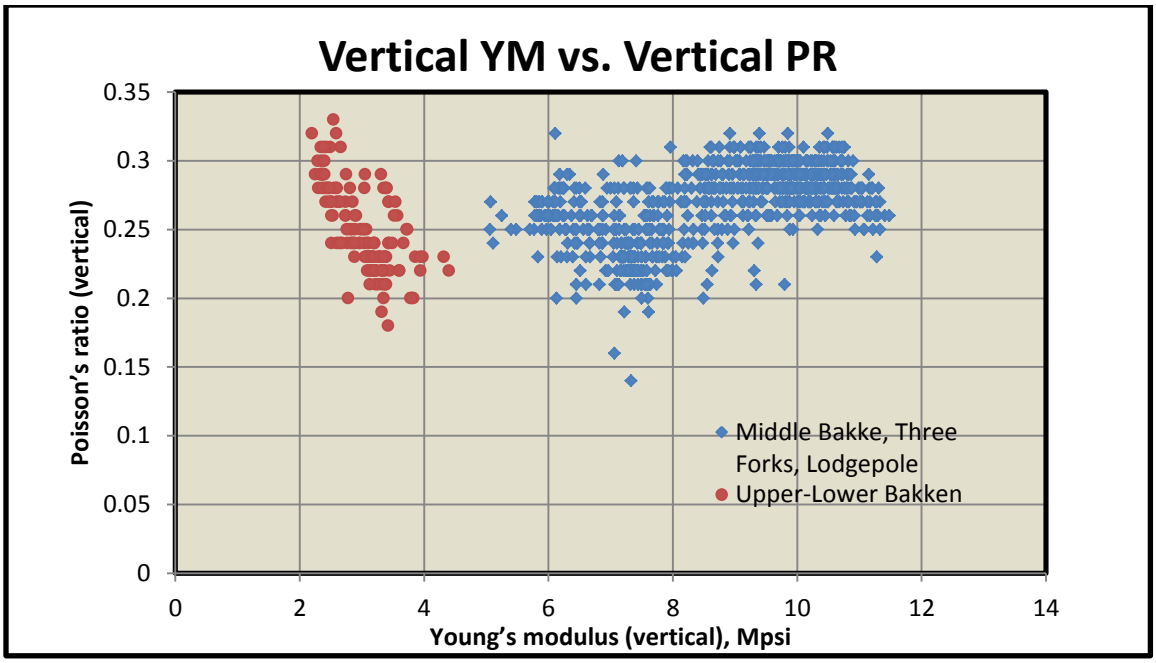

Figure 27 Vertical Young's modulus vs. vertical Poisson's ratio through the LodgePole, the Bakken and the Three Forks.

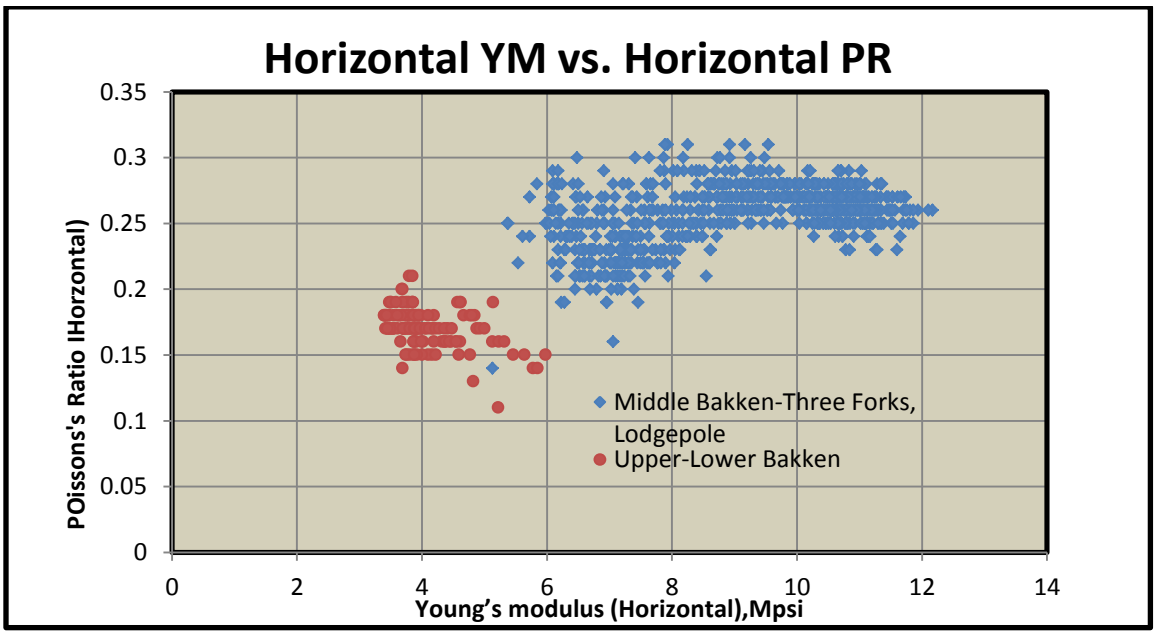

Figure 28 Horizontal Young's modulus vs. horizontal Poisson's ratio through the LodgePole, the Bakken and the Three Forks.

When comparing the last two figures, it was found that from vertical to horizontal directions, shales show a decrease in Poisson's ratio and an increase in Young's modulus. This indicates a major shift from the brittle region to the ductile zone.

Table 5 lists the ratios of horizontal Young's modulus to vertical Young's modulus and the ratios of horizontal Poisson's ratio to vertical Poisson's ratio for different layers at different wells. If the rock is isotropic, either the Young's modulus or the Poisson's ratio should be the same in all directions. Therefore, the ratio of horizontal to vertical properties will be 1. On the contrary, if the rock is anisotropic, then the ratio should deviate from unity. The greater the difference between the ratio and 1, the more anisotropic the rocks is (Zimmerman, et al, 2007). It can be seen from Table 5 that the values for the Upper Bakken and the Lower Bakken are far from 1, while the Middle Bakken are close to 1. This suggests that the Upper Bakken and the Lower Bakken can be considered quite anisotropic and the middle member may be considered as essentially isotropic with some exceptions.

Table 5 Horizontal to vertical YM and PR average values for each member of the Bakken Fm.

	Young's modulus (YM)			Poisson's ratio (PR)		
	Horizontal/Vertical			**Horizontal/Vertical**		
	Wrigley	Ruland	Sikes State	Wrigley	Ruland	Sikes State
Upper Bakken	1.80	1.50	1.64	0.46	0.62	0.53
Middle Bakken	1.02	0.96	1.00	0.96	1.00	0.98
Lower Bakken	1.68	1.29	1.54	0.50	0.71	0.56

Summary

Well log data was acquired by the Sonic Scanner log and was analyzed in Sanish, Manitou and Forthun Fields. Depth and thickness of the Bakken are compared for three different wells. Density, velocity, V_p/V_s ratio, Young's Modulus and Poisson's ratio are analyzed and averaged for the Bakken intervals. The Bakken Formation is deeper and thicker in the Sanish Field and is shallower and thinner in the Forthun Field in the northern part of the state. The Upper and Lower Bakken shales have similar physical characteristics and can be distinguished from other intervals both in the log data and the cross-plots. The Upper and Lower Bakken shales are characterized by low density and low P and S wave velocities hence low V_p/V_s ratios. The V_p/V_s ratio of the Bakken shale is slightly lower than the Middle Bakken. Therefore the V_p/V_s ratio may not be an effective lithology indicator to differentiate between the shales and the Middle Bakken due to the high kerogen content of the shale units, whereas cross-plotting the compressional to shear wave velocities (travel time) can be very helpful to differentiate the units.

The observations show that the vertical Young's modulus is much smaller than the horizontal Young's modulus, while the vertical Poisson's ratio is much greater than the horizontal Poisson's ratio in shale members. This is due to elastic anisotropy of the Bakken shale intervals. The Middle Bakken, which can be considered isotropic, these values are almost similar.

Chapter III

ELASTIC ANISOTROPY OF THE BAKKEN

Introduction

Incorporating anisotropy into seismic data processing will improve the accuracy in pre-stack depth migration, amplitude variation with offset (AVO), and microseismic hydraulic fracture monitoring among which the hydraulic fracturing plays a major role in production enhancement in the Bakken Formation. Considering that shales are vertically transverse isotropic (VTI), the three Thomsen anisotropy parameters with five independent stiffness coefficients can be used to fully characterize them. So far different methods are applied to measure these parameters directly such as walkaway VSP (vertical seismic profiling), multi-offset and multi-azimuthal VSP and laboratory measurements. Although these methods can provide us with reliable anisotropic models, various constraints, including cost and time, could limit their applicability. Recent innovations in the acquisition of broad band sonic waveforms and dispersion analysis have changed the industry's perspective on cost of anisotropy analysis.

This chapter presents the results of analyzing the advanced sonic data taken from two producing wells in the Bakken Formation. One well is located on the crest of the Nesson anticline, the major geologic structure in the area, and the other is so far from the anticline that none of the Nesson geologic feature is observed. Three primary tasks were carried out for this analysis: First, the five stiffness moduli were estimated from the

Stoneley, two flexural waves slowness and the formation density measurements. Secondly, the Thomsen parameters in three Bakken members were calculated and compared, thus a correlation is speculated to relate anisotropy parameters to one another. It was found that the Upper and Lower Bakken are highly VTI because of the highly compacted platy shaped clay particles, while the middle member is isotropic or slightly anisotropic. The well located on top of the Nesson anticline demonstrated a higher degree of anisotropy in the Middle Bakken than the other well in the same member.

Finally, a data inversion of both Stoneley and the two flexural waves was performed to create slowness radial profiles around the borehole and in the far field, which in turn led to a credible perceived information regarding reservoir quality. The well located on the crest of the anticline demonstrated higher variations in the Stoneley wave slowness. Correspondingly, the Stoneley wave was found to be sensitive to mobility and an indicator of higher permeability.

Anisotropy and the Origins

Elastic Anisotropy: Variation of elastic wave velocity with respect to the direction of waves traveled in a homogeneous material (Thomsen, 1986), where homogeneity extends over distances on the order of, or exceeding, a wavelength (Winterstein, 1990). A medium that displays this directional dependence is referred to an anisotropic medium. Sedimentary rocks are often found to be anisotropic. In sedimentary rocks there are many sources of velocity anisotropy, some of them are as follows: (Tsvankin, 2005).

- aligned crystals,
- direct stress-induced anisotropy,
- lithologic anisotropy (i.e., aligned grains),

- Aligned fractures, cracks and pores, subsequently the nature of their infilling material (e.g. clays, hydrocarbons, water, etc.)
- structural anisotropy (i.e., fine layering)

New advancements in sonic logging have made us capable of quantifying anisotropy and the origins azimuthally and radially around the borehole (Pistre, et al., 2006).

Classification of Anisotropic Media

Transverse isotropy is defined as having the same properties (e.g. velocity, stiffness, permeability, resistively) in a medium when measured within a plane that is normal to an axis, but having different values when measuring those properties at other angles to that axis normal to the plane of measurement (Winsterstein, 1990 and Tsvankin, 2005). This axis is called the symmetry axis and is normal to the alignment direction of different properties.

There are two styles of property alignment in mediums: horizontal alignment of properties with vertical axis of symmetry and vertical alignment of properties with horizontal axis of symmetry. These two types of alignments (symmetries) make two types of anisotropies: transversely isotropic with vertical axis of symmetry (VTI) and transversely isotropic with horizontal axis of symmetry (HTI). These are two oversimplified but convenient models that have been created to describe how elastic properties, such as velocity or elasticity, vary in anisotropic media (Tsvankin, 1997 and 2005).

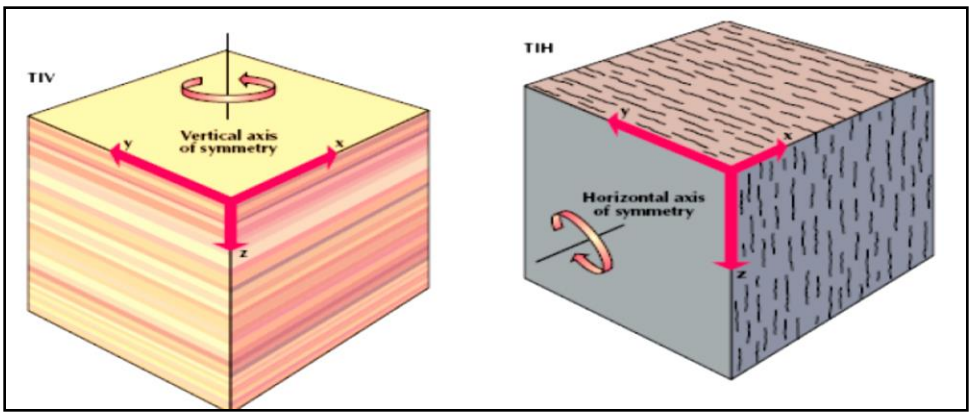

Figure 29 VTI and HTI mediums, (Armstrong, et al., 1994).

Theory and Background

Velocity anisotropy is a key parameter for seismic data processing and interpretation whereas including elastic anisotropy in geomechanical modeling will highly improve the results. Most of the rock constituents of the earth's crust exhibit some degree of anisotropy. Shales are a major component of sedimentary basins (Hornby, 1994) that exhibit a high degree of intrinsic anisotropy due to their microstructures and platy shape clay minerals (Sayers, 2005). As a matter of fact, the anistropic behavior of shales could be simplified by making the assumption that they are Vertically Transverse Isotropic (VTI) (Sayers, 1994; Vernik and Liu, 1997). This has made transverse isotropy the most common anisotropy model in exploration seismology. Neglecting anisotropy in shales may lead to crucial errors in normal move-out (NMO) corrections; dip move-out (DMO) corrections, migration, and amplitude variation with offset (AVO) analysis and finally unrealistic geomechanical models.

VTI Medium

Vertical transverse isotropy, also known as polar anisotropy (Walsh et al., 2006), can be quantified in the manner of including transverse isotropic planes with a vertical axis of

rotational symmetry. A VTI medium can be characterized by having five independent elastic stiffness coefficients. In addition, a VTI medium could also be quantified with the estimation of three dimensionless anisotropy parameters, epsilon (ϵ), gamma (γ) and delta (δ) (Thomsen, 1986). Considering X_3 as the axis of rotational symmetry in the conventional two index notation (Nye, 1985, Higgins et al., 2008) and applying general Hook's law (Equation 1), the non-vanishing elastic stiffness coefficients (Equation 2 & 3) of the elasticity matrix (Equation 2) reads as follows:

$$\sigma_{ij} = C_{ijkl}\varepsilon_{kl} - \alpha P_p \tag{1}$$

Where, σ_{ij}: Stress tensor, C_{ijkl}: Fourth rank stiffness tensor, ε_{kl}: Strain tensor, α: Biot's constant and P_p:Pore pressure, and the conventional two index notation (Nye, 1985) of the stiffness tensor will be:

$$C_{ij} = \begin{pmatrix} C_{11} & C_{12} & C_{13} & 0 & 0 & 0 \\ C_{21} & C_{22} & C_{23} & 0 & 0 & 0 \\ C_{31} & C_{32} & C_{33} & 0 & 0 & 0 \\ 0 & 0 & 0 & C_{44} & 0 & 0 \\ 0 & 0 & 0 & 0 & C_{55} & 0 \\ 0 & 0 & 0 & 0 & 0 & C_{66} \end{pmatrix}, \tag{2}$$

Hence a VTI medium the five non-vanishing elastic stiffness coefficients along with C_{66} are as follows:

$$C_{11} = C_{22}, C_{33}, C_{12} = C_{21}, C_{13} = C_{23} = C_{32} = C_{31},$$
$$C_{44} = C_{55}, C_{66} = \frac{C_{11} - C_{12}}{2} \tag{3}$$

Thomsen Parameters for a VTI Medium

Thomsen (1986) developed the idea of parameterization of the elastic properties of a TI medium in order to elaborate on diagnostic principles that would lead to a better understanding of anisotropy from isotropy. Thomsen anisotropy parameters for a TI medium can be illustrated through the vertical propagating compressional and shear wave velocities along the axis of rotational symmetry (X_3) and three dimensionless anisotropic parameters (Equation 4) defined as follows:

$$\epsilon = \frac{C_{11}-C_{33}}{2C_{33}}, \gamma = \frac{C_{66}-C_{55}}{2C_{55}}, \delta = \frac{(C_{13}+C_{55})^2-(C_{33}-C_{55})^2}{2C_{33}(C_{33}-C_{55})} \quad (4)$$

Epsilon (ε) stands for fractional difference between horizontal (C_{11}) and vertical (C_{33}) P-wave velocities showing P-wave anisotropy. Similarly, gamma (γ) measures the same characteristic for S-wave which is the difference between the horizontally propagating (C_{66}) and vertically propagating (C_{44}, C_{55}) shear wave. In contrast to the simple definition of ε and γ, δ is a more complicated combination of elastic stiffness coefficients. As Thomsen (1986) described, δ is the difference between the smallest offset NMO velocity and the vertical velocity to interpret the small AVO response (Tsvankin, 1997). Based on the fact that in an isotropic medium, the density is uniform throughout the material and the wave's velocity does not change with respect to the direction of propagation, the combination of Equation (4) and Equation. (5), epsilon (ε), gamma (γ) and delta (δ) will approach to zero for the isotropic medium, otherwise their value could represent the strength of anisotropy (Tsvankin, 2005).

Considering the velocity $v_{ij}$of an elastic wave traveling along the X_i axis and polarizing along the X_j, the relationship between v_{ij} and C_{ij} for a TI medium will become:

$$\upsilon_{11} = \upsilon_{22} = \sqrt{\frac{C_{11}}{\rho}}, \upsilon_{33} = \sqrt{\frac{C_{33}}{\rho}}, \upsilon_{12} = \upsilon_{21} = \sqrt{\frac{C_{66}}{\rho}},$$

$$\upsilon_{13} = \upsilon_{31} = \upsilon_{23} = \upsilon_{32} = \sqrt{\frac{C_{55}}{\rho}} \quad (5)$$

Where ρ is the bulk density, υ_{12} is the velocity of a shear wave propagating along the axis (X_1) and polarized along the axis (X_2),υ_{33} is the velocity of a compressional wave traveling along the axis of symmetry (X_3) and polarized along the same axis.

Shale Anisotropy

Shales make up 75 percent of the infill in most sedimentary basins and overlie most hydrocarbon bearing reservoirs (Hornby, 1998). Based on previous research, shales are known to be seismically anisotropic (Johnston and Christensen, 1995; Hornby, 1998). In addition to the mineralogy, the velocity and anisotropy of shales are related to the organic richness of kerogen content. A series of papers (Vernik and Nur, 1990 and 1992; Vernik and Liu, 1997) were published based on the laboratory experiments on a variety of shales, including the Bakken Formation, with different clay and kerogen content, clay mineralogy and porosity at different effective pressures. They found that black, kerogen-rich shales are transversely isotropic, and anisotropy of shales increases substantially with compaction and kerogen content. Vernik and Nur (1992) pointed out that the anisotropy of shales is enhanced by bedding-parallel microcracks, especially at the high pore pressure (typical of the Bakken Formation at depths of about 3 km). Prasad and Mukerji (2003), and Mukerji and Prasad (2004, 2007) analyzed scanning acoustic microscope (SAM) images of the Bakken shale and found that the textural heterogeneity, P wave impedance and velocity, and density increase with increasing maturity (decreasing kerogen content), while textural anisotropy decreases with maturity.

It can be concluded from past studies that the Upper and Lower Bakken behave as a Vertically Transverse Isotropic (VTI) medium due to platy shape clay minerals and high concentration of kerogen, whereas the Middle Bakken could be considered as an isotropic medium. Considering the presence of vertical and sub-vertical natural fractures in the Middle Bakken, its expected to see a slightly anisotropic response in middle member as well.

Quantifying Anisotropy

Seismic Survey

VSP data, such as walkaway, multi-offset, and multi-azimuth recordings along with laboratory measurements are the most suitable set of data which precisely measure the anisotropy of a formation (Leaney, et al., 1999). However, due to various constraints, these set of data may not be available.

Well log (Cross-Dipole & Sonic Scanner)

Cross dipole log or DSI (Dipole Shear Sonic Imager) and the Modular Sonic Imaging Platform (MSIP) or Sonic Scanner designed by Schlumberger for advanced acoustic data acquisition. These instruments are capable of dipole and monopole measurements. The tools are able to perform radial measurements for near and far field slowness in addition to axial and azimuthal measurements. The typical investigation depth is twice or three times of the borehole diameter. To be more accurate, a multi receiver tool with a linear array of eight receiver stations and a monopole transmitter with two orthogonal dipole transmitters are mounted on this instrument (Arroyo, et al., 2006). At each receiver station, a pair of orthogonal dipole receivers that form two arrays are located. Each of these are oriented in the direction of the dipole transmitters. (Close, et al., 2009). The

combination of those sources and receivers enable us to record the full waveform of all types azimuthally. Figure 30 shows a typical form of a Sonic Scanner instrument with sources and receivers configuration on the tool.

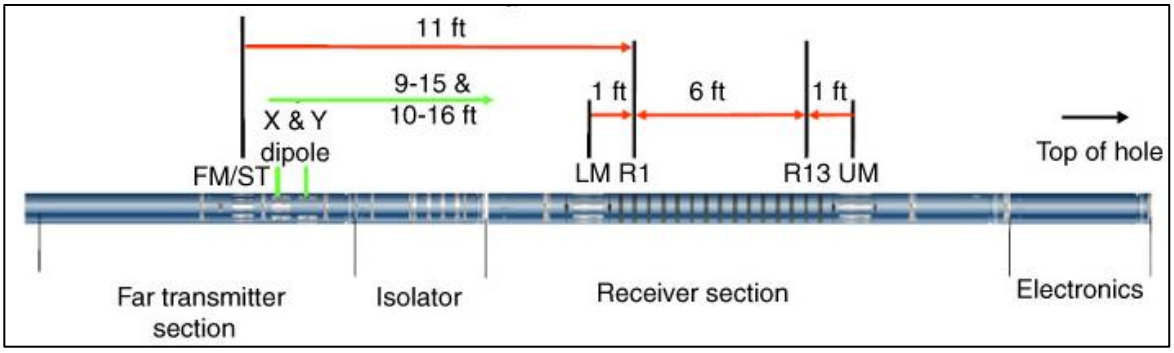

Figure 30 Schematic configuration and geometry of the Sonic Scanner. There are 13 receiver stations half a foot apart with a total of 104 receivers (8 receivers per station, one receiver per 45degree azimuthally), and five transmitters; two near monopole transmitters (lower and upper with TR spacing of 1 to 7 ft), one far monopole with TR spacing 11 to 17 ft and two cross-dipole transmitters X and Y with TR spacing 9-15 ft and 10-16 ft, respectively

Dipole sonic logging enables measurement of the fast and slow shear wave velocities caused by shear splitting and radial variation of shear speed into the formation (Esmersoy, 1994-1995; Burridge and Sinha, 1996). If shear dipole and Stoneley wave measurements are available, an accurate evaluation of a transverse isotropic medium can be accomplished (Pistre, 2005). For vertical wells with flat bedding planes, C_{33} represents the vertically propagating P-wave, while C_{44} and C_{55} are two shear moduli of a TI medium which can be measured by flexural probes. C_{44} and C_{55} are measured in two straight perpendicular planes along the borehole axis. Ultimately C_{66} is recordable in the plane perpendicular to the borehole axis from the Stoneley wave velocity (Norris and Sinha, 1993, Walsh et al., 2007).

For a vertical well such as the one shown in Figure 31, X_3, the axis of symmetry in shale layers, is assumed to be along the borehole axis. This assumption is made when the well

is vertical going perpendicular through 0° dipping formation layers, for dipping layers the assumptions will differ, thus the formation is azimuthally isotropic in the X_1–X_2 plane as shown in Figure 31. C_{44} and C_{55} are the two moduli corresponding to the fast and slow shear waves obtained from the dipole flexural modes. Consequently, for a VTI medium we expect $C_{44} = C_{55}$ and C_{66} will be horizontally propagating shear wave from the low frequency asymptote dispersion (Pistre et al., 2005; Wlash et al., 2006), with some corrections (Sinha et al., 2006).

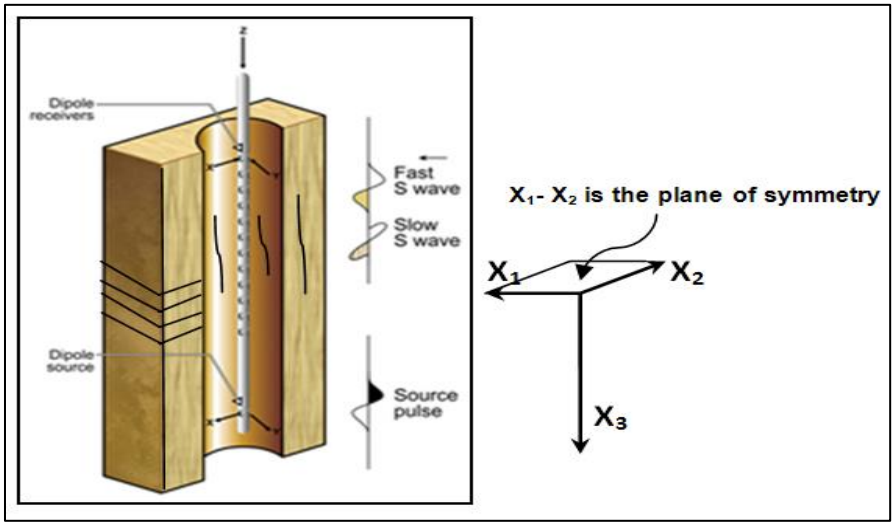

Figure 31 Well coordination in a VTI medium (Modified from Haldorsen et al., 2006)

ANNIE Model Approximation

As shown in Equations (1-3), in order to entirely characterize a VTI medium five independent elastic moduli are needed. However, only three of these five moduli (C_{33}, C_{44}-C_{44} & C_{66}) could be measured by advanced sonic logging in the vertical wells perpendicular to the bedding plane. Therefore ANNIE model, a simple assumption, has been proposed (Schoenberg et al., 1996) to estimate the two remaining elastic parameters C_{11} and C_{13}. ANNIE model is derived as a result of seismic observations which NMO

velocity compared to vertical velocities are small, thus Thomsen δ can be set to zero (Equation. 6).

$$C_{13} + 2C_{44} - C_{33} = 0, \quad (6)$$

Note that C_{44} & C_{55} can be replaced by one another for a VTI medium in Equation. (6). The second assumption is that for many types of shale C_{13}=C_{12} resulting in (Equation. 7):

$$C_{13} = C_{12} = C_{11} - 2C_{66}, C_{66} - C_{44} = \frac{C_{11} - C_{33}}{2} \quad (7)$$

This allows us to express (Equation8):

$$(C_{11},\ C_{13}) = f(C_{33}, C_{44}\ \&\ C_{66}) \quad (8)$$

Methodology

Geological Setting

Figure 32 depicts the location of the wells Ruland (A) and Sikes State (B) from which the sonic data were taken. Sonic Scanner facilitated the sonic logging in such openhole wells when they are filled with fluid. (Pistre et al., 2005). As seen in Figure 32, Well A is right on top of the Nesson anticline and well B is far away where no geological evidence of the Nesson anticline exists. The depths of study for Well A and B are 10,294ft to 10,430ft and 9,715ft to 9,812ft, respectively.

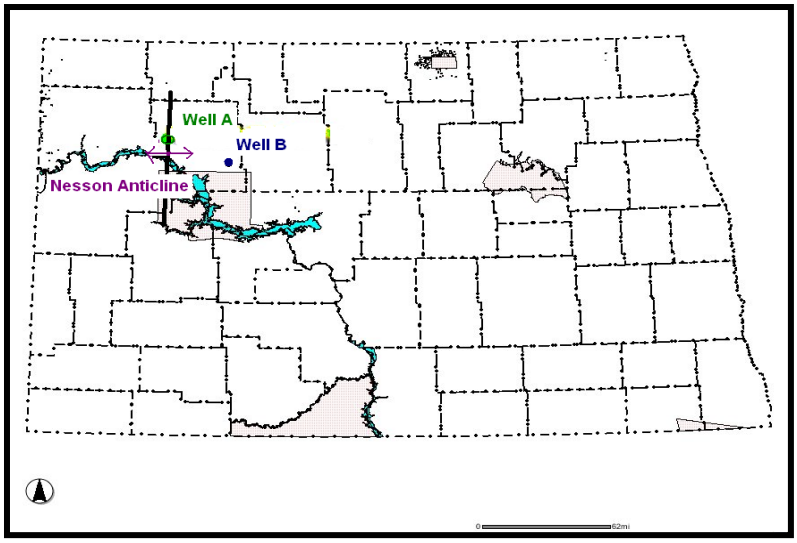

Figure 32 Well locations (A & B) in North Dakota part of Williston Basin.

Compressional, shear, Stoneley and flexural wave slowness were obtained at different depths of investigation in the formation through short and long spacing sets of sources and receivers. A monopole source can generate non-dispersive P-wave, dispersive S-wave and low frequency slightly dispersive Stoneley wave. Dipole transmitters generate a chirp with a frequency sweep or flexural modes (Arroyo et al., 2006). These waves' slowness measurements produce different values in three separate planes, two along the borehole axis and one orthogonal to the wellbore. In addition, dispersion data (slowness vs. frequency) was derived for each set of wave modes for further anisotropy type analysis. Finally, the inversion of slowness data was performed for radial profiling (Sinha et al., 2006) for fluid flow analysis.

Data Processing

Advanced data processing using Best-Delta-Time module of Geoframe (Mark of Schlumberger) software was carried out as the following (Halderson et al., 2006; Arroyo et al., 2006), Figure 36:

1. Semblance processing of all arrivals received on each and every array of the tool (Kimbal and Marzetta, 1983)
2. 4-component Alford rotation of fast and slow S-wave for shear anisotropy analysis (Alford, 1986)
3. Dispersion curve analysis in order to identify type of anisotropy, either intrinsic or stress-induced.
4. 3D anisotropy processing of flexural waves to calculate C_{44} and C_{55} in a vertical plane from the shear data along the borehole axis, C_{66} from the Stoneley wave in a horizontal plane perpendicular to the borehole axis, and C_{33} from compressional data (Figure 31).
5. Dipole radial profiling for near wellbore and far offset formation evaluation.

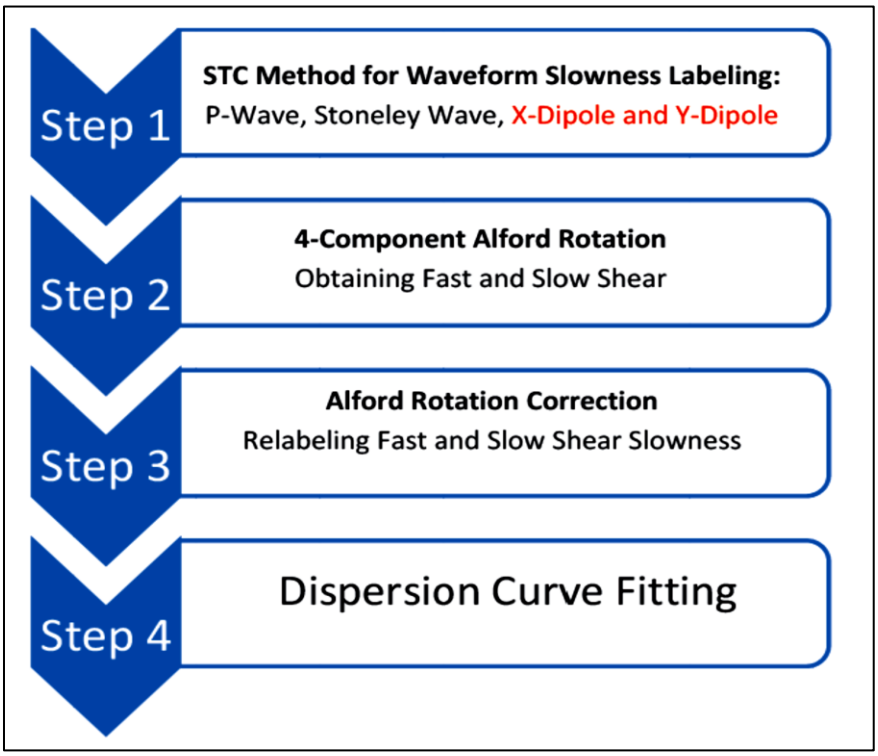

Figure 33 Data processing steps that were taken.

Alford Rotation

While working with multicomponent-multisource shear data such as the data acquired by the Sonic Scanner tool, there is the possibility for severe distortion (Alford, 1986) by shear polarization splitting resulting from propagation through an azimuthally anisotropic medium (Tsvankin 2005). Alford rotation is an algorithm that uses a simple one-dimensional model to express distorted data in terms of the fundamental solutions for an azimuthally anisotropic medium. The model suggests that the sources and receivers of the acquisition system must be oriented to conform with the principal axes of the azimuthally anisotropic medium before a simple interpretation of the shear data is valid. Mathematical operations are developed which are then applied to the multicomponent-multisource shear data to compensate for the shear polarization splitting.

Equation (9) defines an operation in which the field sources are rotated counterclockwise through an angle θ, and the receivers are rotated counterclockwise through an angle θ.

$$U = R(\theta)V(\theta)R^T \tag{9}$$

Where $R(\theta)$ is a rotation matrix:

$$R(\theta) = \begin{pmatrix} \cos\theta & \sin\theta \\ -\sin\theta & \cos\theta \end{pmatrix} \tag{10}$$

$V(\theta)$ is the solution matrix for a set of sources and receivers oriented in an acquisition system related to the natural system through the angle θ and can be constructed in terms of the fundamental solutions for the natural system (U). $V(\theta)$ is presented in Equation (11):

$$V(\theta) = \begin{vmatrix} \cos^2\theta\, u_{11} + \sin^2\theta\, u_{22} & .5\sin 2\theta\ (u_{11} - u_{22}) \\ .5\sin 2\theta\ (u_{11} - u_{22}) & \sin^2\theta\, u_{11} + \cos^2\theta\, u_{22} \end{vmatrix} \qquad (11)$$

Equation (11) helps us to maximize energy for the fast and slow shear waves.

The operation in Equation (9) allows the construction of the simpler solutions in terms of the solutions in the acquisitions system. Performing the multiplications in Equation (9) will result in Equation (12). Finally we will have *V* as the following matrix:

$$V(\theta) = \begin{vmatrix} (\cos^2\theta\, v_{11} + \sin^2\theta\, v_{11}) & \cos^2\theta\, v_{12} - \sin^2\theta\, v_{21} \\ +.5\sin 2\theta\ (v_{21} - v_{12}) & +.5\sin 2\theta\ (v_{22} - u_{11}) \\ (\cos^2\theta\, v_{21} - \sin^2\theta\, v_{12}) & (\cos^2\theta\, v_{22} + \sin^2\theta\, v_{11}) \\ +.5\sin 2\theta\ (v_{22} - v_{11}) & -.5\sin 2\theta\ (v_{21} - v_{12}) \end{vmatrix} \qquad (12)$$

Equation (12) transforms the data into simpler solutions, given the angle θ.

Semblance Processing

The structure of this algorithm is quiet simple. A set of time windows is applied to the waveforms with the window positions determined by two parameters: an assumed arrival time at the first receiver and an assumed slowness. For a range of values of arrival time and slowness, the scalar semblance is computed for the windowed waveform segments. Local maxima of the semblance function are identified by a peak-finding algorithm, and the corresponding slowness values are plotted as colored-scale marks on a graph whose axes are slowness and depth. The intensity of each mark is proportional to the height of the semblance peak (Kimbl and Marzetta, 1983).

If the tool contains an array of M pressure-sensitive receivers on the axis of the borehole located at ranges $\{Z_1, Z_2, \ldots Z_m\}$ with respect to the transmitter, then we arrive at the following form:

$$r_m(t) = a[t - s(Z_m - Z_1) - \tau], \quad 1 \le m \le M \tag{13}$$

Where $r_m(t)$ is the waveform recorded by the receiver located at range Z_m, S is the slowness of the wave-front across the array and τ is the arrival time of the wave-front at the receiver.

Given the set of waveforms $\{r_m(t), 1 \le m \le M\}$ arrivals of the form of Equation (13), we can compute the quantity known as semblance over a set of time windows. The windows are specified by two parameters: the slowness, S, and the starting time of the window on the first waveform, τ. For a given S and τ, the semblance is a scalar quantity, denoted by $\rho^2(S, \tau)$, defined as follows:

$$\rho^2(s,\tau) = \frac{\frac{1}{M}\int_{t=0}^{T_w}\left[\sum_{m=1}^{M} r_m[s(Z_m - Z_1) + \tau]\right]^2 dt}{\sum_{m=1}^{M}\int_{t=0}^{T_w}\{r_m[t + s(Z_m - Z_1) + \tau]\}^2 dt} \tag{14}$$

Here, T_w is the window width, chosen to be equal to the expected duration of the arrivals. The semblance is a measure of the presence or absence of an arrival with slowness S and arrival time τ. It will lie between 0 and 1 and is equal to 1 if and only if the M segments delineated by the windows are all identical in both shape and magnitude.

The results of semblance processing can be shown for every single depth on a slowness-arrival time plot or can be put together in the shape of a set of slices cut from the plots to make a well log.

Radial Profiling and Dispersion Curves

The Stoneley shear radial profiling (SRP) algorithm inverts differences between the measured and reference Stoneley dispersions defined by a chosen equivalent isotropic and radially homogeneous formation in a vertical or deviated well for radial variations in the effective shear modulus C_{66} in the borehole cross-sectional plane. The SRP algorithm accounts for sonic tool effects and yields the horizontal shear modulus C_{66} outside any near-wellbore altered annulus.

The dipole shear radial profiling (SRP) algorithm inverts differences between the measured and a chosen equivalent isotropic and radially homogeneous reference dipole dispersions in a vertical or deviated well for radial variations in C_{44} and C_{55} in the two orthogonal planes (Figure 31) containing the radial polarization and propagation directions. The SRP algorithm also accounts for sonic tool effects measured dispersions in terms of an equivalent tool model with calibrated parameters that replace a complex sonic tool structure. To improve accuracy of the inverted profile, one must select an equivalent isotropic and radially homogeneous reference state that minimizes differences between the measured and reference dispersions (Sinha, et. al., 2006).

Equation (15) expresses the radial profiling of the three shear moduli (Burridge and Sinha, 1996; Sinha and Kostek 1996):

$$\frac{\Delta V_i}{V_i} = \int_a^{\infty} G_i(r) \frac{\Delta \mu(r)}{\mu} r dr \qquad (15)$$

Where $\frac{\Delta V_i}{V_i}$ denotes the fractional difference in the measured (or synthetic) Stoneley or flexural velocity at a given wave number *I* from that in a radially homogeneous and an equivalent isotropic reference state, *a* is the borehole radius, and $G_i(r)$ is the data kernel calculated in the reference state from the Stoneley-wave eigensolution for the SRP algorithm and the flexural wave eigensolution for the SRP algorithm. The term $\frac{\Delta \mu(r)}{\mu}$ accounts for radial variations in the fractional change in the effective shear modulus from that in the reference state (Sinha, 1997). In Equation 15, $\frac{\Delta \mu(r)}{\mu}$ denotes $\frac{\Delta C_{44}}{C_{44}}$ or $\frac{\Delta C_{55}}{C_{55}}$ in the case of dipole radial profiling of a vertical shear modulus and $\frac{\Delta C_{66}}{C_{66}}$ in the case of Stoneley radial profiling of a horizontal shear modulus.

A solution to the integral Equation (15) for the SRP algorithm can be expressed as (Burridge and Sinha, 1996):

$$\frac{\Delta C_{66}}{C_{66}} = \sum_i a_i(r_0) \frac{\Delta V_i}{V_i} \qquad (16)$$

Where,

$$a_i = \frac{S_{ij}^{-1}(r_0) u_j}{u_i S_{ij}^{-1}(r_0) u_j} \qquad (17)$$

$$S_{ij}(r_0) = \int_a^\infty (r - r_0)^2 G_i(r) G_j(r) r dr \tag{18}$$

$$u_i = \int_a^\infty G_i(r) r dr \tag{19}$$

r_0 denotes the radial position in the formation; $i, j = 1,2, \ldots, n$; and a is the borehole radius. The data kernel G_i is calculated in terms of the Stoneley-wave eigensolution for an equivalent isotropic and radially homogeneous reference state as is described by Burridge and Sinha, (1996).

Consider Figure 31 in the case of a borehole parallel to the X_3-axis in weakly anisotropic formations (Thomsen, 1986) fractional changes in the measured dipole dispersions from those in an equivalent isotropic reference state can be inverted to estimate fractional changes in the shear moduli C_{44} and C_{55} in the X_2-X_3 and X_3-X_1 planes, respectively. In contrast, the Stoneley dispersion can be inverted to estimate the shear modulus C_{66} in the X_1-X_2 plane. The same solution can be derived for shear moduli C_{44} and C_{55} in the X_2-X_3 and X_3-X_1 planes.

Discussion and Results

Using Equation (5), the average value of the stiffness coefficients plus the epsilon and gamma anisotropy parameters for Well A, in the three different members of the Bakken Formation (UB, MB and LB) were calculated (Table 6). C_{33}, C_{44}, C_{55} and C_{66} were obtained from the direct measuring of the compressional, shear flexural and Stoneley wave velocities within the formation along with the formation density. C_{44} and C_{55} are elastic stiffness moduli in vertical planes parallel and perpendicular to the fast shear

azimuth. C_{11} is calculated through ANNIE model assumptions using Equations (6-8) utilizing C_{44} and C_{55}. The next step is to derive epsilon and gamma using Equation (4), the two dimensionless anisotropy parameters. In order to derive epsilon and gamma, C_{44} and C_{55} were used interchangeably.

Table 6 Stiffness coefficients of Well A in three members of the Bakken Formation.

	Density(gr/cc)	C_{33}-MPsi	C_{44}-MPsi	C_{55}-MPsi	C_{66}-MPsi	C_{11}(ANNIE_C_{55})-MPsi	C_{11}(ANNIE_C_{44})-MPsi
UB	2.16	2.59	0.87	0.88	1.62	4.17	4.20
MB	2.61	8.58	2.90	2.96	2.97	8.61	8.72
LB	2.18	2.53	0.82	0.84	1.44	3.74	3.77

From Table 6, we can see $C_{44} \neq C_{55} \neq C_{66}$, thus introducing another type of anisotropic behavior also known as orthorhombic isotropy. In other words, $C_{44} < C_{55}$ for the whole Bakken is strong evidence that the dipole shear slowness in the two orthogonal saggital planes along the borehole axis are different. This difference is possibly caused by vertically aligned fractures from stress differences in the cross sectional plane perpendicular to the borehole axis causing shear splitting. C_{55} is representing the fast shear azimuth which is assumed to be in the direction of maximum horizontal stress. C_{44} in the perpendicular plane represents slow shear wave direction and the direction of the minimum horizontal stress crossing the borehole.

The average difference between C_{44} and C_{55} for the middle member is slightly greater than the same difference values for upper and lower members (Table 6). This can be an indication of more open fractures in the middle member than in the lower and upper members. In addition, the main reason that $C_{44} \neq C_{55}$ in UB and LB –which are playing the role of source rock for the Bakken petroleum system– is that they contain high

amounts of Total Organic Carbon (TOC), I believe this inequality might not account for the occurrence of the fractures.

Table 7 presents the average anisotropy parameters of the three Bakken members in Well A. By definition, epsilon and gamma are interpreted as the fractional difference of vertical and horizontal traveling, compressional and shear waves (Tsvankin, 2005). From table 7 the following are deduced:

Positive values of epsilon and gamma are seen in both the UB and LB standing for the shale anisotropy. This anisotropy is a combination of shale microlayering and high concentrations of TOC.

Table 7 Thomsen anisotropy parameters of Well A in three members of the Bakken Formation.

	Epsilon(ANNIE_C_{44})	Epsilon(ANNIE_C_{55})	Gamma(C_{44})	Gamma(C_{55})
UB	0.23	0.22	0.29	0.25
MB	-0.01	-0.02	-0.01	-0.03
LB	0.14	0.12	0.21	0.17

Negative values of epsilon and gamma for MB strongly denote a permeable formation (Pistre, 2005; Walsh et al., 2006). This originates from the fluid flow in fractures acting as barriers to the vertical traveling wave. Although these values are small (Table 7), neglecting them will lead to consider MB as completely isotropic

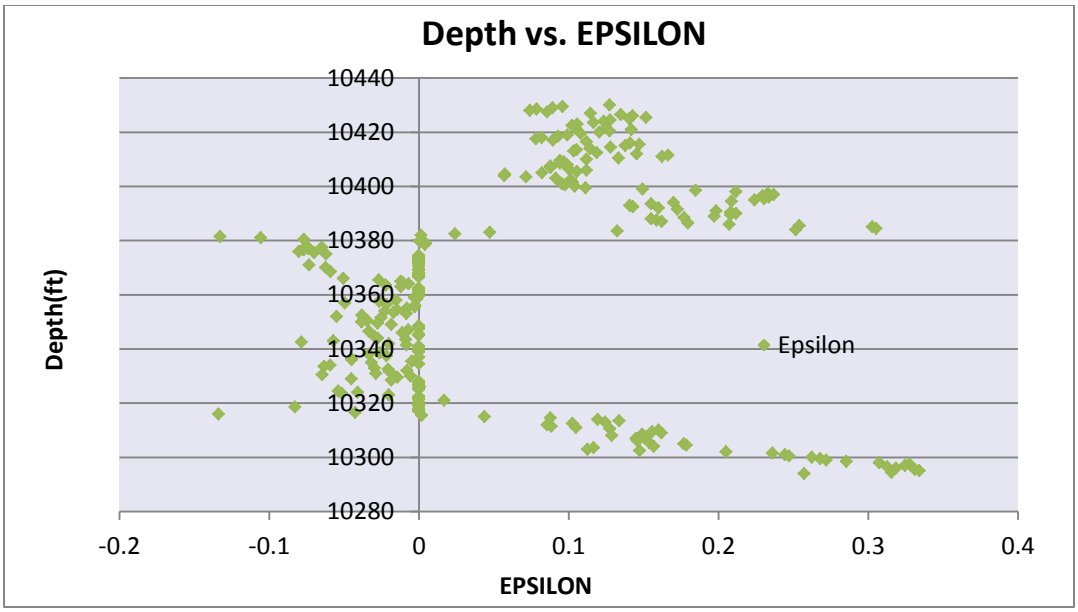

Figure 34 Epsilon versus depth in the Bakken Formation for well A.

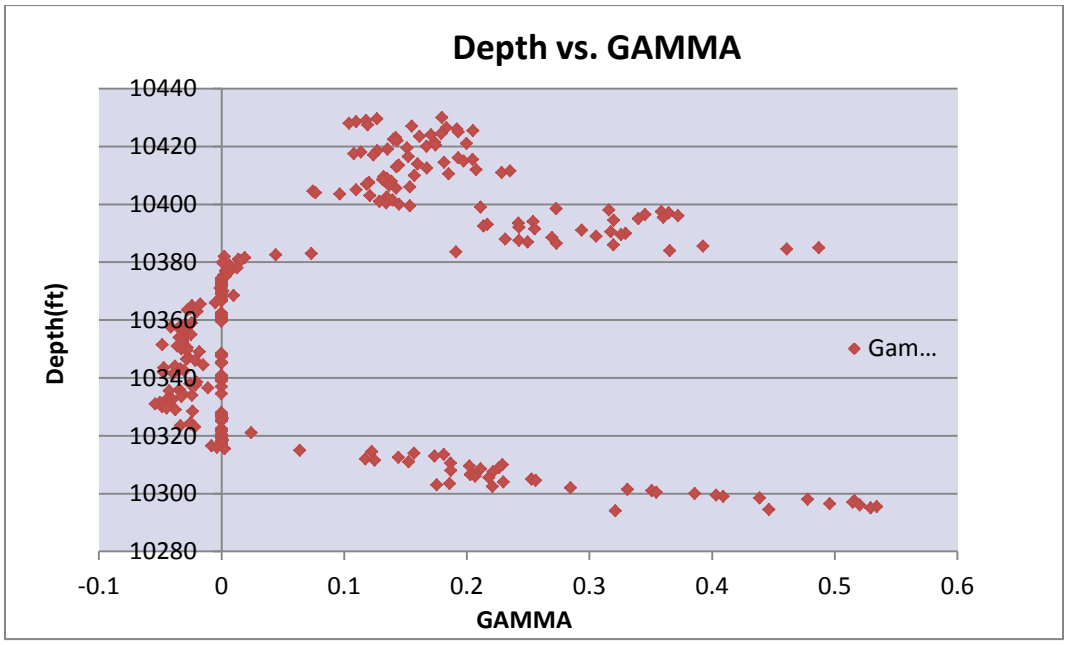

Figure 35 Gamma versus depth in the Bakken Formation for well A.

The above figures represent Thomsen (1986) anisotropy parameters through the Bakken Formation in well A. Note how epsilon and gamma change through depth, from positive values in the Upper Bakken to almost zero and negative in the Middle Bakken and then

back to positive values in lower shale member. Figure 34 and 35 are the values obtained in well A (on top of the Nesson Anticline).

Anisotropy relations

Different authors described the linear relation between P- and S-wave anisotropy. Wang (2002) showed the general linear relationship between P- and S-wave anisotropies with a small deviation of P-wave than S-wave anisotropy for most analyzed samples. The relation is also described for the best fit by a regression formula as:

$$\gamma = -0.01049 + 0.9560\varepsilon \quad (20)$$

Tsuneyama and Mavko (2005) derived a slightly different regression formula from a compiled data set for brine-saturated sandstones and shales as follows:

$$\gamma = -0.0282 + 1.2006\varepsilon \quad (21)$$

These Equations (20 and 21) show that S-wave anisotropy may be estimated from P-wave anisotropy, or vice versa. Such estimations are independent of pressure, pore fluids, and lithology. This is particularly useful when P-wave anisotropy is available but S-wave anisotropy is not.

Figure 36 represents epsilon versus gamma plotted for upper and lower shaly members of the Bakken Formation obtained in both well A and B. A strong relationship between epsilon and gamma in the VTI section of the Bakken Formation is revealed. A mathematical correlation to relate these two parameters for lower and upper members can be seen in Equation (22):

$$\gamma = 1.49\varepsilon \quad (22)$$

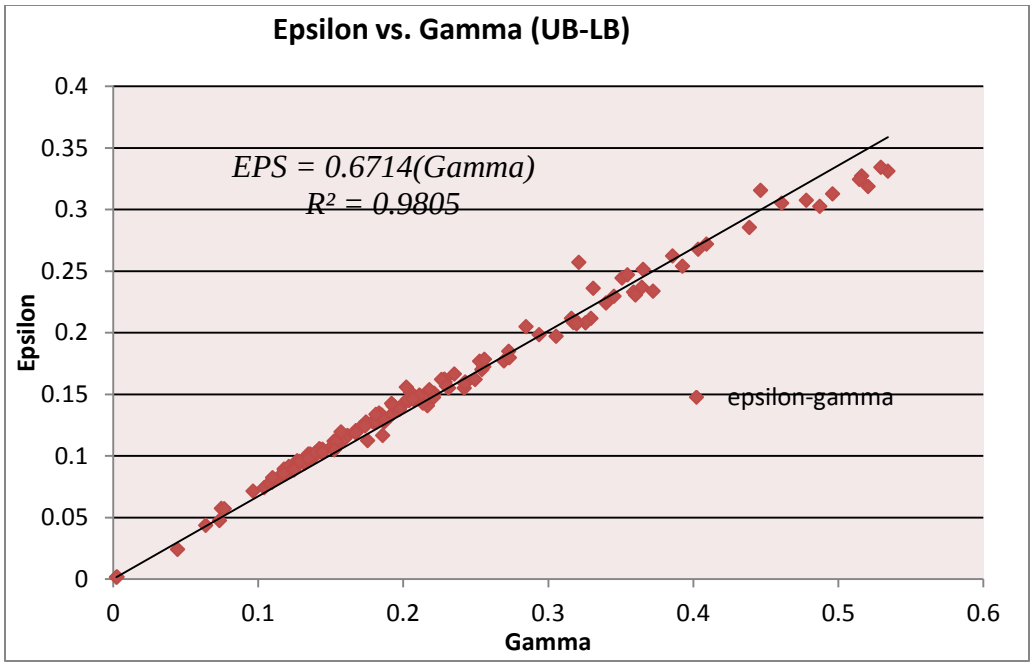

Figure 36 Epsilon-Gamma relationship for upper and lower shaly members in the Bakken Formation.

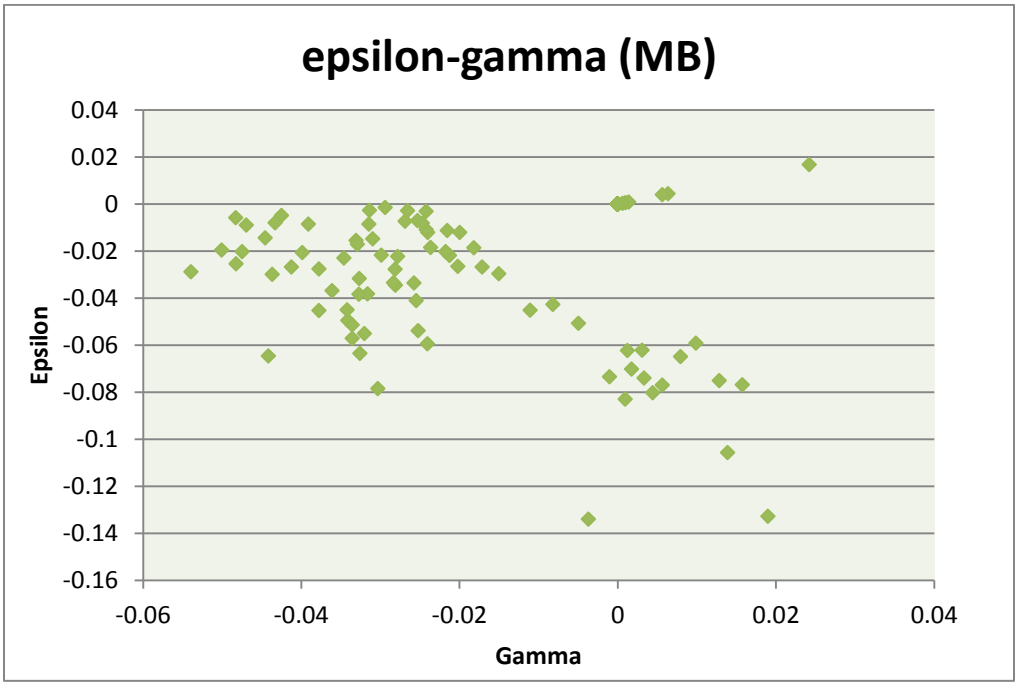

Figure 37 Epsilon-Gamma relationship for the middle member in the Bakken Formation.

Figure 37 shows the relationship between epsilon and gamma in the Middle Bakken. Due to very small and scattered values of epsilon and gamma, developing a mathematical correlation for middle member was unsuccessful. This is could be mainly due to the presence of anisotropic sections through isotropic middle member. More research, such as laboratory investigation on several middle member core samples is highly recommended.

Dispersion Plot and Radial Slowness Variation Profiling (RSVP)

In order to determine the type of anisotropy, dispersion analysis seems inevitable (Plona et al, 2000 and 2002; Arroyo et al., 2006). Dispersion plots are graphical representations of frequency versus slowness for different wave types. In such graphs, slowness in high frequency represents the near wellbore, while far field slowness is related to the low frequency region. A dispersion plot enables us to determine whether the formation is isotropic or anisotropic, homogeneous or inhomogeneous as well as the cause of the anisotropy. In this regard, four different cases can be created as follows:

1. Homogeneous-isotropic: No shear splitting occurs; two recorded flexural wave dispersion curves match each other and overlie the modeled curves.
2. Inhomogeneous-isotropic: Both fast and slow flexural modes match each other, but show different slowness with modeled curves at high frequency (near wellbore).
3. Homogeneous-anisotropic: In the case of intrinsic anisotropy, flexural modes match each other, but do not overlie the modeled curves. They merge to the true slowness at zero frequency (Arroyo et al., 2006).

4. Inhomogeneous-anisotropic: The two flexural dispersion curves cross each other as a result of stress induced anisotropy and altered zone around the borehole.

Radial slowness variation profiles (RSVP) are beneficial for formation characterization (Sinha et al., 2006 and 2007). Compressional, shear, and Stoneley wave slowness variations in a deep penetration into the formation provide valuable information of true formation properties. Compressional slowness radial variation is obtained from the difference in P-wave slowness detected from far and near offset monopole transmitters (Arroyo et al., 2006). Dipole slowness radial profile (DRP), (red and blue curves in Figures 38b, 39b, 40b, 41b, 42b and 43b) are constructed from the inversion of the difference between measured and modeled slowness at large selection of frequency interval (Sinha et al., 2006 and 2006).

Stoneley shear radial profiling (SRP) (green dashed line in Figures 38b, 39b, 40b, 41b, 42b and 43b) is the outcome of the inversion of the differences between the measured and Stoneley dispersion responses of a reference homogeneous-isotropic formation (Sinha et al., 2006). SRP analysis is a powerful technique that delivers direct continuous information of formation mobility (Brie et al., 1998).

Dispersion and SRP plots are created for three different depths of the Bakken Formation each of which represents a member of the formation in well A (Figures 38, 39 and 40) and well B (Figures 41, 42 and 43). Figure 38a displays the dispersion plot at depth 10,304 ft., which corresponds to UB in well A in that the fast and slow shear flexural modes overlie each other, but do not match the modeled curves. This validates the assumption that the Bakken Formation is more likely to be homogeneous and vertically transverse isotropic. This anisotropy originates from the platy shape clay particles as the

major constituent minerals of the shaly UB. As previously mentioned, shales are known as the best candidates for transverse isotropy. However, our observations in Table 6 imply that $C_{44} \neq C_{55}$, thereby not quite matching the results concluded from dispersion plots, in contradiction to our assumptions that UB is a VTI medium. Reconsidering the low frequency region of the dispersion plot in Figure 38a, some degree of separation on both modeled curves and flexural modes can be observed. Since the difference between C_{44} and C_{55} in Table 6 is not significant, we may yet consider the UB as VTI and not orthorhombic isotropy; LB demonstrates similar behavior (Table 6 and Figure 38a). It should also be noted that the values shown in Table 6 are the averages of elastic moduli, and do not represent the exact values for the corresponding depths in Figures 38a, 39a and 40a.

Alternatively, the dispersion plot of middle member (Figure 39a) exhibits a perfect match between the flexural modes and the modeled curves, indicating homogeneous isotropic medium. Considering the SRP plot in Figure 39b, the mismatch of Stoneley slowness with the overlying flexural modes (slower Stoneley compared to faster shear dipoles) confirms the idea of a quiet permeable Middle Bakken. This confirms the negative outcome of epsilon and gamma in Table 7 for Well A through the MB section.

Figures 38b and 40b show the SRPs for UB and LB. As expected, Stoneley slowness was found to be less than the shear dipole slowness, confirming $C_{66} > (C_{44})$ & (C_{55}), and making UB and LB a TI material. Additionally, it can be observed in the same figures that the fast and slow shear slowness curves do not match completely, which resulted in $C_{44} \neq C_{55}$.

Same analysis was performed for the advanced sonic data acquired in Well B for the Bakken Formation. The four shear moduli (C_{33}, C_{44}, C_{55} and C_{66}) were directly measured, and through the ANNIE model assumptions C_{11} was calculated from Equations (7 and 8). The results are summarized in Table 8. Thomsen anisotropy parameters (epsilon and gamma) are derived from the measured and calculated stiffness coefficients, and are shown in Table 9.

Dispersion and shear radial profiling plots through previously mentioned data processing workflow (Halderson et al., 2006, Arroyo et al., 2006 & Sinha et al., 2006) are generated and developed for well B. Figures 41, 42 and 43 are the graphical presentation of such plots for Upper Bakken, Middle Bakken and Lower Bakken in Well B, respectively.

Table 8 Stiffness coefficients of Well B in three members of Bakken Formation.

	C11(ANNIE_C_{44})-MPsi	C11(ANNIE_C_{55})-MPsi	C_{33}-MPsi	C_{44}-MPsi	C_{55}-MPsi	C_{66}-MPsi	Density(g/cc)
UB	4.69	4.57	3.19	1.08	1.14	1.70	2.31
MB	8.55	8.37	8.78	3.01	3.10	2.92	2.62
LB	4.34	4.21	3.37	1.16	1.23	1.65	2.28

Table 9 Thomsen anisotropy parameters of Well B in three members of Bakken Formation

	Epsilon(ANNIE_C_{44})	**Epsilon(ANNIE_C_{55})**	**Gamma(C_{44})**	**Gamma(C_{55})**
UB	0.305	0.299	0.467	0.450
MB	0.009	0.003	0.014	0.004
LB	0.262	0.256	0.409	0.392

From the average values of stiffness moduli for the three members of the Bakken summarized in Table 8, we can see that the measured C_{44} and C_{55}, corresponding to the

shear stiffness coefficients in two perpendicular sagittal planes, are close to each other for the entire sections. This mathematically results in equality for C_{11} derived by ANNIE model from either C_{44} or C_{55}. $C_{44}=C_{55}$ illustrates that the dipole shear slowness is behaving isotropic. In comparison to C_{44} or $C_{55,}$ the greater C_{66} in UB and LB indicates transverse isotropy with a vertical axis of symmetry parallel to the borehole axis. $C_{44}=C_{55}<C_{66}$ is the verification of no shear splitting, no vertical fracture existence and no fluid mobility (Walsh et al., 2006, Sinha et al., 2006). Fluid mobility in a horizontal plane will lower the C_{66} compared to C_{44} and C_{55}. For the middle member, $C_{44}=C_{55}=C_{66}$ matches the isotropic characteristics of this interval. Isotropic behavior of MB is confirmed by Table 9, where the discrepancies between epsilon and gamma computed from either of C_{44} or C_{55} are negligible and very close to zero. It is worth mentioning that UB and LB show strong anisotropy, with P-wave anisotropy close to 30% for UB, and 26% for LB calculated from Equation (4); additionally, S-wave anisotropy computed at 46% and 40% for UB and LB respectively (Equation 4).

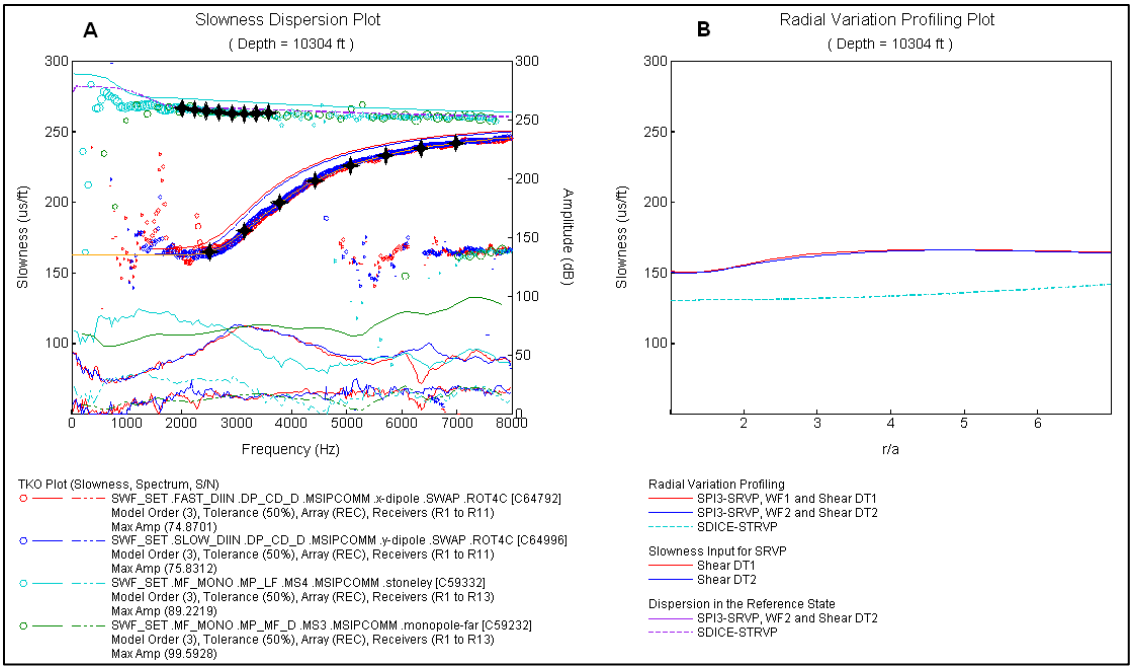

Figure 38 Dispersion plot (a) and radial slowness variation profile (b) for Upper Bakken in Well A.

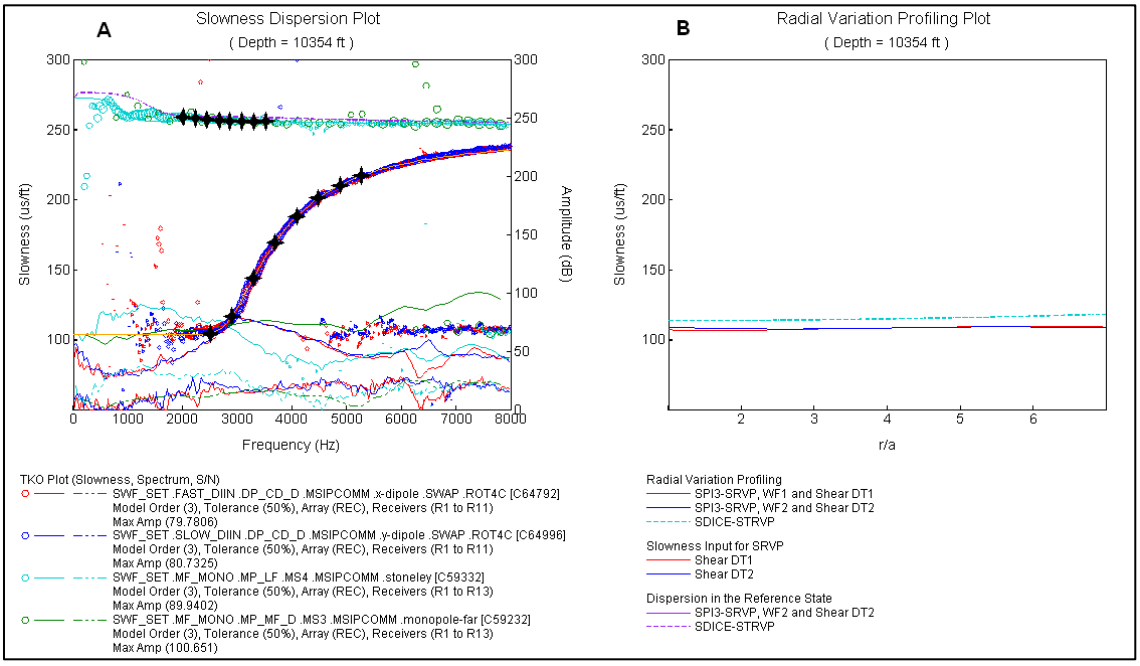

Figure 39 Dispersion plot (a) and radial slowness variation profile (b) for Middle Bakken in Well A.

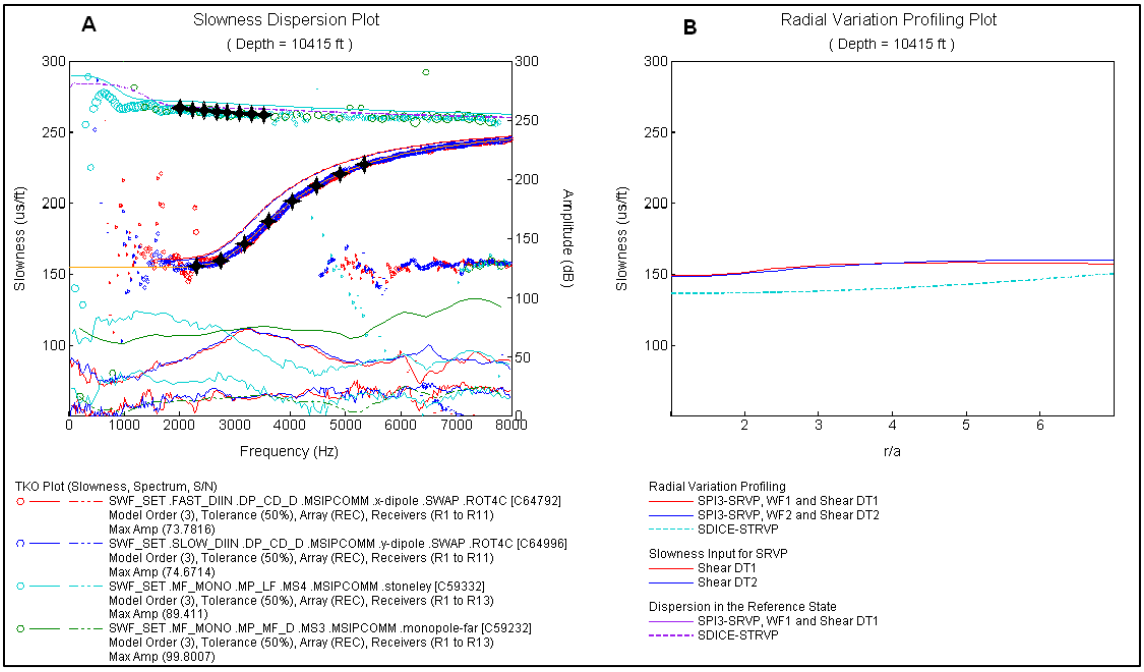

Figure 40 Dispersion plot (a) and radial slowness variation profile (b) for Lower Bakken in Well A.

Comparing the epsilon and gamma estimated from well A and well B, and considering the concept of Thomsen anisotropy parameters, it is concluded that the greater magnitude of these parameters in well B than well A may be caused by the pure VTI effect of shales in the Bakken Formation in the corresponding well. It could be interpreted that no vertical fractures exist in well B. In well A, the presence of vertical fractures resulted in smaller fractional differences of horizontally and vertically propagating P-& S-waves.

Additional compelling evidence proving the presence of vertical fractures in well A, specifically in middle member, is that epsilon and gamma are negative compared to $\epsilon = \gamma = 0$ in well B. The same conclusion can be made when comparing the stiffness moduli from Table 6 and Table 8. The MB in well A, showing ($C_{44} \neq C_{55}$) $< C_{66}$, originated from the fluid mobility and vertical fractures, whereas MB in well B is isotropic ($C_{44}=C_{55}=C_{66}$).

Figures 41 and 43 show the dispersion and SRP plots at depths 9,720ft and 9,808ft in well B. They represent perfect VTI caused by clay minerals in UB and LB. In Figures 41 and 43, flexural modes overlie each other and do not match the modeled curves in dispersion plots. On the SRP plots, flexural modes slowness do not separate and are slower than the Stoneley waves. Dispersion and SRP plots of MB shown in Figure 42 have the characteristics of an isotropic medium.

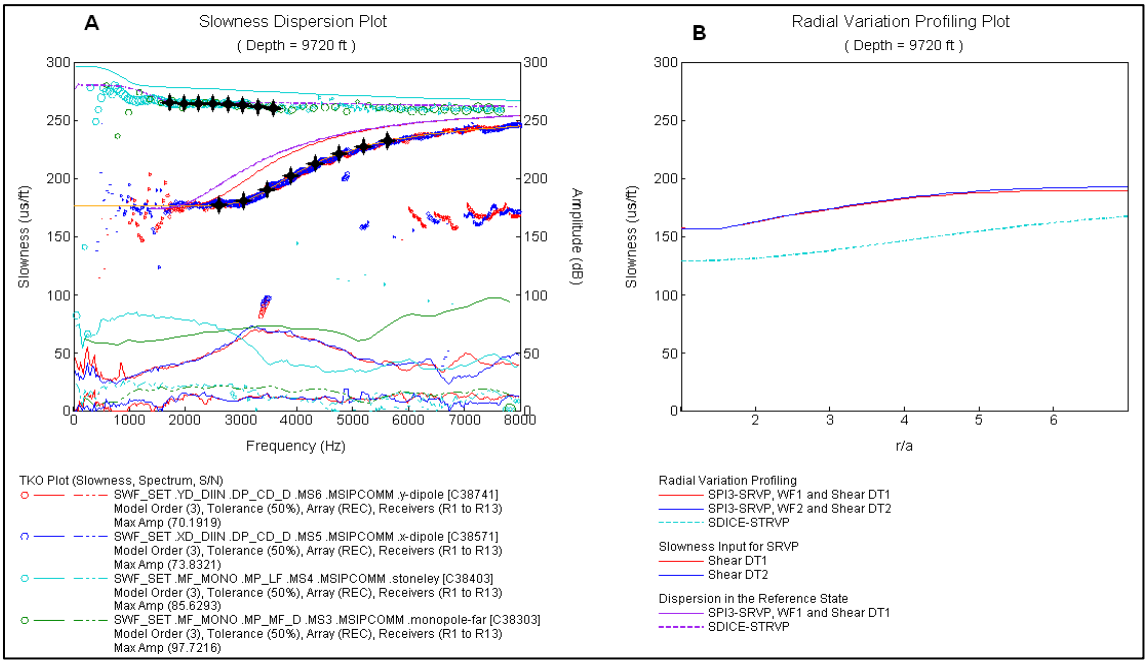

Figure 41 Dispersion plot (a) and radial slowness variation profile (b) for Upper Bakken in Well B.

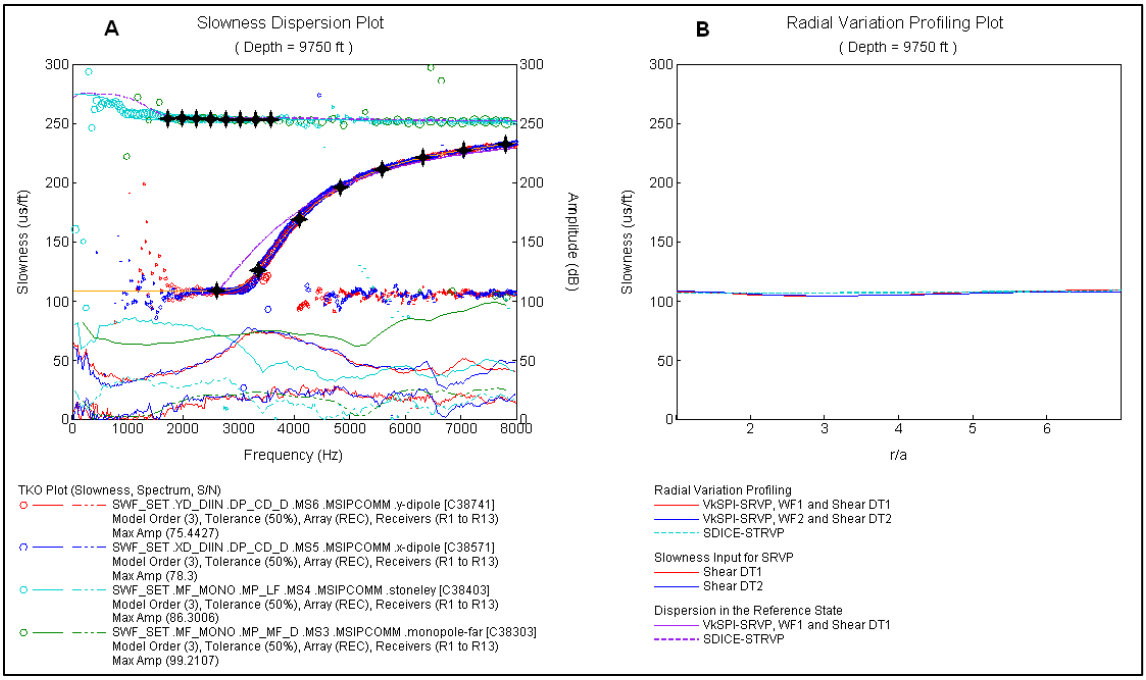

Figure 42 Dispersion plot (a) and radial slowness variation profile (b) for Middle Bakken in Well B

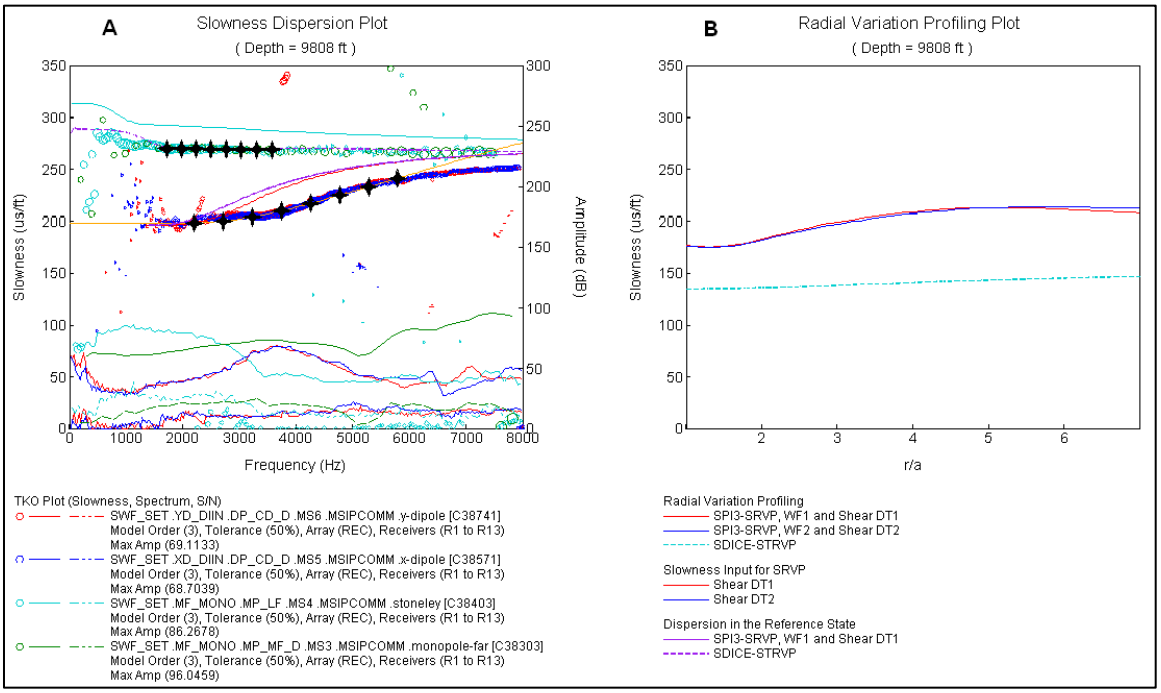

Figure 43 Dispersion plot (a) and radial slowness variation profile (b) for Lower Bakken in Well B.

Summary

The Nesson anticline as the major geologic feature in the North Dakota part of Williston Basin has caused vertical fractures in the Bakken Formation. Higher mobility and slight orthorhombic isotropy in the Bakken Formation are the results of Nesson folding. These latest properties are well studied from borehole advanced sonic log data acquired in this region.

Advanced sonic logging measurement is a powerful method for elastic stiffness characterization and anisotropy type analysis. Study of independent shear moduli along with Thomsen anisotropy parameters –evaluated in two wells in North Dakota– infers that the influence of structural geology on shear anisotropy is significant.

In well A the relationships $(C_{44} \neq C_{55}) > C_{66}$ and $(\epsilon \neq \gamma < 0)$, the result of anisotropy analysis, signify the presence of fractures along the Nesson anticline within the Middle Bakken. It can also be inferred that the slight orthorhombic isotropy in LB and UB confirms the fracture extension into these members which yields $(C_{44} \neq C_{55}) < C_{66}$

Applying dispersion plot analysis and radial slowness variation profiling to the dipole sonic data taken from two Bakken wells, fluid mobility and shear anisotropy in a tight reservoir (the Bakken formation) were successfully characterized.

Chapter IV

GEOMECHANICAL MODELING AND WELLBORE STABILITY

Introduction

This chapter consists of three main sections. In the first part, the necessity of geomechanical modeling and different elements encountered in wellbore stability with related literature has been introduced. In the second section, mathematical solutions for wellbore stability and stresses at the borehole with related formulae are presented. Finally, the results of numerical modeling for different well deviation angles are displayed.

The final section of this chapter includes elastic, elastoplastic and chemo, thermo-poro-elasticity conditions in geomechanical modeling. In addition Mohr-Coulomb failure criterion, which is the widely used failure criterion in wellbore stability analysis, has been acquired. I have presented 3-Dimensional geomechanical models for isotropic and anisotropic members of the Bakken Formation. The main contribution of this chapter is to include elastic anisotropy of the Bakken Formation in geomechanical models. The results cover vertical, inclined and horizontal well geomechanical models. The wellbore deviation angle has been increased every 15˚ from the vertical to the horizontal, and the stresses and deformations that take place around the borehole have been analyzed. 3-D geomechanical modeling is performed using FLAC3D, a product of ITASCA Consulting

Group. To analyze stresses at the borehole wall SFIB module of GMI software (Geomechanics International), a product of Baker-Hughes has been utilized.

Fundamentals of Geomechanical Modeling

Wellbore instability can be induced chemically or mechanically, or a combination of both.

Chemically Induced Instability

Chemically induced instability usually takes place in shale bearing zones when shales water absorption and swelling leads to hole enlargement, or in salt layers when the salt is dissolved by the drilling fluid and causes a reduction in the hole size. This study wants to understand how shales can be a major issue in the Bakken Formation, especially in the upper and lower members by including elastic anisotropy along with other properties.

Mechanically Induced Instability

Formations at depth exist under a state of compressive in-situ stresses. When a well is drilled through the formation, a significant amount of rock volume is removed which causes stress alteration. As a result, the surrounding rocks at the borehole must compensate for the eliminated load. Stress concentration around the borehole is the direct result of this process. Thus, in cases of weak formations such as unsolicited sands or shales, the formation may fail. The failures could be categorized under three main classes, as shown in Figure 44:

1. Formation breakdown, or unintended hydraulic fracturing that will result in loss of drilling fluid circulation.

2. Hole enlargement due to brittle rock fracture or rupture.

3. Hole size reduction, which can happen due to ductile yield of the rock.

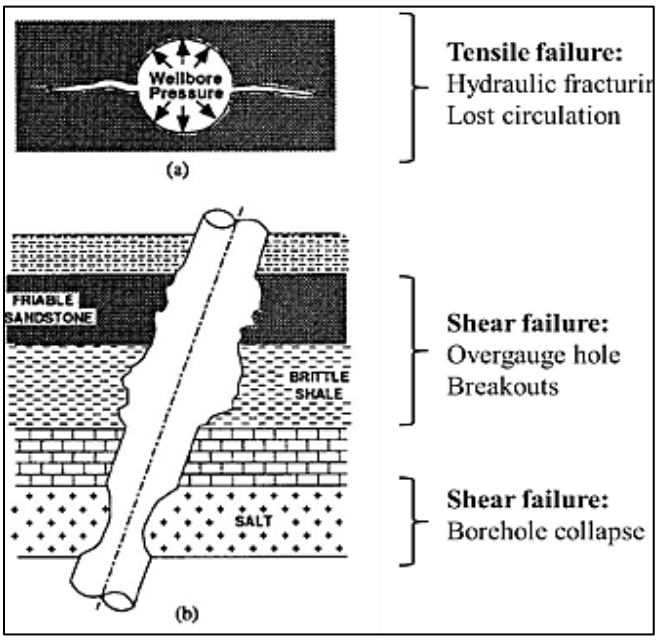

Figure 44 Three main classes of wellbore failure (modified from Duseault, 1994).

Factors Influencing Wellbore Stability

To obtain a good prediction of wellbore stability and geomechanical behavior of the reservoir, we should try to recognize the governing parameters and various possible conditions occurring around the borehole. There is a comprehensive list of factors encountered in wellbore stability analysis and geomechanical modeling, but the major ones that are controllable, predictable and measurable are rock strength, stiffness, permeability, temperature, pore pressure and concentration (Figure 45).

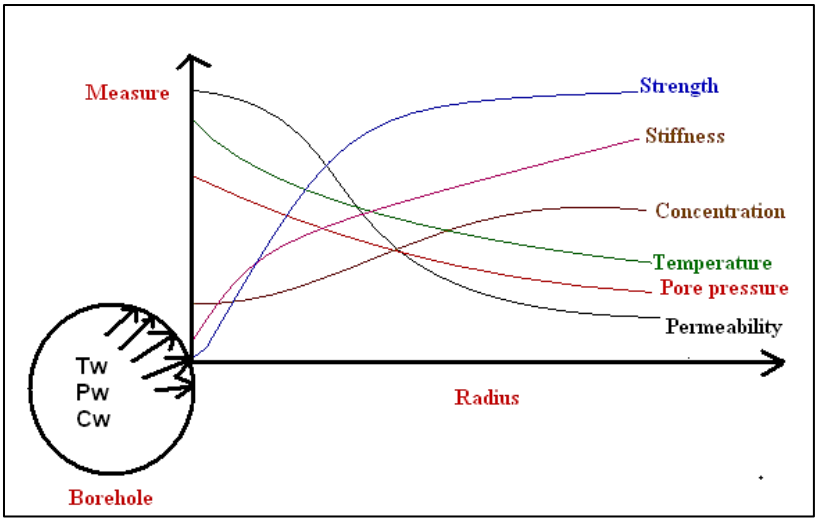

Figure 45 Alteration of different parameters around the borehole (modified from Duseault, 1994)

In-Situ Stress Field

Formation stresses play an important role in geophysical prospecting and development of oil and gas reservoirs. Both the direction and magnitude of these stresses are required in (a) planning for borehole stability, (b) hydraulic fracturing for enhanced production, and (c) selective perforation for sand control. The formation stress state is characterized by the magnitude and direction of the three principal stresses, one vertical and two horizontal. In this regard formations could be either normally stressed or tectonically stressed. In a normally stressed formation, the maximum principal stress is the vertical effective stress (σ_v), equal to the overburden stress. The other two principal in situ stresses (σ_H, σ_h) are located in a horizontal plane. For well compacted and cemented formations, the overburden stress varies linearly with depth (Figure 46). In tectonically stressed regions which may contain active faults, salt domes or severe folding and fracturing, the principal in-situ stresses are not necessarily oriented in vertical or horizontal directions that have led into structural deformations. Since Williston Basin is

considered as an intracratonic basin without any complex structural features, it can be categorized under normally stressed regions.

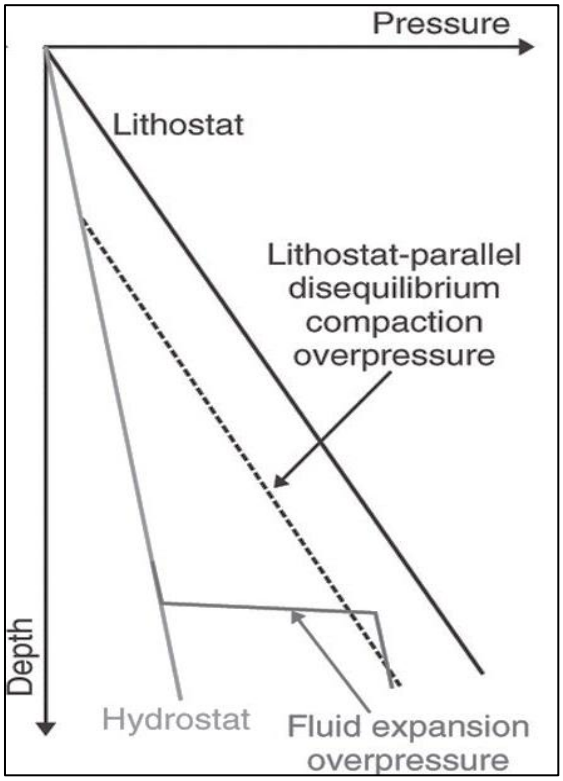

Figure 46 Stress variation versus depth.

Observations show that changes of in-situ stresses can cause major borehole instability problems associated with drilling specifically in tectonically active areas. In addition to in-situ stresses, pore pressure plays an important role in wellbore stability. Pore pressure, or reservoir pressure, is the amount of pressure exerted by the in situ pore fluid to the internal pore walls (Zimmerman, 2007). For normally pressured formations, the pore pressure gradient is constant at approximately 10.4 KPa/m. In geo-pressured (overpressured) formations such as the Bakken, pore pressure gradient can exceed 20.4 KPa/m. Figure 46 shows the stress and pressure variation versus depth.

Wellbore Pressure

Drilling wellbore pressure, which is maintained by drilling mud, tries to protect the wellbore from failure. On one hand, excess mud pressure will prevent blow-outs; on the other hand, it can cause pipe sticking problems, washouts or unintended fractures and lead into wellbore failure. It is important to maintain an appropriate and safe mud pressure window to avoid such problems. In general, the safe mud weight window needs to be determined by accurate models (McLean, 1987; Fjaer et al., 1992; Fam, et al., 2003).

Fractures and Damages in the Formation

Discontinuities, such as bedding planes, fractures and damages in the formation which are considered as weak planes, can cause wellbore instability problems. Mud can infiltrate into either natural or drilling-induced open fractures that cross the wellbore wall, increasing tensile stresses and resulting in wellbore instability problems.

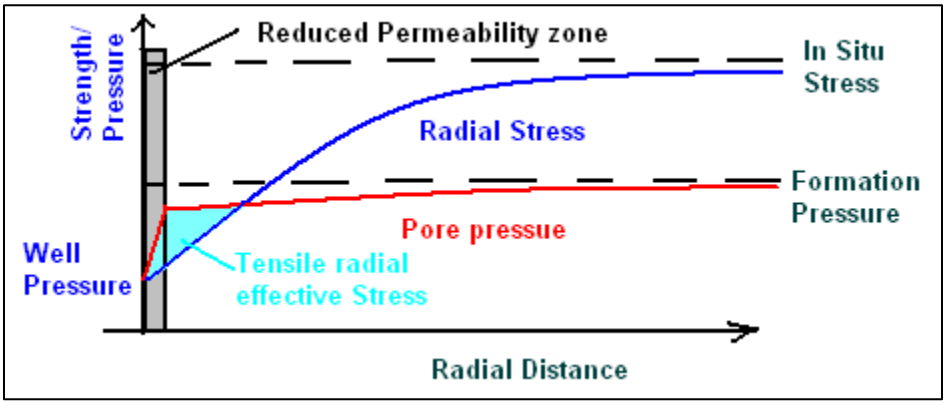

Figure 47 Reduced radial effective stress due to formation damage.

Formation damage, which means the invasion of the mud filtrate into the formation and reducing formation permeability, can reduce the wellbore stability. Figure 47 explains that the effective radial stress near the wellbore has been reduced due to high pore

pressure gradients set up in the damaged zone. In certain conditions, the pore pressure may be high enough to induce tensile effective radial stresses (Fam, et al., 2003).

Thermal Effect

Thermal effects can affect borehole stability, and should be considered in stress analysis (Maury, 1994). Cooling the wellbore wall, which is one of the main roles of the drilling fluid, can cause an increase in mud weight and result in the increase of tangential stresses, causing shear failures (Li, et al., 1998). Thermal effects become more important when drilling in naturally fractured reservoirs.

Fluid Flow into the Wellbore

Permeability of the formation should also be included for more accurate geomechanical modeling. In high permeable formations, an effective mud cake will form around the wellbore wall, preventing mud losses and wellbore failures. This mud cake is beneficial in borehole stability, and its characteristic is partially dependent on the formation permeability. Mud cakes will only develop on the edge of sufficiently permeable formations. In impermeable (tight) rocks like shales, the mud cake is negligible. Flowing formation fluid in to the wellbore drops formation pressure, thus the mud pressure remains greater than the pore fluid pressure (Fjaer et al., 1992; Charlez, 1997).

Chemical Effects (in Shales)

One of the main causes of shale instability is believed to be the unfavorable interactions between the shale and drilling mud (van Oort, 2003). This is primarily due to the shale acting as an osmosis membrane, helping the movement of water/ions into or out of shale. This movement causes alterations in mechanical and physiochemical properties of the shale, and can lead to wellbore instability problems. As previously mentioned shale water

absorption will increase pore pressure, thus decreasing the effective in-situ stresses and resulting in wellbore failures. Shale swelling which happens by clay minerals absorbing water will result in clay bond strength loss, thus ending in wellbore failure (Hale et al., 1992).

Numerical Modeling of Wellbore Stability

Requirements of Numerical Modeling

There are number of input parameters that influence wellbore stability and impact the accuracy of numerical models. However it is necessary to validate the models with laboratory experiments, but typical laboratory work cannot meet the conditions under which the numerical models were run. Thus, all numerical modeling projects should generally be considered as theoretical until proven under laboratory-controlled conditions.

There are an abundance of numerical models developed for analyzing wellbore instability, among which elastic and elastoplastic models are the most common used in the industry.

Elastic Models

The first elastic solution to predict wellbore stability was developed by Hubbert and Willis (1957) in a vertical borehole under non-hydrostatic far field stresses and constant borehole fluid pressure conditions. Fairhurst (1968) developed a solution for the stress distribution around an inclined borehole. The equations derived by Fairhurst (1968) were used by Bradley (1979) to model the stresses around a circular opening in a general case for the inclined well and not parallel to the principal stresses' directions. It should be mentioned that all these solutions were simple, and did not take temperature or pore

pressure gradients, mud cake effectiveness, material anisotropy or time dependency into account. Santarelli and Brown (1987) derived a stress-dependent elastic modulus solution for borehole stability. Aadnoy and Chenevert (1987) included the influence of rock anisotropy in inclined boreholes in further stability models to solve for stresses at the borehole wall. This model was later improved by Ong and Roegiers (1993), accounting for the stress as a function of borehole radius and adding an anisotropic shear failure criterion. Roegiers and Detournay (1988) developed a model that was able to predict stresses, displacements and fracture initiations at inclined borehole walls. Mody and Hale (1993) presented a model taking into account the chemical effects of drilling fluid and the formation. Sherwood and Bailey (1994) modified Biot's (1957) linear theory of poroelasticity for shale swelling around a cylindrical borehole. Linear elastic solutions are the most widely used models in the industry for mud weight design and borehole stability analyses due to their ease of use and less dependency on input parameters.

Elastoplastic and Poro-elastoplastic Models

An elastoplastic method suggests that even after the borehole might be stressed beyond its elastic limit to undergo a reversible deformation, the non-elastic region remains intact and load-bearing. A number of elastoplastic and nonlinear analytical and semi-analytical models for borehole stability include the work of Gnirk (1972) and Papamichos et. al., (1995). More recently, poro-elastoplastic models have been developed, which take the effects of the fluid flow and elastoplastic behavior of the rock into consideration (Zimmerman, 2007).

Numerical Methods

Numerical methods include finite element, finite difference, boundary element, and discrete element methods. Among these, finite difference method (FDM) and finite element method (FEM) are two of the most popular ones to analyze the extremely complex issues in wellbore instability. In this chapter, the geomechanical models are run under FDM.

Analytical Solutions for Wellbore Stability

Stress Distribution Around the Wellbore

A schematic diagram (Figure 48) and solutions of a vertical borehole in a linear elastic formation with horizontal in-situ stresses, and on its internal boundary by a wellbore pressure P_w (known as the plane strain problem), is as follows (Yu, 2000):

$$\sigma_r = \frac{P_0}{2}[(1+K)(1-\frac{a^2}{r^2}) - (1-K)(1-\frac{4a^2}{r^2}+\frac{3a^4}{r^4})\cos 2\theta] + \frac{P_w a^2}{r^2} \quad (23)$$

$$\sigma_\theta = \frac{P_0}{2}[(1+K)(1+\frac{a^2}{r^2}) + (1-K)(1+\frac{3a^4}{r^4})\cos 2\theta] - \frac{P_w a^2}{r^2} \quad (24)$$

$$\sigma_z = \sigma_v - \mu\frac{4a^2}{r^2}\frac{(1-K)P_0}{2} \quad (25)$$

$$\tau_{r\theta} = \frac{P_0}{2}[(1-K)(1+\frac{2a^2}{r^2}-\frac{3a^4}{r^4})\sin 2\theta] \quad (26)$$

$$\tau_{rz} = \tau_{\theta z} = 0 \quad (27)$$

Where μ is the Poisson's ratio, K is at rest earth pressure coefficient, a is borehole radius and P_0 is the external pressure of the borehole.

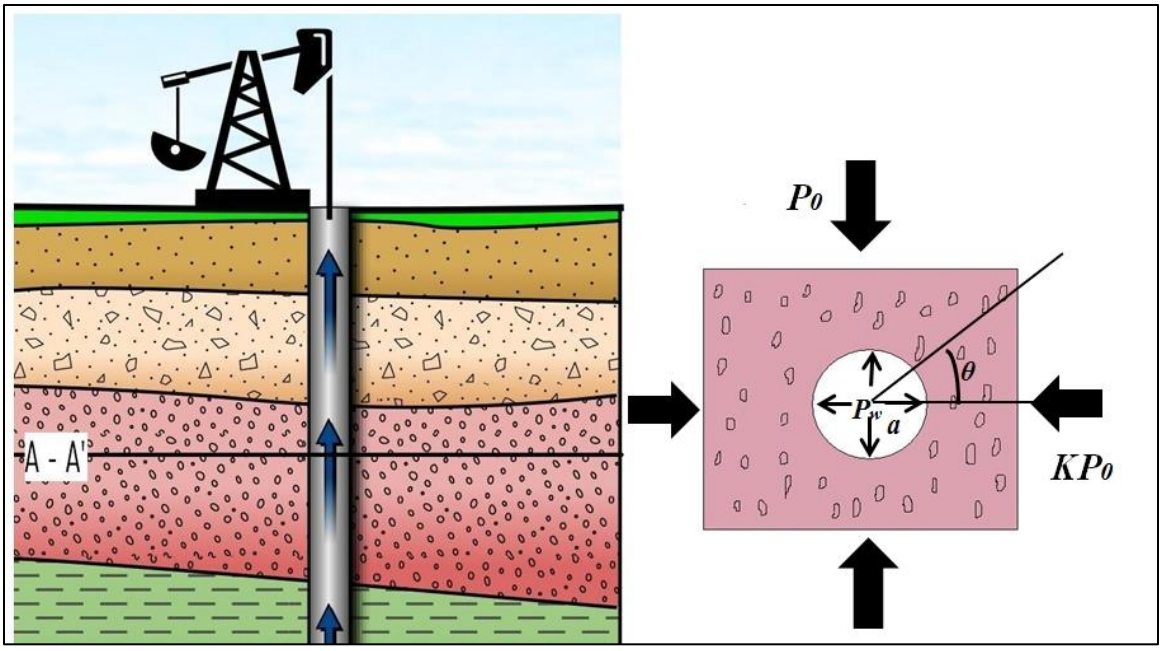

Figure 48 A vertical borehole in an anisotropic in-situ stress with internal wellbore pressure.

A more general solution would be a deviated borehole in an elastic formation (Figure 49) which is solved in a local coordinate system whose *z* axis is parallel to the wellbore axis and *x* axis is chosen to be parallel to the lowermost radial direction of the wellbore following equations. The global coordinate (virgin formation stress coordinate, *x'*, *y'*, *z'*) can be then converted into the local coordinate (borehole coordinate, *x, y, and z*) system (Fjaer, et al, 1992):

$$\begin{bmatrix} \sigma_x^0 \\ \sigma_y^0 \\ \sigma_z^0 \\ \sigma_{xy}^0 \\ \sigma_{yz}^0 \\ \sigma_{xz}^0 \end{bmatrix} = \begin{bmatrix} l_{xx'}^2 & l_{xy'}^2 & l_{xz'}^2 \\ l_{yz}^2 & l_{yy'}^2 & l_{yz'}^2 \\ l_{zx'}^2 & l_{zy'} & l_{zz'}^2 \\ l_{xx'}l_{yx'} & l_{xy'}l_{yy'} & l_{zz'}l_{yz'} \\ l_{yx'}l_{zx'} & l_{zy'}l_{yy'} & l_{zz'}l_{yz'} \\ l_{yx'}l_{zx'} & l_{zy'}l_{yy'} & l_{zz'}l_{xz'} \end{bmatrix} \begin{bmatrix} \sigma_H \\ \sigma_h \\ \sigma_v \end{bmatrix} \quad (28)$$

Where,

$$\begin{bmatrix} l_{xx'} & l_{xy'} & l_{xz'} \\ l_{yx'} & l_{yy'} & l_{yz'} \\ l_{zx'} & l_{zy'} & l_{zz'} \end{bmatrix} = \begin{bmatrix} \cos\varphi_x \cos\varphi_z & \sin\varphi_x \cos\varphi_x & -\sin\varphi_z \\ -\sin\varphi_x & \cos\varphi_x & 0 \\ \cos\varphi_x \cos\varphi_z & \sin\varphi_x \cos\varphi_z & \cos\varphi_z \end{bmatrix} \tag{29}$$

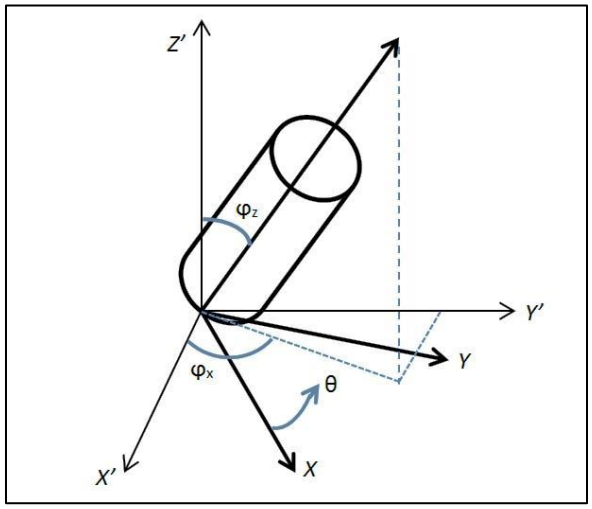

Figure 49 Schematic diagram for an inclined wellbore subjected to in situ stresses.

σ_H, σ_h and σ_v are the far-field stresses, σ_x^0 , σ_y^0, σ_z^0, τ_{xy}^0 τ_{yz}^0 and τ_{xz}^0 are the local wellbore coordinate stresses. φ_x is the azimuth angle, and is the anti-clockwise angle between the projection of the wellbore axis on the horizontal plane and the direction of the maximum horizontal in-situ stress. φ_z is the wellbore inclination, the angle between the wellbore axis and the vertical direction. After the conversion, the analysis can be worked out in the local coordinate system. Then the complete stress solutions are:

$$\begin{aligned} \sigma_r = &\left(\frac{\sigma_x^0 + \sigma_y^0}{2}\right)\left(1-\frac{r^2}{a^2}\right) + \left(\frac{\sigma_x^0 - \sigma_y^0}{2}\right)\left(1+3\frac{r^4}{a^4}-4\frac{r^2}{a^2}\right)\cos 2\theta \\ &+\tau_{xy}^0\left(1+3\frac{r^4}{a^4}-4\frac{r^2}{a^2}\right)\sin 2\theta + P_w\frac{r^2}{a^2} \end{aligned} \tag{30}$$

$$\sigma_\theta = \left(\frac{\sigma_x^0 + \sigma_y^0}{2}\right)(1+\frac{r^2}{a^2}) - \left(\frac{\sigma_x^0 - \sigma_y^0}{2}\right)\left(1+3\frac{r^4}{a^4}\right)\cos 2\theta$$
$$-\tau_{xy}^0\left(1+3\frac{r^4}{a^4}\right)\sin 2\theta - P_w\frac{r^2}{a^2} \quad (31)$$

$$\sigma_z = \sigma_z^0 - \mu\left[2(\sigma_x^0 - \sigma_y^0)\right]\left(\frac{r^2}{a^2}\right)\cos 2\theta + 4\tau_{xy}^0\left(\frac{r^2}{a^2}\right)\sin 2\theta \quad (32)$$

$$\tau_{r\theta} = \left(\frac{\sigma_x^0 - \sigma_y^0}{2}\right)(1-3\frac{r^4}{a^4}+2\frac{r^2}{a^2})\sin 2\theta + \tau_{xy}^0(1-3\frac{r^4}{a^4}+2\frac{r^2}{a^2})\cos 2\theta \quad (33)$$

$$\tau_{\theta z} = (-\tau_{xz}^0 \sin\theta + \tau_{yz}^0 \cos\theta)(1+2\frac{r^2}{a^2}) \quad (34)$$

$$\tau_{rz} = (\tau_{xz}^0 \cos\theta + \tau_{yz}^0 \sin\theta)(1-2\frac{r^2}{a^2}) \quad (35)$$

Where σ_θ , σ_r and σ_z are tangential stress, radial stress and axial stresses respectively and $\tau_{r\theta}$, $\tau_{\theta z}$, τ_{rz} are three components of the shear stress. θ is the angle from the maximum principal horizontal stress and *a* is the borehole radius.

Failure Criterion in Wellbore Stability

A failure criterion should be chosen to predict the wellbore instability. Mohr-Coulomb, which is an elastopastic failure model, and has been used extensively in industry is addressed and used for the analysis in this chapter.

Mohr-Coulomb Failure Criterion

The analysis begins with a simple case: a vertical borehole in a linear elastic formation with horizontal in-situ stresses, and the mud weight P_w on its internal boundary exerted

by the fluid pressure. In this case, the largest stress difference occurs at the borehole wall, $r = a$. According to Equations (36 – 39), the stresses at the borehole wall are:

$$\sigma_r = P_w \tag{36}$$

$$\sigma_\theta = P_0[1+K+2(1-K)\cos 2\theta] - P_w \tag{37}$$

$$\sigma_z = \sigma_v - 2\mu(1-K)P_0 \cos 2\theta \tag{38}$$

$$\tau_{r\theta} = \tau_{rz} = \tau_{\theta z} = 0 \tag{39}$$

Since all shear stresses vanish, σ_θ (tangential stress), σ_r (radial stress) and σ_z (axial stress) are principal stresses, and can be used directly in the failure criterion. The Mohr-Coulomb criterion is given as follows:

$$\sigma_1 - \alpha\sigma_3 = Y \tag{40}$$

Where,

$$\alpha = \frac{1+\sin\varphi}{1-\sin\varphi}, Y = \frac{2C\cos\varphi}{1-\sin\varphi} \tag{41}$$

And φ and C are the friction angle and cohesion respectively.

The minimum wellbore pressure

To prevent wellbore collapse when wellbore pressure is decreasing, the minimum wellbore pressure should be calculated. In this situation, two cases are considered (Fjaer, et al., 1992 and Charlez, 1997):

Case I: $\sigma_\theta > \sigma_z > \sigma_r$

Therefore, the Mohr-Coulomb criterion can be written as follows according to Equation (40):

$$\sigma_\theta - \alpha\sigma_r = Y \tag{42}$$

So the minimum wellbore pressure which can initiate the shear failure can be obtained:

$$P_w = \frac{[(1+K)+2(1-K)\cos 2\theta]P_0 - Y}{1+\alpha} \tag{43}$$

Case II: $\sigma_z > \sigma_\theta > \sigma_r$

The minimum wellbore pressure in this case can be obtained:

$$P_w = \frac{[\sigma_v - 2\mu(1-K)P_0\cos 2\theta] - Y}{\alpha} \tag{44}$$

The maximum wellbore pressure

If the wellbore pressure is increased significantly, the tensile failure can occur at the borehole wall when the smallest principal stress becomes tensile and equal to the tensile strength of the rock around the borehole:

$$\sigma_3 + T_r = 0 \tag{45}$$

Where, T_0 is the tensile strength of the rock around the borehole.

It is likely assumed that the tangential stress is the minor principal stress. Therefore, the maximum wellbore pressure is:

$$P_w = P_0[1+K+2(1-K)\cos 2\theta] + T_0 \tag{46}$$

Elastic-Perfectly Plastic Solutions

In this section, it is assumed that the rock around the borehole exhibits perfect elastoplastic behavior. The new solutions for borehole pressure are derived using Mohr-Coulomb criterion. Assuming the initial radius of the borehole R_0, and the internal borehole pressure P_i, the initial stresses around the borehole obey the Kirsch solutions. Then the borehole pressure is decreased to a value P_w, and the borehole radius is reduced to the current radius *a*. In the initial loading, the rock around the borehole behaves in a linear elastic manner, and the stress distribution can be expressed by Equations (23 – 27). When the borehole pressure is decreased to a certain limit, the yield is commenced. After initial yielding, the rock is assumed to exhibit perfectly plastic behavior, and a plastic zone develops around the borehole with a plastic radius R_p which travels outwards as the borehole pressure decreases (Figure 50).

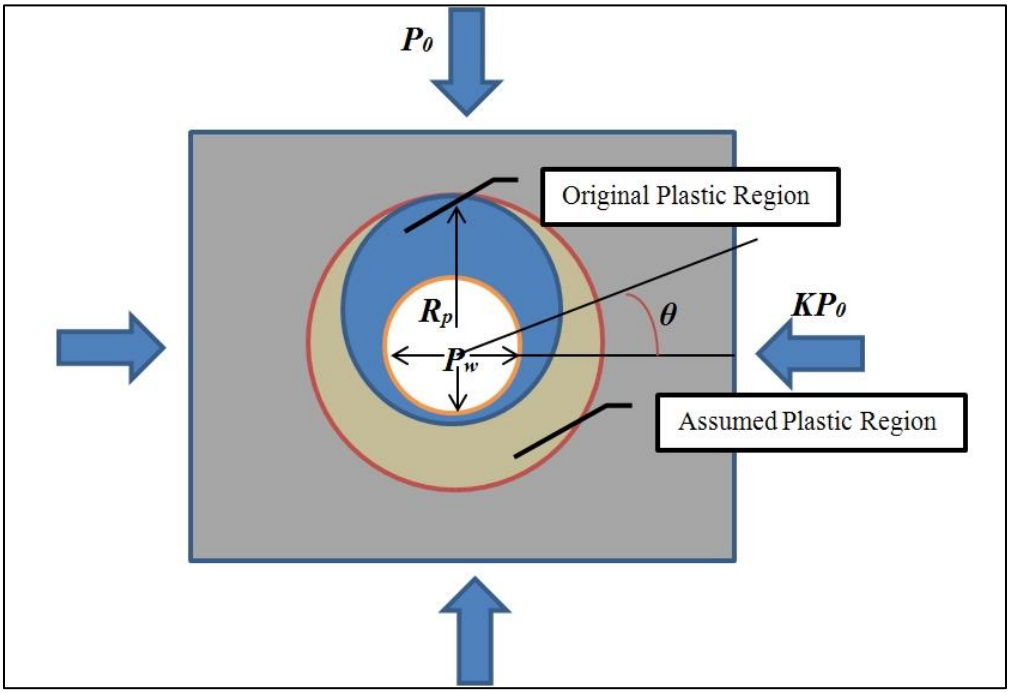

Figure 50 Definition of the problem and geometry of the zones around the borehole.

Two solutions are presented here under Mohr-Coulomb failure criterion based on *K* (earth pressure at rest), 1) when *K>1* and 2) when *K<1*.

- *K>1*

The focus of attention is the point that experiences yielding that is the furthest from the borehole axis i.e. $\theta = 90°$.

Elastic response and initial yielding

Before yielding, the stresses at this point can be expressed as:

$$\sigma_r = P_0 - \frac{a^2}{r^2}[\frac{P_0}{2}(5-3K) - P_w] + \frac{a^4}{r^4}[\frac{3P_0}{2}(1-K)] \quad (47)$$

$$\sigma_\theta = KP_0 - \frac{a^2}{r^2}[\frac{P_0}{2}(1+K) - P_w] - \frac{a^4}{r^4}[\frac{3P_0}{2}(1-K)] \quad (48)$$

According to Mohr-Coulomb criterion, Equation 40, as the borehole pressure decreases, the initial yielding occurs at the borehole wall *(r = a)* when the following condition is satisfied where $\sigma_1 = \sigma_\theta$ *and* $\sigma_3 = \sigma_r$:

$$[(3K-1)P_0 - P_w] - \alpha P_w = Y \quad (49)$$

The critical borehole pressure P_{1y} for the initial yield at the crown of the borehole is:

$$P_{1y} = \frac{3K-1}{1+\alpha}P_0 - \frac{Y}{1+\alpha} \quad (50)$$

At the point $r = R_p$, $\theta = 90^\circ$,(i.e. above the crown at the interface between the plastic zone and the elastic region), the radial stress can be given by:

$$\sigma_r^e = P_{1y} = \frac{3K-1}{1+\alpha} P_0 - \frac{Y}{1+\alpha} \tag{51}$$

Elastoplastic stress analysis

After initial yielding takes place with the decrease of the borehole pressure at the borehole wall, a plastic zone within the region $a \le r \le R_p$ forms around the inner wall of the borehole. The stresses in the plastic zone must satisfy the equilibrium equation:

$$\frac{\partial \sigma_r}{\partial \sigma} + \frac{\sigma_r - \sigma_\theta}{r} = 0 \tag{52}$$

Also, the stresses in the plastic region must satisfy the yield conditions:

$$\sigma_\theta - \alpha \sigma_r = Y \tag{53}$$

Substituting Equation (53) into Equation (52) and equating , one obtains:

$$\sigma_r = \frac{C}{\alpha - 1} r^{\alpha - 1} - \frac{Y}{\alpha - 1} \tag{54}$$

Using the boundary conditions for $r = a$, $\sigma_r = P_w$, a value for C can be obtained:

$$C = \frac{\alpha - 1}{a^{\alpha - 1}} P_w + \frac{Y}{a^{\alpha - 1}} \tag{55}$$

Therefore, the radial stress above the crown in the plastic zone can then be written as:

$$\sigma_r^p = \left(\frac{r}{a} \right)^{\alpha - 1} \left[P_w + \frac{Y}{\alpha - 1} \right] - \frac{Y}{\alpha - 1} \tag{56}$$

The radial stress should be continuous across the elastoplastic boundary, and so the following condition must be satisfied:

$$\sigma_r^p = \sigma_r^e \ at \ r = R_p, \theta = 90^\circ \tag{57}$$

Where the superscripts *e* and *p* denote the elastic and plastic zones, the borehole pressure P_w can then be expressed as:

$$P_w = \left[\frac{3K-1}{\alpha+1}P_0 - \frac{2Y}{1-\alpha^2}\right]\left(\frac{a}{R_p}\right)^{\alpha-1} + \frac{Y}{1-\alpha} \tag{58}$$

An axisymmetric cavity contraction theory is used to represent stresses at point ($r = R_p$, $\theta = 90^\circ$) for the asymmetric problem (where $K \neq 1$), therefore the following assumptions can be made:

- The plastic region, where its radius is the distance between the center of the borehole and the furthest yield point, is axisymmetric (Figure 50).
- The displacement for each point on the elastoplastic zone boundary is the same.
- Displacement depends on the maximum plastic radius and not the position angle θ.

With the above assumptions, the displacement at the interface between the elastic and plastic zone is given by the elasticity solution (Yu, 2000):

$$u\Big|_{r=R_p} = \frac{P_{1y} - P_0}{2G}\left(\frac{R_p}{r}\right)^2 r = \frac{\left[\left(1-\frac{3K-1}{\alpha+1}\right)P_0 + \frac{Y}{1+\alpha}\right]}{2G}R_p \tag{59}$$

Where G is the shear modulus of the rock around the borehole, $G = E/2(1+\mu)$. For unloading cavity contraction, the following solution can be derived (Yu, 2000):

$$R_0^{1+\beta} - a^{1+\beta} = (R_p - u)^{1+\beta} - R_p^{1+\beta} \tag{60}$$

Where

$$\beta = \frac{1+\sin\psi}{1-\sin\psi} \tag{61}$$

Where ψ denotes the dilation angle of the rock.

Since soft rocks have a small dilation angle, it can be assumed that the rock volume does not change within the plastic zone. Therefore $\sin\psi = 0$ can be achieved, which leads to:

$$R_0^2 - a^2 = (R_p - u)^2 - R_p^2 \tag{62}$$

It has been found that the dilation angle has relatively little influence on the solutions.

Substituting Equation (59) into Equation (62) and neglecting the higher-order terms gives:

$$\frac{a}{R_p} = \left(\frac{R_0^2}{R_p^2} - \frac{\left(1 - \frac{3K-1}{1+\alpha}\right)P_0 + \frac{Y}{1+\alpha}}{G} \right)^{0.5} \tag{63}$$

And substituting Equation (63) into Equation (58) yields:

$$P_w = \left[\frac{3K-1}{1+\alpha} P_0 - \frac{2Y}{1-\alpha^2} \right] \left(\frac{R_0^2}{R_p^2} - \frac{\left(1 - \frac{3K-1}{1+\alpha}\right)P_0 + \frac{Y}{1+\alpha}}{G} \right)^{0.5} + \frac{Y}{1+\alpha} \tag{64}$$

K<1

In this situation, the initial yield and the furthest points are at the spring-line of the borehole, i.e. $\theta = 0^{\circ}$.

The critical borehole pressure P_{2y} for initial yield at the spring-line of the borehole is:

$$P_{2y} = \frac{3K-1}{1+\alpha} P_0 - \frac{Y}{1+\alpha} \tag{65}$$

A similar approach can be used to obtain the equivalent limiting borehole pressure equation:

$$P_w = \left[\frac{3-K}{1+\alpha} P_0 - \frac{2Y}{1-\alpha^2}\right] \left(\frac{R_0^2}{R_p^2} - \frac{\left(1-\frac{3-K}{1+\alpha}\right)P_0 + \frac{Y}{1+\alpha}}{G} \right)^{\frac{\alpha-1}{2}} + \frac{Y}{1-\alpha} \tag{66}$$

Wellbore Stability in Laminated Formations

Strength anisotropy, which exists due to the presence of weak planes, is one of the unique properties of laminated shales. Therefore, both the stress state around the wellbore and the variable strength properties of laminated formations should be considered in wellbore stability calculations.

Anisotropic Strength Model

In this model, it is assumed that under triaxial compressive strength the pore pressure within the shale sample is zero (drained-test conditions). A shale sample, as shown in Figure 51, is subjected to a typical compressive strength test. Based on the operation angle (β), which is defined as the angle between the bedding plane and the axial stress, two possibilities for laminated rock failure may exist: either across or along the bedding plane.

- If the sample fails across the bedding plane, then the strength is defined as "normal strength", $\sigma_{1n}^{'}$.
- If the sample fails along the bedding plane, then the strength is defined as the "bedding plane strength", $\sigma_{1b}^{'}$ at that operation angle.

According to Mohr-Coulomb failure criterion, the normal strength can be calculated using the following equation (Jaeger and Cook, 1979),

$$\sigma_{1n}^{'} = \sigma_3^{'} + 2(C_0 + \mu\sigma_3^{'})\left[(\sqrt{1+\mu^2}) + \mu\right] \tag{67}$$

Similarly, the bedding plane strength can be calculated using the following equation (Jaeger and Cook, 1979),

$$\sigma_{1b}^{'} = \sigma_3^{'} + \frac{2(C_{0w} + \mu_w\sigma_3^{'})}{(1+\tan\beta\mu_w)\sin 2\beta} \tag{68}$$

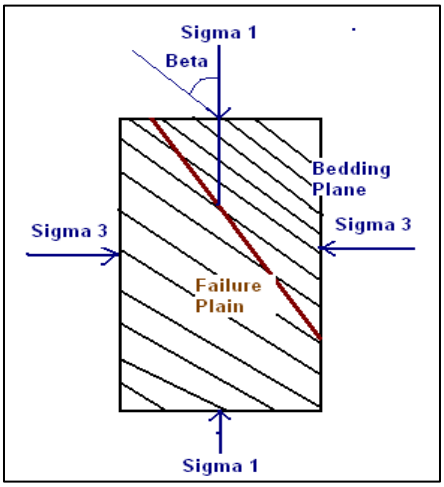

Figure 51 Shale sample under triaxial stress.

Differentiating Equation (68) with respect to β shows that $\sigma_{bs}^{'}$ has a minimum value when: $\tan 2\beta_w = \frac{1}{\mu_w}$ (β_w is special operation angle at which the bedding strength becomes minimum), this minimal value of $\sigma_{bs,\min}$ is:

$$\sigma'_{1b,\min} = \sigma'_3 + 2(C_{0w} + \mu_w \sigma'_3)\left[(\sqrt{1+\mu_w^2}) + \mu_w\right] \quad (69)$$

By equating Equations (67) and (68), two values of operation angle, denoted as $\beta_1 \; and \; \beta_2, \beta_1 \prec \beta_2$, can be calculated as:

$$\beta_1, \beta_2 = \tan^{-1}\left(\frac{a \pm \sqrt{a^2 - b^2 - 2ab\mu_w}}{b + 2a\mu_w}\right) \quad (70)$$

Where, μ_w is the weak plane coefficient of friction and,

$a = (C_0 + \mu\sigma'_3)\left[(\sqrt{1+\mu^2}) + \mu\right]$ and $b = C_{0w} + \mu_w\sigma'_3$.

Where μ is the intrinsic coefficient of friction. The cohesion (C_0) can be determined through uniaxial compressive strength (UCS) test, geophysical well logs or from correlations.

Discussion and Results

Mechanical Earth Model

To carry out a complete geomechanical study, a mechanical earth model (MEM) should be generated. A MEM is a numerical representation of reservoir properties in 1-D, 2-D or even 3-D style. A MEM contains data related to the rock failure mechanisms, in-situ stress, stratigraphy and geologic structure of the reservoir (Sayers, et. al., 2009, Sayers, et. al., 2007, Plumb, et. al. 2000, Plumb et. al., 2004). As mentioned previously, a MEM should be made any time before the drilling. It will be updated with new information anytime when drilling is in progress and later during the production. Figure 52 depicts a normal path for constructing a proper MEM.

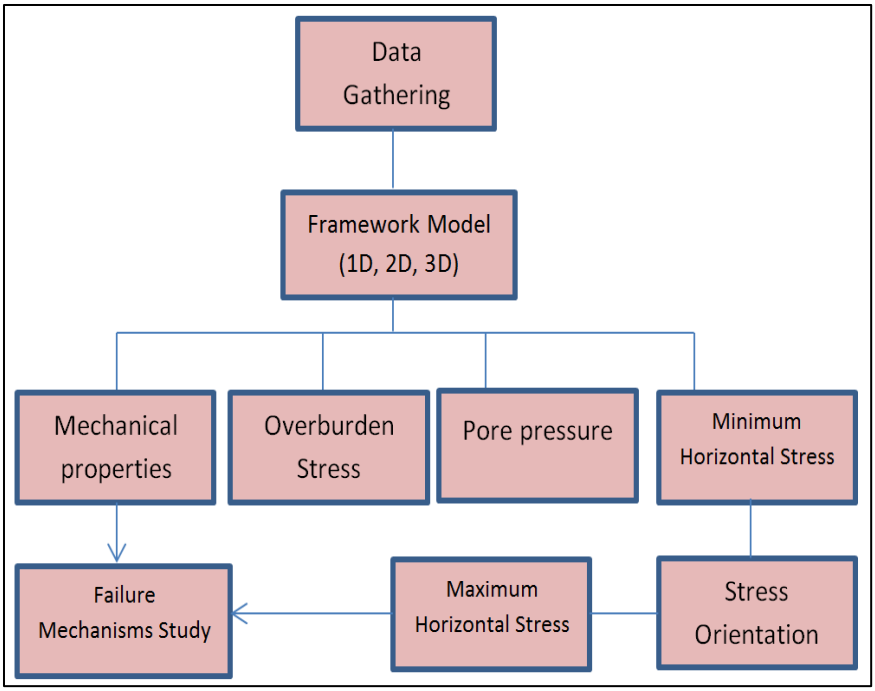

Figure 52 Mechanical Earth Model (MEM) flowchart.

Figure 53 illustrates the major contributions of this thesis made by incorporating elastic anisotropy in to constructing a more precise MEM for geomechanical modeling.

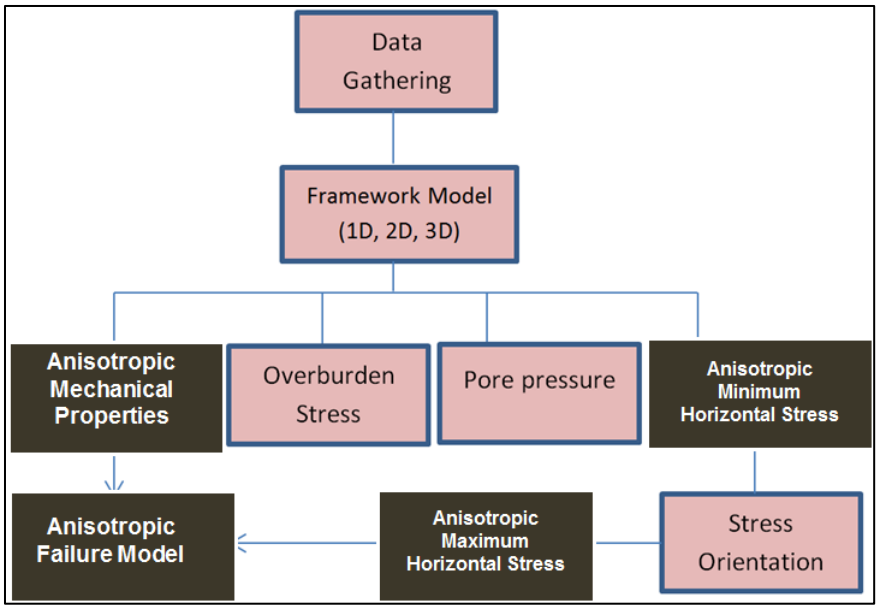

Figure 53 Anisotropic MEM flowchart.

Mechanical Anisotropy

Anisotropy has been neglected in constructing MEM and geomechanical (numerical) modeling for decades. In the petroleum industry, isotropy assumptions have been frequently applied to geomechanical modeling not because they are good approximations, but since anisotropic measurements were not available and relevant modeling were sophisticated. Moreover, isotropy assumptions have led to inaccurate results (Higgins, et. al., 2008, Thiercelin and Plumb, 1994) in geomechanical models. Mechanical anisotropy means elastic properties of the rock, such as Young's modulus, Poisson's ratio and shear modulus, change due to the direction of the measurement. Recent advancements in sonic logging technology have made the three dimensional (3-D) analysis of mechanical anisotropy possible around the wellbore with high levels of precision (Pistre, et. al., 2005, Walsh, et. al., 2006).

Stress Determination

Vertical Stress

Total vertical stress is defined as the combination of the weight of the rock matrix which is vertical effective stress and the pressure exerted by the fluids in the pore spaces overlying the depth of interest, as shown in Equation (71).

$$S(h)=\int_0^h \rho(z)gdz \qquad (71)$$

Where $S(h)$ is the total vertical stress at depth h, $\rho(z)$is the density at depth z below the surface, and g is the acceleration due to gravity. Equation (71) can be rearranged in the form of Equation (72):

$$\sigma_v = S(h) - P_p \qquad (72)$$

Where σ_v is the vertical effective stress and P_p is the pore pressure which is caused by the fluid in the pore spaces, $S(h)$ can be computed by integrating bulk densities from the density log data. It should be noted that if water column exists above the surface, $\rho_w g z_w$ should be added to Equation (71); ρ_w is the water density and z_w is water depth.

Pore Pressure

A good knowledge of pore pressure is necessary to prevent blow outs and to ensure a safe well design (Sayers, 2009). Pore pressure (P_p) can be measured directly from repeated formation test (RFT) and drill stem test (DST) with high accuracy during drilling. When these data are not available, qualitative pore pressure estimation from velocity data can be utilized. Several methods for velocity-based pore pressure estimation have been proposed in the literature (Sayers, et. al., 2006 and Gutierz, et. al., 2006). The most widely used method in the petroleum industry is the Eaton formalism (Eaton, 1972 and Sayers, 2009). This approach is based on the fact that the relationship that the ratio of the observed sonic log value (or slowness) to the normal velocity value (or slowness) has with the pore pressure follows Equation (73), (Mouchet and Mitchel, 1989, Ruth and Hillis, 2000):

$$P_p = S - (S - P_p)\left(\frac{\Delta t_{normal}}{\Delta t_{observed}}\right)^3 \qquad (73)$$

Where P_p is pore pressure (MPa), P_h is the hydrostatic pressure (MPa), S is total vertical stress (MPa) and Δt is slowness (µs/ft).

Horizontal Stress

Horizontal stress for an isotropic medium has been extensively used in the industry and was derived from the solution of the linear poroelastic equation (Jaeger and Cook, 1979). Horizontal stresses for an isotropic poroelastic medium under uniform tectonic horizontal

strain can be expressed as follows, Equations (74) and (75), (Thiercelin and Plumb, 1994):

$$\sigma_h - \alpha P_p = \frac{\nu}{1-\nu}(\sigma_v - \alpha P_p) + \frac{E}{1-\nu^2}\varepsilon_h + \frac{E\nu}{1-\nu^2}\varepsilon_H \tag{74}$$

$$\sigma_H - \alpha P_p = \frac{\nu}{1-\nu}(\sigma_v - \alpha P_p) + \frac{E}{1-\nu^2}\varepsilon_H + \frac{E\nu}{1-\nu^2}\varepsilon_h \tag{75}$$

where E is Young's modulus, ν is Poisson's ratio, σ_h is the minimum horizontal principal stress, σ_H is the maximum horizontal principal stress, σ_v is the vertical (overburden) stress, α is Biot's constant, ε_h is the minimum horizontal strain and ε_H is the maximum horizontal strain.

Horizontal stresses for a transversely isotropic medium with a vertical axis of symmetry under uniform tectonic horizontal strain can be developed as (Thiercelin and Plumb, 1994, Waters et. al., 2011)

$$\sigma_h - \alpha P_p = \frac{E_{horz}\nu_{vert}}{E_{vert}(1-\nu_{horz})}(\sigma_v - \alpha(1-\xi)P_p) + \frac{E_{horz}}{1-\nu_{horz}^{\ 2}}\varepsilon_h + \frac{E_{horz}\nu_{horz}}{1-\nu_{horz}^{\ 2}}\varepsilon_H \tag{76}$$

$$\sigma_H - \alpha P_p = \frac{E_{horz}\nu_{vert}}{E_{vert}(1-\nu_{horz})}(\sigma_v - \alpha(1-\xi)P_p) + \frac{E_{horz}}{1-\nu_{horz}^{\ 2}}\varepsilon_h + \frac{E_{horz}\nu_{horz}}{1-\nu_{horz}^{\ 2}}\varepsilon_h \tag{77}$$

Where E_{horz} is Young's modulus in the plane of isotropy, E_{vert} is Young's modulus along the axis of symmetry, which is the direction of anisotropy, ν_{horz} is Poisson's ratio in the plane of isotropy, ν_{vert} is Poisson's ratio along the axis of symmetry. α is Biot's constant and ξ is the poroelastic constant. It is clear that the variants of Equations (74)

and (75) are very well improved from isotropic E and ν to anisotropic ones in Equations (76) and (77).

Elastic Parameters

Isotropic Elastic Parameters

Elastic properties are the main input parameters which should be measured for calculating the horizontal stresses. Conventional sonic logging enables measurement of the dynamic isotropic Young's modulus and Poisson's ratio along the wellbore by Equations (78) and (79) (Mavko, et. al, 1998, Wndt, et. al., 2007):

$$\nu = \frac{(V_p^2 - 2V_s^2)}{2(V_p^2 - V_s^2)} \tag{78}$$

$$E = \frac{\rho V_s^2 (3V_p^2 - 4V_s^2)}{(V_p^2 - V_s^2)} \tag{79}$$

Where ρ is the formation density, v_p is the compressional wave velocity and v_s is the shear wave velocity.

Anisotropic Elastic Parameters

For an anisotropic elastic medium assuming vertical transverse isotropy (VTI), by applying linear Hook's law expressed in Equation (80) and taking X_3 as the axis of rotational symmetry, the stiffness matrix becomes Equation (81) in the conventional two index Voigt notation (Nye, 1985)

$$\sigma_{ij} = C_{ijkl}\varepsilon_{kl} \tag{80}$$

where σ_{ij} is the stress tensor, C_{ijkl} is the fourth rank stiffness tensor and ε_{kl} is the strain tensor.

$$C_{ij} = \begin{pmatrix} C_{11} & C_{12} & C_{13} & 0 & 0 & 0 \\ C_{21} & C_{22} & C_{23} & 0 & 0 & 0 \\ C_{31} & C_{32} & C_{33} & 0 & 0 & 0 \\ 0 & 0 & 0 & C_{44} & 0 & 0 \\ 0 & 0 & 0 & 0 & C_{55} & 0 \\ 0 & 0 & 0 & 0 & 0 & C_{66} \end{pmatrix} \tag{81}$$

The inverse of Equation (80) in which the strain tensor is expressed as a linear function of the stress for a linear elastic transverse isotropic medium can be written as $\varepsilon_{kl} = S_{ijkl}\sigma_{ij}$ where $S = C^{-1}$.Thus the non-vanishing elastic compliance coefficients become $S_{11} = S_{22}$, S_{33}, $S_{12} = S_{21}$,$S_{13} = S_{23} = S_{32} = S_{31}$,$S_{44} = S_{55}$ and $S_{66} = 2(S_{11} - S_{12})$ in the two index notation.

The compliance tensor S_{ij} of a vertical transverse isotropic medium can be expressed in terms of Young's modulus and Poisson's ratio as follows (Amadei, et. al., 1987, Jaeger et. al., 2007):

$$C_{ij} = \begin{pmatrix} \frac{1}{E_1} & \frac{-\nu_{21}}{E_1} & \frac{-\nu_{31}}{E_1} & 0 & 0 & 0 \\ \frac{-\nu_{12}}{E_1} & \frac{1}{E_1} & \frac{-\nu_{31}}{E_3} & 0 & 0 & 0 \\ \frac{-\nu_{13}}{E_3} & \frac{-\nu_{31}}{E_3} & \frac{1}{E_3} & 0 & 0 & 0 \\ 0 & 0 & 0 & \frac{1}{\mu_{13}} & 0 & 0 \\ 0 & 0 & 0 & 0 & \frac{1}{\mu_{13}} & 0 \\ 0 & 0 & 0 & 0 & 0 & \frac{1}{\mu_{12}} \end{pmatrix} \tag{82}$$

If X_3 is taken as the axis of vertical rotational symmetry and $X_1 - X_2$ the plane of symmetry, then $E_1 = E_{horz}$ is the horizontal Young's modulus in the plane of symmetry, $E_3 = E_{vert}$ is the vertical Young's modulus along the axis of symmetry, $\nu_{12} = \nu_{21} = \nu_{horz}$ is the horizontal Poisson's ration in the plane of symmetry (isotropy) and $\nu_{31} = \nu_{13} = \nu_{vert}$ is the vertical Poisson's ratio along the vertical axis of symmetry. The anisotropic Young's modulus and Poisson's ratio for a vertically transverse isotropic medium in terms of elastic stiffness coefficients (C_{ij}), Equations (83)-(86), will be obtained by mathematical calculations after re-inversing the compliance tensor, Equation (82), $C = S^{-1}$. Thus, the horizontal and vertical E and ν will be as follows (Higgings, et. al., 2008 and Mavko, et. al., 1998):

$$E_{horz} = \frac{(C_{11} - C_{12})(C_{11}C_{33} - 2C_{13}^2 + C_{12}C_{13})}{C_{11}C_{13} - C_{13}^2} \tag{83}$$

$$E_{vert} = C_{33} - \frac{2C_{13}^2}{C_{11} + C_{12}} \tag{84}$$

$$\nu_{horz} = \frac{C_{12}C_{33} - C_{13}^2}{C_{11}C_{33} - C_{13}^2} \tag{85}$$

$$\nu_{vert} = \frac{C_{13}}{C_{11} + C_{33}} \tag{86}$$

To evaluate the anisotropic elastic parameters from Equations (83)-(86), elastic stiffness coefficients (C_{ij}) are needed. Advanced sonic logging has made capturing the relevant elastic stiffness coefficients (C_{ij}) azimuthally and radially deep in the formation, and in the area around the well (Sinha et. al., 2007 and Sinha et. al., 2007) possible with high accuracy.

Geophysical Log Presentation

Figure 54 represents the corresponding Neutron-Density log (first track), gamma ray log (second track) and formation lithology (third track) through the Bakken Formation for the Ruland well.

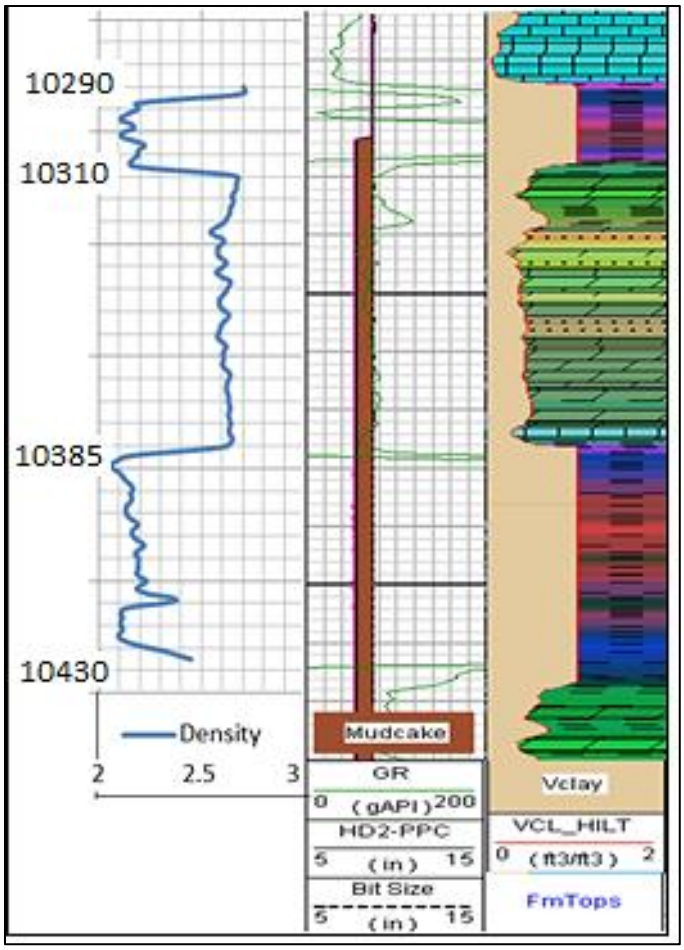

Figure 54 Conventional logs through the Bakken Formation-Neutron-Density (first track), Gamma Ray (second track) and formation lithology and clay volume (third track).

Stress Profile Determination

Figure 55 depicts the stress profile through the Bakken interval. The total vertical stress is obtained from Equation (72). Due to the availability of complete density data in the well, density trend analysis was found to be unnecessary (Sayers, 2006).

To calculate the pore pressure, Equation (73) was applied. For this analysis, a compressional wave velocity (slowness) trend throughout the well was obtained and is presented in Figure 56. Upon closer examination into the slowness variation trend (blue line), a deflection from the normal velocity-compaction trend is observed in the Bakken interval (red oval). This represents the overpressure nature of this layer. Eaton relation, Equation (73), was used to adapt the slowness-depth data to delineate the normal velocity (slowness) trend that would be created only due to the compaction (Eaton, 1972).

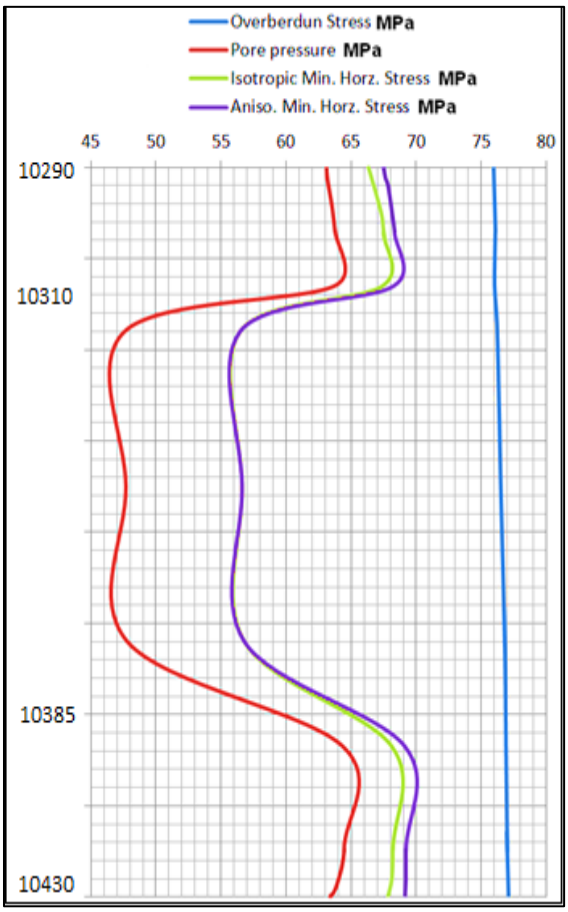

Figure 55 Stress profile through the Bakken Formation.

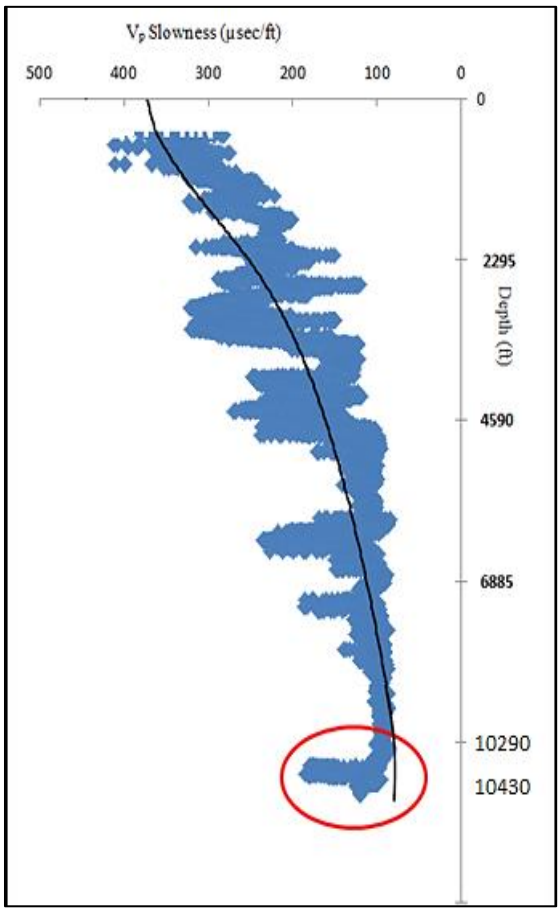

Figure 56 Compressional wave slowness trend- Deflection from the normal velocity is observed in the Bakken (red oval) due to the overpressure nature of this formation.

This deviation from the normal velocity (slowness) trend can be explained by unloading effects which originated with the decrease in the effective stress acting on the rock frame. The decrease in the effective stress normally takes place due to an increase in the pore pressure in a specific interval (Bowers, 1994). Considering the petroleum system governing the Bakken, this overpressure behavior can be explained by the conversion of kerogen to hydrocarbon in the upper and lower shale members. Additionally, the high clay volume content of the middle member (Figure 54) in the vicinity of clastic and carbonate facies has caused a high degree of heterogeneity. Consequently, migration of the generated and expelled hydrocarbon from the upper and lower members into the middle section through the vertical fractures can explain the abnormal overpressure characteristics of the Middle Bakken. The pore pressure profile is represented in Figure 55. Ultimately, we can declare that the highly compacted shales of UB and LB, along with high clay volume content of MB, are the primary reasons for the high overpressure nature of these intervals.

Minimum horizontal stress profile under isotropic assumptions in the Bakken Formation is shown in Figure 55. This stress profile (green curve in Figure 55) was calculated using Equation (74) under isotropic-poroelasticity relations. Minimum horizontal stress for transverse isotropic medium was estimated from Equation (76) and plotted in Figure 55 (purple line). Comparing these two minimum horizontal stress profiles, we can achieve better results when anisotropy assumptions are included in calculations. Therefore, anisotropy will alter the magnitude of minimum horizontal stress towards more accurate approximations.

In order to evaluate the horizontal stress magnitude from Equations (75)-(77), lateral tectonic strains, $\varepsilon_h, \varepsilon_H$ should be evaluated. It is often assumed that after fluid is withdrawn from a reservoir where the vertical stress is the major acting principal stress, lateral strain is inhibited by the rock adjacent to the reservoir, thus uniaxial strain assumptions maybe acceptable (Zimmerman et. al., 2007). To approximate the minimum horizontal stress, uniaxial strain assumption was taken into account. This means that the only strain is in the vertical direction thus the lateral tectonic strains, $\varepsilon_h, \varepsilon_H$ in Equations (74)-(77), were assumed zero (Thiercelin and Plumb 1994). Adding the predicted tectonic strain values if measured, will result in more accurate outcomes (Fjar, et. al., 1992). Since Williston Basin is considered an intracratonic basin and is currently under tectonic equilibrium, setting the lateral strains, $\varepsilon_h, \varepsilon_H$ equal to zero is reasonable.

To calculate horizontal stress from Equation (74) and equation (76) Biot's constant $\alpha = 1$ and poroelastic constant $\xi = 0$ were applied. If exact measured value of Biot's constant is input, it will estimate the minimum horizontal stress results more accurately.

Maximum Horizontal Principal Stress (A New Approach)

A novel accurate method to calculate the maximum horizontal principal stress in the Ruland well is used. In order to calculate horizontal principal stresses, C_{44}, C_{55} and C_{66} should be calculated from the slow shear, fast shear and Stoneley wave velocities respectively including formation density. The measurements are shown in Figure 57. First column denotes the formation tops, the first, track blue and red curves are representing C_{55} and C_{44} respectively and the second track represents C_{66}.

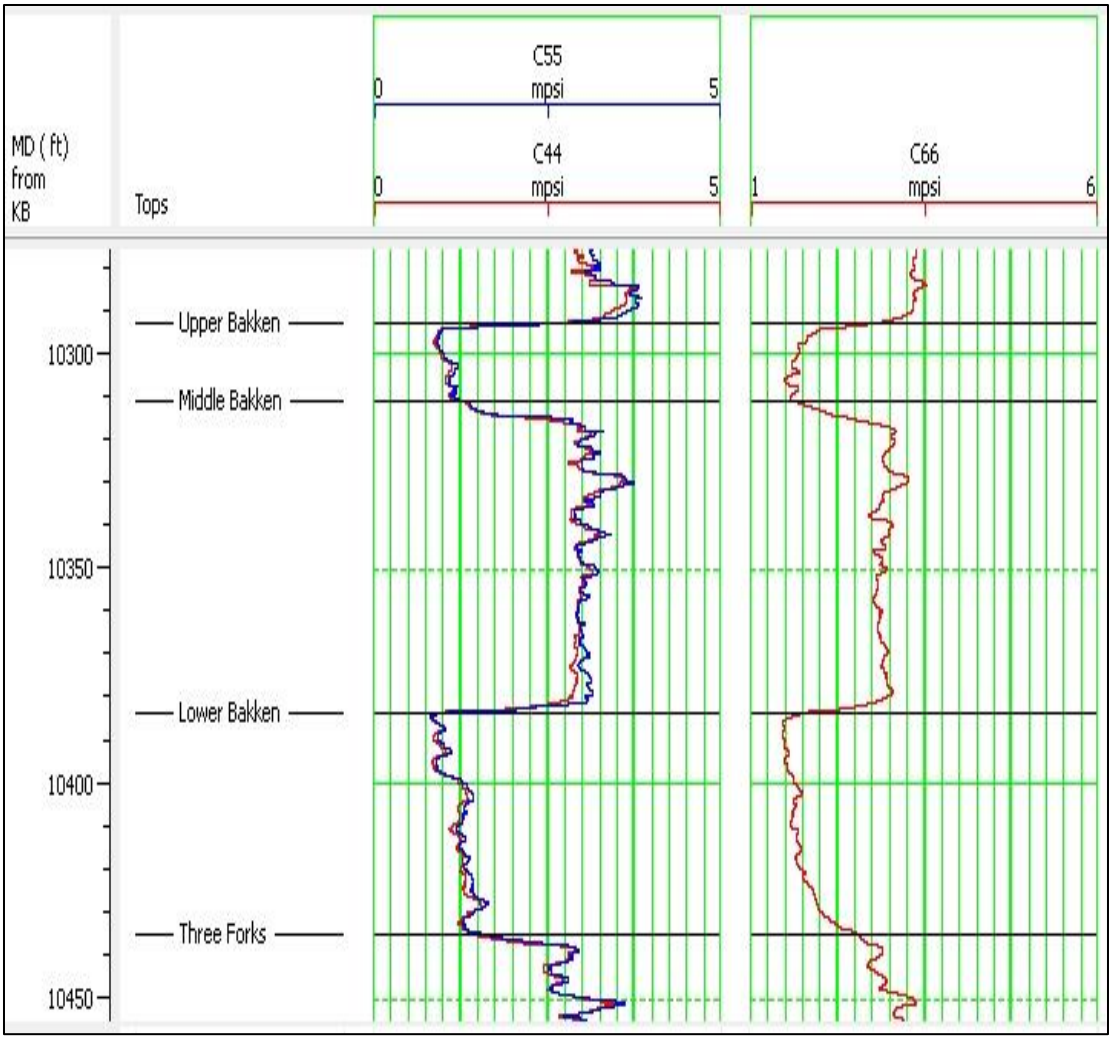

Figure 57 Three shear moduli measured through the Bakken Formation in Ruland well.

A better estimation of anisotropic maximum principal horizontal stress is to take the effect of the elastic properties of the formation in the horizontal and vertical directions and three formation moduli into consideration. This procedure is accomplished by Equations (87) and (88). The results are depicted in the following figure. The black star in the figure shows the measured pore pressure in the Middle Bakken obtained from DST (Drill Stem Test).

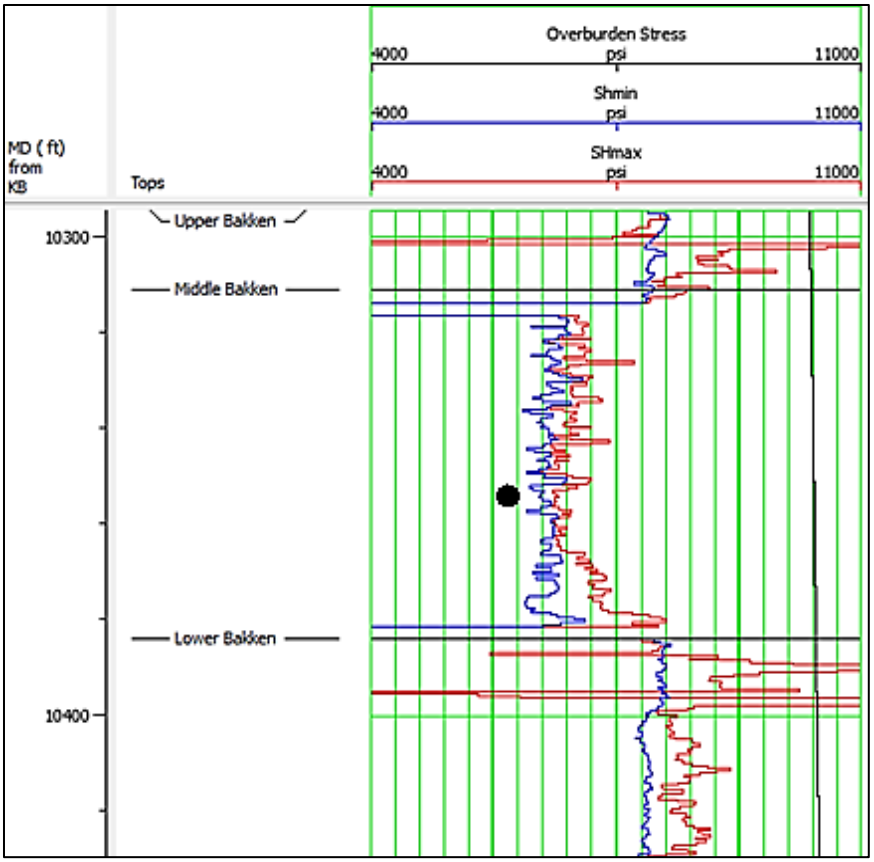

Figure 58 Anisotropic horizontal principal stresses and overburden stress through the Bakken Formation- The black star shows the DST measurement.

The following approach to calculate maximum principal horizontal stress was developed by Sinha, et. al., (2008). In this method, the minimum principal horizontal and overburden stress's magnitude as a function of depth are used as input to estimate the magnitude of maximum horizontal principal stress. The value of minimum principal horizontal stress is input from previous calculations. To perform this task, acousto-elastic parameter A_E in terms of the far-field shear moduli C_{55} and C_{66} is defined as:

$$A_E = \frac{C_{55} - C_{66}}{\sigma_v - \sigma_h} \tag{87}$$

In this equation it is assumed that the effects of permeability on the shear moduli (C_{55} & C_{66}) are similar and negligible (Sinha, et. al., 2007).

Once the acousto-elastic parameter (A_E) has been determined for a given lithology interval, we can calculate the maximum horizontal principal stress magnitude (σ_{Hmax}) as a function of depth from the following equation:

$$\sigma_H = \sigma_h + \frac{C_{55} - C_{44}}{A_E} \tag{88}$$

Clay minerals have a huge impact on the difference between the Stoneley shear modulus C_{66} and the dipole shear moduli C_{44} or C_{55}. This generally makes shear modulus C_{66} in the isotropic plane of shale (along the clay minerals surfaces) to become larger than shear modulus C_{44} or C_{55} in the orthogonal planes; therefore C_{66} needed to be reduced by 40% before combining it with the shear moduli C_{44} and C_{55} for stress magnitude estimation (Sinha, et. al., 2008) in the upper and lower shale members.

Maximum Principal Horizontal Stress Orientation

The direction of maximum principal horizontal stress is found to be N65E by counting and recording the orientation of the fractures which have caused slowness or time based shear anisotropy greater than 20% around the well. The results are plotted in a rose diagram showing the orientation of fracture planes with their frequencies (Figure 59). These fractures are believed to be tensile and exist along the maximum principal horizontal stress. As previously described where shear splitting takes place, fast shear azimuth (FSA) propagation which is along the natural fractures can be used to determine the maximum principal horizontal stress orientation. The fast shear wave is polarized along the fracture planes and propagates with a higher velocity compared to the slow shear wave which is polarized across the fracture planes. The FSA is obtained through Alford rotation algorithm as described in the previous chapter.

Slowness and time based anisotropy can be defined as Equations (89) and (90) respectively:

$$Anisotropy\% = \frac{DT_{SS} - DT_{FS}}{\left[DT_{SS} + DT_{FS}\right]/2} \times 100 \tag{89}$$

$$Anisotropy\% = \frac{TT_{SS} - TT_{FS}}{TT_{FS}} \times 100 \tag{90}$$

Where DT is the wave slowness $(\mu s/ft)$ and TT is the travel-time for arriving fast and slow shear waves at each receiver spacing on the Sonic Scanner tool.

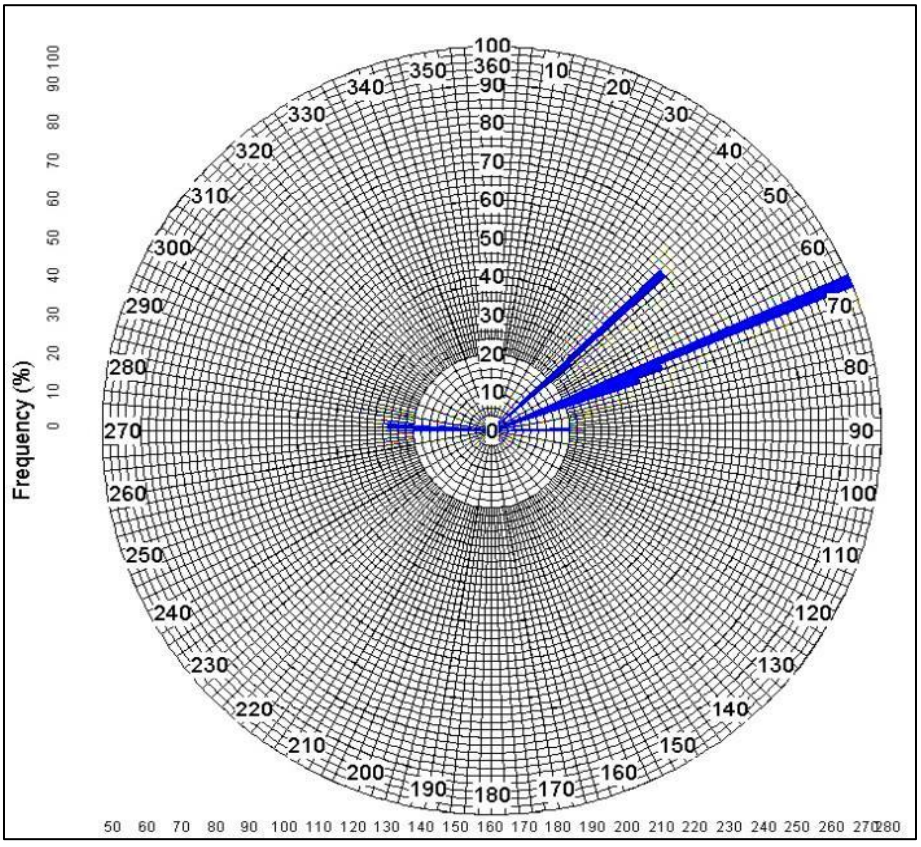

Figure 59 Rose diagram of natural fractures that have caused more than 20% shear anisotropy, frequency and fracture plane orientation are presented.

Derivation of Elastic Parameters

Isotropic dynamic Poisson's ratio and Young's modulus were derived from Equations (78) and (79) with compressional and shear wave velocities. The calculated Poisson's ratio and Young's modulus values are considered as the dynamic elastic parameters, and should be converted to static ones to better represent the geomechanical characteristics of the formation. The dynamic Poisson's ratio was not converted to the static value since the laboratory measurements indicate that the static and dynamic Poisson's ratios will not differ dramatically. Dynamic isotropic Young's modulus was transformed to the static one using the Wang (2000) correlation for the soft rocks (Wang, 2000 and Sayers, et. al., 2009):

$$E_{static} = 0.4145 E_{dynamic} - 1.0593 \qquad (91)$$

where E is Young's modulus in GPa. Isotropic static and dynamic Poisson's ratio and Young's modulus logs for the whole Bakken interval are presented in Figures 60 and 61. Anisotropic static Young's modulus in the direction of the vertical axis of rotational symmetry is plotted in Figure 62. The anisotropic Young's modulus in the horizontal direction (the plane of symmetry) can be found in Figure 62 as well. The dynamic Young's modulus was converted to the static value using Equation (91). Dynamic anisotropic Poisson's ratio log was developed through Equations (85) and (86) in the horizontal and vertical directions respectively; the corresponding log is shown in Figure 63. The dynamic anisotropic Poisson's ratio was not converted to the static one because the differences are not significant.

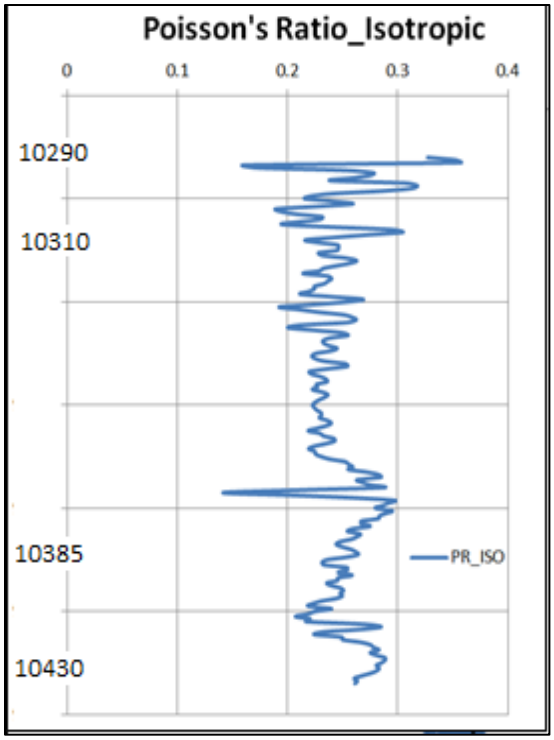

Figure 60 Isotropic dynamic Poisson's ratio of the Bakken Formation

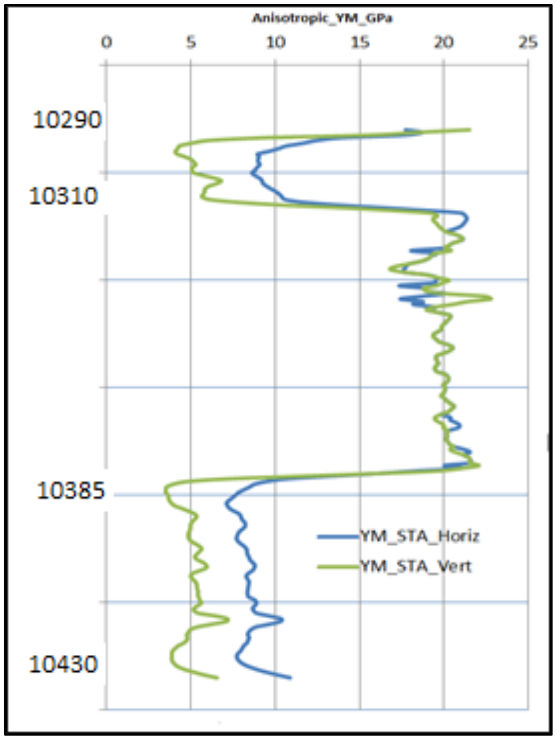

Figure 62 Anisotropic horizontal and vertical static Young's modulus of the Bakken Formation.

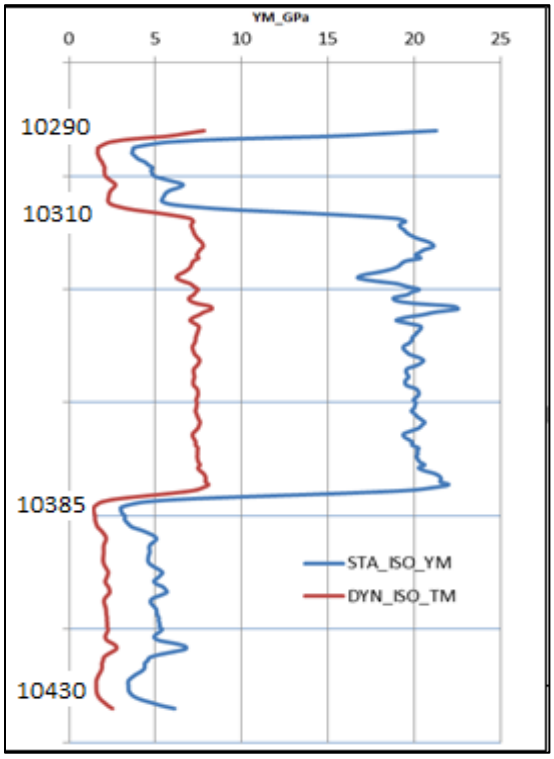

Figure 61 Isotropic static and dynamic Young's modulus of the Bakken Formation.

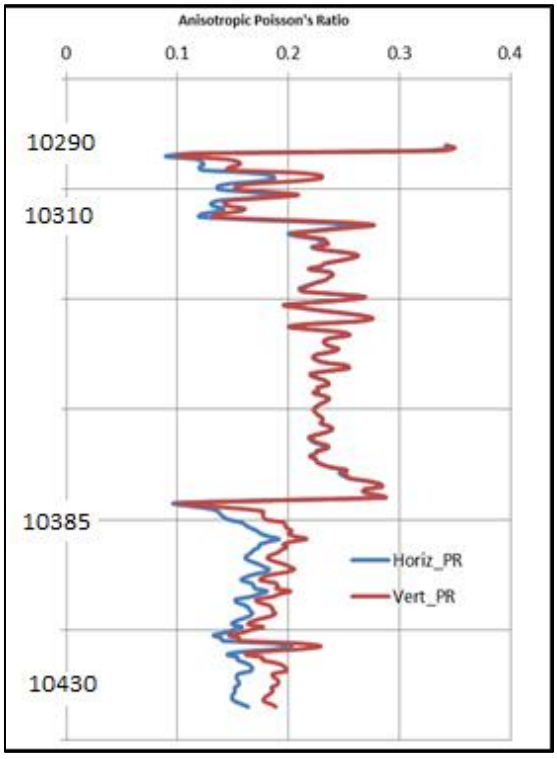

Figure 63 Anisotropic Poisson's ratio of the Bakken Formation.

It is evident that the Young's modulus values measured in the horizontal direction (in the plane of symmetry) are much greater than that in the vertical direction (along the axis of symmetry) for both upper and lower shales (Figure 62). This phenomenon reflects their VTI behavior. Accordingly, the dynamic Poisson's ratio measured in the vertical direction was slightly larger than that in the horizontal direction for the upper and lower shale members (Figure 63). These two findings strongly demonstrate the anisotropic behavior of shales and the presence of horizontal planes of weakness. This demonstrates that a VTI material is typically stiffer in the plane of isotropy than in the direction of anisotropy (Zimmerman, et. al., 2007).

In the Middle Bakken, overlapping the horizontal and vertical static Young's modulus curves for most of this interval stands for its isotropic behavior. This specifies that Young's modulus and Poisson's ratio are not dependent on the direction of measurement (Figure 62). However, upon closer inspection of the Middle Bakken, the cross-over of the vertical and horizontal static Young's modulus curves (green and blue curves in Figure 62) indicates the occurrence of anisotropy in other direction. This type of anisotropy, known as horizontal transverse isotropy (HTI), makes the vertical Young's modulus greater than the horizontal Young's modulus. It was interpreted as the existence of the vertical fractures in specific zones. The latest observation matches perfectly with the results obtained regarding seismic anisotropy in the previous chapter.

In order to confirm this interpretation, the available drilling cores from this zone were analyzed; the existence of vertical fractures was confirmed (red circle in Figure 64). The presence of vertical fractures in this specific zone makes it a perfect candidate for hydraulic fracturing operations. To evaluate the mechanical properties of this specific

section, horizontal transverse isotropy (HTI) assumptions should be applied. HTI is a type of anisotropy which exists in a medium with vertical parallel fractures (Tsvankin, 2005). Therefore, the plane of symmetry will be vertical and the axis of rotational symmetry is set to be horizontal.

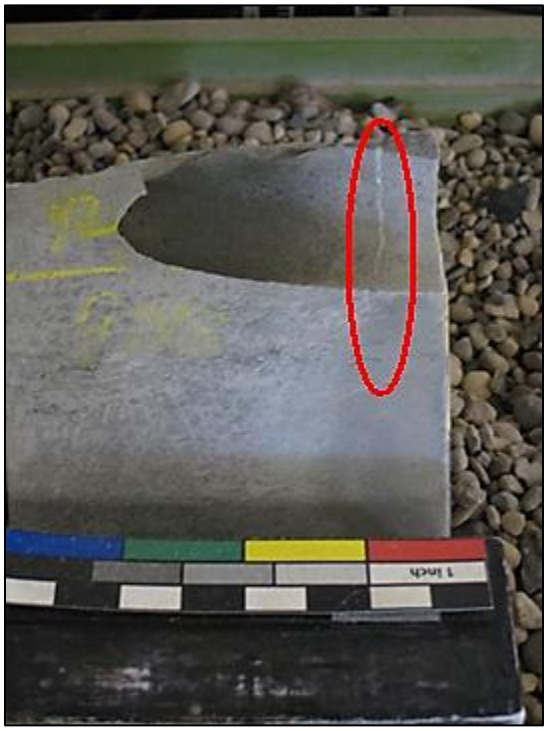

Figure 64 Core view with a vertical fracture in the Middle Bakken.

Isotropic static shear modulus (Figure 65) and the anisotropic static shear modulus in the horizontal (anisotropy) plane (Figure 66) for lower and upper members were derived from Equation (92). This equation defines the relationship between static Young's modulus, Poisson's ratio and the static shear modulus:

$$G = \frac{E}{2(1+\nu)} \tag{92}$$

Where E is static Young's modulus in GPa, G is the static shear modulus in GPa and ν is Poisson's ratio.

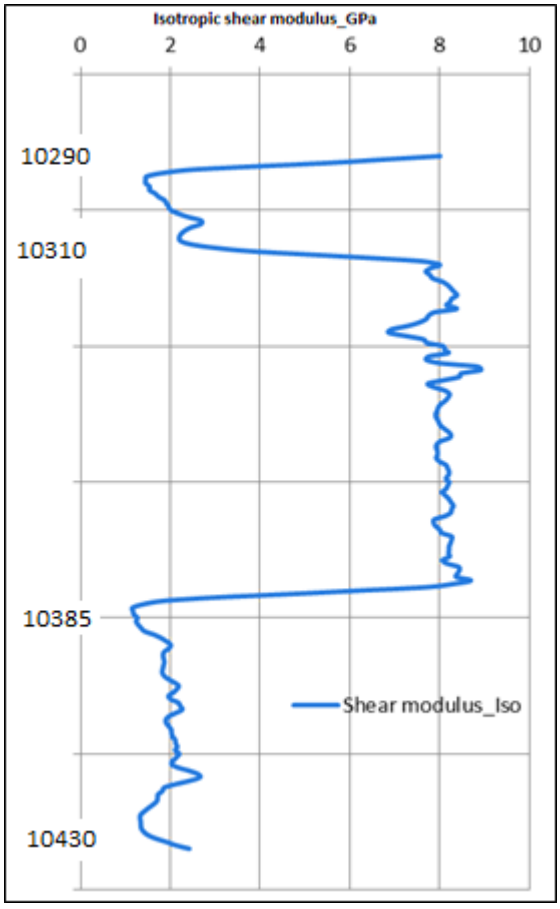

Figure 65 Isotropic static shear modulus of Bakken.

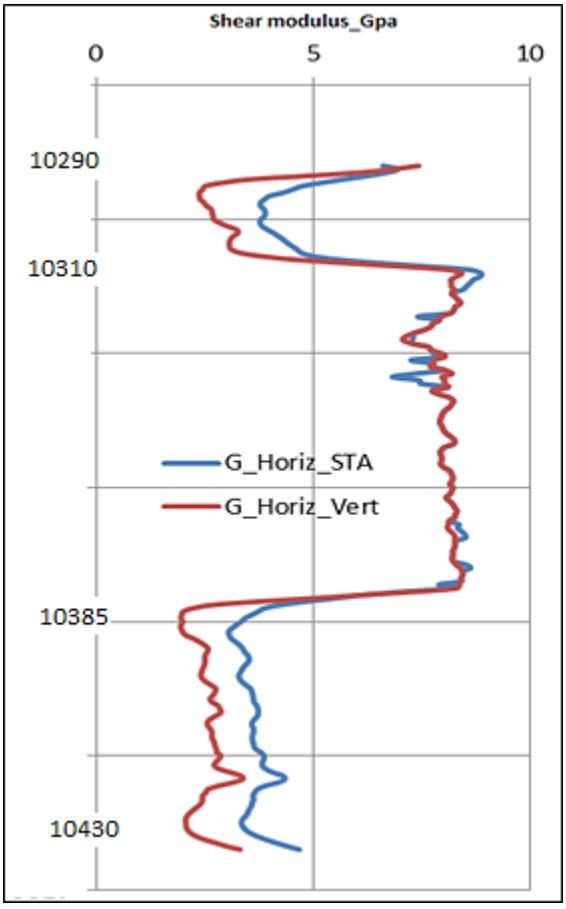

Figure 66 Anisotropic static shear modulus of Bakken in horizontal and vertical directions.

Anisotropic static shear modulus (Figure 66) of lower and upper VTI members along the axis of symmetry was calculated using Equation (93), (Lekhnitskii, 1981):

$$G_{vert} = \frac{E_{vert}E_{horz}}{E_{horz}(1+2\nu_{vert})+E_{vert}} \tag{93}$$

Where E_{horz},E_{vert} are the static Young's moduli in the plane of symmetry and in the direction of anisotropy (vertical), respectively, and ν_{vert} is Poisson's ratio in the direction of anisotropy.

Tables 10 and 11 show the average values of the calculated static elastic parameters in the three members of the Bakken Formation under anisotropic and isotropic assumptions, respectively.

Table 10 Anisotropic elastic properties for the Bakken Formation.

	E_{vert} (GPa)	G_{vert} (GPa)	ν_{vert}
U B	5.01	2.53	0.18
M B	19.93	7.94	0.24
L B	5.83	2.77	0.16
	E_{Horz}(GPa)	**G_{Horz}(GPa)**	**ν_{Horz}**
U B	8.44	3.62	0.16
M B	19.92	7.97	0.24
L B	10.09	4.08	0.15

Table 11 Isotropic elastic parameters of the Bakken Formation

	G (GPa)	E (GPa)	ν
U B	1.84	4.67	0.26
M B	8.02	19.90	0.24
L B	2.07	5.46	0.24

It should be emphasized that due to the equal values of the average elastic parameters in the horizontal and vertical directions for MB (Table 10), this layer is considered isotropic in the following numerical modeling.

3-D Numerical Modeling

The numerical solution for verifying the analytical models was determined by creating a series of 3-D finite difference models in a software program called FLAC3D (Fast Lagrangian Analysis of Continua in 3Dimensions). FLAC3D is a commercial software

for advanced geotechnical analysis of rock, soil, and structural support in three dimensions. FLAC3D has been widely used to analyze, solve, and test a wide variety of complex problems in geomechanics, civil, and mining engineering. It has been applied in this research due to its explicit calculation scheme, which enables a large 3-D calculation to be made without excessive memory requirements. Additionally, FLAC3D can give graphical contour plots of stress and displacement in the model which eases the analysis process.

3-D geomechanical modeling is limited to the Upper and Middle Bakken, since the Upper and Lower Bakken show almost the same elastic behavior; therefore only the results of the Upper and Middle Bakken are presented. The analysis is focused on the fact that the Upper Bakken is vertically transverse isotropic (VTI) and the middle member is isotropic. In addition, geomechanical modeling results comprise of vertical, inclined and horizontal wells in the Bakken Formation. Since the wells in the Williston Basin are producing primarily from the Middle Bakken, the results from geomechanical model for a horizontal well only represents the Middle Bakken, so the models are assumed isotropic. For a well to become horizontal in the middle member, the kick-off point (KOP), where the well becomes inclined, starts in the upper member. Hence, the well deviation angle is increased by every 15˚ from the vertical to the horizontal (0˚ to 90˚).

Vertical Well (0˚ Deviation Angle)

Figure 67 represents the steps that were taken to fulfill the geomechanical modeling of vertical, inclined and horizontal wells. The first step was to make the 3-D grids model and characterize this medium by assigning elastic parameters to an undrilled Bakken Formation. The average elastic properties assigned are summarized in Table 10 and Table

11 for anisotropic and isotropic cases. Then the calculated isotropic and anisotropic horizontal stress, vertical stress and the pore pressure were assigned to the isotropic and anisotropic models correspondingly. The program was executed to bring the model to its mechanical equilibrium state conditions.

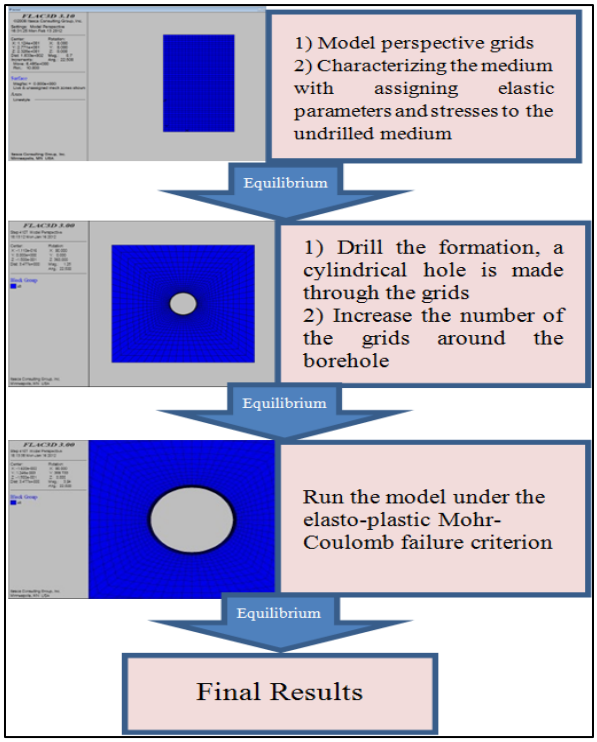

Figure 67 Flowchart of the geomechanical modeling.

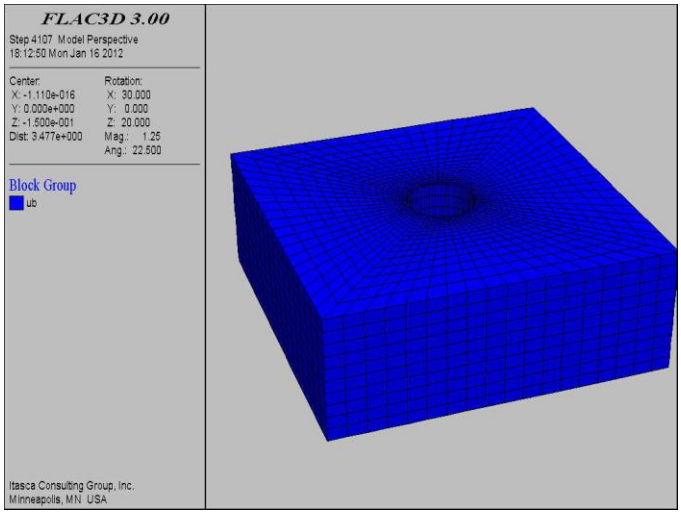

Figure 68 (3-D) view of the model with the well drilled in the middle.

The model was set under elastoplastic conditions. The second step was to drill the formation. In this step, a cylindrical hole was made through the grid model to represent the drilled Bakken Formation. In order to evaluate the results precisely around the borehole, it was decided to increase the number of grids in this specific zone. The program was then executed for a second round, and a new mechanical equilibrium was achieved. In this step, the deformations and displacements in the formation take place. Displacements around the borehole and in the far field in isotropic and anisotropic input parameters for vertical well through UB, MB and UB-MB interface are shown in figures 69 and 70.

In the following figures, displacements in X-Z plane (side view) are in meter (m). From the figures, it can be determined that modeling under anisotropic assumptions which are more realistic show a lower degree of displacement around the borehole than the isotropic model. The magnitude of displacement for isotropic model is at least twice that of the isotropic model. It can also be realized that the total displacement which takes place in UB is greater in magnitude than MB.

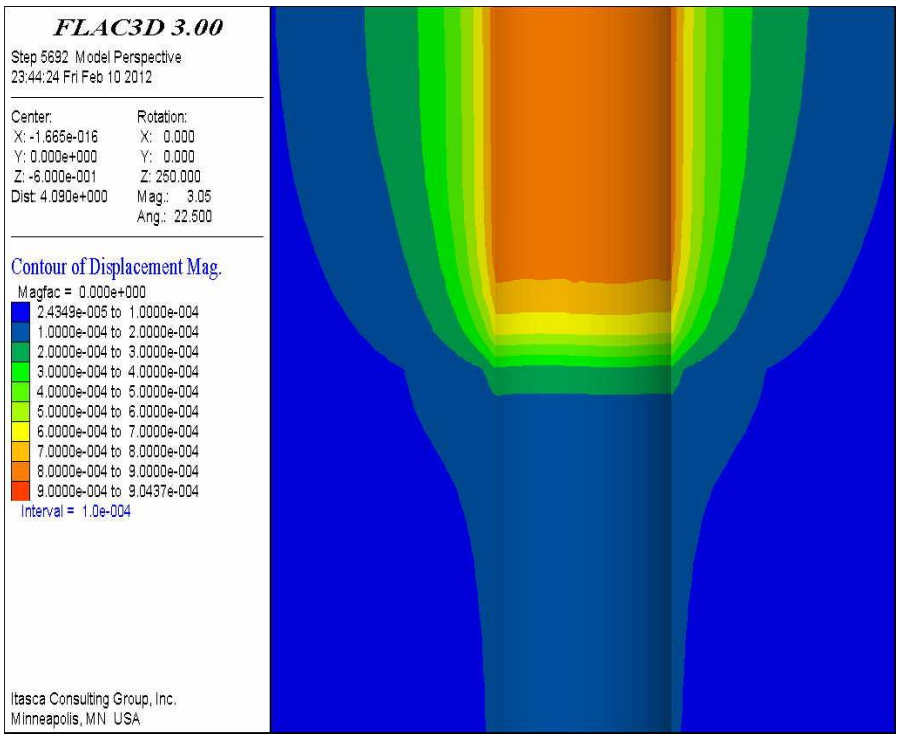

Figure 69 Contours of displacement magnitude in UB, MB and UB-MB interface under isotropic assumptions in X-Z plane

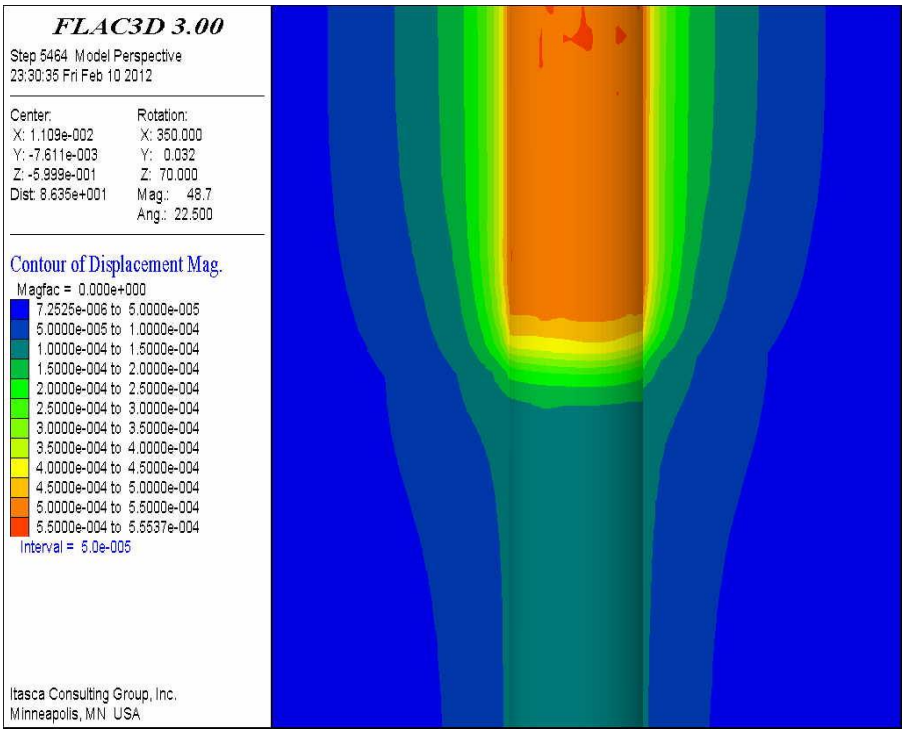

Figure 70 Contours of displacement magnitude in UB, MB and UB-MB interface under anisotropic assumptions in X-Z plane.

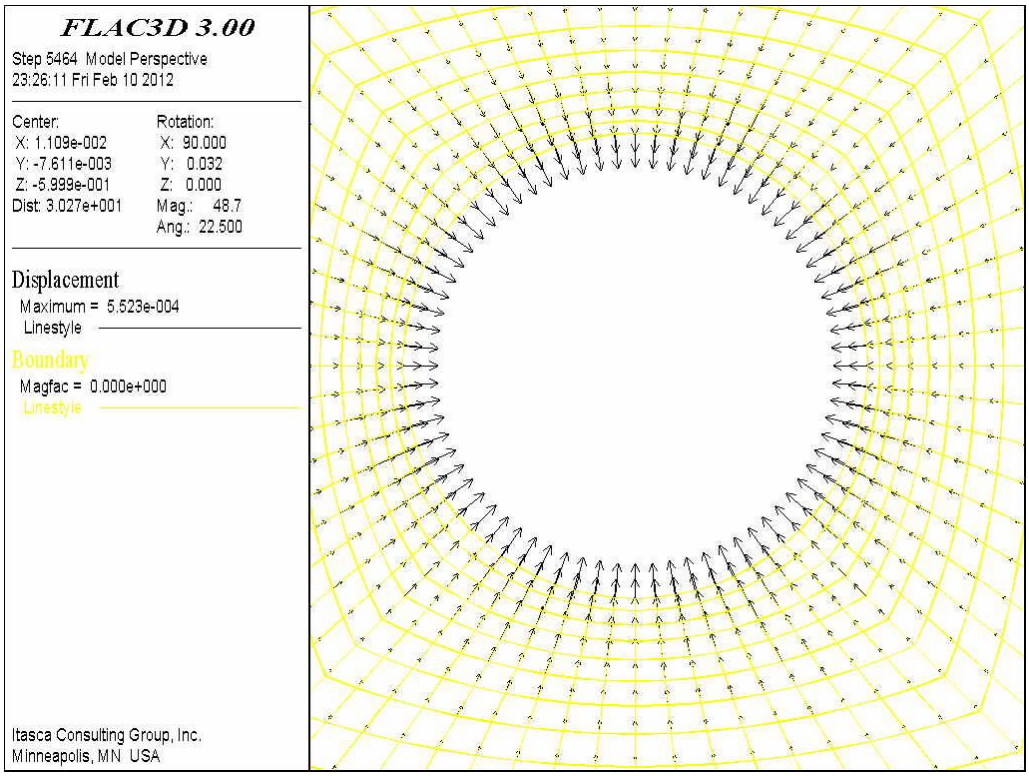

Figure 71 Displacement vectors in UB under anisotropic assumptions in X-Y plane.

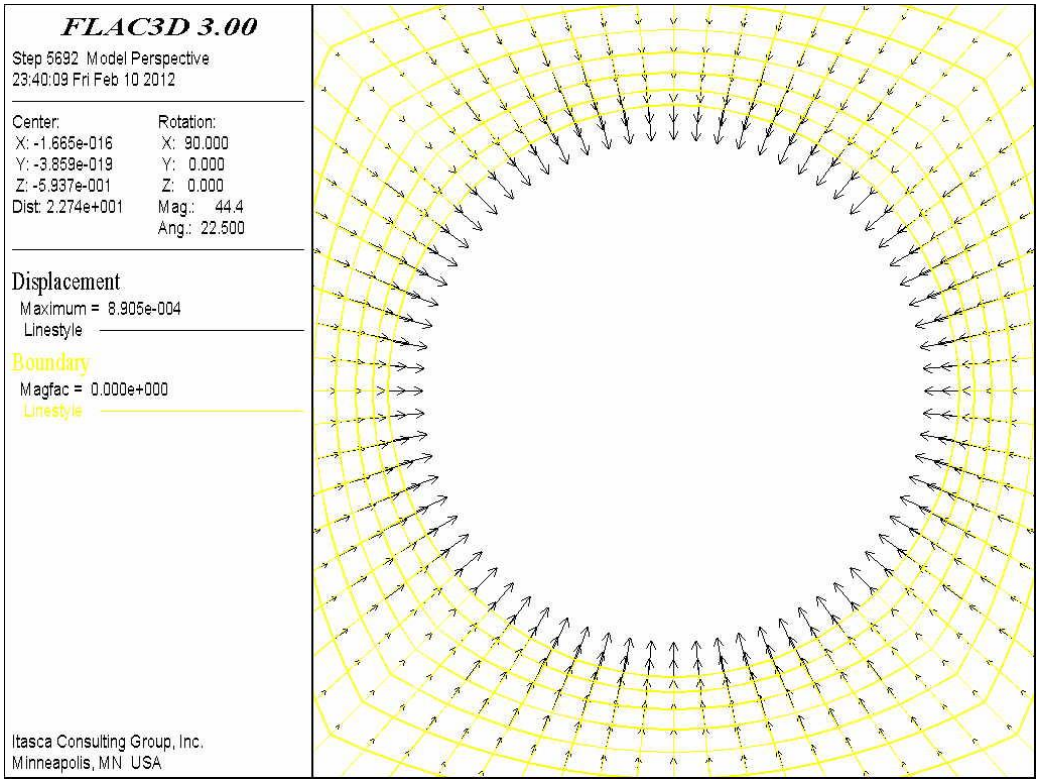

Figure 72 Displacement vectors in UB under isotropic assumptions in X-Y plane.

Figures 71 and 72 represent the total displacement vectors in UB under anisotropic and UB under isotropic assumptions. It can be determined that the maximum total displacement which is defined by Equation (94) displays a higher magnitude in the anisotropic UB.

$$d_t = \sqrt{x^2 + y^2 + z^2} \tag{94}$$

The displacement vectors in X-Y plane plotted for the Middle Bakken under isotropic assumption is shown in the following figure.

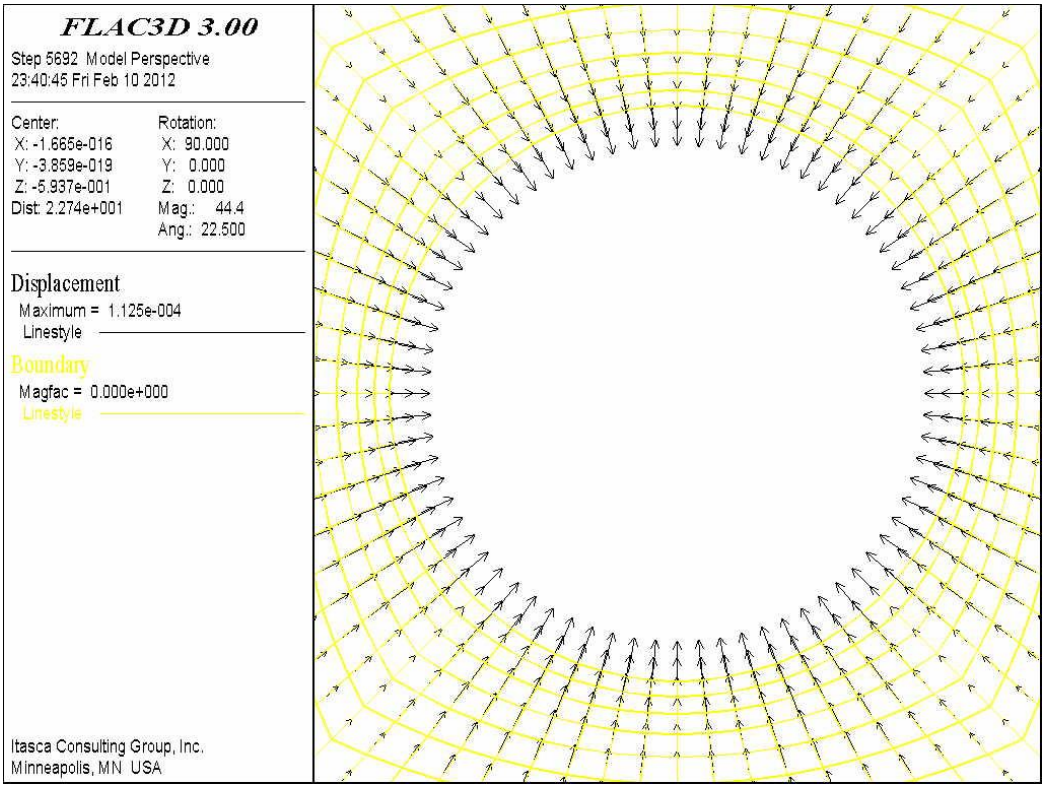

Figure 73 Total displacement vectors in MB under isotropic assumptions.

The following figure shows the total displacement magnitude in a 3-D view for the Upper and Lower Bakken. From Figure 74 it can be concluded that a higher degree of

displacement takes place in the region adjacent to the wellbore wall in the Upper Bakken, whereas in the middle member the displacement at the borehole wall is more moderate.

It can be observed that the displacements around the borehole in the Upper Bakken are much more severe than the displacement which takes place in the middle member. This difference is partially due to the lithology of the Upper Bakken compared to the Middle Bakken. Regarding the fact that shale is the main constituent of the upper member and deforms easier than carbonates and clastics with higher stiffness values (the main constituent of middle member) it was expected to see higher degrees of displacement in the upper member than the lower member.

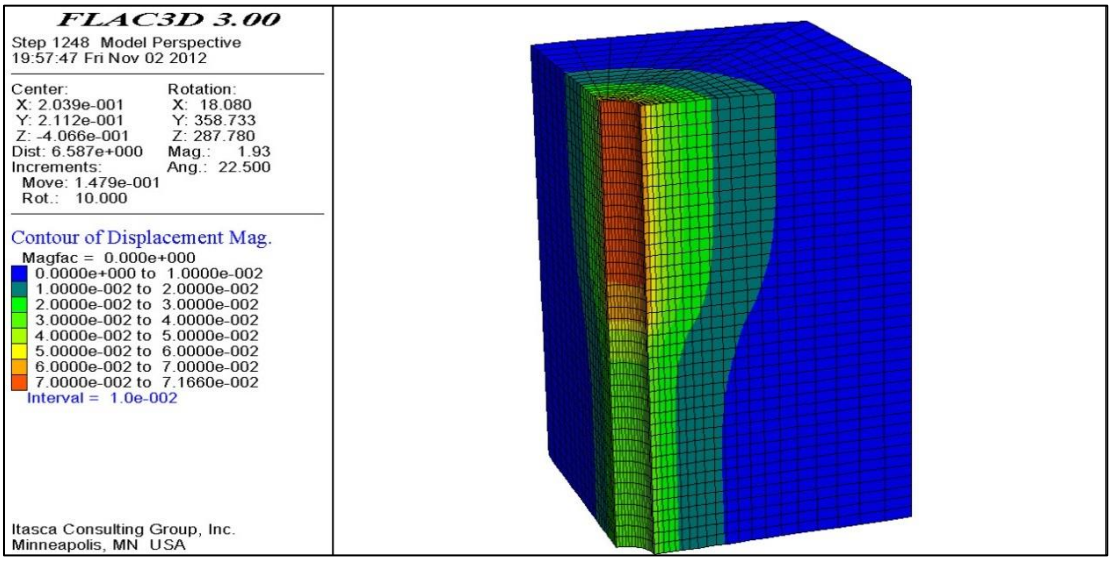

Figure 74 Displacement around the borehole in the Upper and Lower Bakken under anisotropic assumptions.

The third step and final step in geomechanical modeling was to run the equilibrated model under the elastoplastic Mohr-Coulomb failure criterion. To recall Mohr-Coulomb formulation: (Chang, et al., 2006 and Zimmerman, et al., 2007):

$$T = S_0 + \sigma \tan \varphi \tag{95}$$

$$\sigma_1 = C_0 + \sigma_3 \tan^2(45 + \frac{\varphi}{2}) \tag{96}$$

In Equation (95), σ is the normal stress, T is the shear stress, S_0 is cohesion and φ is the angle of internal friction. In Equation (96), σ_1 is the maximum principal stress and σ_3 is the minimum principal stress. C_0, the unconfined compressive strength, given by (Jaeger and Cook, 1979, Sayers, et. al., 2009 and Zimmerman, et. al., 2007):

$$C_0 = 2S_0 \tan(45 + \frac{\varphi}{2}) \tag{97}$$

In order to model the medium under elastoplastic Mohr-Coulomb failure criterion, the unconfined compressive strength (UCS,C_0) must be known. To achieve this goal, two separate methodologies were tested. The first method was to acquire the compressional sonic velocity or slowness (Horsud, 2001), whereas the second method uses Young's modulus to predict the UCS (Chang, et al., 2006).

In the first method, for the Lower and Upper Bakken shale intervals, Equation (98) was applied to generate the UCS profile (Horsud, 2001)

$$C_0 = 0.77 V_p^{2.93} \tag{98}$$

Equation (98) is defined between compressional sonic velocity (km/s) and UCS (MPa) for shales (Horsud, 2001). For the Middle Bakken, core lithology investigation like acid treatment was carried out and indicated that the dominant lithology in MB in Ruland well is primarily limestone. Therefore, a relevant correlation, Equation (99), between

compressional sonic slowness (μsec/ft) and UCS for limestone, was applied to calculate the UCS (Millitzer and Stoll, 1973):

$$C_0 = \frac{(\frac{7682}{\Delta t})^{1.82}}{145} \quad (99)$$

The second method uses the static Young's modulus (GPa) to predict the UCS (MPa). Separate empirical correlations were used: one for the upper-lower shales, Equation (100) (Horsud, 2001), and another one for middle limestone, Equation (101) (Chang, et. al., 2006). Figure 80 is the UCS profile of the Bakken Formation generated from each of those methods.

$$C_0 = 7.22E^{0.712} \quad (100)$$

$$C_0 = 13.8E^{0.51} \quad (101)$$

Based on the fact that the generated UCS log from Young's modulus is more reliable than that derived from the velocity data (Plumb 1994), and also to maintain the consistency of using static elastic data until the end of this study, it was decided to use Young's modulus to create the unconfined compressive strength log. The average UCS values (Table 12) from Equations (99) and (100) were set as the input parameters in Mohr-Coulomb failure analysis in the geomechanical modeling.

Table 12 Elastic parameters used for elasto-plastic Mohr-Coulomb failure criterion in the Bakken Formation.

	Cohesion (MPa)	**UCS from E (MPa)**	**φ°**
U B	6.4	22.63	31
M B	15.63	63.11	37.3
L B	6.72	23.91	31.3

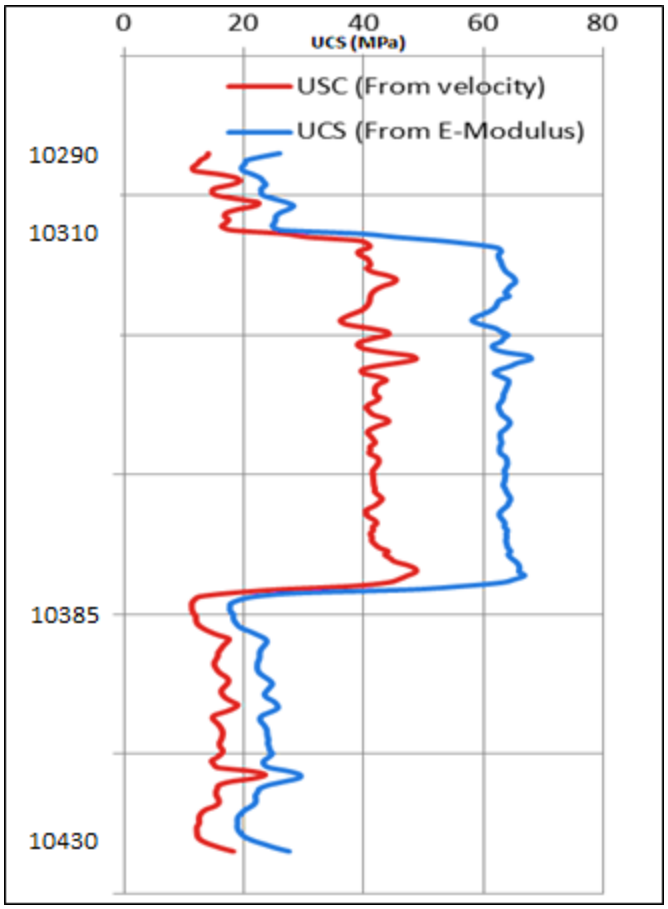

Figure 75 Unconfined compressive strength from velocity and Young's modulus data for the Bakken Formation.

The average friction angle in Table 12 was calculated from two separate correlations: Equation (101) for the lower-upper members (Odunlami, et. al., 2011) and Equation (103) for the middle member (Chang, et. al., 2006).

$$\varphi = 18.35 V_p^{0.5148} \tag{102}$$

$$\varphi = \tan^{-1}\left(\frac{(GR - GR_{sand})/\mu_{shale} + (GR_{shale} - GR)/\mu_{sand}}{GR_{shale} - GR_{sand}}\right) \tag{103}$$

In Equation (102), φ is the internal angle of friction in degree, and v_p is the compressional wave velocity in km/s. In Equation (103), GR is the gamma ray reading of

the formation. GR_{sand} and GR_{shale} are the gamma ray reference values for sand and shale layers, respectively. μ_{shale} and μ_{sand} are the internal friction coefficients defined as $\mu = tan\,\varphi$ for pure sand and pure shale. Equation (103) principally uses gamma ray log for the estimation of the internal friction angle. As gamma ray measures the amount of the clay volume content of the formation, Equation (103) implies that a shalier rock possesses a lower value of internal friction angle. It has been shown that the internal friction angle decreases with the increase of porosity, clay volume or the sum of both properties within a rock (Plumb, 1994). It should be mentioned that relative low values of friction angle were found in the Bakken Formation due to the presence of hydrocarbon in the middle member and high total organic content (TOC) of the upper and lower shale members.

The following figures display the results of the final step of the geomechanical modeling under anisotropic and isotropic input properties. Figures 76 and 77 depict the variation of principal horizontal stresses (Mpa) (maximum and minimum principal horizontal stress) around the well in UB, MB and UB-MB interface in the X-Z plane under anisotropic assumptions. Figures 78 and 79 represent the changes in horizontal principal stresses around the well under isotropic calculations

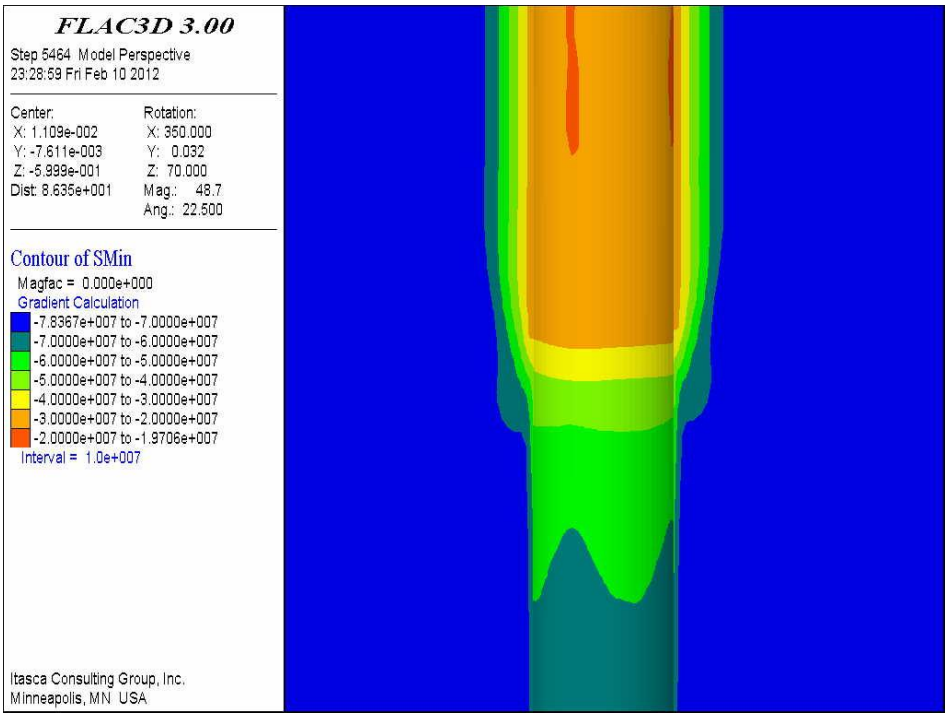

Figure 76 Contours of minimum horizontal principal stress in UB, MB and UB-MB interface under anisotropic stress assumptions (X-Z plane).

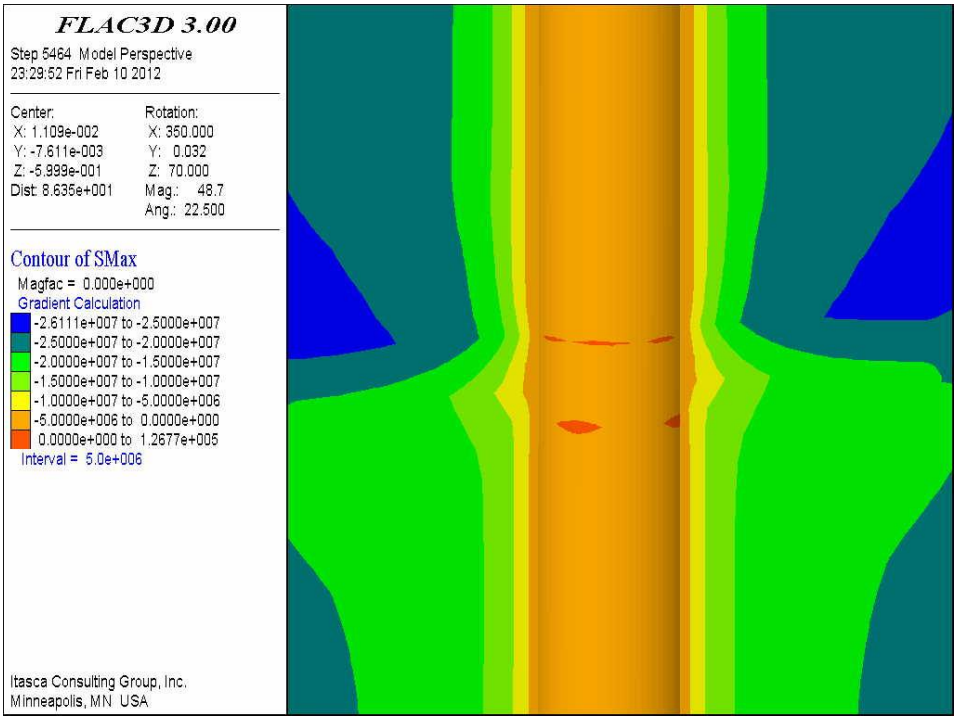

Figure 77 Contours of maximum horizontal principal stress in UB, MB and UB-MB interface under anisotropic stress assumptions (X-Z plane).

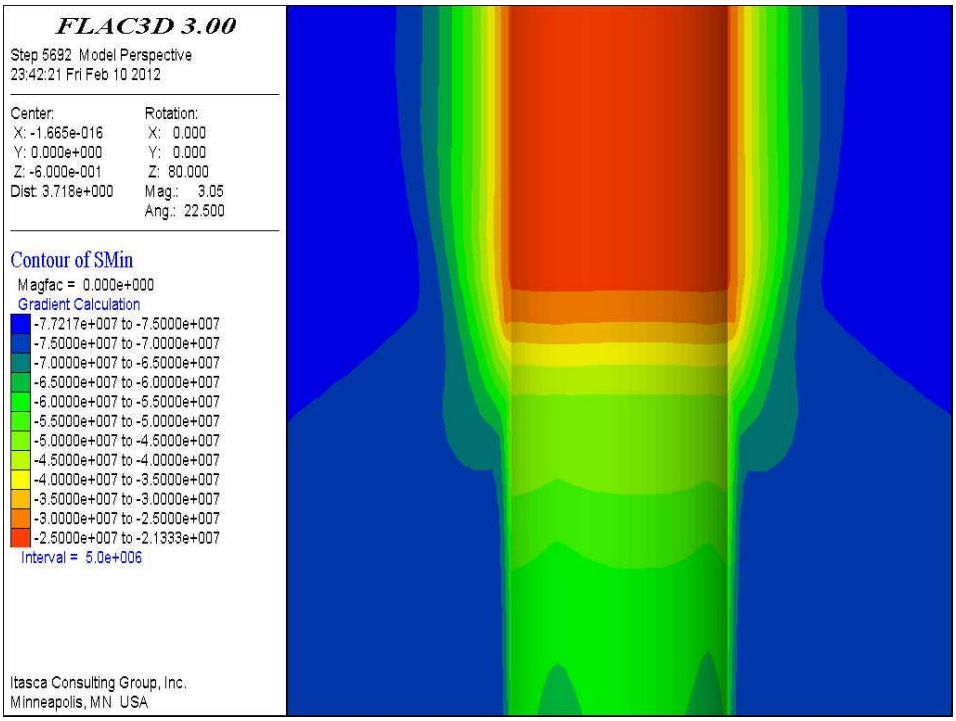

Figure 78 Contours of minimum horizontal principal stress in UB, MB and UB-MB interface under isotropic stress assumptions (X-Z plane).

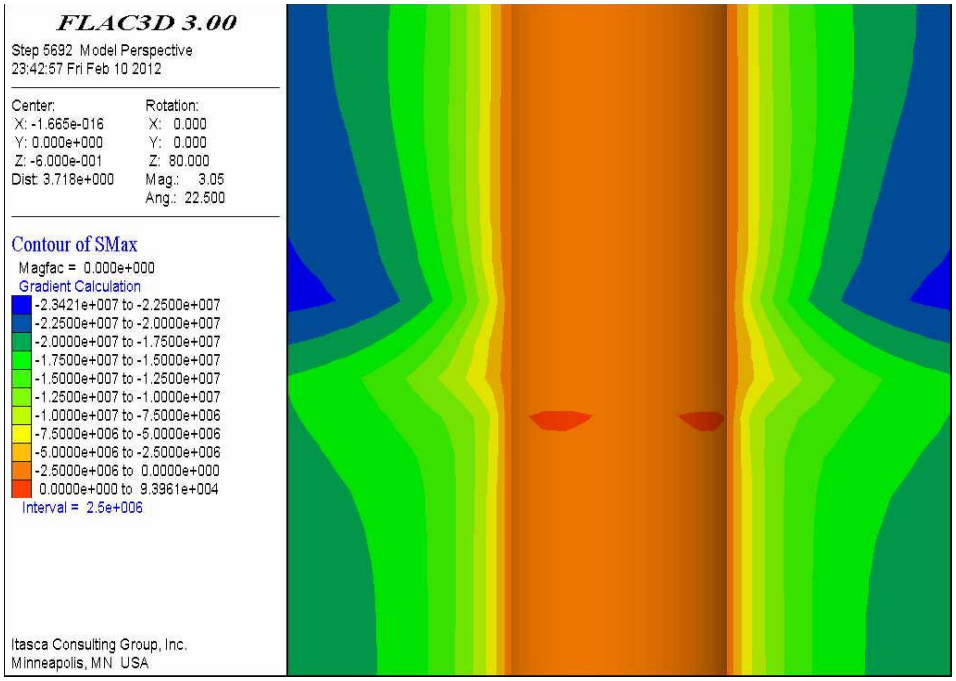

Figure 79 Contours of maximum horizontal principal stress in UB, MB and UB-MB interface under isotropic stress assumptions (X-Z plane).

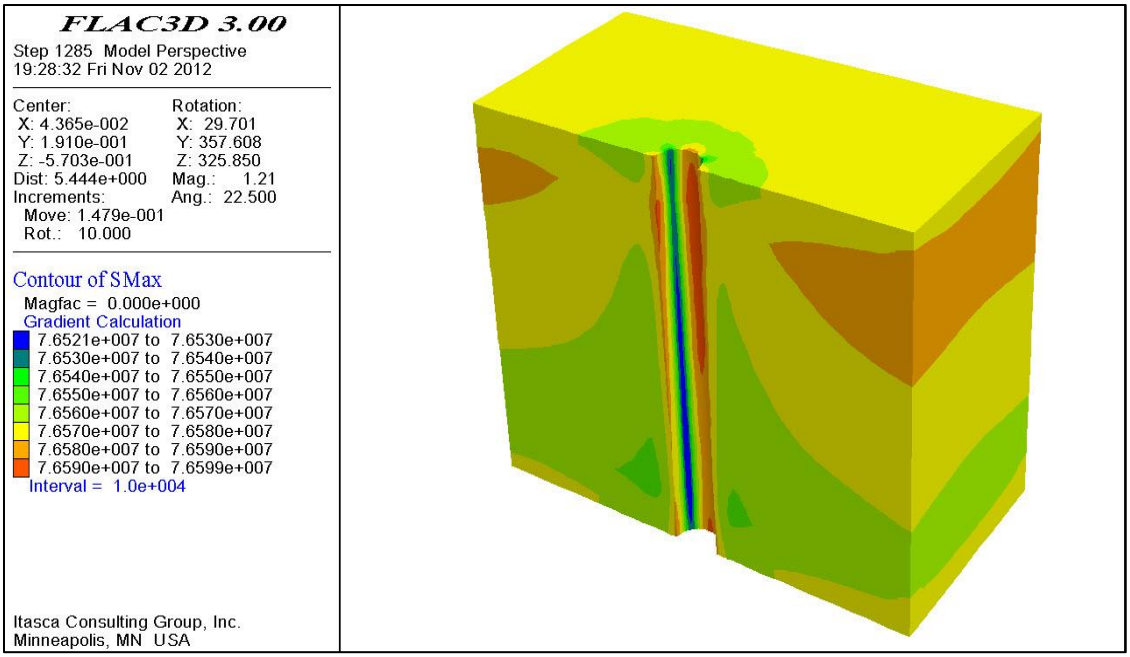

Figure 80 (3D) view contours of maximum horizontal principal stress in UB under anisotropic assumptions

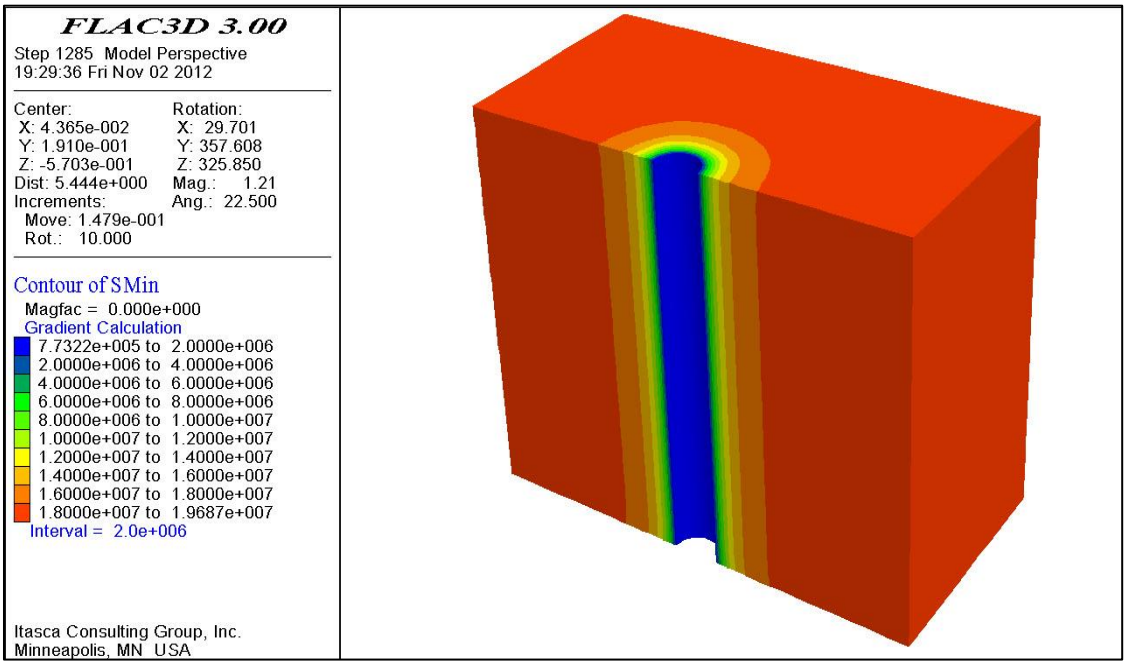

Figure 81 (3D) view of minimum horizontal stress contours in Middle Bakken under isotropic assumptions.

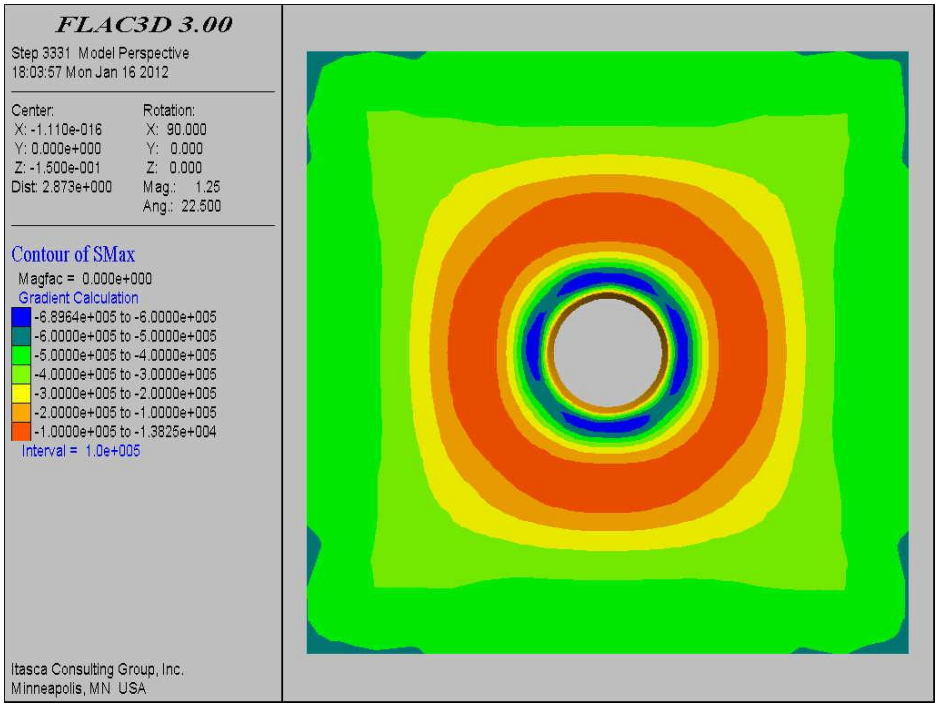

Figure 82 Top view of maximum horizontal principal stress magnitude contours in UB under anisotropic assumptions (X-Y plane)..

.

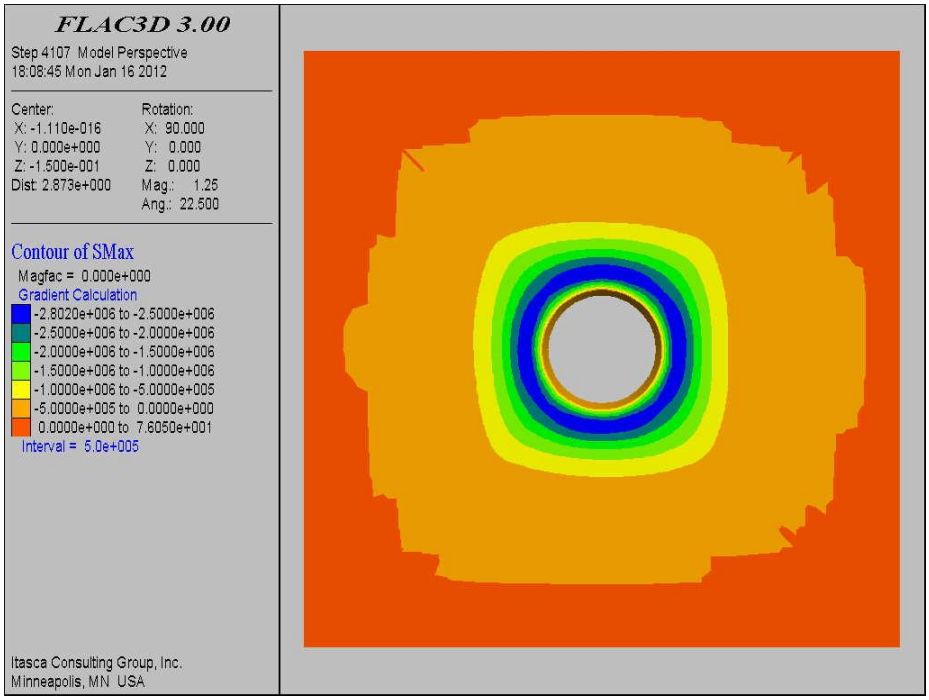

Figure 83 Top view of maximum horizontal principal stress magnitude contours in UB under isotropic assumptions (X-Y plane).

Comparing Figures 82 and 83, which denotes the maximum horizontal principal stress magnitude in X-Y plane, under anisotropic and isotropic assumptions, it was found that modeling the Upper Bakken under anisotropic assumptions can better define the stresses (hoop stress) around the borehole compared to the isotropic models. It can be seen in Figure 82 that the hoop stress is more configured around the borehole. Hoop stress is compressive in the direction of minimum principal horizontal stress and tensile in the direction of maximum principal horizontal stress. This phenomenon is more visible when closer investigation is carried out in the vicinity of the wellbore wall (the blue contours). Hoop stress, if exceeds rock strength, will cause the formation to fail or tensile fractures to form. The concentration of hoop stress is a good indication of maximum and minimum principal horizontal stresses in nature. In the borehole, breakouts will occur where the hoop stress is concentrated, and reveals the direction of the minimum principal horizontal stress.

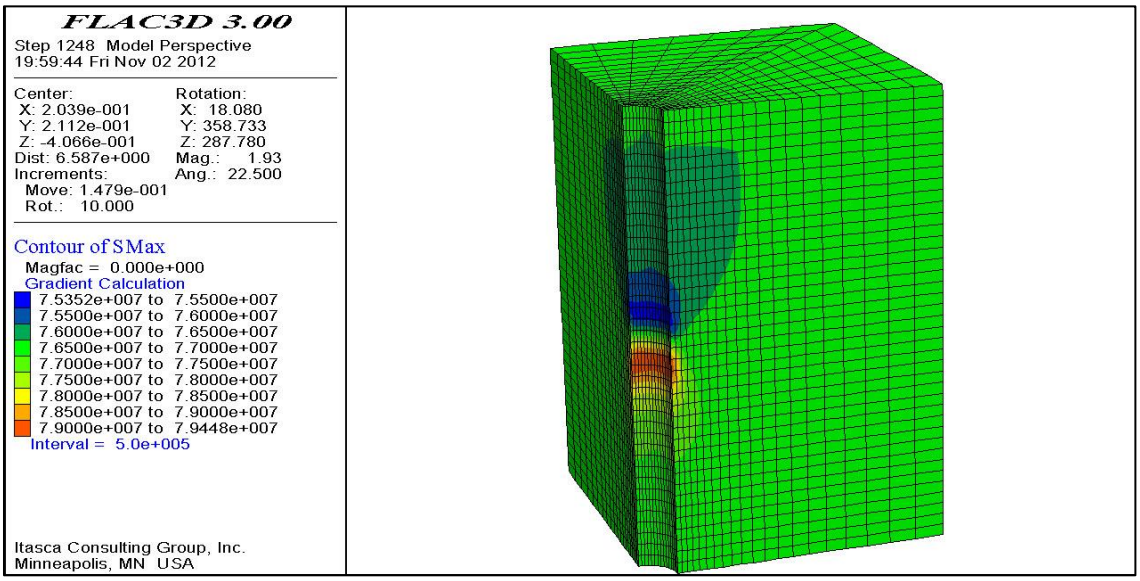

Figure 84 Contours of maximum principal horizontal stress in a 3D view under anisotropic assumptions for the interface of UB-MB.

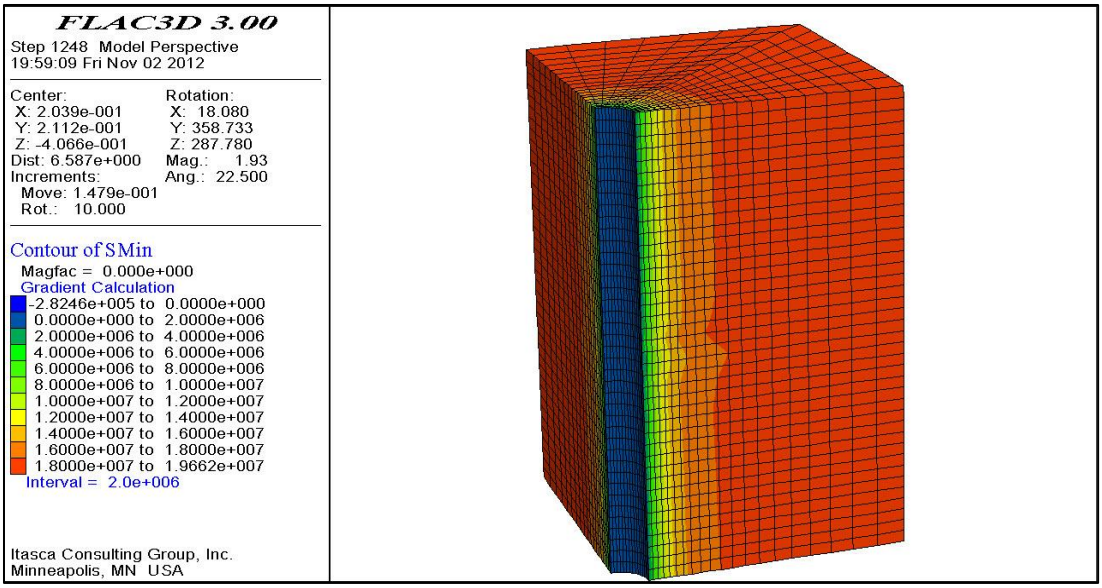

Figure 85 Contours of minimum principal horizontal stress in a 3D view under anisotropic assumptions for UB, MB and the interface of UB-MB.

Running the model under elastoplastic Mohr-Coulomb failure criterion will lead to the creation of plastic regions around the borehole. The following figures represent the position of various elastic and plastic regions which are developed around the borehole in a vertical well under isotropic UB, anisotropic UB and isotropic MB, (Figures 86-88).

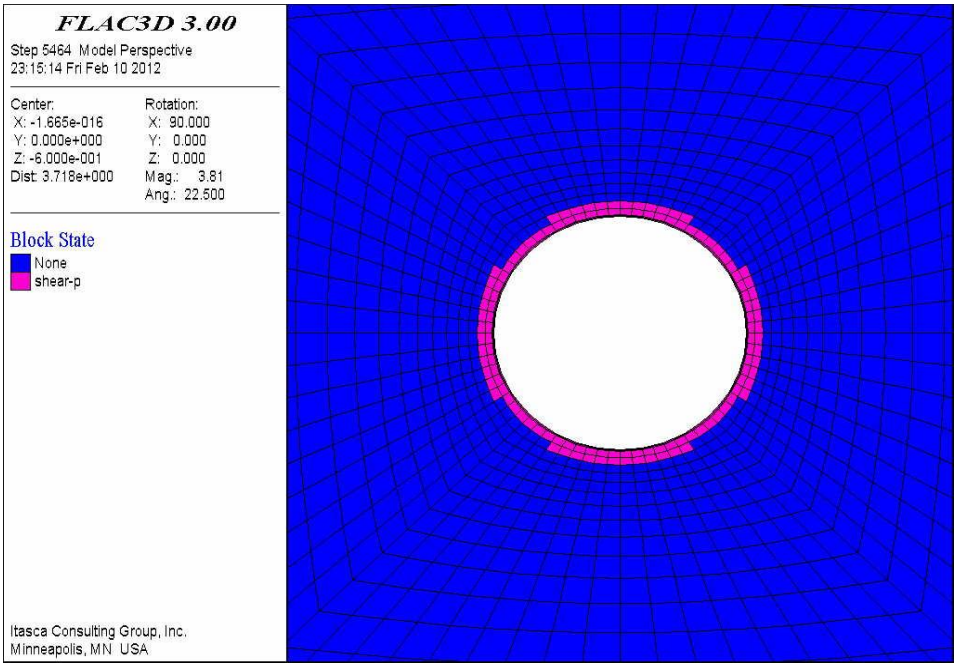

Figure 86 Plastic regions around the borehole in isotropic MB.

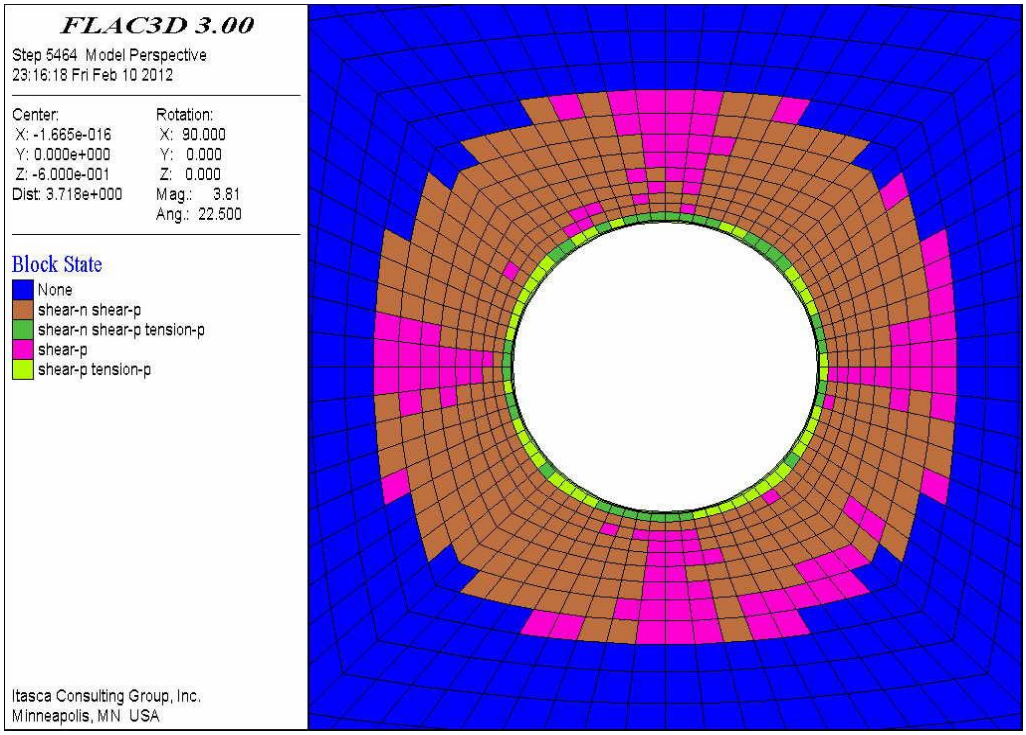

Figure 87 Plastic regions around the borehole in UB under anisotropic assumptions.

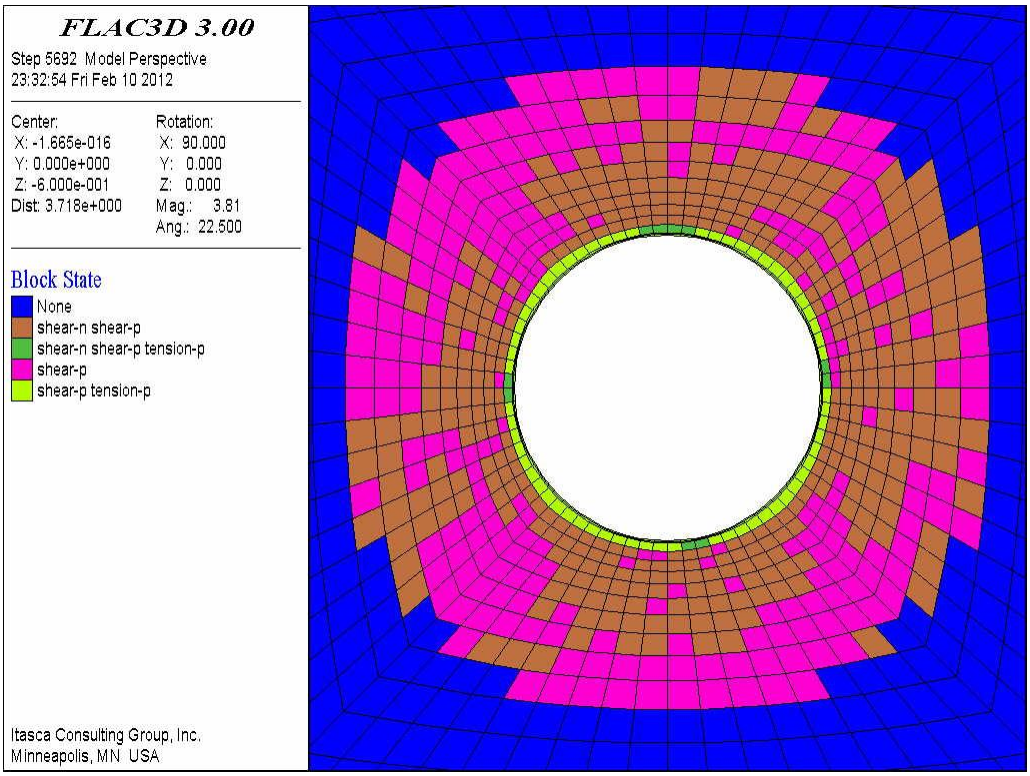

Figure 88 Plastic regions around the borehole in UB under isotropic assumptions.

Figure 87 indicates that using anisotropic parameters such as elastic mechanical properties and the stresses for UB will cause the formation to behave elastically right after the formation has undergone a shear failure in the vicinity of the borehole (brown region) with better defined plastic areas matching the direction of principal horizontal stress (purple blocks). On the contrary, Figure 88 illustrates that under isotropic assumptions for the UB, grids will stay in the shear failure state (red region).

Inclined Well (15˚ attack Angle)

An attack angle, which is the orientation of the wellbore with respect to the bedding planes, is usually used to evaluate the wellbore stability of laminated formations (Okland and Cook, 1998; Willson *et al.*, 1999). According to Okland and Cook's (1998) definition, the attack angle is equal to 90◦ when the wellbore is perpendicular to the bedding planes and 0◦ when the well is drilled parallel to the bedding planes. However, Willson et al., (1999) have a completely different definition of this angle. They define the attack angle as zero when the well is drilled perpendicular to the bedding planes, and 90˚ when the well lies in the bedding planes.

In this analysis, the first definition (Okland and Cook's (1998)) defines the attack angle. It was assumed that the Bakken, especially in the upper member, is horizontal with zero dipping angle. Geological study of the Bakken Formation in the Williston Basin generally confirms this assumption. Therefore the attack angle is increased every 15˚ up to 90˚ and the simulations are performed.

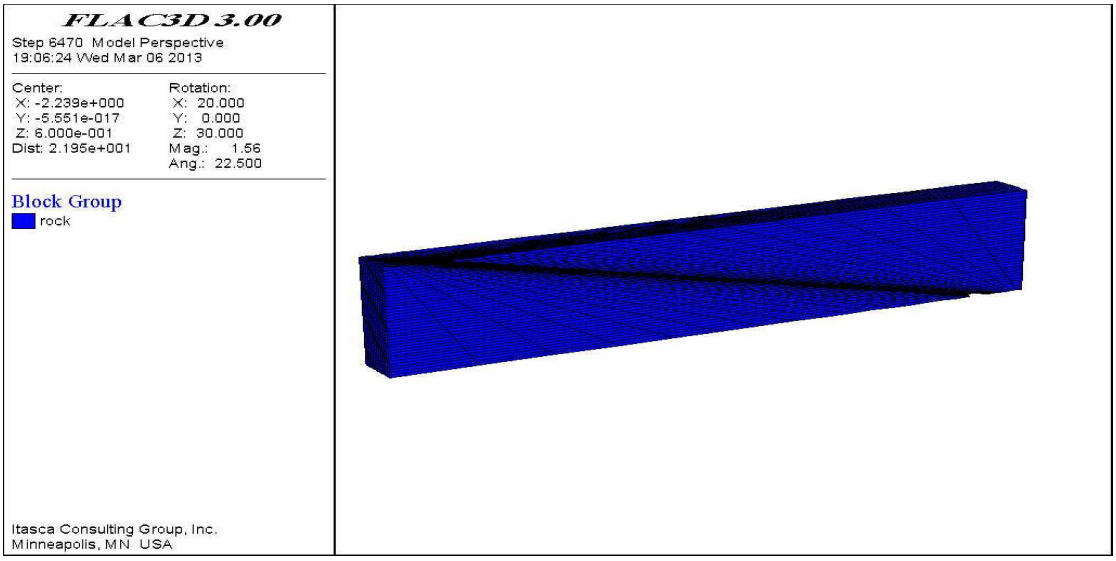

Figure 89 The schematic model of the well with 15˚ attack angle.

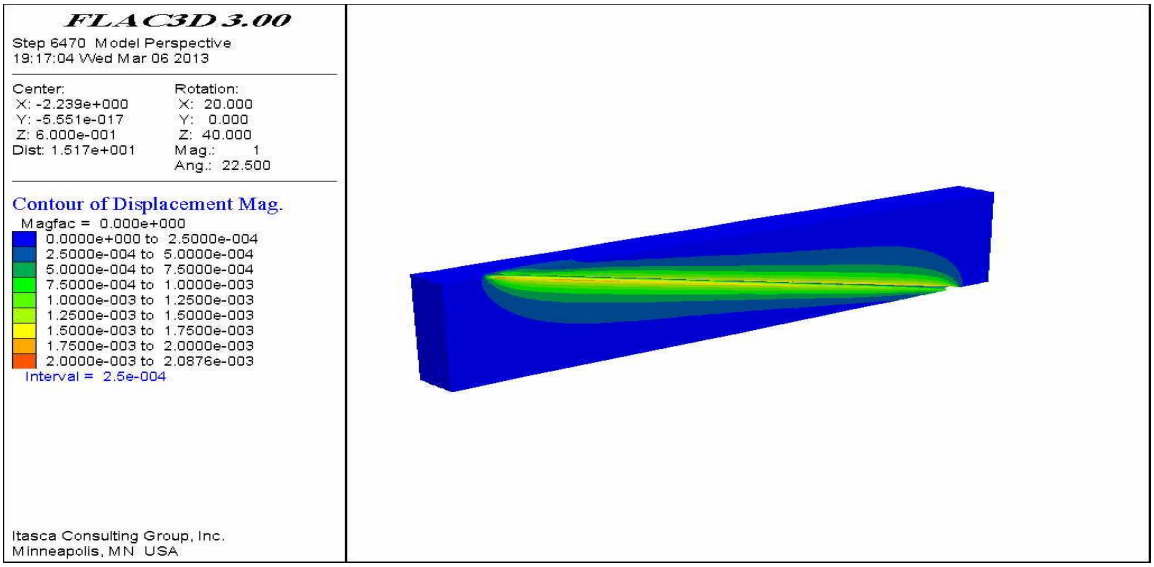

Figure 90 Side-view of the well with total displacement magnitude contours in color scale.

Considering the Cartesian coordinates (Figure 91), the well is drilled in the direction of maximum principal horizontal stress. The following figures display the displacements and horizontal stress contours in a plane parallel to the X-Y plane with X axis parallel to the maximum principal horizontal stress and Y axis parallel to the minimum principal horizontal stress.

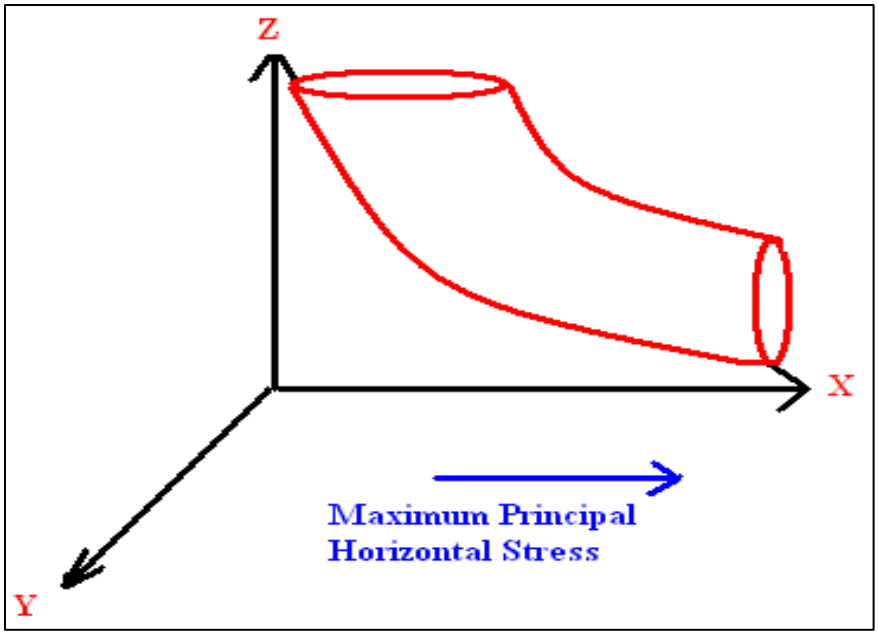

Figure 91 Inclined well schematic with respect to the Cartesian coordinates.

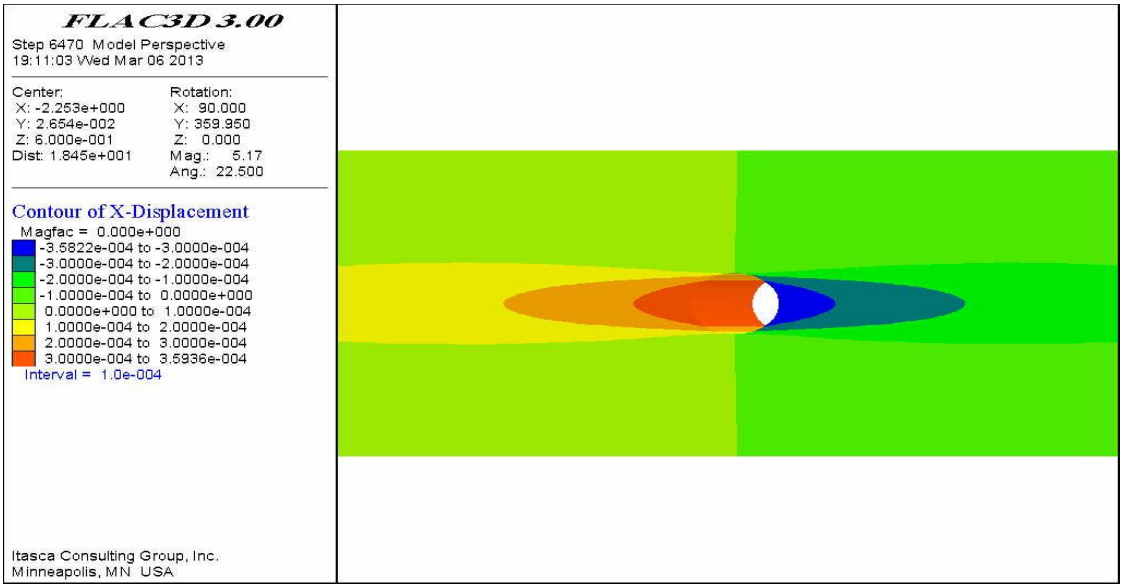

Figure 92 Displacement contours in the X direction (maximum principal horizontal stress orientation).

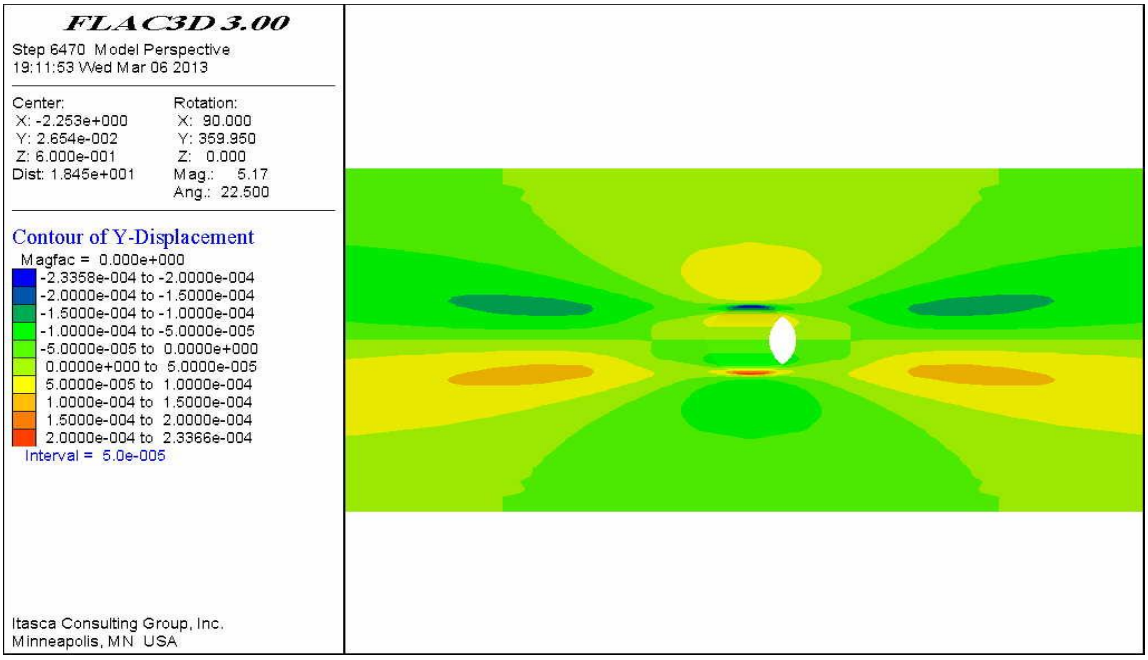

Figure 93 Displacement contours in the Y direction (minimum principal horizontal stress orientation).

.

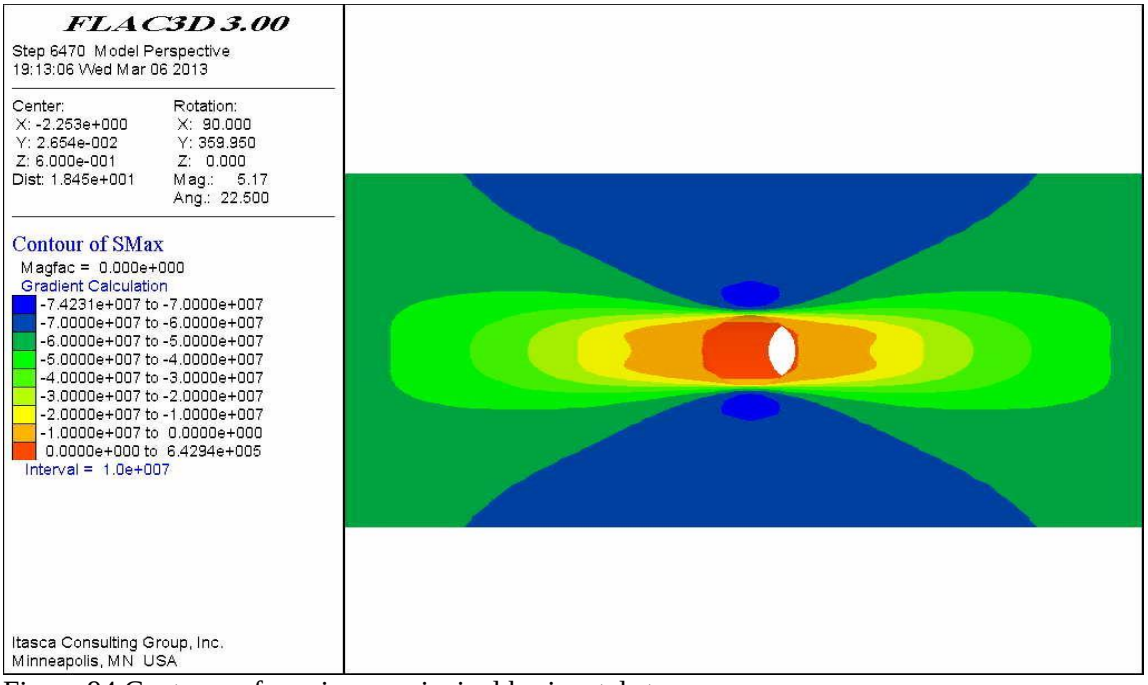

Figure 94 Contours of maximum principal horizontal stress.

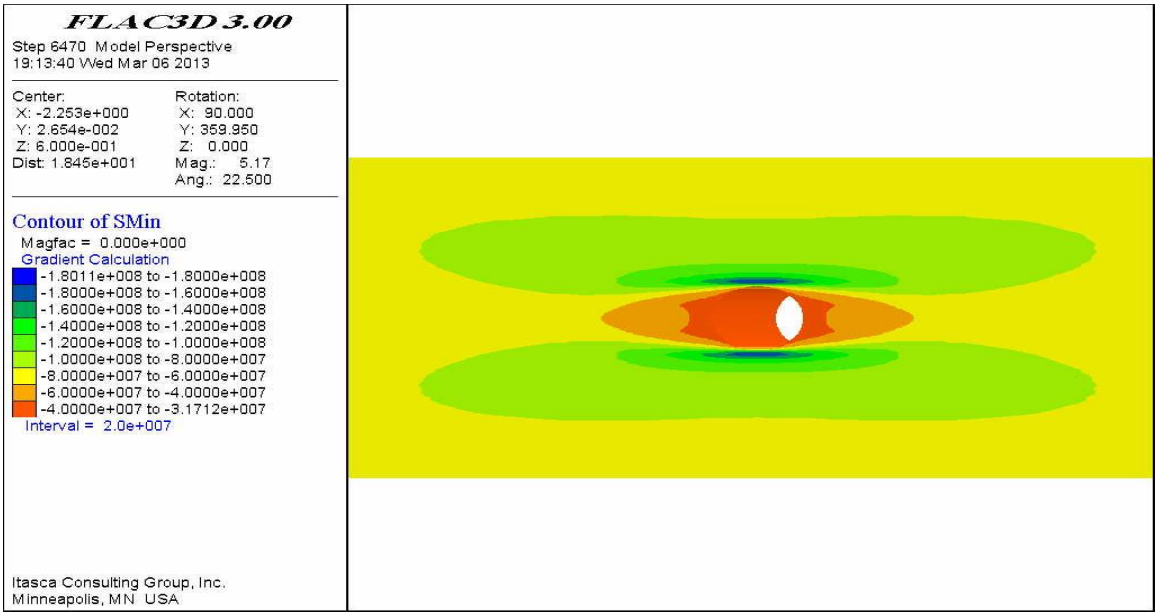

Figure 95 Contours of minimum horizontal principal stress.

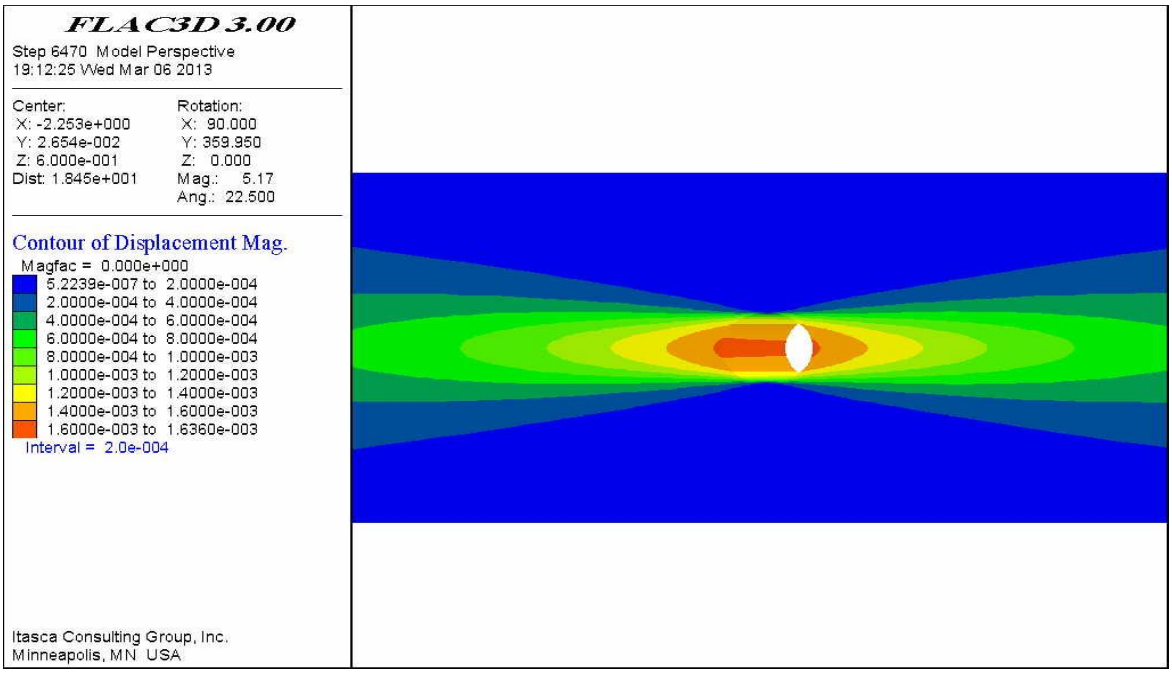

Figure 96 Contours of total displacement magnitude.

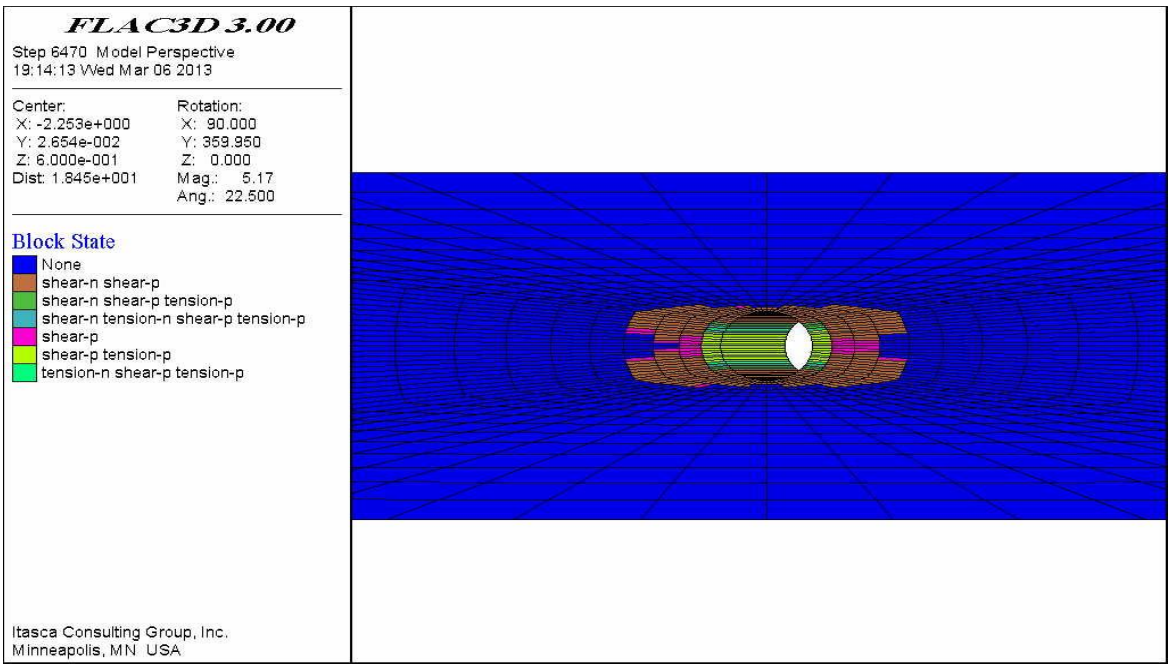

Figure 97 Development of elastic and plastic regions of shear and tensile failures around the borehole.

From the previous figures it is understood when the well is deviated 75˚ from the vertical angle (15˚ attack angle), it will cause the well to undergo a severe tensile and shear failures. A combination of plastic shear and tensile failure deformations take place in the direction of maximum principal horizontal stress. A more precise investigation at the position where these failures occurred could provide good information of the direction of the maximum principal horizontal stress around the wellbore in a real case. In addition, wellbore breakouts which are considered as a set of non-radial shear failure planes, happen in the direction of minimum horizontal principal stress which in this case is in Y axis direction.

Inclined Well (30˚ attack Angle)

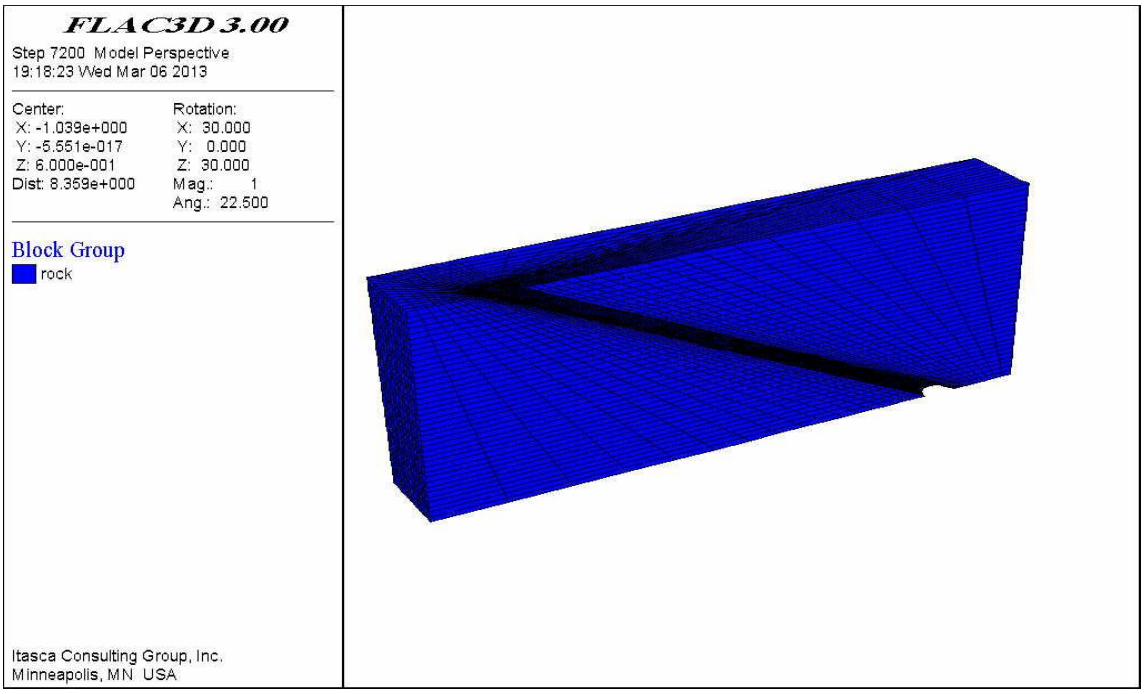

Figure 98 The schematic model of the well with 60˚ of deviation angle (30˚ attack angle).

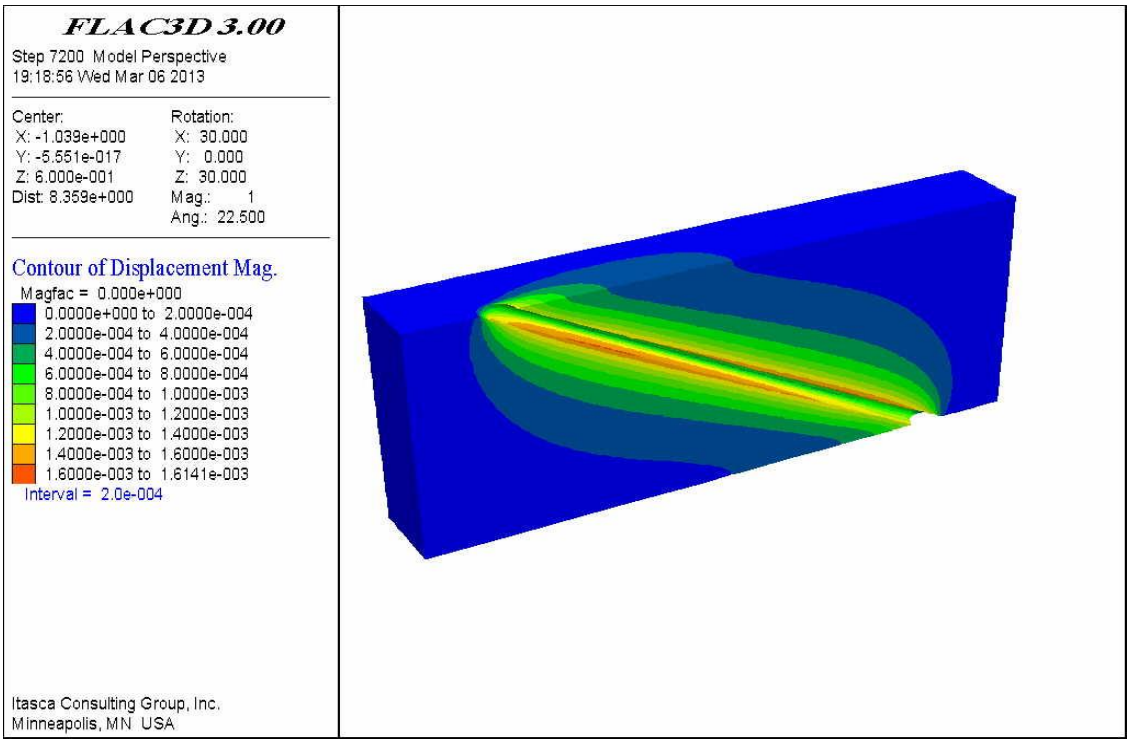

Figure 99 Side-view of the well with total displacement magnitude contours in color scale.

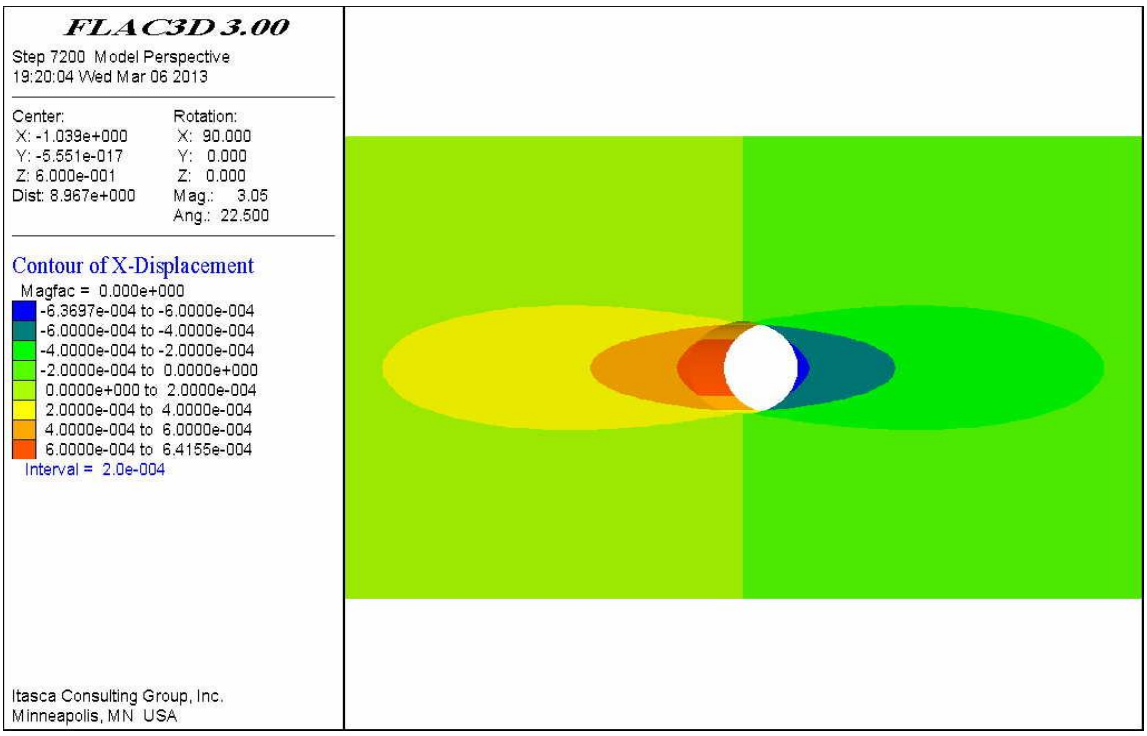

Figure 100 Displacement contours in the X direction (maximum principal horizontal stress orientation).

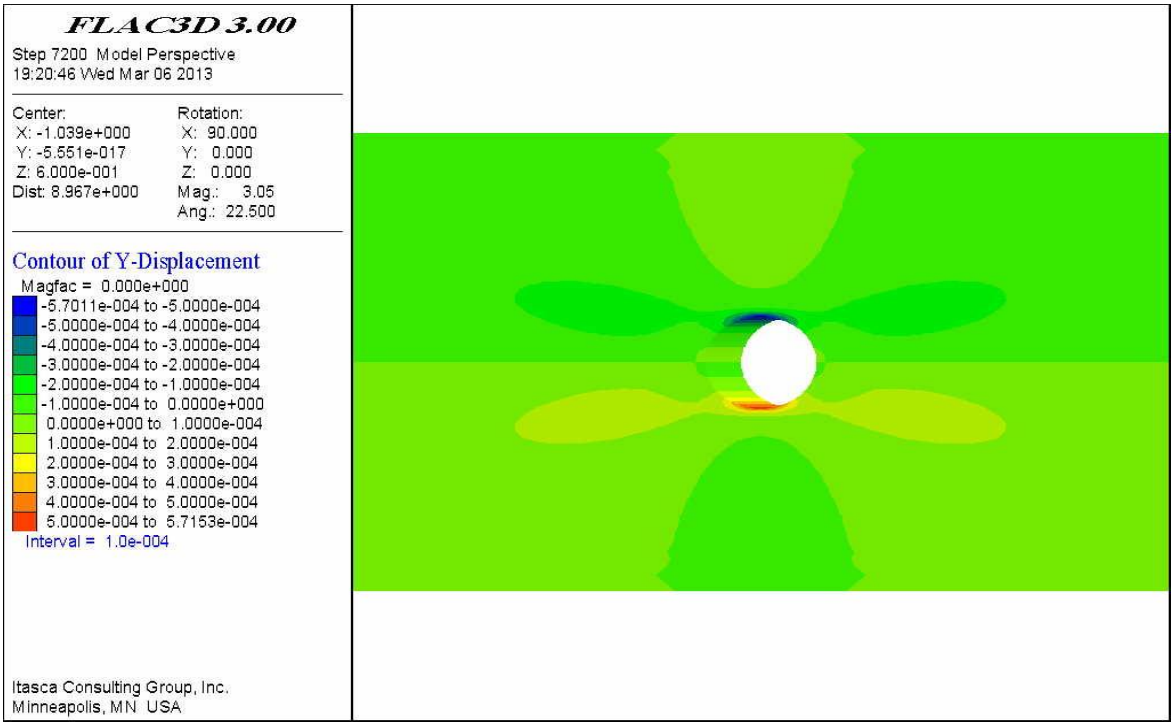

Figure 101 Displacement contours in the Y direction (minimum principal horizontal stress orientation).

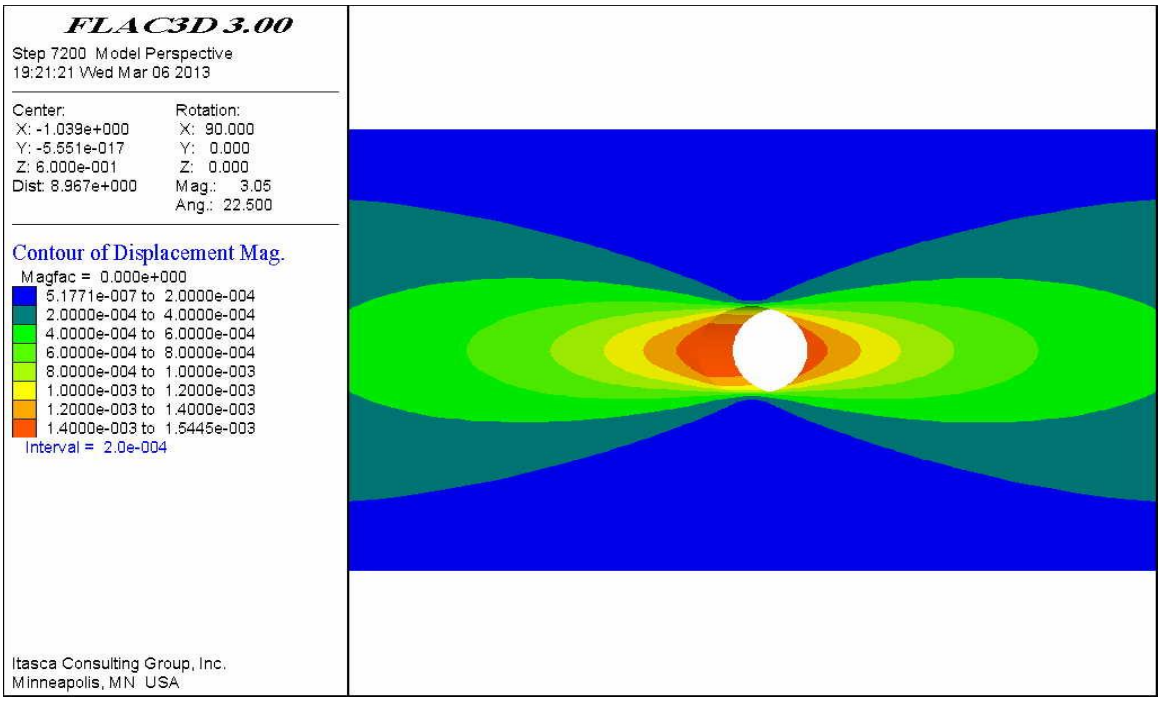

Figure 102 Contours of total displacement magnitude.

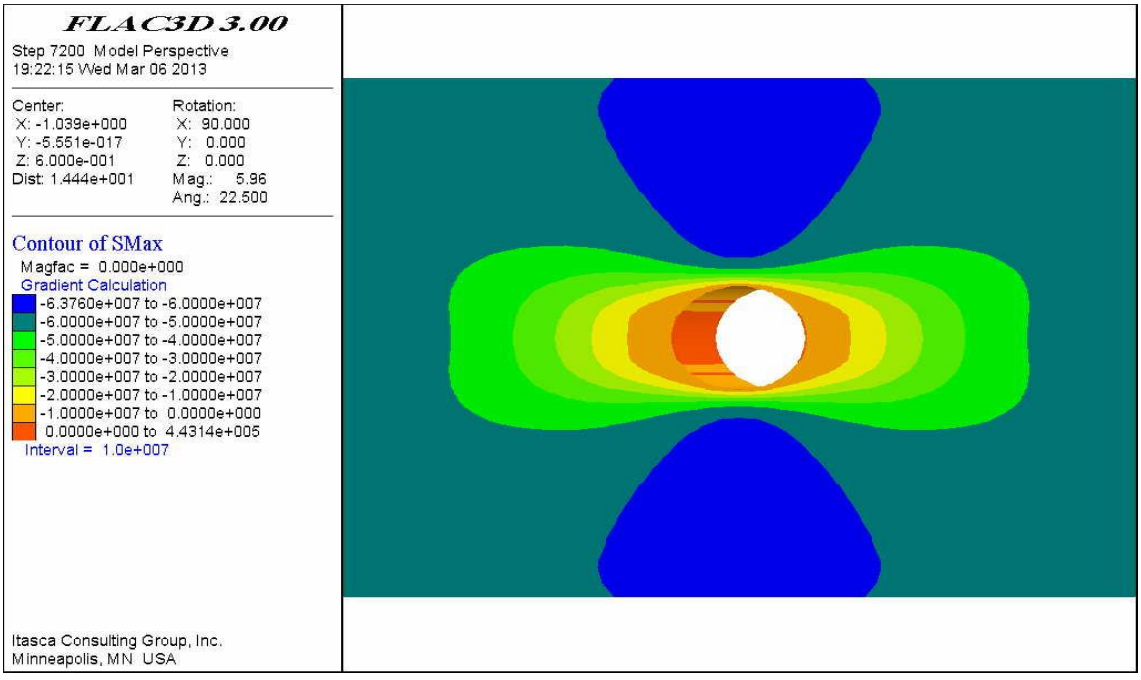

Figure 103 Contours of maximum principal horizontal stress.

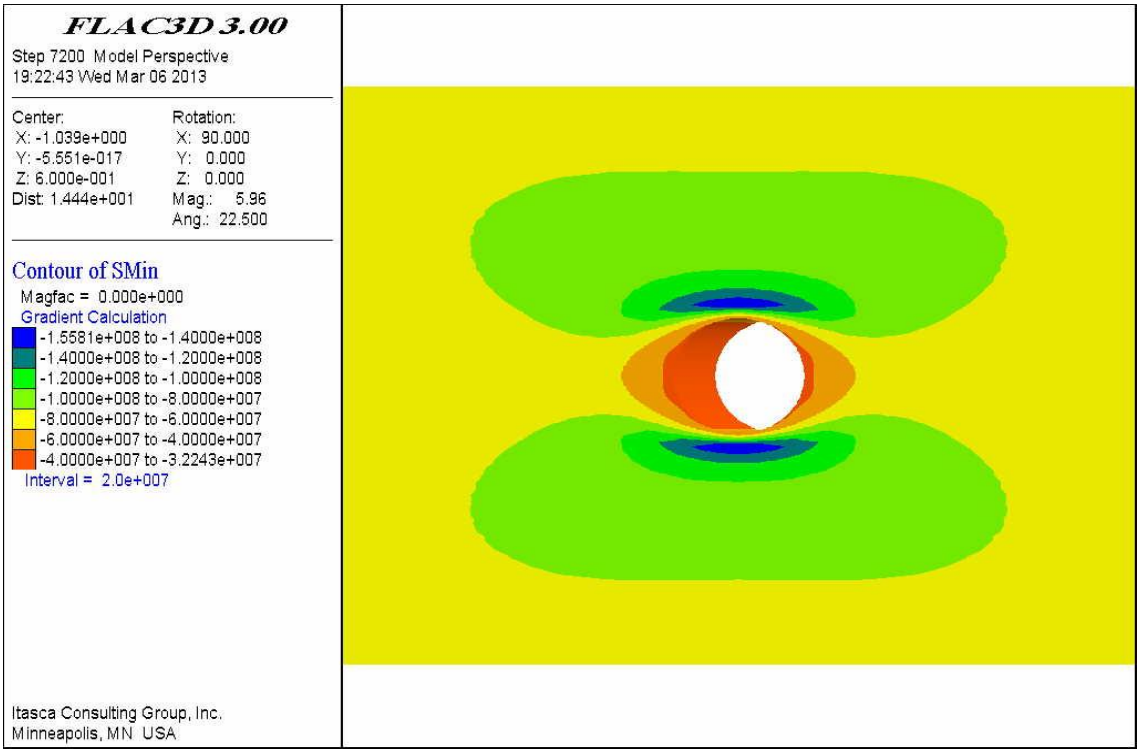

Figure 104 Contours of minimum principal horizontal stress.

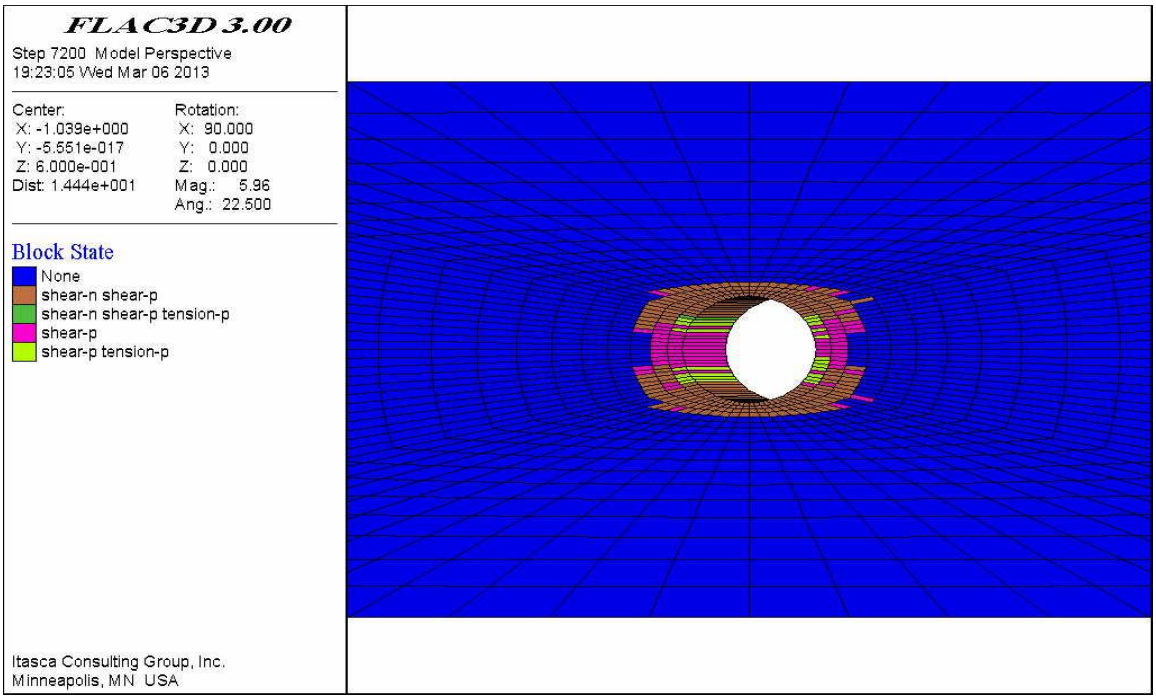

Figure 105 Development of elastic and plastic regions of shear and tensile failures around the borehole.

When comparing the results of the past two attack angles, 15˚ and 30˚, it was found that displacements are in the lower ranges of variation in the 60˚ well deviation angle opposed to the 75˚ deviation angle (30˚ and 15˚ attack angle respectively). Additionally, the variation of horizontal stresses are more moderate in the 30˚ attack angle rather than in the 15˚ angle. It's also noteworthy that plastic and failure regions are more severe in 15˚ of attack angle than 30˚ case (75˚ and 60˚ inclination angle respectively).

Inclined Well (45˚ attack Angle)

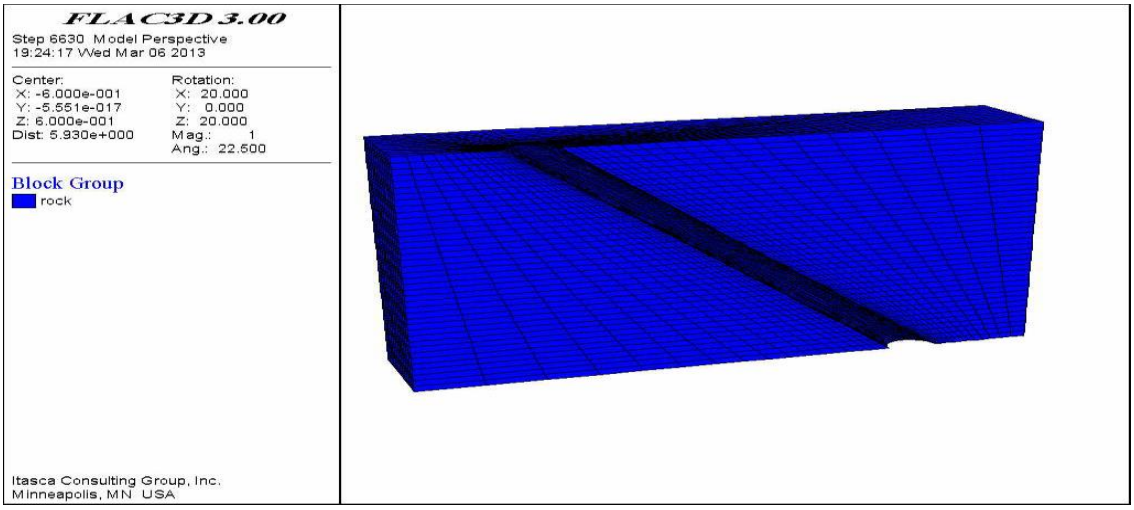

Figure 106 The schematic model of the well with 45˚ of deviation angle.

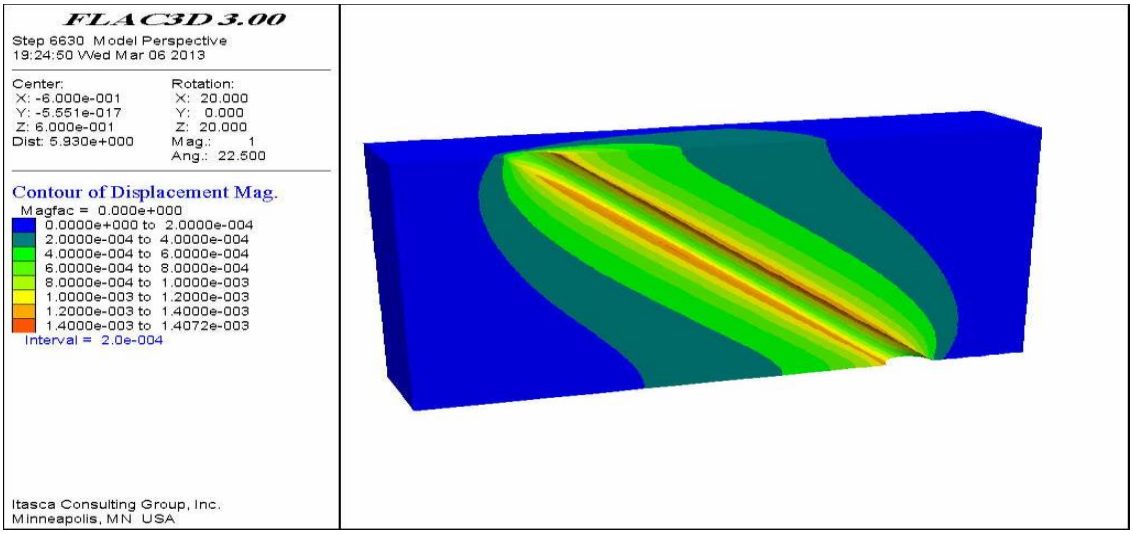

Figure 107 Total displacement contours along the well in the UB.

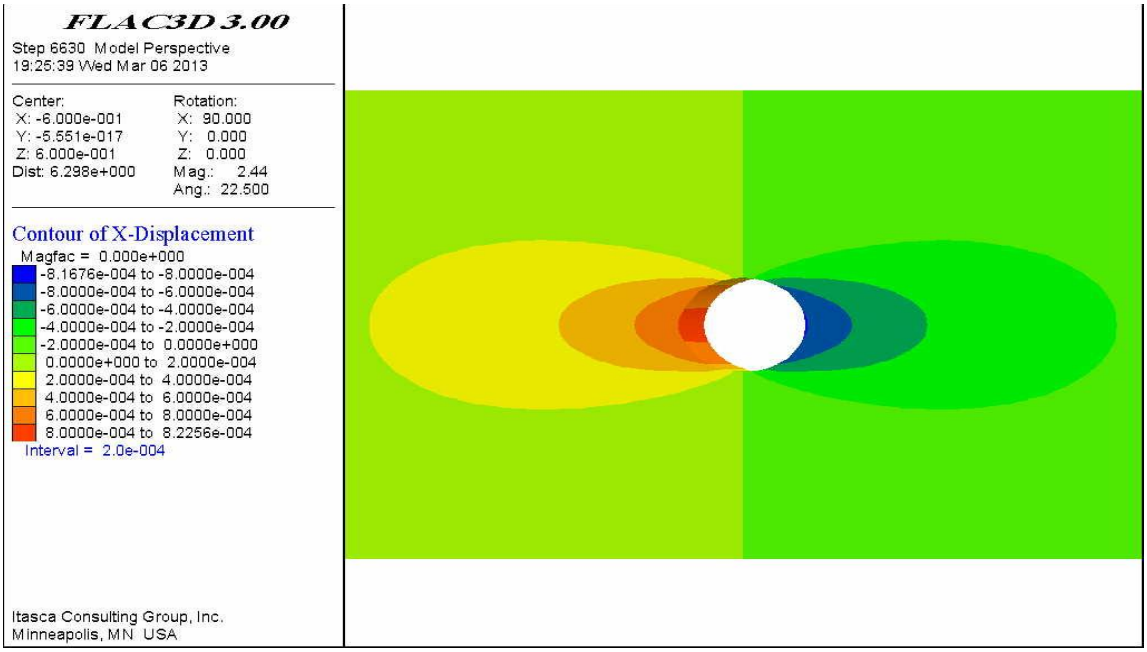

Figure 108 Displacement contours in the X direction (maximum principal horizontal stress direction).

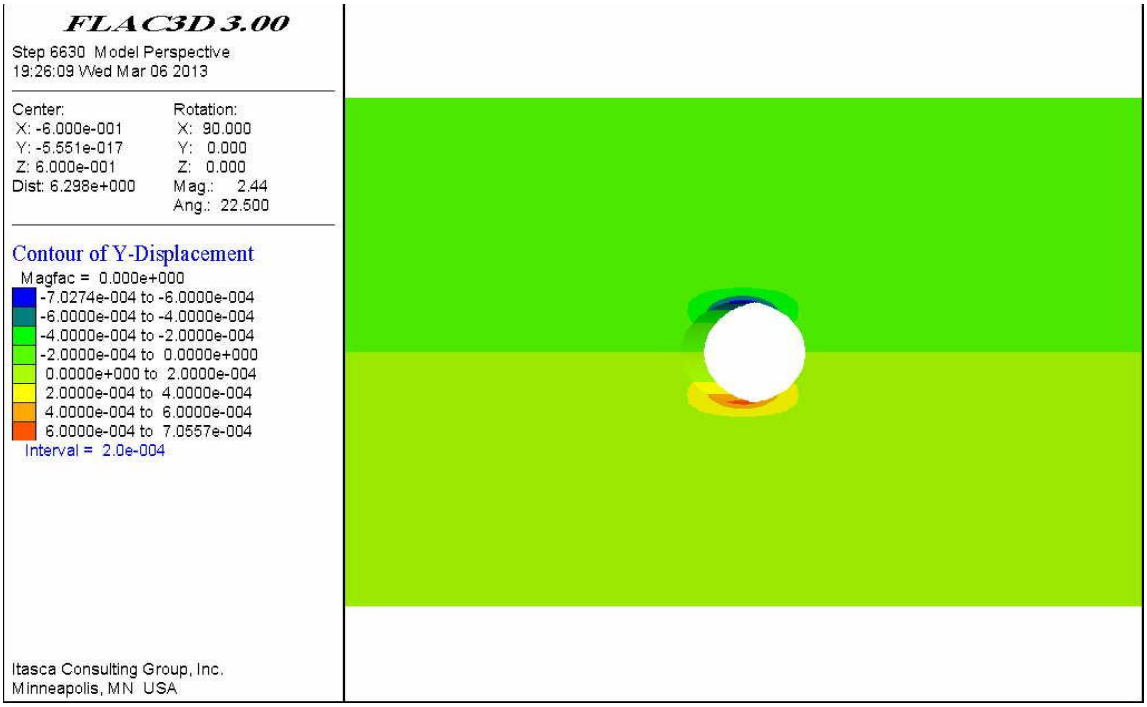

Figure 109 Displacement contours in the Y direction (minimum principal horizontal stress direction).

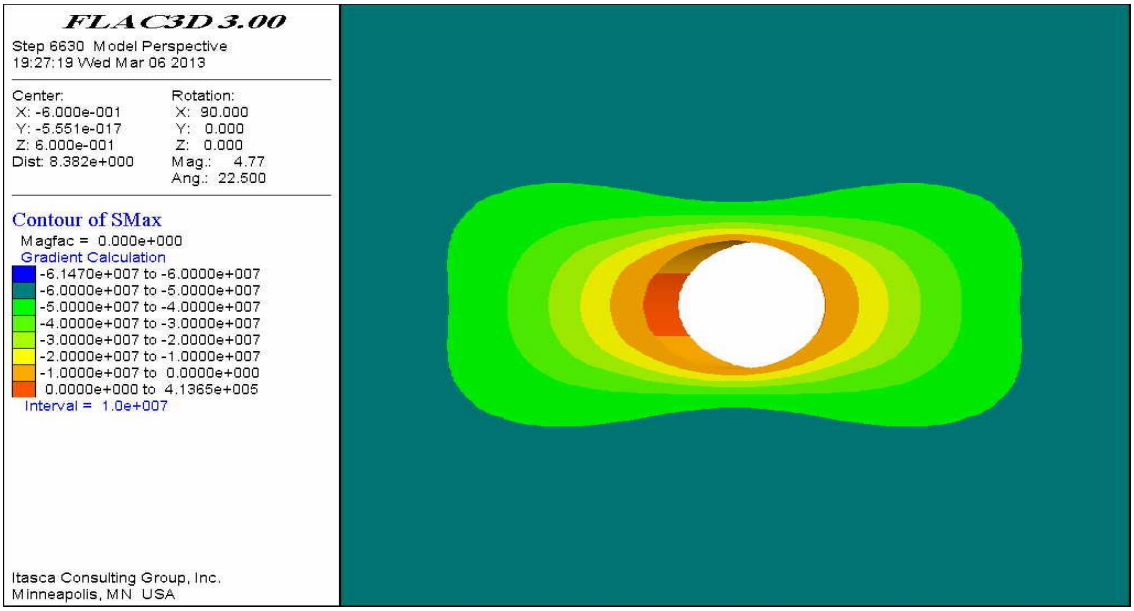

Figure 110 Contours of maximum principal horizontal stress.

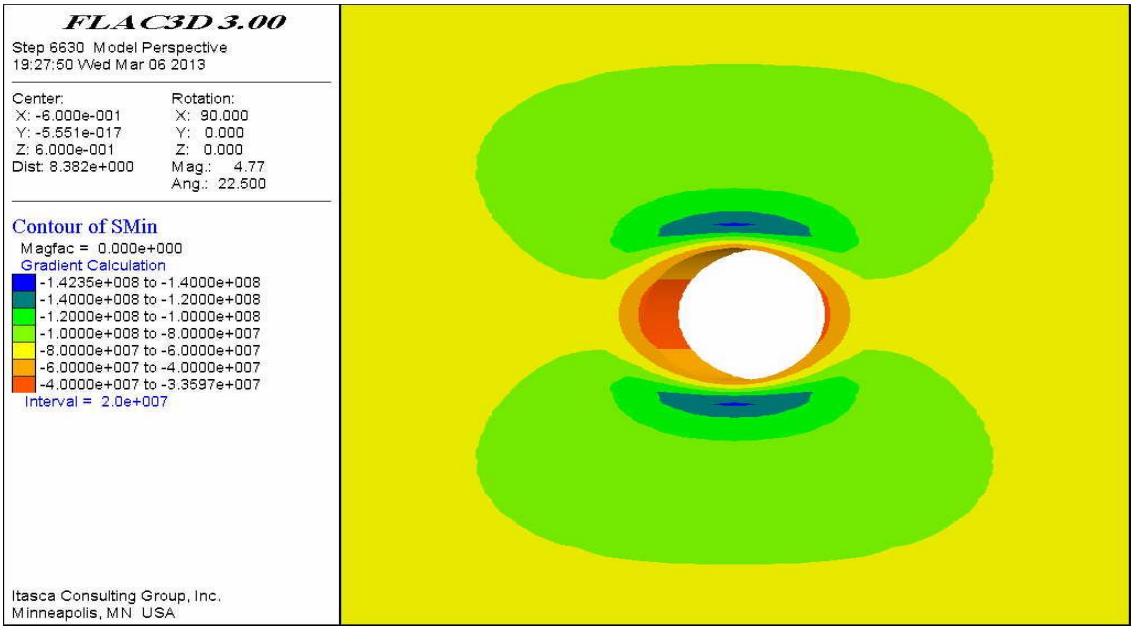

Figure 111 Contours of minimum principal horizontal stress.

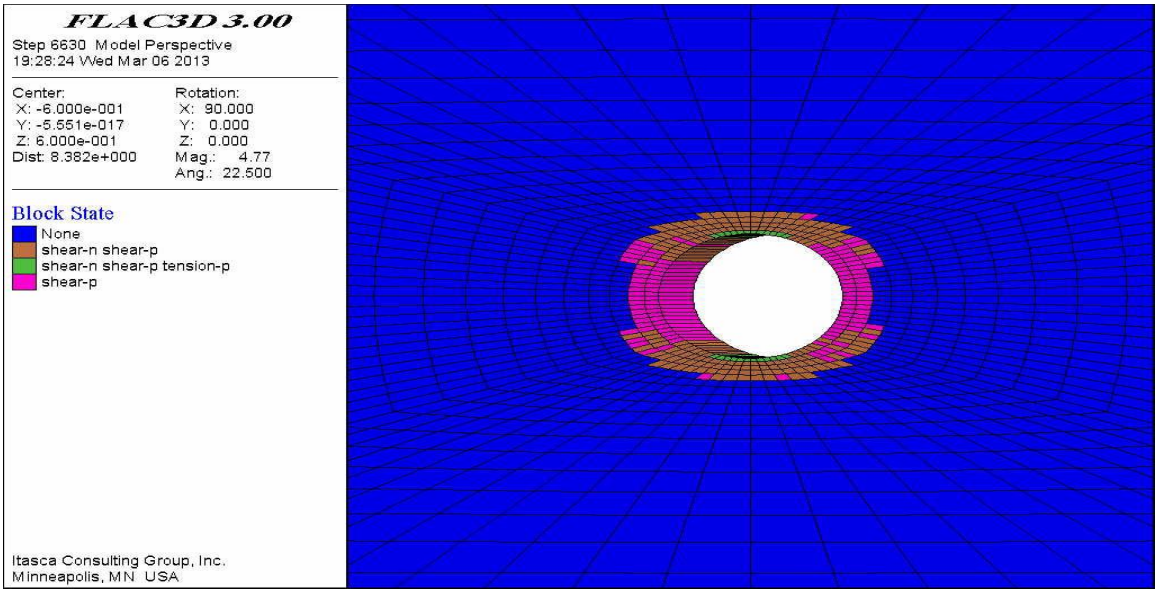

Figure 112 Development of elastic and plastic regions of shear and tensile failures around the borehole.

Inclined Well (60˚ attack Angle)

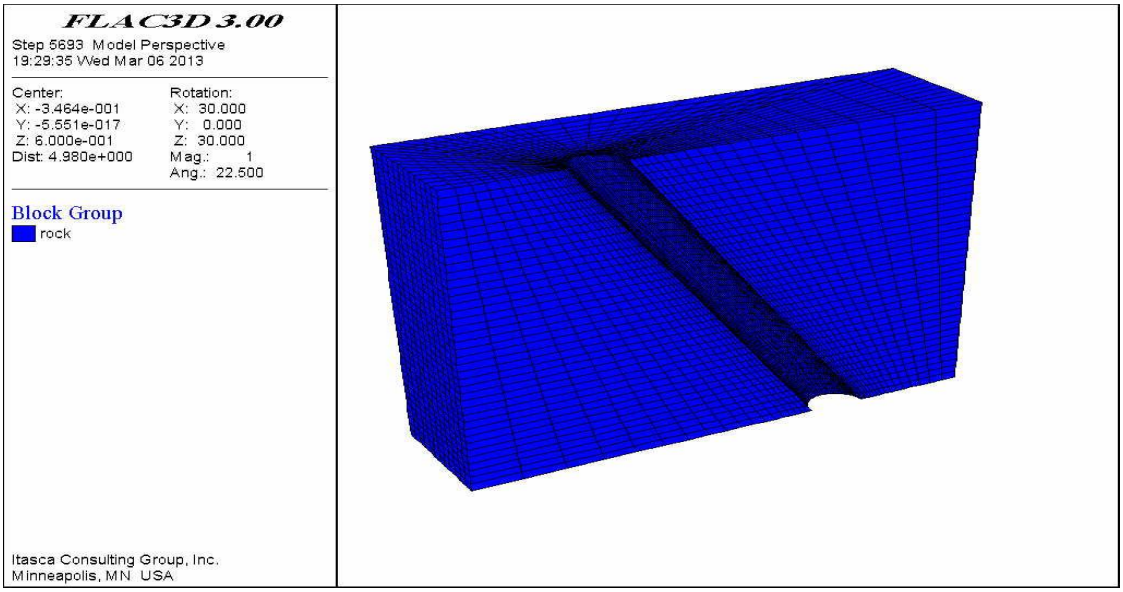

Figure 113 Schematic diagram of the well model for 60˚ of attack angle.

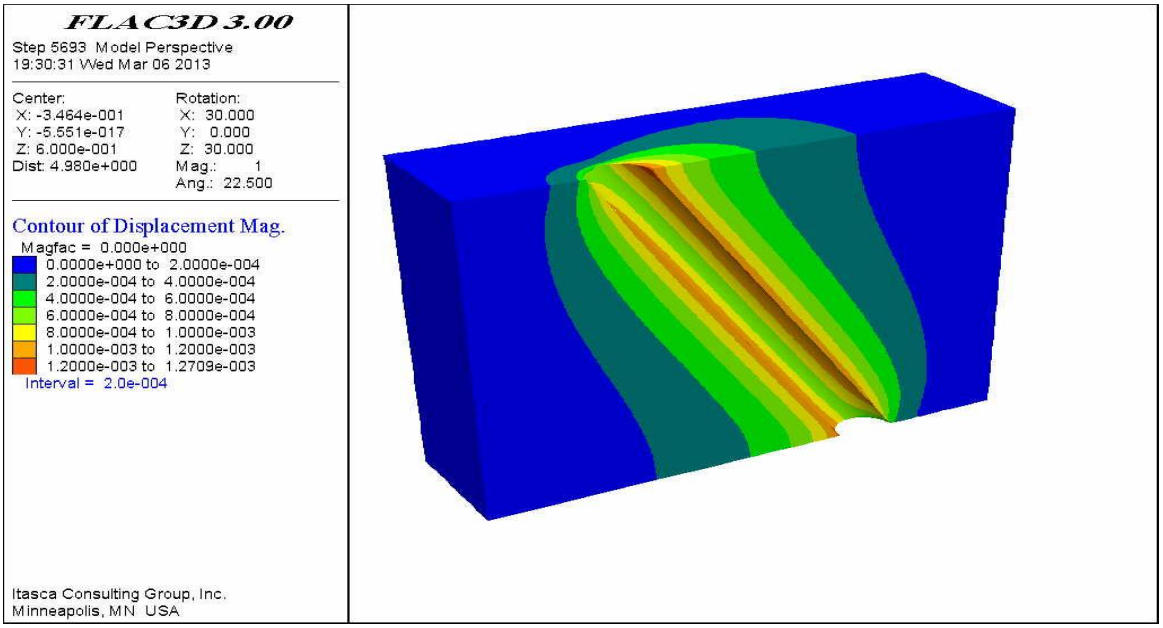

Figure 114 Total displacement contours along the well in the UB.

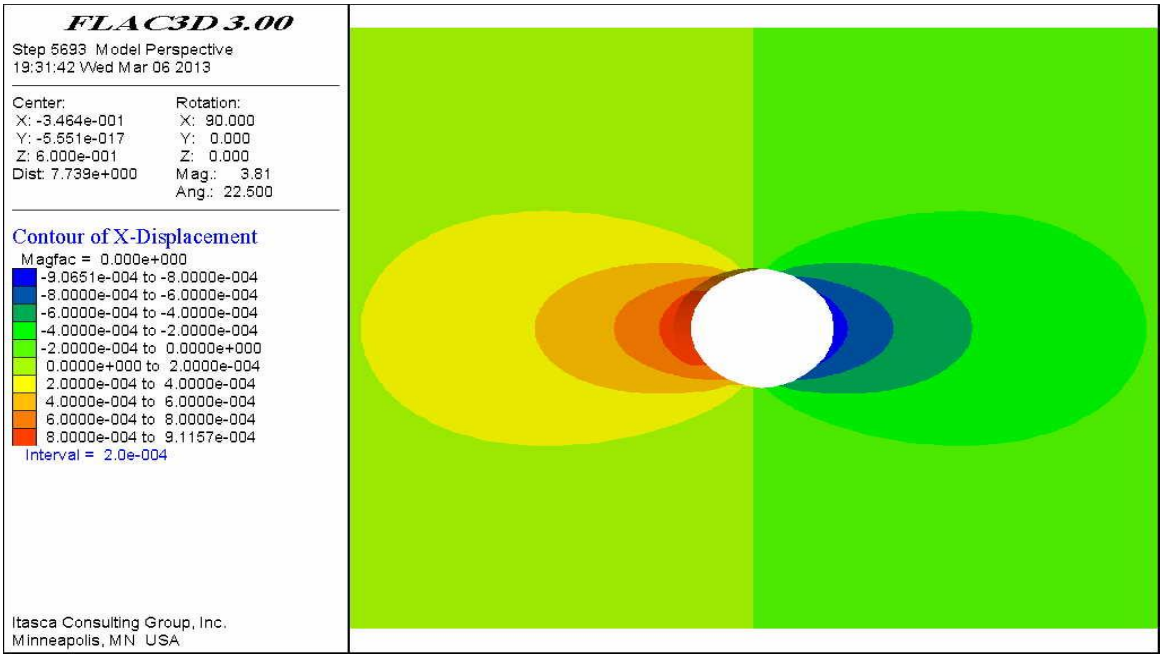

Figure 115 Displacement contours in the X direction (maximum principal horizontal stress direction).

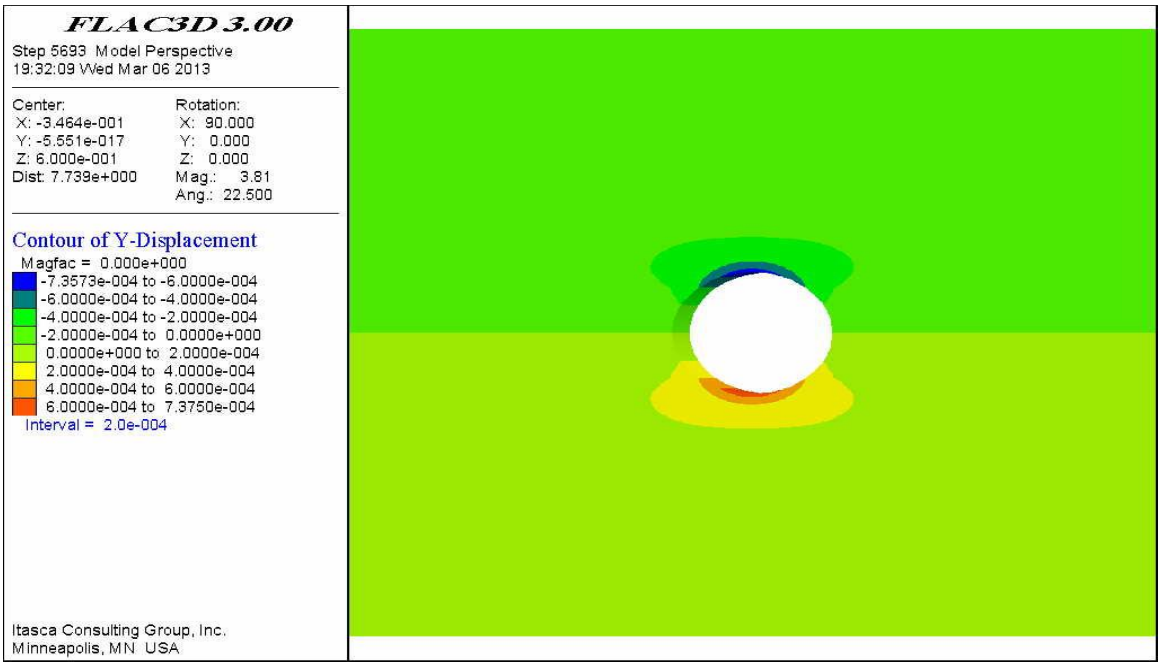

Figure 116 Displacement contours in the Y direction (minimum principal horizontal stress direction).

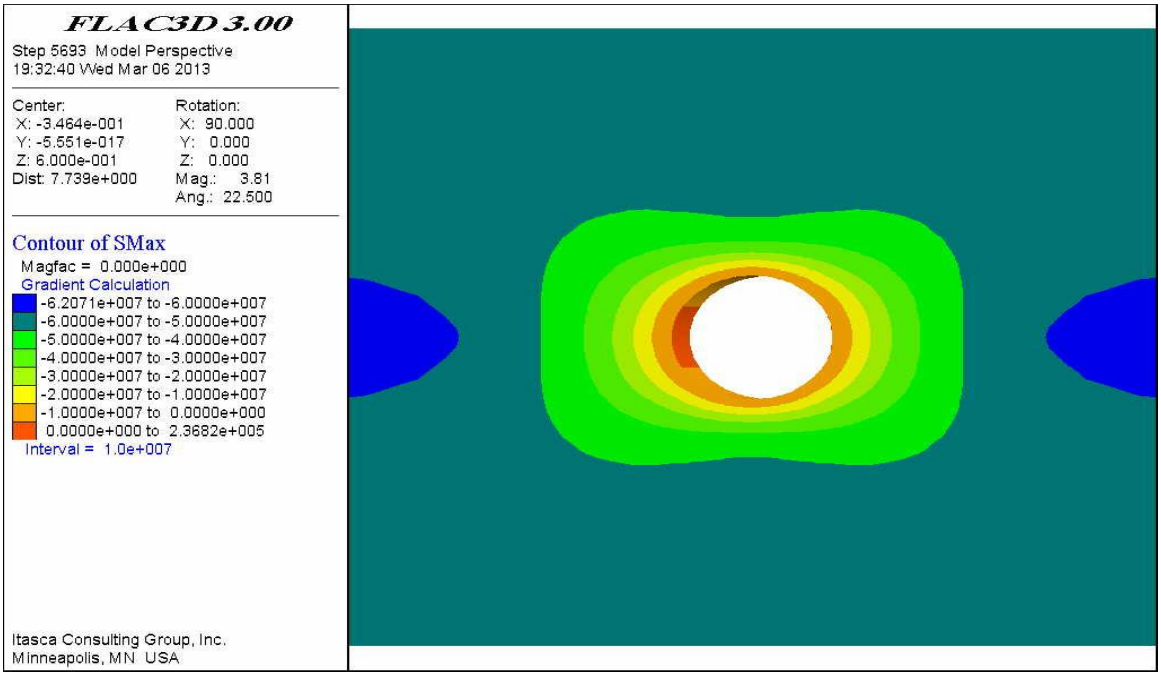

Figure 117 Contours of maximum horizontal principal stress.

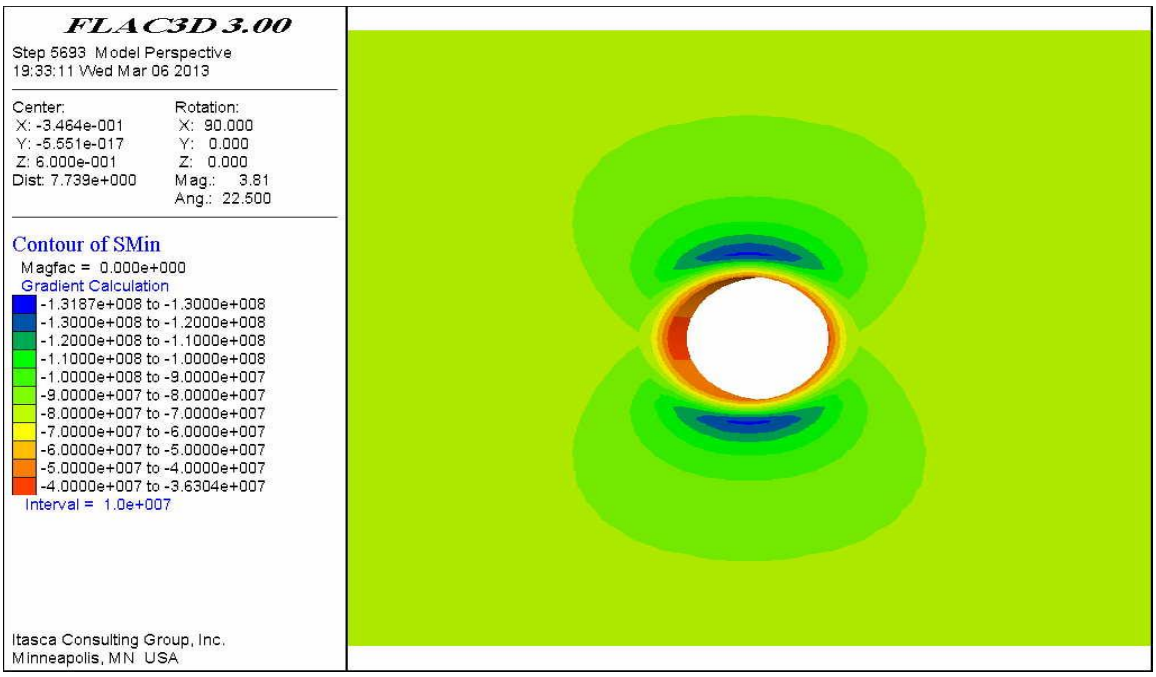

Figure 118 Contours of minimum horizontal principal stress.

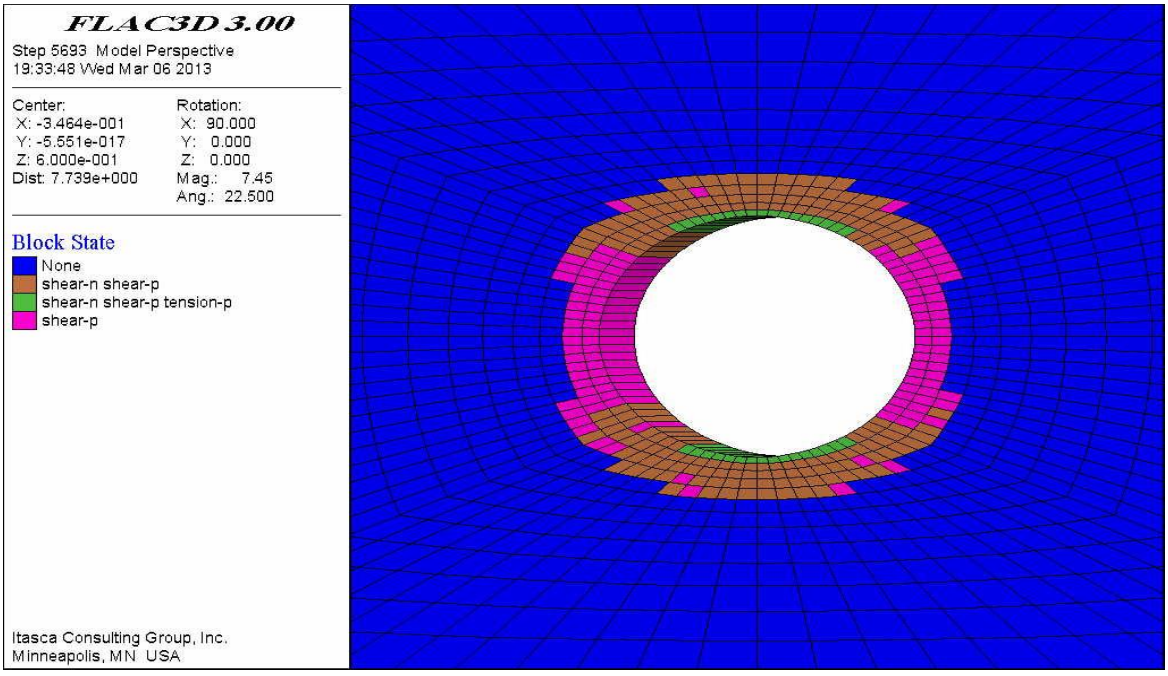

Figure 119 Development of elastic and plastic regions of shear and tensile failures around the borehole.

Inclined Well (75˚ attack Angle)

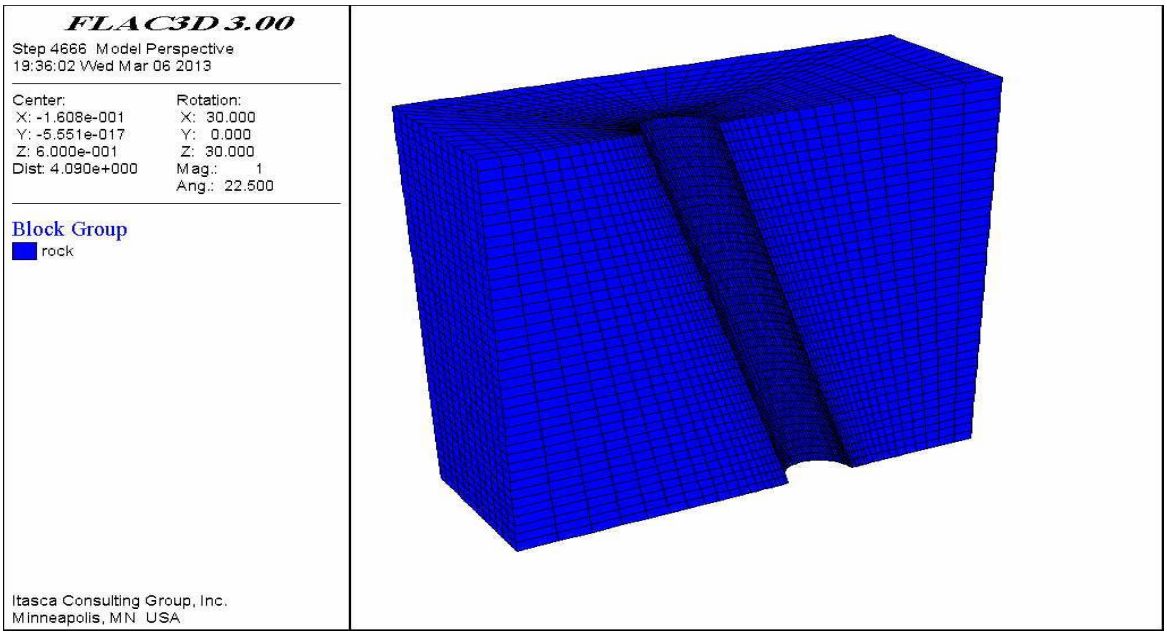

Figure 120 Schematic diagram of the well with 15˚ deviation angle.

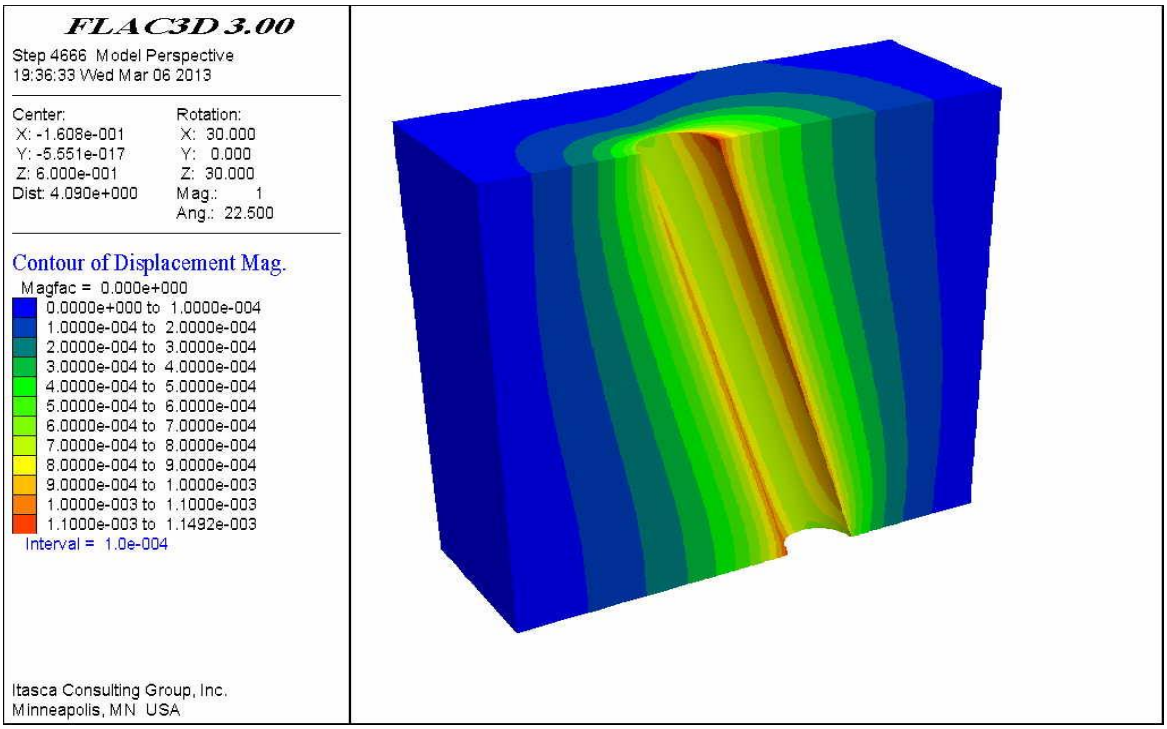

Figure 121 Total displacement contours around the well in the UB.

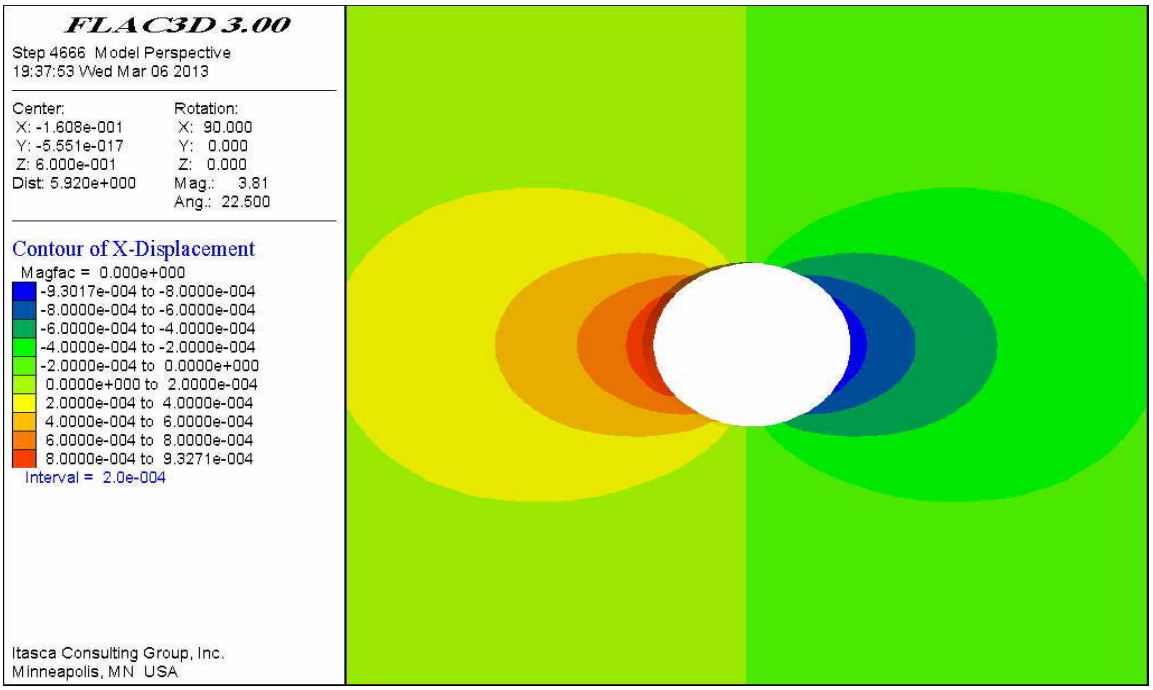

Figure 122 Displacement contours in the X direction (maximum horizontal principal stress direction).

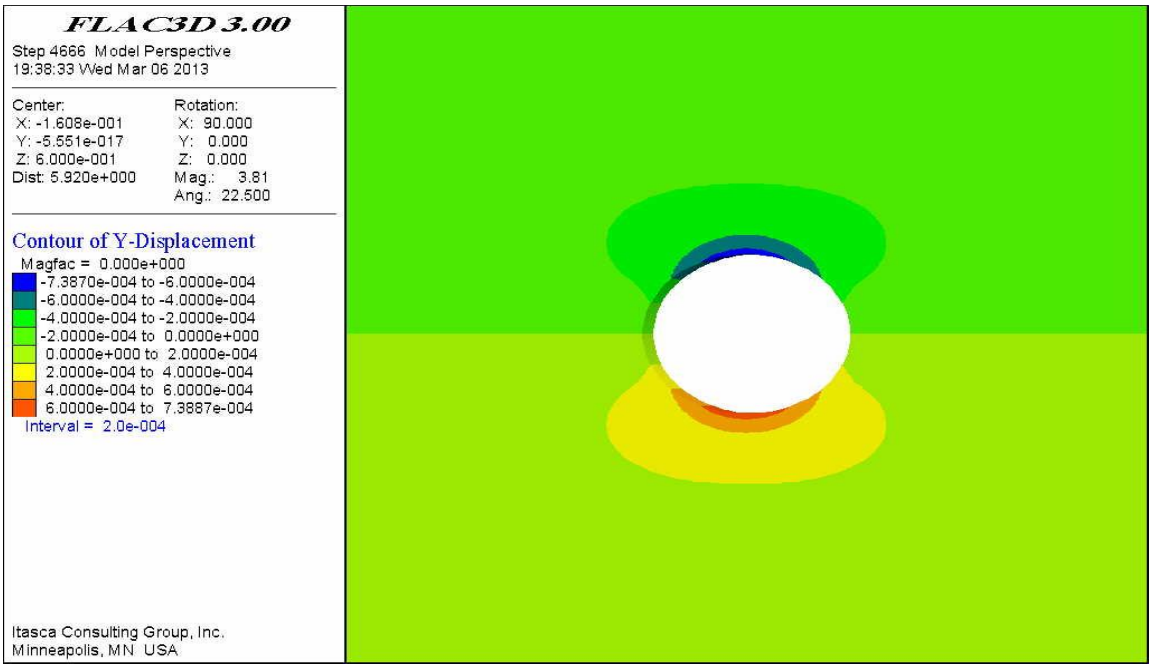

Figure 123 Displacement contours in the Y direction (minimum principal horizontal direction).

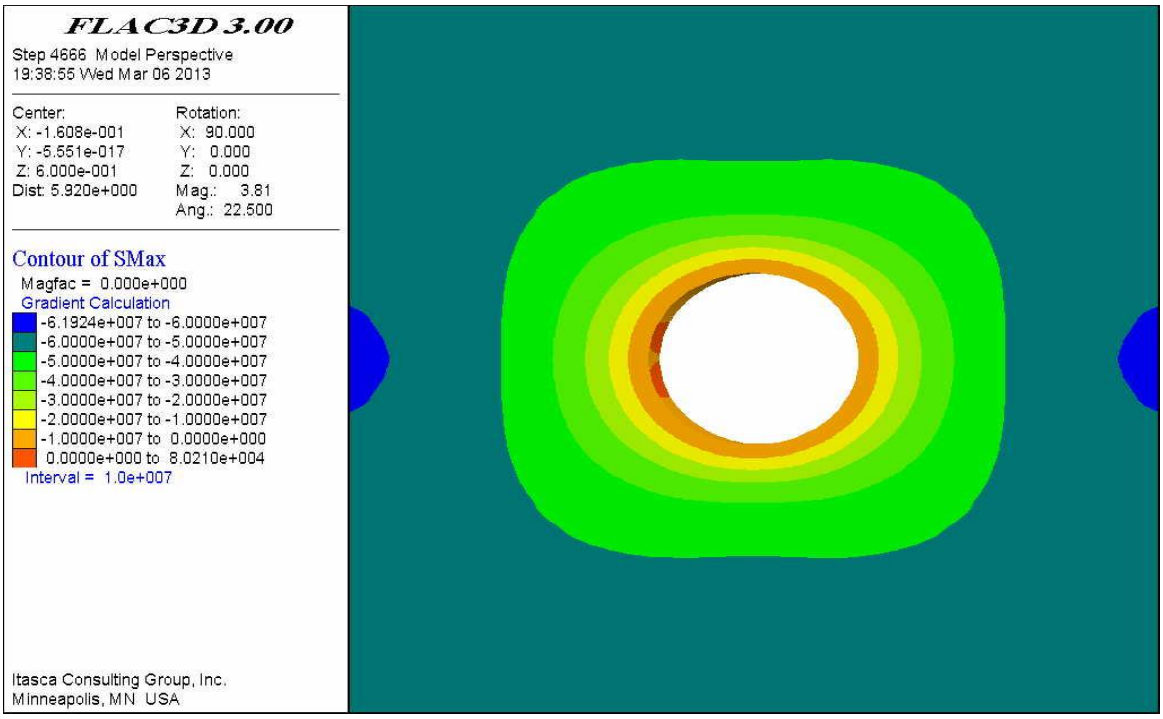

Figure 124 Contours of maximum principal horizontal stress.

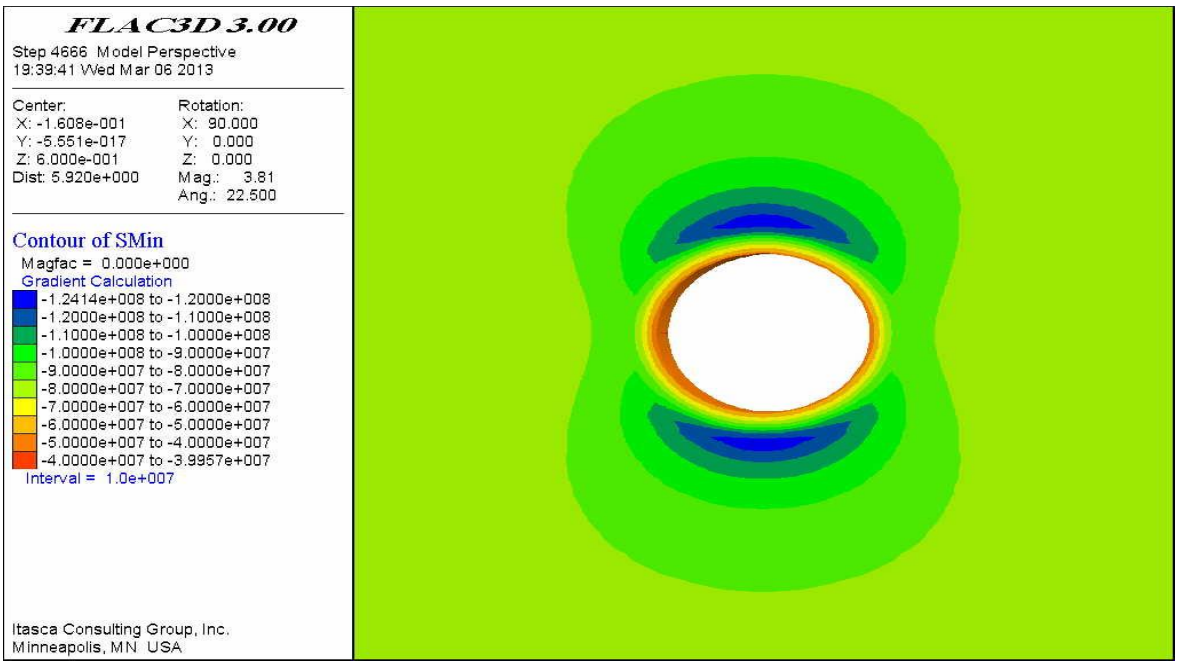

Figure 125 Contours of minimum principal horizontal stress.

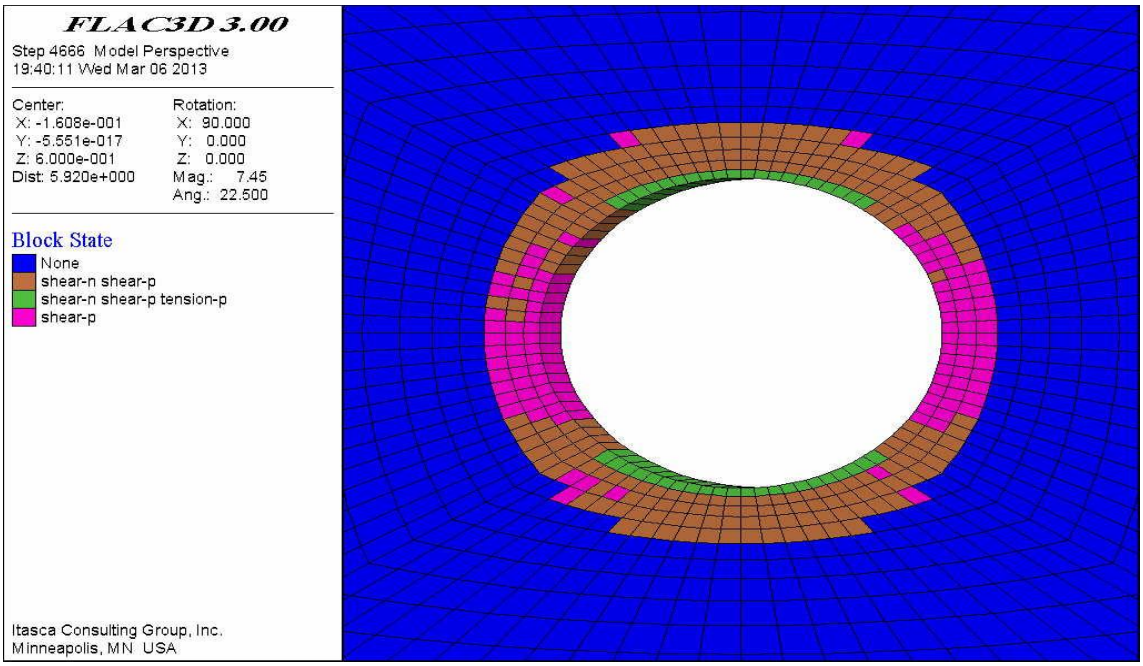

Figure 126 Development of elastic and plastic regions of shear and tensile failures around the borehole.

Horizontal well in the Middle Bakken

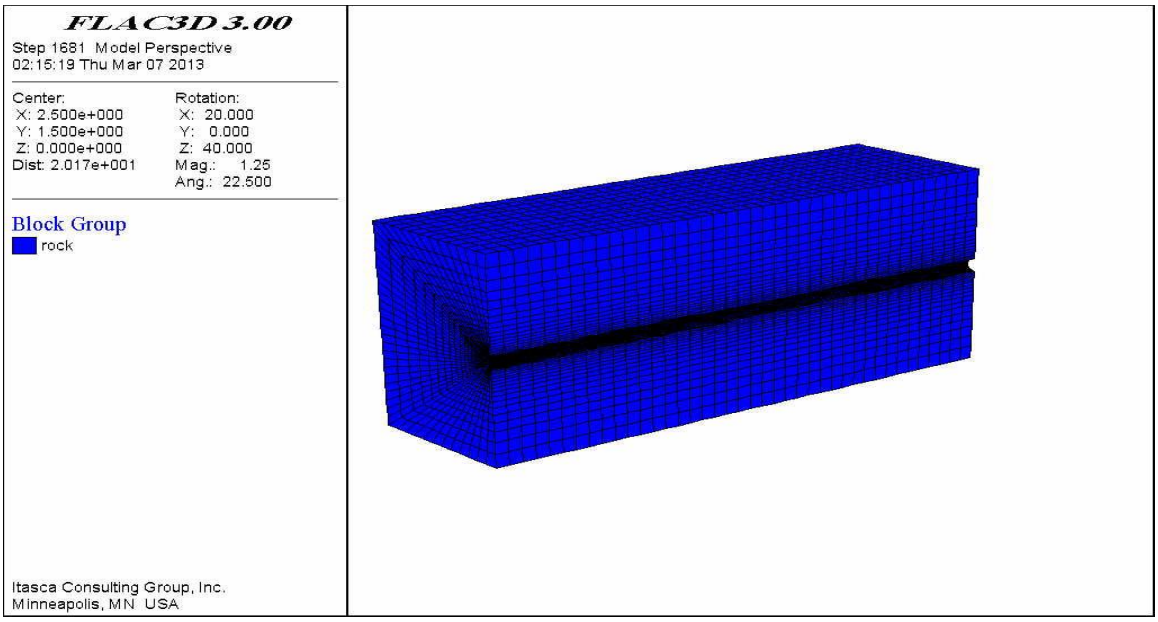

Figure 127 Schematic diagram of a horizontal well in the MB.

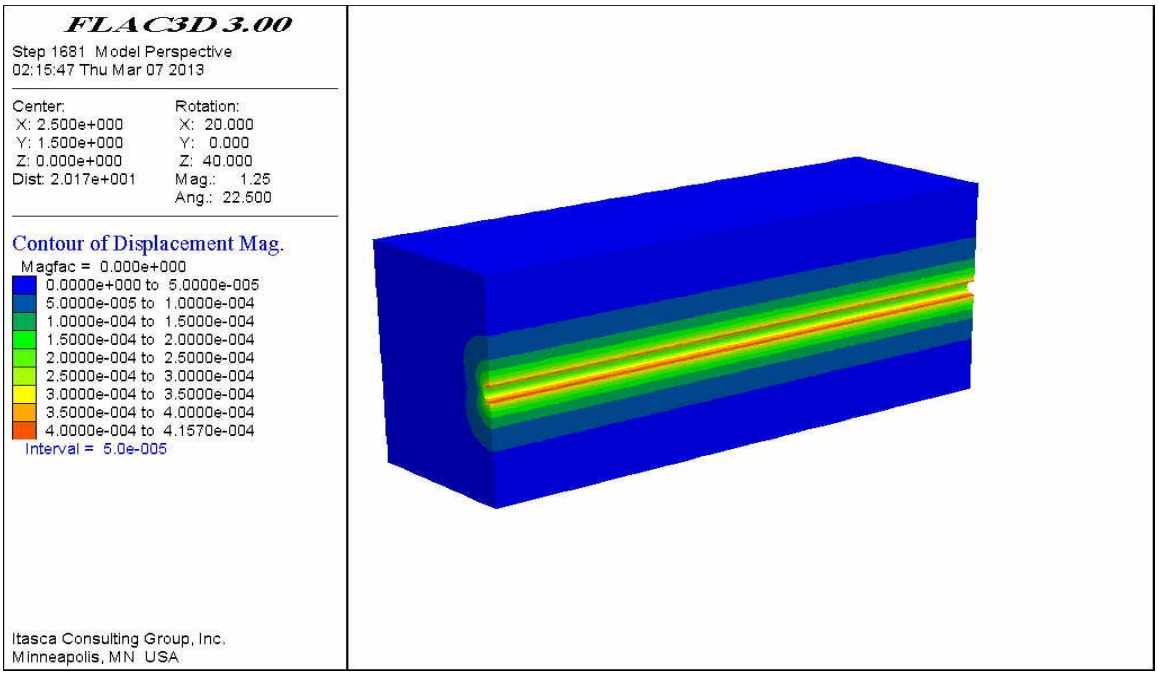

Figure 128 Total displacement contours in a horizontal well in the MB.

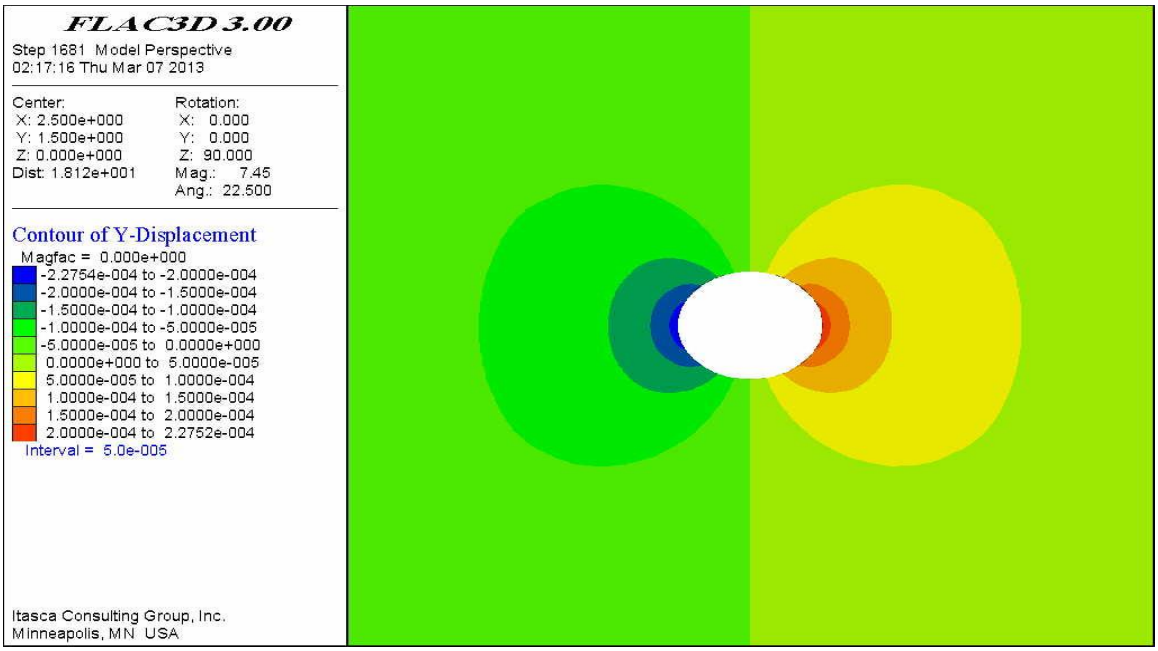

Figure 129 Displacement contours in a horizontal well in the MB in the Y direction (minimum principal horizontal stress direction).

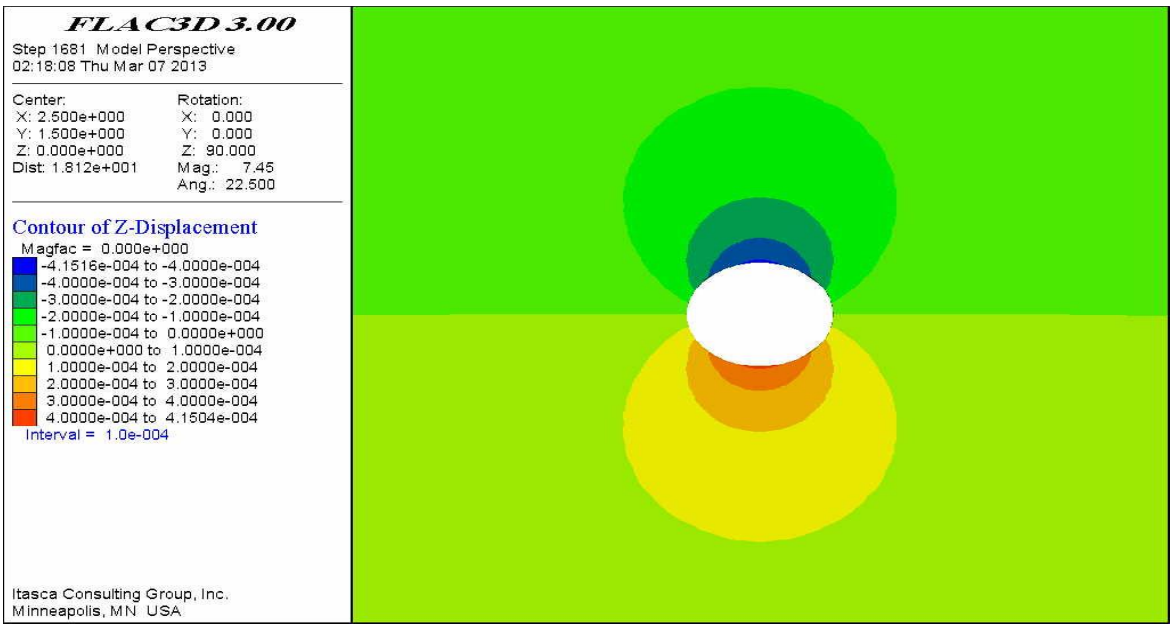

Figure 130 Displacement contours in the Z direction in a horizontal well in the MB (overburden stress direction).

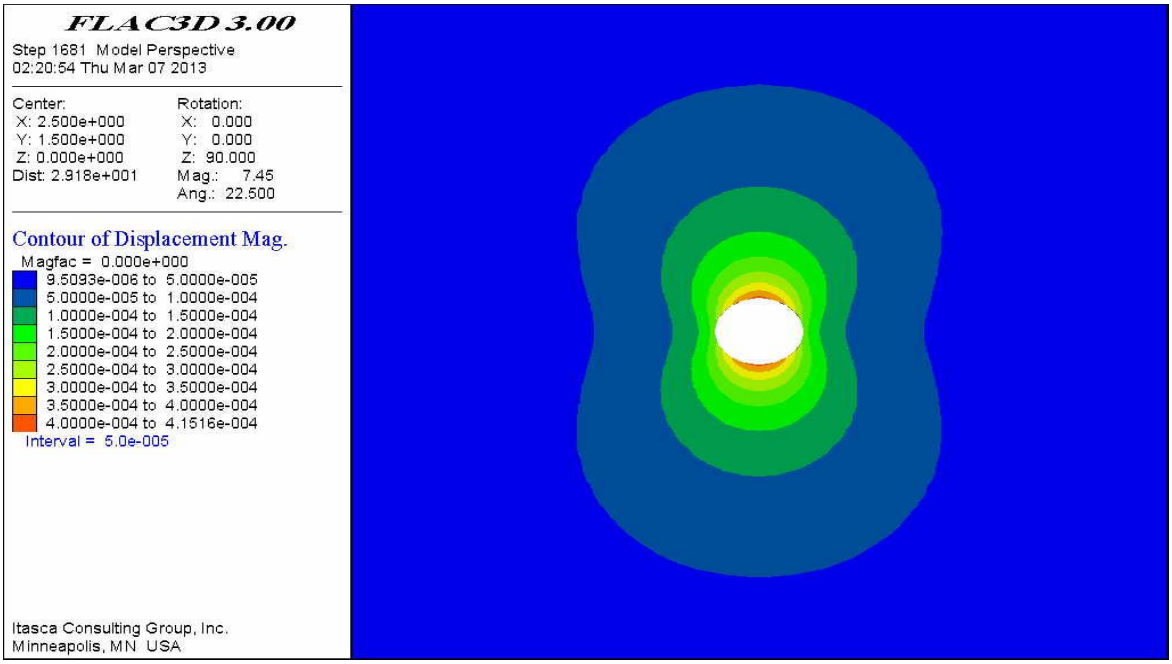

Figure 131 Contours of total displacement magnitude in a horizontal well in MB.

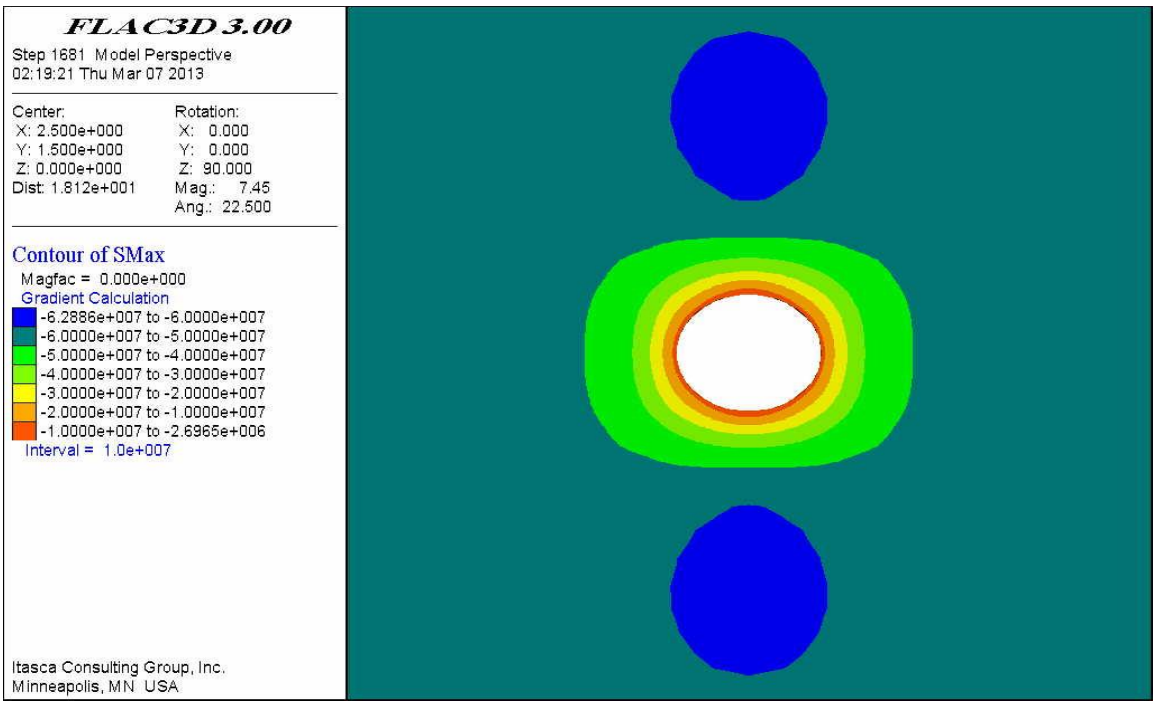

Figure 132 Contours of maximum principal horizontal stress.

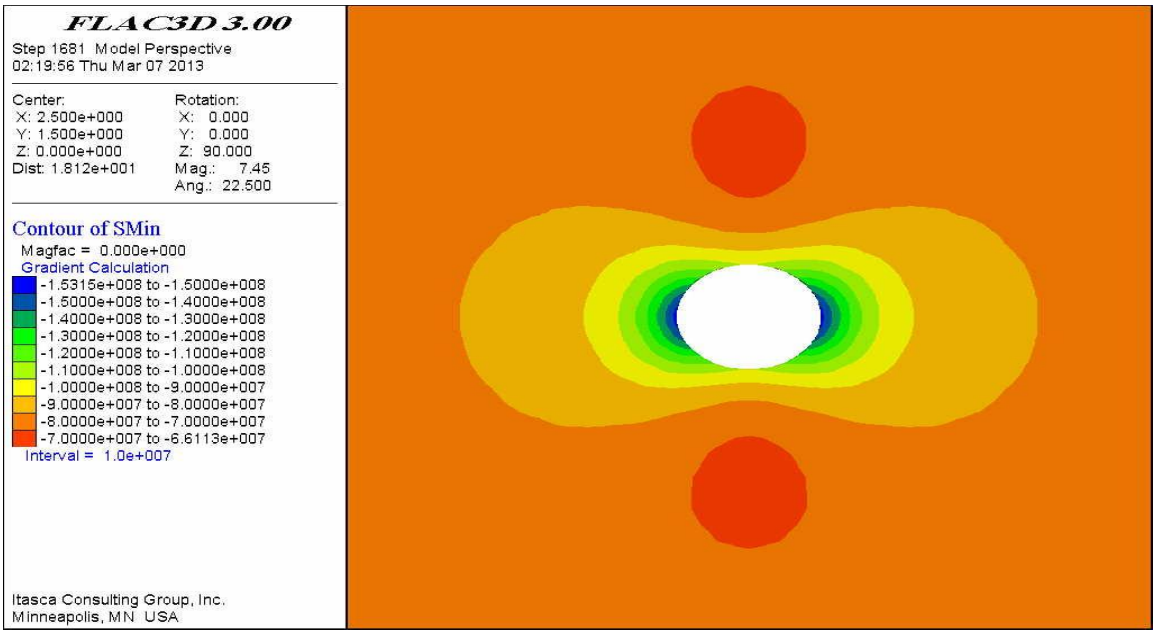

Figure 133 Contours of minimum horizontal principal stress.

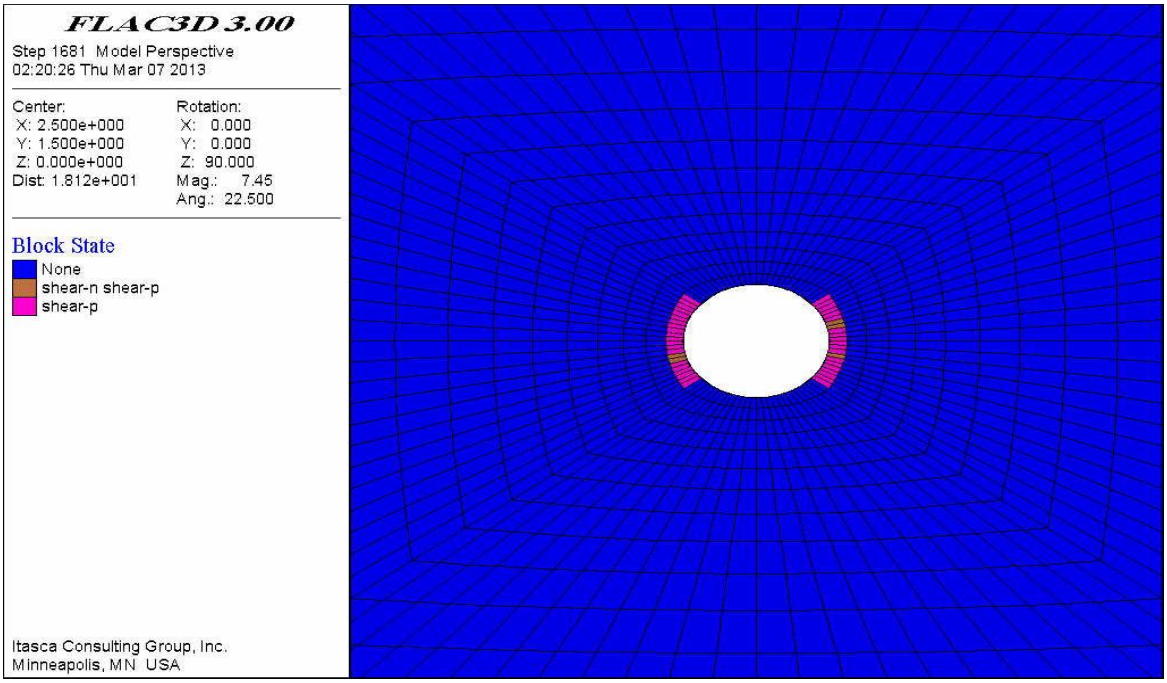

Figure 134 Development of elastic and plastic regions and failures around the borehole in a horizontal well in the MB.

To model a horizontal well in the Middle Bakken, drilled in the X direction (the direction of maximum principal horizontal stress), vertical stress or overburden stress will act as the maximum principal stress and plays an important role in causing deformations and failures around the borehole. Nevertheless displacements in the Z direction (the direction of vertical effective stress) are much higher than X or Y directions. In addition, it can be observed that the latest modeling results did not show any major failures around the wellbore. As was expected, some minor shear failures or breakouts can exist in the Y direction (the direction of minimum horizontal principal stress). It's also interesting that opposed to the previous attack angles no tensile failure was detected in the direction of principal stresses, neither minimum principal horizontal stress nor vertical stress.

The following figure depicts how maximum total displacement versus well deviation angle decreases from a vertical well to a horizontal well in anisotropic conditions in the UB and isotropic MB (from 90˚ to 0˚ attack angle).

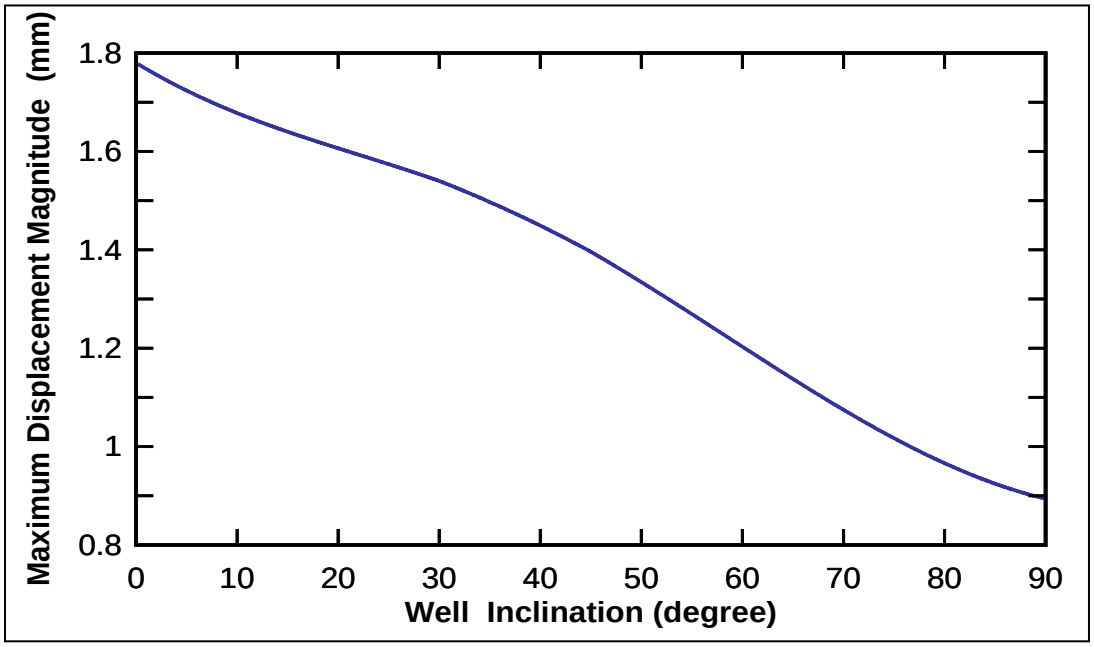

Figure 135 Observed maximum total displacement versus well deviation angle.

As expected and perceived, maximum displacement happens in a vertical well and decreases versus well deviation angle until a horizontal well is achieved. A horizontal well indicates the minimum value of total maximum displacement; at least half of which takes place in a vertical well.

Considering anisotropic behavior of middle member, the cohesion and internal friction angle plays an important role in the geomechanical modeling and they should be very well defined in vertical and horizontal directions (different planes of weakness or anisotropy) with respect to the well deviation angle. Thus, cohesion and internal friction angle vary along Z axis (the axis of symmetry). These two components can be defined

through the following equations in two different directions, vertical and horizontal orientations or a combination of both in deviated wells. In the following relations, *h* denotes horizontal and *v* vertical directions. *C* is cohesion and φ is internal friction angle.

$$C = C_h \cos^2\theta + C_v \sin^2\theta \quad (104)$$

$$\varphi = \varphi_h \cos^2\theta + \varphi_v \sin^2\theta \quad (105)$$

Table 13 summarizes the values for cohesion and internal friction angles used as input in the modeling of different well deviation angles in the Upper Bakken.

Table 13 Anisotropic internal friction angle (Φ) and Cohesion (C) values used as input for geomechanical modeling in UB.

Degree	**C_h(Mpa)**	**C_v Mpa**	**Φ_h**	**Φ_v**	**θ**	**C**	**Φ**
90	12	10	35	30	0	12.000	35.000
75	12	10	35	30	15	11.866	34.665
60	12	10	35	30	30	11.500	33.750
45	12	10	35	30	45	11.000	32.500
30	12	10	35	30	60	10.500	31.250
15	12	10	35	30	75	10.134	30.335
0	12	10	35	30	90	10.000	30.000

Stress Polygons

Stress polygons estimate the range of possible stress states at any given depth and pore pressure while that stress in the crust is limited by the frictional strength of faults

favoring normal, strike-slip, and thrust faulting (Zoback, 2007). For these set of diagrams the following conditions may exist:

- $\sigma_{hmin} = \sigma_{Hmax}$ line is the lower limit of possible stress states.
- Lines bounding the composite polygon on its upper and left sides are thresholds of failure.
- Stress states to the left and above those lines cannot exist in the natural state.
- Different stress polygons apply for differing depths, pore pressures, and friction coefficients.

Stress polygons in the Middle Bakken (MB) at the reservoir depth for two different stress states' conditions: 1) initial reservoir conditions and 2) after 5 years of production with reservoir pressure decline was created. This analysis was performed in order to improve our understanding of the possibility of geomechanical hazards that may occur in the region such as: faulting, subsidence and induced seismic events specifically due to the reservoir depletion with a major decline in pore pressure.

To predict limiting stress differences at any specific depth, in order to create the polygons, the following conditions should be satisfied (Anderson, et al., 1951):

- Normal Faulting

$$\frac{\sigma_1}{\sigma_2} = \frac{S_v - P_p}{S_{hmin} - P_p} \leq \left[\left(\mu^2 + 1\right)^{0.5} + \mu\right]^2 \quad (106)$$

- Strike Slip Faulting

$$\frac{\sigma_1}{\sigma_3} = \frac{S_{Hmax} - P_p}{S_{hmin} - P_p} \leq \left[\left(\mu^2 + 1\right)^{0.5} + \mu\right] \quad (107)$$

- Reverse Faulting

$$\frac{\sigma_1}{\sigma_3} = \frac{S_{Hmax} - P_p}{S_v - P_p} \leq \left[\left(\mu^2 + 1\right)^{0.5} + \mu\right]^2 \qquad (108)$$

σ_1, σ_2 and σ_3 are the principal stresses, P_p is pore pressure and μ is the friction angle. The stress polygons are created under elastic Mohr-Coulomb failure criterion assumptions at the reservoir depth in the horizontal section of the well at 10311ft TVD. From Equations (106)-(108), it is recognized that pore pressure and depth (expressed in terms of overburden pressure, $S_{v)}$ are the main governing parameters for such analysis; Pore pressure was predicted from reservoir simulation and history matching after 5 years of production (Figure 136). In addition, applying elastic Mohr-Coulomb failure criterion to the formation means that Hook's Law is the governing relation on the media and the contributing corresponding parameters such as Poisson's ratio, Young's modulus, compressive strength and friction angle are independent of the processes followed by the production.

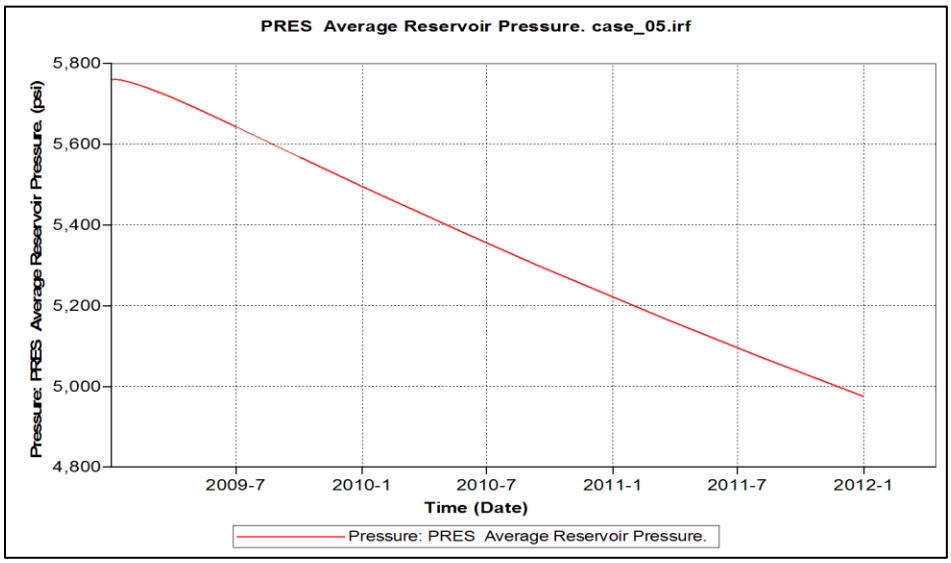

Figure 136 Current reservoir pressure obtained from reservoir simulation after 5 years of production.

Figure 137 is the stress polygon indicating the magnitude of principal stresses for initial reservoir pressure and includs the failure occurrence's width in degrees as a function of compressive strength (red contours) of the rock. The solid black lines outline the polygon that defines the limits of Mohr-Coulomb failure for frictional equilibrium of pre-existing faults in the region. It should be mentioned that these limits are independent of any criteria related to the wellbore. These limits are only dependent on pore pressure, vertical stress (depth) and the value of sliding friction. If the stress state lies inside this polygon then the strength of the crust does not allow a larger stress difference between the greatest and least principal stresses to occur. The dashed lines separate the three triangular regions representing normal faulting (NF), strike-slip faulting (SS), and reverse faulting (RF) stress conditions.

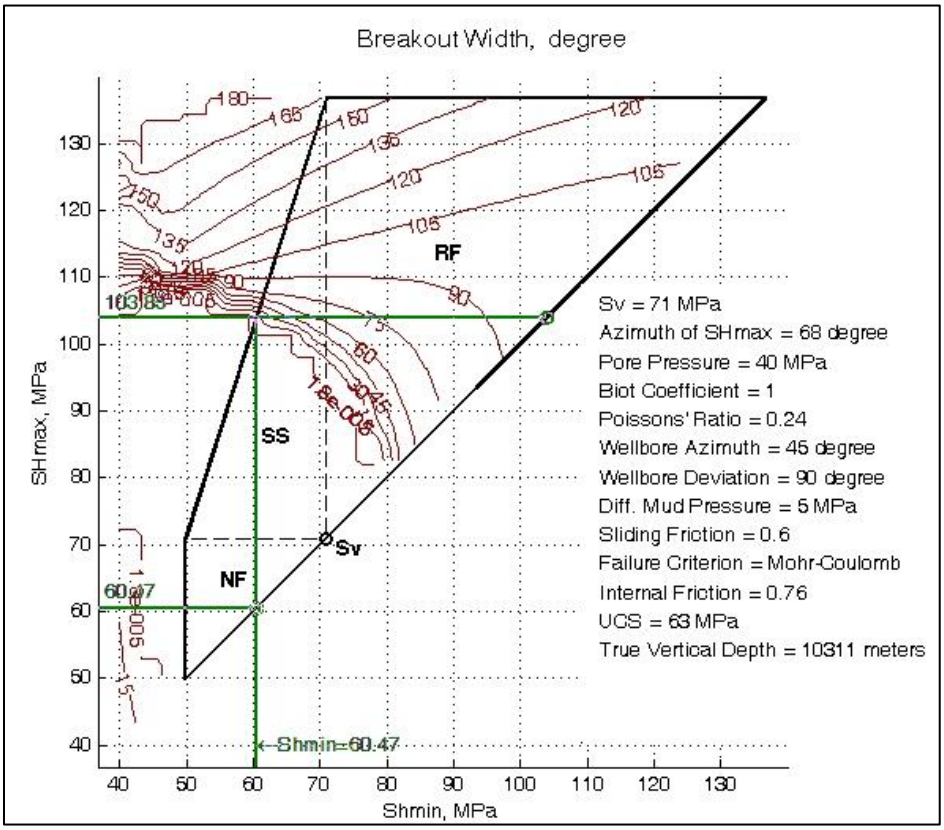

Figure 137 Stress polygon for initial reservoir condition.

The red contours (rock strength) in Figure 137 separate the permissible stress states based on breakout occurrences for a series of rock strengths. This study delineates that reservoir stress state (σ_{hmin} = 55Mpa and σ_{Hmax} = 60Mpa) lies below the reservoir rock compressive strength and in the normal fault zone. Figure 137 illustrates that for the presented range of rock strengths, red contours delimit that only strike-slip or reverse faulting stress regimes are probable which are even beyond the principal stresses of the reservoir.

Stress Analysis at the Wellbore Wall

Figures 138-141 depict the stress (Mpa) changes both at the borehole wall and a radius from the wellbore in the reservoir initial stress conditions in a vertical well in the MB. Figure 138 is radial stress, Figure 139 is tangential stress, Figure 140 is hoop stress and Figure 141 shows the stress variations at the borehole wall where the red and blue curves represent the maximum and minimum tensile stresses. It is found that tensile stress, the main source of tensile fractures, is lower than the critical stress (red line on top of the plot in Figure 141), thus there isn't any evidence of tensile fractures at the borehole wall.

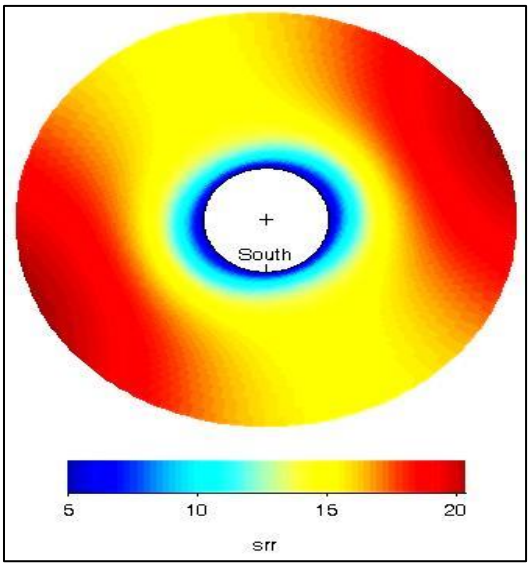

Figure 138 Radial stress (Mpa) around the borehole.

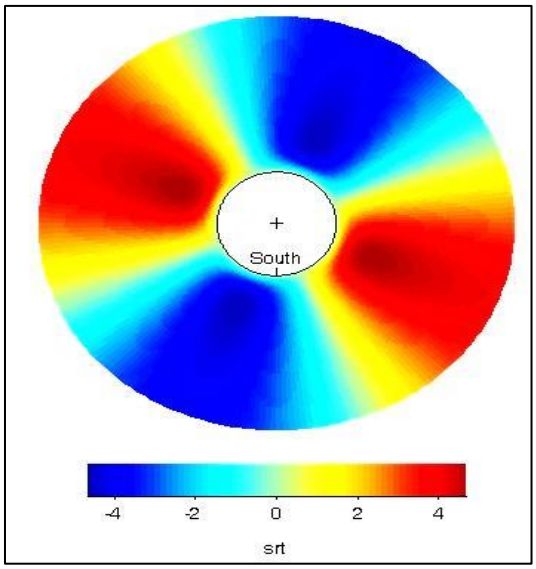

Figure 139 Tangential stress (Mpa) around the borehole.

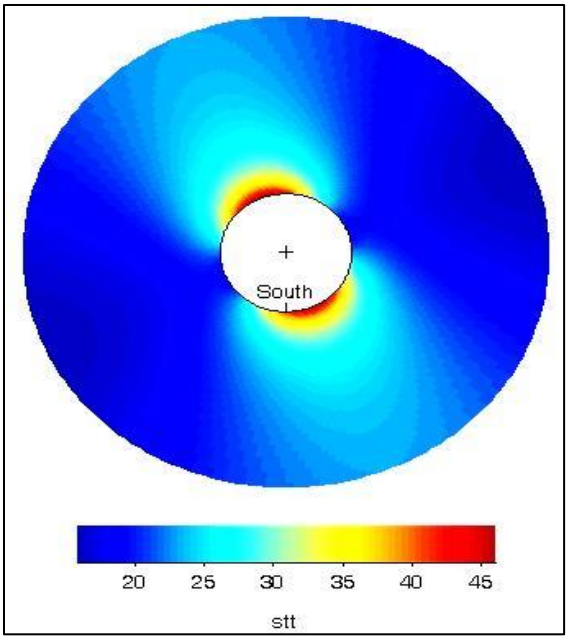

Figure 140 Hoop stress (Mpa) around the borehole.

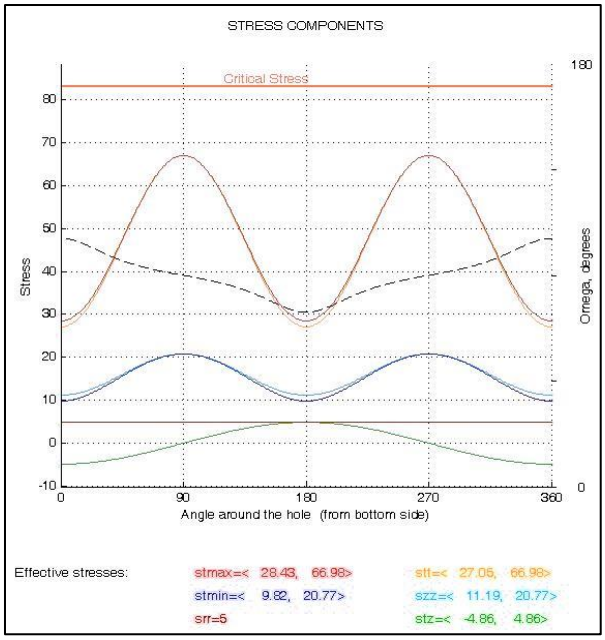

Figure 141 Circumferential Stresses (Mpa) variation at the borehole wall.

Figure 142 denotes the stress polygon after 5 years of production in the reservoir. The main characteristic of this plot is the noticeable shift of red contours –which represent a range of breakout width with respect to the rock strength– to the lower left part of the polygon. As a result, the rock strength in the new conditions mainly cover the possible strike slip (SS) and normal (N) fault area of the plygon. It can be deduced that the possibility of breakouts is more likely for lower rock strengths. This is concluded since reservoir stress (σ_{hmin}=58Mpaand σ_{Hmax}=58Mpa) exceeds the reservoir rock strength (red contours).

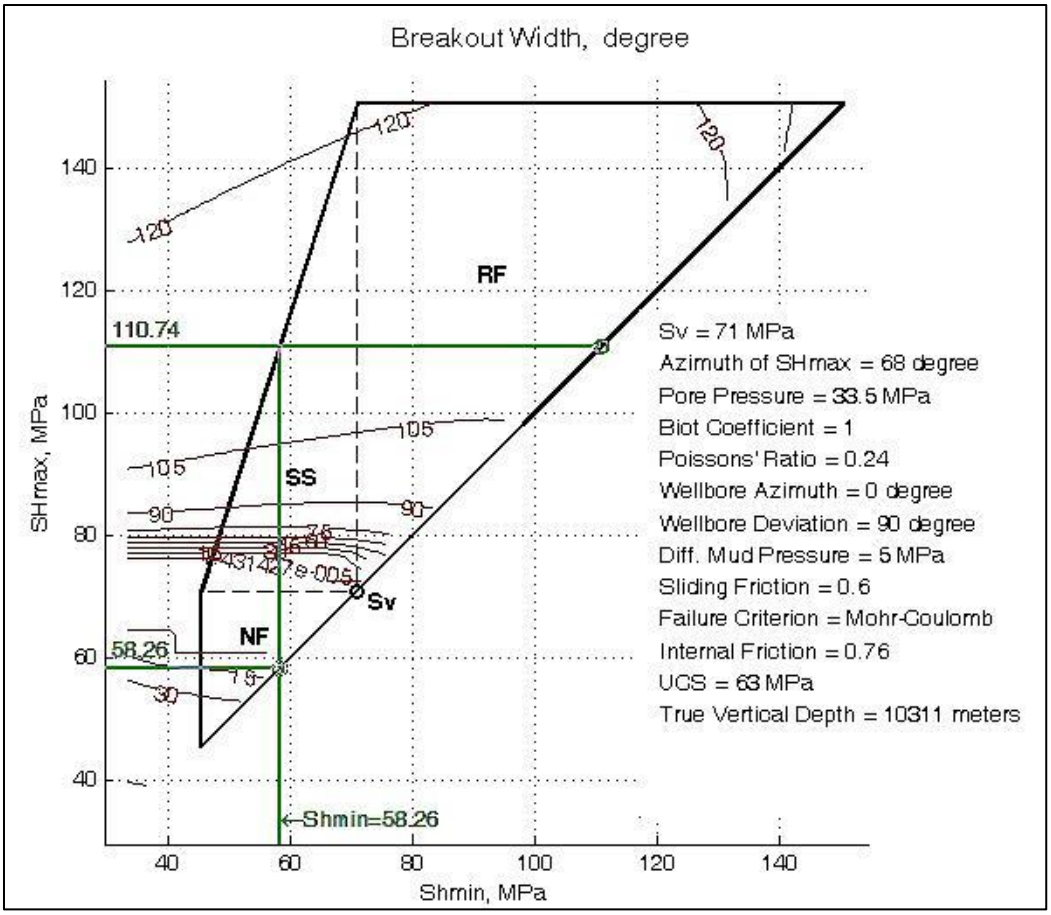

Figure 142 Stress polygon of the depth understudy after 5 years of production with a decrease in pore pressure.

Figures 143-146 depict the stress variations at the borehole wall and in a radius from the wellbore in a vertical well through MB when reservoir pressure is declined due to 5 years of production. Figure 143 is radial stress, Figure 144 is tangential stress, Figure 145 is hoop stress and Figure 146 represents the stress variations at the borehole wall. From Figure 146 it is realized that in new reservoir stress conditions the tensile stress (orange curve) exceeds the critical stress. This phenomenon shows a huge impact on the stability of the wellbore, resulting in failures such as shear or tensile fractures and breakouts. Considering the final outcome of the wellbore stress analysis after 5 years producing from the reservoir, it can be concluded that the detected fractures to study the orientation

of the maximum principal horizontal stress are tensile and occurring at the borehole wall or deeper in the formation. It should be noted that these fractures could exist due to the reservoir stress alteration after reservoir depletion.

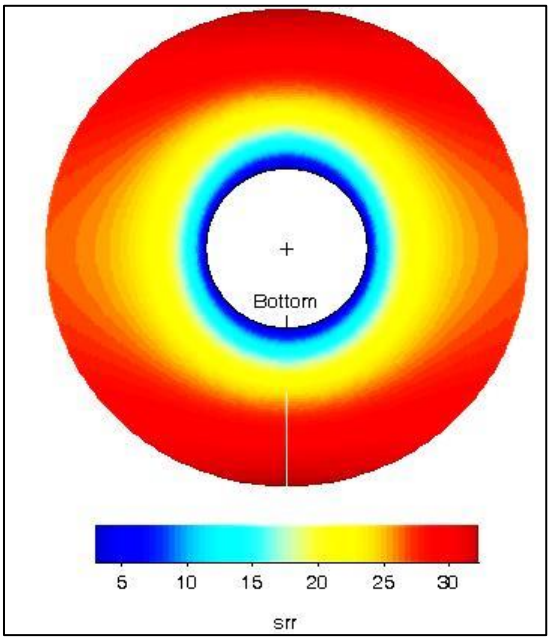

Figure 143 Radial stress (Mpa) around the borehole after production.

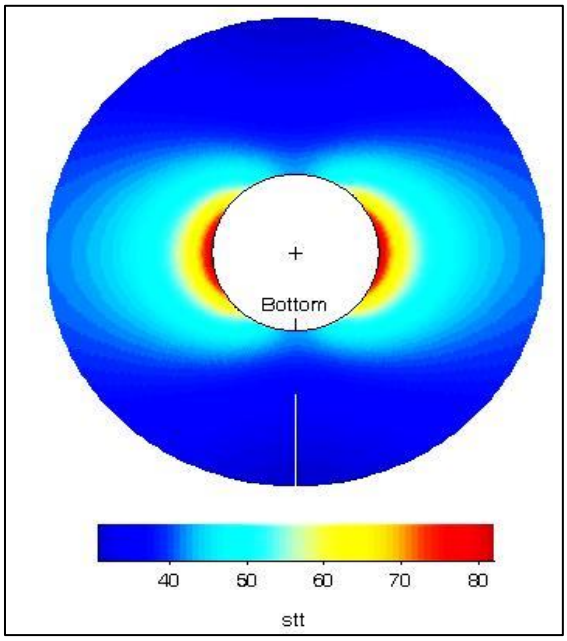

Figure 145 Hoop stress (Mpa) around the borehole after production.

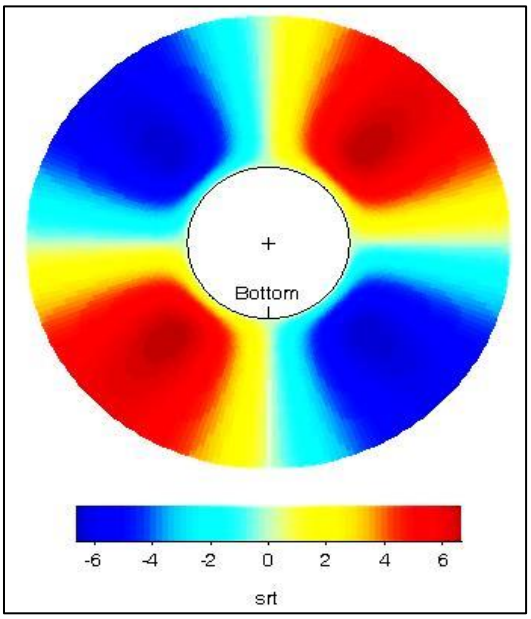

Figure 144 Tangential stress (Mpa) around the borehole after production.

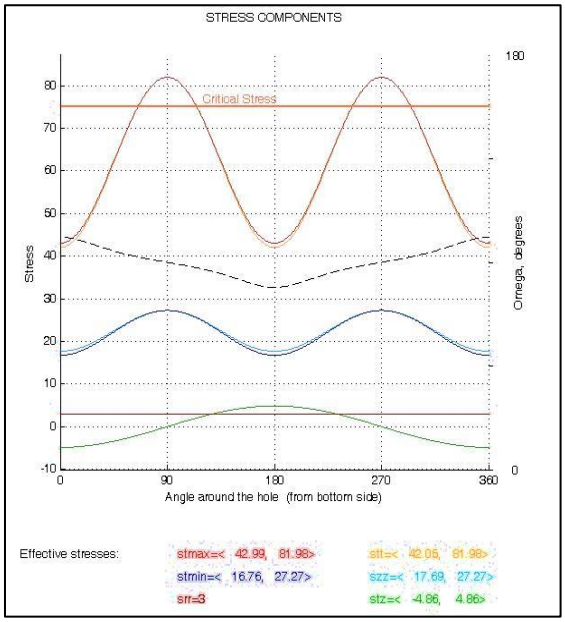

Figure 146 Circumferential stress (Mpa) variation at the borehole wall

Stability Plots

The following figures represents the stability status of the wellbore at the specific depth of 10311ft- the horizontal section of the well in the reservoir- created under Mohr-Coulomb failure criterion assumptions. Comparing Figure 147, stability plot for the initial reservoir stress conditions and Figure 148, the stability plot after 5 years of production, it indicates that shear failures are possible in the depleted reservoir stress state. Producing from the reservoir which causes pore pressure reduction will result in breakouts or non-radial shear failure planes under specific mud weight and rock compressive strength. The black circle denotes the reservoir stress conditions and the red counters are indicating the breakouts.

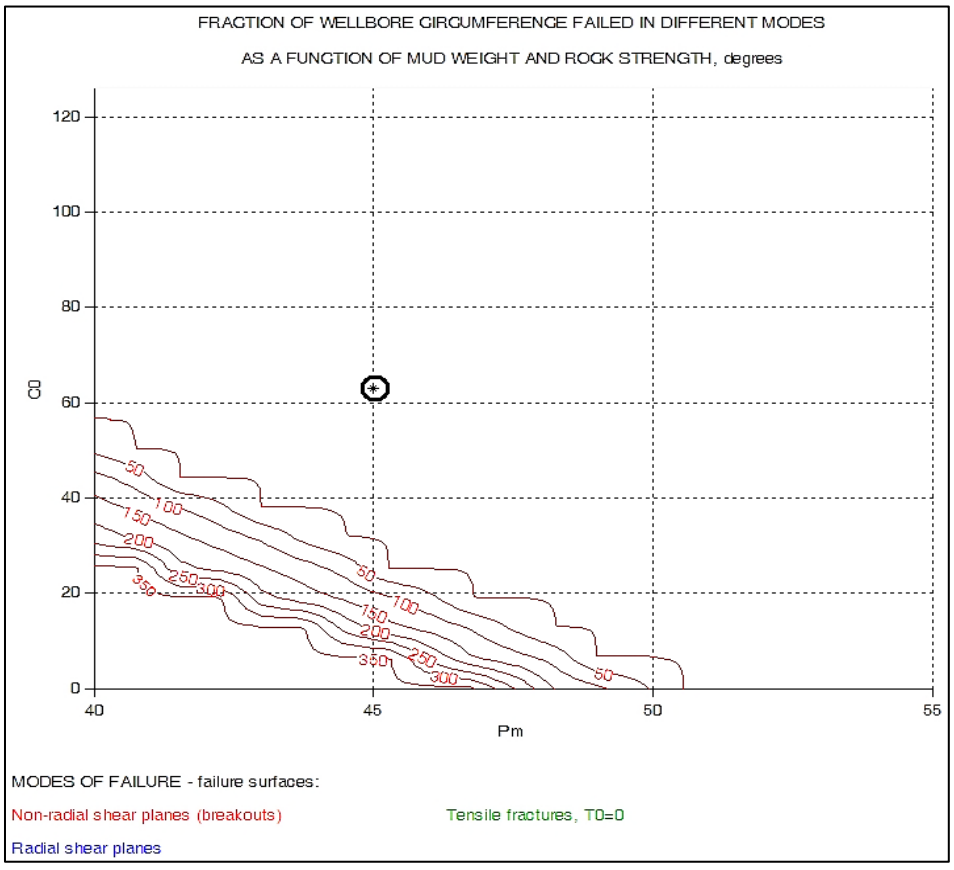

Figure 147 Fraction of wellbore circumference mode as a function of mud weight and compressive strength of initial reservoir condition. Circle indicates reservoir stress conditions.

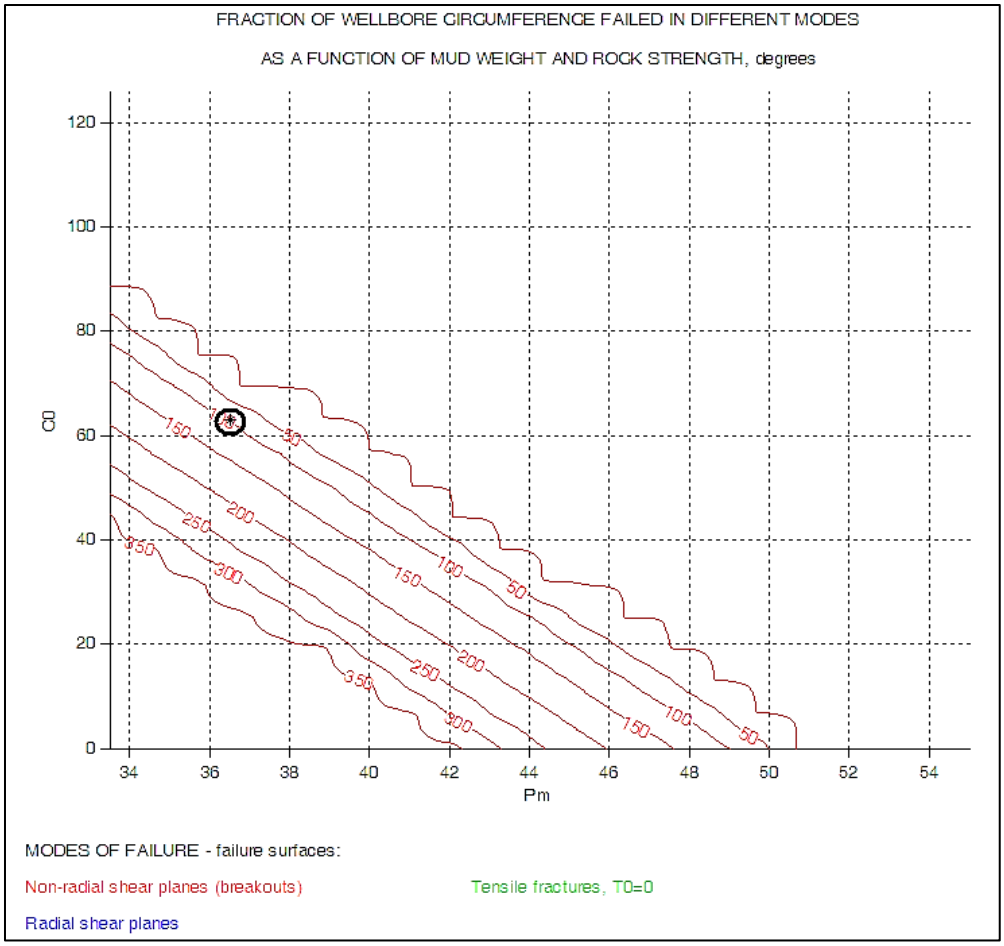

Figure 148 Fraction of wellbore circumference failed in difference mode as a function of mud weight and compressive strength after 5 years of production. Circle indicates reservoir stress conditions.

Chemo-thermo-poro-elasticity

In this section besides the anisotropic properties of shale, other major physical, chemical, thermal and poro-elastic parameters of shale that have influence on the wellbore stability are included in the geomechanical modeling The simulation is performed in a vertical well through the Upper Bakken. Since shale properties are responsible for the main instability problems, the pure shaly member of the Bakken Formation was chosen for this study.

The mechanical input parameters of the Upper Bakken, such as Young's modulus, Poisson's ratio, shear modulus, vertical stress and the principal horizontal stresses are the same as those input earlier in the 3-D geomechanical modeling.

Other shale properties were input in the model from literature, listed in the following table, (Zhang, et. al., 2003, Domenico and Schwartz, 1997, Havens, 2012):

Table 14 Chemical, thermal and poroelastic parameters input for modeling.

	B	**PR_{ud}**	**K**	**a_{wm}**	**a_{wsh}**	**I_m**	**T**	**V**	**α**
UB	0.9	0.3	1 µD	0.78	0.7	10%	200F°	0.018	0.9

B is Skempton coefficient (dimensionless) and is defined to be the ratio of the induced pore pressure to the change of stress applied under undrained (no fluid is allowed to move into or out of the control volume) conditions. PR_{ud} is undrained Poisson's ratio, *K* is permeability, a_{wm} is chemical activity of the mud (dimensionless), a_{wsh} is chemical activity of the pore fluid (dimensionless), I_m is the membrane efficiency (dimensionless), *T* is formation temperature (F°), *V* is partial mole volume of water and α is Biot's coefficient. Biot coefficient is defined (Biot and Willis, 1957) as: $\alpha = 1 - \frac{K}{K_m}$, (*K* is dry rock bulk modulus and K_m is pure matrix compressibility).

The arrows in the following figures represent the direction of the maximum horizontal principal stress that was found earlier to be N65E.

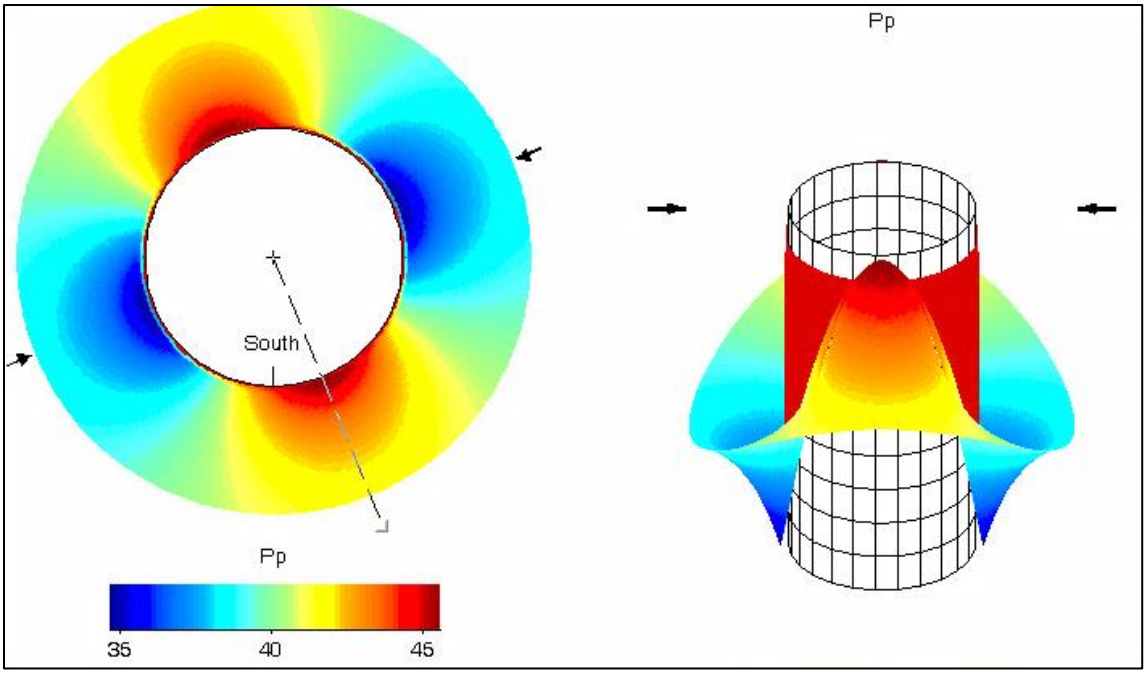

Figure 149 Pore pressure variation around the borehole.

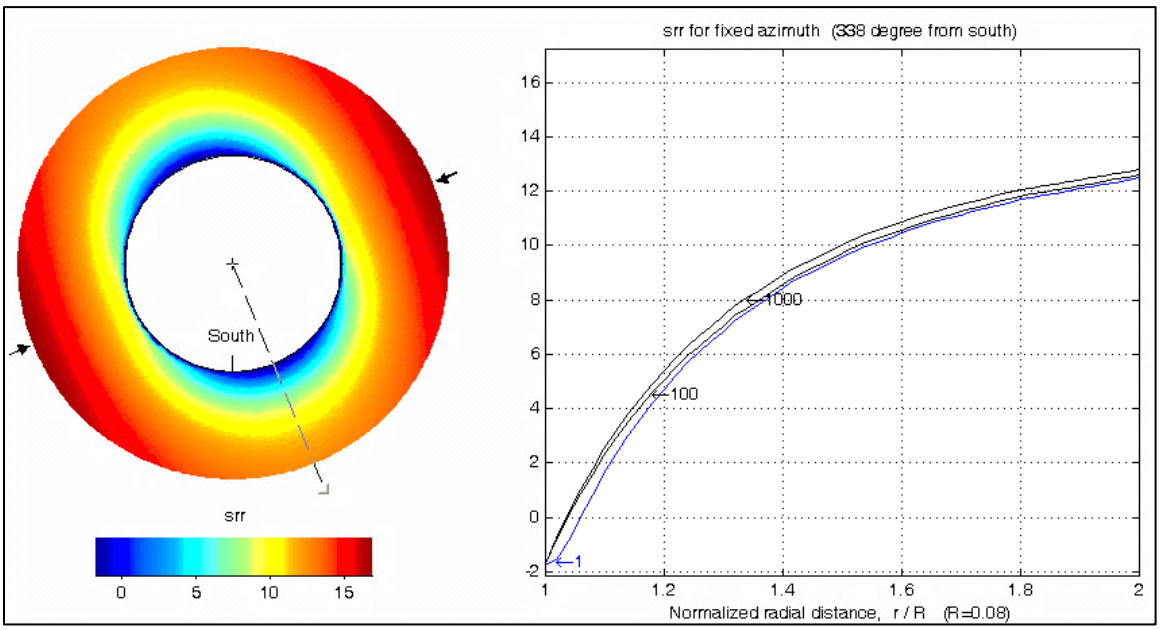

Figure 150 Left) Radial Stress around the borehole. Right) Radial stress variation in the direction of σ_{hmin} in radii from the wellbore.

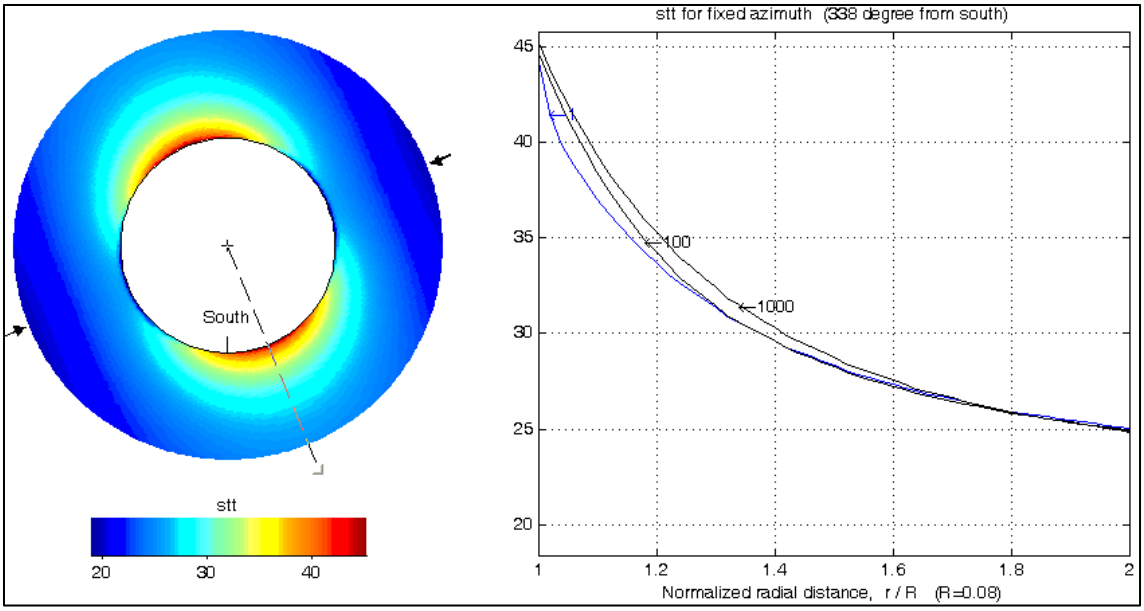

Figure 151 Left) Hoop Stress around the borehole. Right) Hoop stress variation in the direction of σ_{hmin} in radii from the borehole.

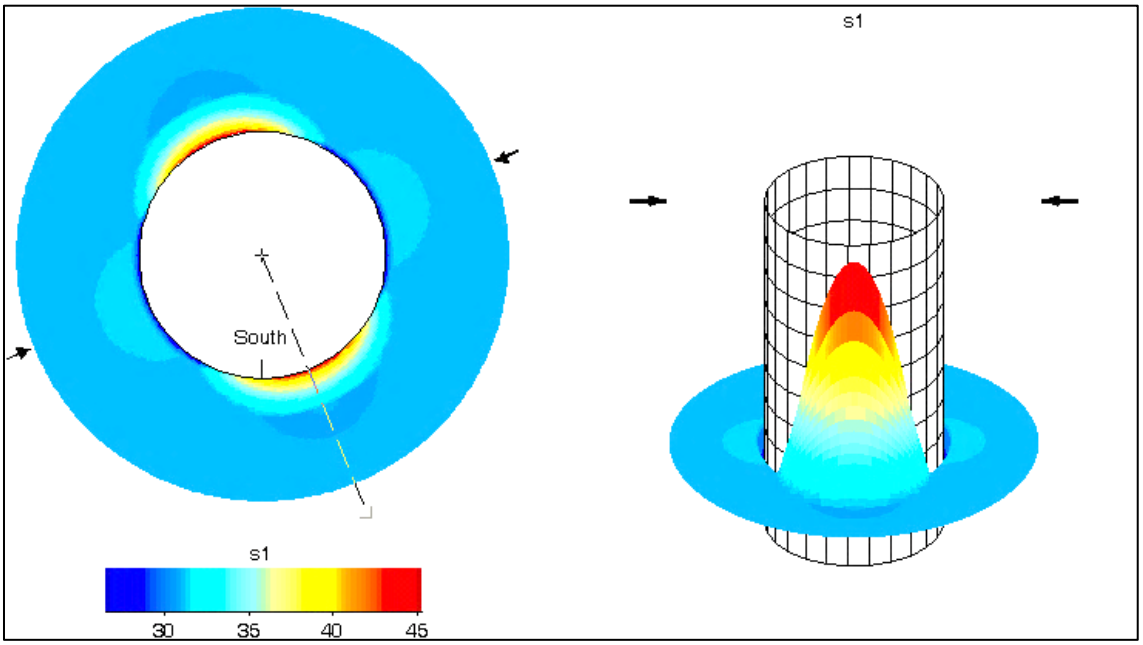

Figure 152 Maximum principal horizontal stress around the borehole

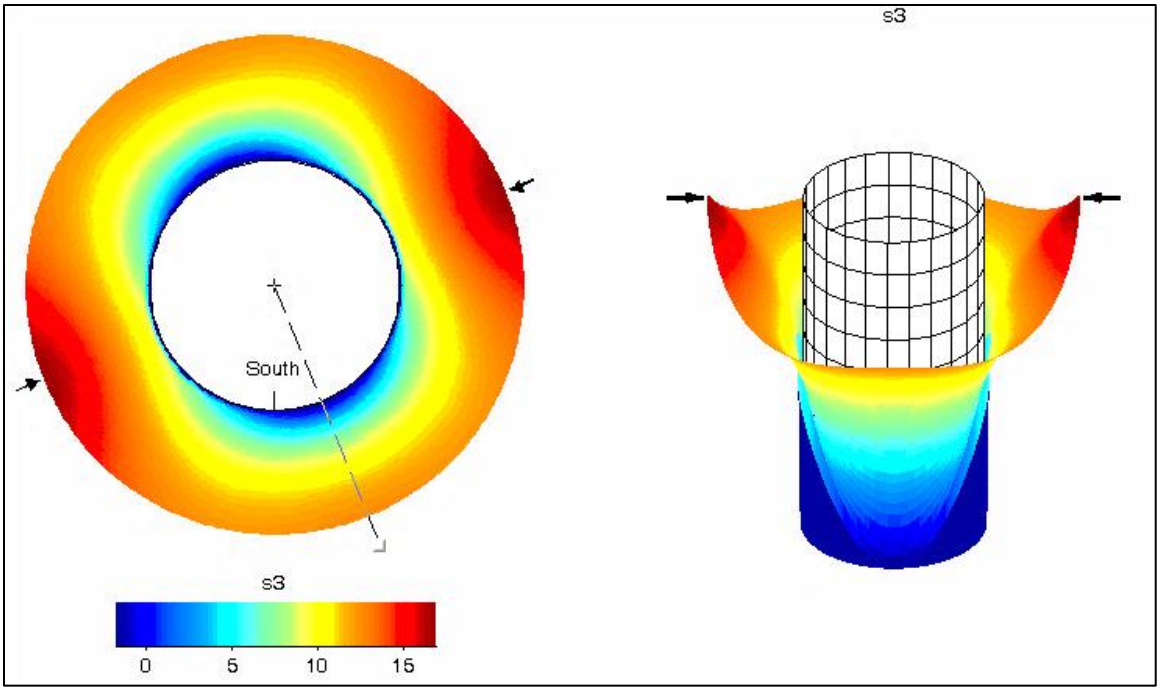

Figure 153 Minimum principal horizontal stress around the borehole.

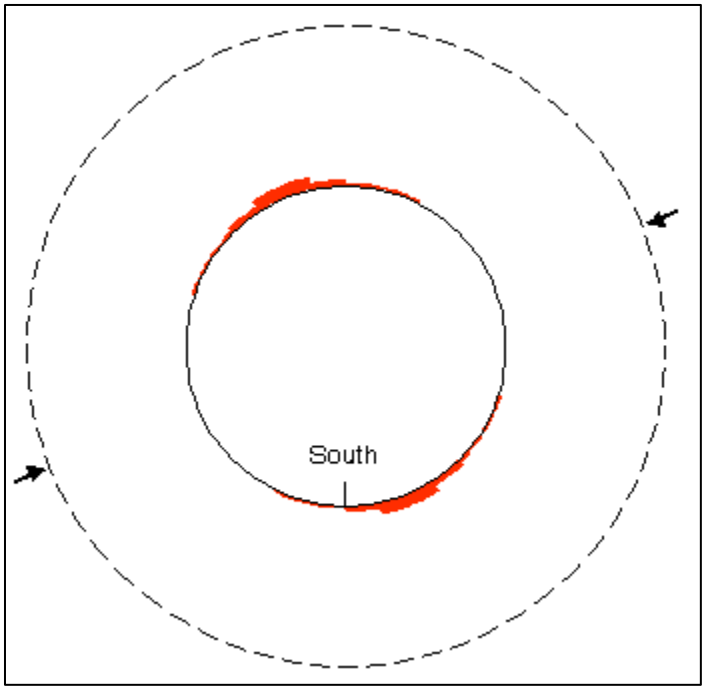

Figure 154 Failure (break outs) occurrence around the borehole.

The previous figures describe how stresses vary around and in a distance from the borehole wall. The latest modeling results explain how including chemical, thermal and poro-elastic properties of the shale can cause a minor set of shear failure planes in the form of breakouts around the borehole in the Upper Bakken. The orientation of the breakouts is parallel to the direction of minimum principal horizontal stress.

Summary

The anisotropic Mechanical Earth Model (MEM) for the Bakken Formation was generated. This task was performed by calculating the elastic parameters and the effective stresses in three different members of the Bakken Formation. These parameters were generated by running an advanced sonic log in a well in North Dakota. The dynamic elastic moduli –Young's modulus and Poisson's ratio – were converted to static ones through empirical correlations. These values were calculated under isotropic and anisotropic formulae. It was found that UB and LB are highly VTI with $E_{horiz} > E_{vert}$ and $\nu_{vert} > \nu_{horiz}$. Although MB is assumed to follow mechanical isotropy in most portions of the interval, in some sections it shows $E_{vert} > E_{horiz}$ and $\nu_{horiz} > \nu_{vert}$. This warrants the HTI behavior of this portion which is related to the presence of vertical fractures. The existence of the vertical fractures was also proven by core inspection.

In-situ stress and pore pressure profiles were generated under isotropic and anisotropic conditions. It was well understood that UB-LB is highly overpressured due to the kerogen to hydrocarbon transformation in low porosity-permeability shales. The Middle Bakken was found to be less overpressured due to the migration of hydrocarbon from UB and LB into the middle member. In addition, anisotropic stress model was found to better describe the stress conditions in the layers.

Geomechanical (numerical) modeling was performed under isotropic and anisotropic conditions in three main steps to evaluate the deformations and horizontal stress variations around the borehole. In the final step, the Mohr-Coulomb failure criterion was applied to the models and it was perceived that in anisotropic models for UB, the formation will undergo a shear failure followed by an elastic behavior in comparison to the isotropic models. Anisotropic approximations will highly improve the geomechanical modeling results and better represent the true behavior of the Bakken Formation.

A full geomechanical modeling and stress variation analysis was performed in a horizontal well in the Middle Bakken. This procedure includes stress polygons and stability plots generation to study the possibility of future faulting or breakouts in the study area. Results confirmed the possibility of wellbore failure in the form of non-radial shear failures, also known as breakouts, after 5 years of production due to the reduction in reservoir pore pressure. Initial reservoir pressure was measured through DST and current pore pressure was predicted by reservoir simulation and history matching. In addition, the stress polygons describe a shift from the possibility of reverse faulting stress conditions in the area towards the strike slip and normal faulting after 5 years of production. This explains that in order to prevent future natural hazards, reservoir pressure should be maintained by injection.

A new approach to estimate the magnitude of anisotropic maximum horizontal principal stress was utilized. The magnitude of maximum principal horizontal stress was found through measurement of three shear moduli of the formation and calculating the acousto-elastic parameter of the formation. The direction of maximum principal horizontal stress was found to be ~N65E from the direction of the fast shear azimuth (FSA). The direction

of the fast shear azimuth was obtained by analyzing existing fractures around the borehole that have caused shear anisotropy more than 20%. These fractures were found to be tensile from further stress and stability studies.

Finally, stress analysis including all shale's physical, chemical, thermal and elastic parameters as well as anisotropy was carried out to understand formation failures and breakouts around the wellbore. The latest study shows the failure is minor and closer to the reality when all these properties are included in geomechanical modeling.

Chapter V

CONCLUSIONS AND FUTURE WORK

Summary and Conclusions

Field data from several wells in three producing fields, Sanish, Manitou and Forthun, in Williston Basin, ND have been acquired by the Sonic Scanner log. The data were analyzed in order to better understand the geophysical and geomechanical properties of the Bakken Formation which is the major producing reservoir in Williston Basin. It was found that the Bakken Formation thickness is about 100ft and is deeper in the middle of the basin, Sanish field, and gets thinner to the margins in the Forthun field. The Bakken Formation is comprised of two shaly members, upper and lower, and the middle clastic-carbonate. The Upper and Lower Bakken shales have similar physical characteristics and show very high gamma ray responses. These two units have lower compressional and shear wave velocity, density, elastic properties and are highly anisotropic, whereas the middle member represents higher values for compressional and shear wave velocities, density and is slightly anisotropic where natural fractures exist.

The Nesson anticline –the major geologic feature in the North Dakota part of the Williston Basin– has caused vertical fractures in the Bakken Formation. The presence of this geological structure has caused higher mobility in the middle member along with slight HTI behavior and slight orthorhombic isotropy in the Upper and Lower Bakken

Formation. These conclusions were drawn by acquiring advanced sonic log measurements in the field. The measurements let the study of elastic stiffness parameters and the anisotropy type of the Bakken Formation possible. The analysis of three independent shear moduli along with Thomsen (1986) anisotropy parameters indicated the presence of natural fractures in the well drilled on top of the Nesson anticline within the Middle Bakken. These fractures extend into the upper and lower shale members. Fluid mobility and shear anisotropy should be investigated for the petrophysical aspects to find a higher quality reservoir in the Middle Bakken. This task was carried out by creating and analyzing dispersion plot and radial slowness variation profiles. It is always useful to predict anisotropy parameters from each other when one is missing. Therefore a mathematical correlation to estimate epsilon and gamma from one another for transverse isotropic upper and lower members was developed.

Anisotropic Mechanical Earth Model (MEM) of the Bakken Formation as a major contribution to the Bakken geomechanical studies was generated. Anisotropic and isotropic elastic parameters and the effective stresses in the three different members of the Bakken Formation were evaluated. Effective stress prediction is important for accurate geomechanical modeling. Regarding the anisotropic elastic moduli of the Bakken, Young's modulus and Poisson's ratio signifies that UB and LB are highly VTI with the horizontal Young's modulus greater than the vertical Young's modulus and vertical Poisson's ratio greater than the horizontal Poisson's ratio. The anisotropic elastic moduli were input in poro-elasticity relations to calculate horizontal principal stresses. The results were highly improved when anisotropy is included. Pore pressure study shows that UB-LB are highly overpressured due to the kerogen to hydrocarbon

transformation in low porosity-permeability shales. The Middle Bakken was found to be less overpressured due to the migration of hydrocarbon from UB and LB into this member. The final step was to numerically model the geomechanical response of the Bakken Formation under isotropic and anisotropic assumptions in and around the wellbore. The models include vertical, inclined and horizontal wells and confirmed that higher deviation angles (lower attack angles) reflect major instability problems around the borehole with severe development of plastic regions around the borehole. Displacement around the borehole decreases by increasing the well deviation angle from vertical to horizontal. In addition, it was concluded that using anisotropic assumptions to predict geomechanical behavior of the Bakken Formation better represents the formation response.

It is crucial to understand how producing from the formation that leads to reservoir depletion may cause geologic hazards in a larger scale in the basin. For this study, stress polygons and stability plots before and after 5 years of production were created. It was concluded that future faulting or breakouts around the borehole are highly probable. The final section of this thesis was to model stresses at the borehole wall in the upper member in a vertical well including all chemical, thermal and poro-elastic properties of the shale. It was understood that a minor set of shear failures in the form of breakouts are probable in the direction of minimum horizontal principal stress.

Future Work and Recommendations

To perform more accurate seismic anisotropy and geomechanical modeling it is highly recommended to run laboratory experiments on the Bakken preserved samples to validate the results. Compressional and shear wave velocity anisotropy versus confining pressure

on the Bakken samples can be a good technique to study the anisotropic nature of the shale members. In addition, it is useful to increase pore pressure and see how the results may affected in different reservoir pressures. Biot's coefficient is an important parameter for poro-elastic geomechanical modeling and stress magnitude determination. It is highly recommended to measure the Biot's coefficient both on shale and clastic-carbonate samples to improve the results. Elastic parameters, such as Poisson's ratio, Young's modulus and shear modulus in vertical and horizontal directions are useful when measured in the lab on fresh samples under destructive methods. They can have a very significant contribution to better characterize the geomechanical models. To continue this work, we need to understand how anisotropy parameters can be a fucnction of with the TOC and kerogen content of the shale; hence geochemical analysis seems inevitable. Although using X-ray diffraction (XRD) and X-ray fluorescence (XRF) methods to understand anisotropy of the formation is highly challenging, these tests can be constructive in expanding our knowledge regarding the chemical and elemental composition of the Bakken Formation and how they affect the anisotropy of the samples. If field data was available, this study could be extended to other regions in the Williston basin. Although image logs are not usually available in the area, analyzing this type of data gives us better evidence on accuracy of the geomechanical models and will improve the instability results for future studies. Finally, it would be highly beneficial to run geomechanical models under different failure criterions than Mohr-Coulomb and compare the results.

REFERENCES

Aadnoy, B. S., and M. E. Chenevert, 1987, Stability of highly inclined boreholes, SPE Drilling Engineering, 12: 264-374.

Alford, R., 1986, Shear data in the presence of azimuthal anisotropy: Dilley, Texas presented at the 56th SEG annual meeting, Houston, 2-6 November, expanded abstracts.

Amadei, B. W. Savage and H. Swolfs, 1987, Gravitational stresses in anisotropic rock masses. Int. J Rock Mech. and Mining sc. and Geomech. Abstracts, 24:1, 5-14.

Anderson, E. M., 1951, The dynamics of faulting and dyke formation with applications to Britain. Edinburgh: Oliver and Boyd.

Armstrong, P., D. Ireson, B. Chmela, K. Dodds, C. Esmersoy, D. Miller, B. Hornby, Sayers, C., Schoenberg, M., S. Leaney and H. Lynn, 1994, The promise of elastic anisotropy, Oilfield Review, vol. 6, no. 4, 36 -47

Arroyo Franco, J. L., M. A. Mercado Ortiz, G. S. De, L. Renlie, and S. Williams, 2006, Sonic investigation in and around the borehole, Oilfield Review, vol. 18, no. 1, 14-31.

Biot, M. A. and D. G. Willis, 1957, The elastic coefficient of the theory of consolidation, J. Appl. Mech., 24, 594-601.

Bowers, G., 1995, Pore pressure estimation from velocity data: Accounting for overpressure mechanisms besides undercompaction. J SPE Drilling and Compl.,10:2, 89-95.

Bradley, W. B., 1979, Failure of inclined boreholes, J. of Energy Resources Technology, Vol. 101: 232-239.

Brie, A., D. Johnson, and F. Pampuri, 1998, Quantitative formation permeability evaluation from Stoneley waves, SPE49131, ATCE, New Orleans, September 27-30.

Burridge, R., and B. Sinha, 1996, inversion for formation shear modulus and radial depth of investigation using borehole flexural waves, SEG, 66th annual meeting, expanded abstract.

Castagna, J. P., M. L. Batzle, and R. L. Eastwood, 1985, Relationships between compressional-wave and shear-wave velocities in silicate rocks: Geophysics, 50, 571–581.

Chang, C., M. Zoback and A. Khaksar, 2006, Empirical relations between rock strength and physical properties in sedimentary rocks, J. Pet. Sc. and Eng., 51, 223-237.

Charlez, P. A., 1997, Rock Mechanics. Vol 2: Petroleum Applications. Editions Technip.

Cheadle, S. P., J. Brown, and D. C. Lawton, 1991, Orthorhombic anisotropy: A physical seismic modeling study: Geophysics, 56, 1603-1613.

Close, D., D. Cho, F. Horn, and H. Edmundson, 2009, The sound of sonic: A historical perspective and introduction to acoustic logging, CSEG Recorder, May, 35-43.

Domenico, P. and F. W. Schwartz, 1997, Physical and Chemical Hydrogeology, 2nd Edition, John Wiley and sons, Inc.

Durham, L. S., 2009, Experience paid off at Parshall: AAPG Explorer, http://www.aapg.org/explorer/2009/06jun/johnson0609.cfm, accessed 20 December.

Duseault, M. B., 1994. Analysis of borehole stability. Computer Methods and Advances in Geomechanics Belkema: 125-137.

Eaton. B., 1972, Graphical method predicts geopressures world wide. World Oil, 182, 51-56.

EIA, 2010, Shale Gas Plays/Lower 48 States.

EIA, 2011, Review of Energy Recourses: U.S. shale gas and shale oil plays.

Esmersoy, C., A. Boyd, M. Kane, and S. Denoo, 1995, Fracture and stress evaluation using dipole shear anisotropy logs, SPWLA 36th annual logging symposium.

Esmersoy, C., K. Koster, M. Williams, A. Boyd and M. Kane, Dipole shear anisotropy logging, in: 64th Annual Internat. Meet., Soc. Expl. Geophys., 1994, pp. 1139–1142.

Fairhurst, C., 1968. Methods of Determining In Situ Rock Stress at Great Depth, TR1- 68 Missouri River Div. Corps of Engineering.

Fam, M. A., M. B. Dusseault, and J. C. Fooks, 2003, Drilling in mudrocks: rock behavior issues, J. of Petroleum Science and Engineering, 38: 155-166.

Fertl, W., 1981, Openhole Crossplot Concepts -A Powerful Technique in Well Log Analysis, March, SPE of AIME.

Fjaer, A., R. Holt, A. Raaen, R. Risnes and P. Horsud, 1992, Petroleum related rock mechanics, Elsevier Publishing.

Gnirk, P. F., 1972. The mechanical behavior of the uncased wellbores situated in elastic/plastic media under hydrostatic stress. SPEJ, Feb. p. 45-59.

Grover, P. W., 1996, Stratigraphy and diagenesis of the Mississippian Bakken Shale-Lodgepole Limestone sequence, Williston Basin, North Dakota: Ph.D. thesis, Texas A&M University.

Gutierz, M., N. Braunsdor and B. Couzens, 2006, Calibration and ranking of pore pressure prediction models. TLE December, 1516-1523.

Haldorsen, J., D. Johnson, T. Plona, , B. Sinha, H. Valero, , and K. Winkler, 2006, Borehole acoustic waves, Oilfield review, 18 (1), 34-43.

Hale, A. H., Mody, F. K. and D. P. Salisbury, 1992, Experimental Investigation of the Influence of Chemical Potential on Wellbore Stability", IADC/SPE Paper 23885, presented at the 1992 IADC/SPE Drilling Conference in New Orleans, Louisiana, Feb. 18-21,.

Havens, J., 2012, Mechanical properties of the Bakken Formation, M.S. Thesis, Colorado School of Mines.

Hayes, M. D., 1984, Conodonts of the Bakken Formation (Devonian and Mississippian), Williston Basin, North Dakota: M.S. thesis, University of North Dakota.

Higgings, S., S. Goodwin, Q. Donald, A. Donald, T. Bratton, and G. Tracy, 2008, Anisotropic stress models improve completion design in the Baxter shale, In Proceedings of SPE ATCE, Denver, 21-24 September, SPE 115736.

Hornby, B. E., 1998, Experimental laboratory determination of the dynamic elastic properties of wet, drained shales,:J Geophys Res, 103(B12)

Hornby, B. E., 1994, The elastic properties of shales: PhD thesis, University of Cambridge.

Horsud, P., 2001' Estimating mechanical properties of shales from empirical correlations. J. SPE Drilling and Compl., 68-73, SPE 56017.

Hubbert, M. K. and D. G. Willis, , 1957, Mechanics of hydraulic fracturing. Transactions of American Institute of Mining Engineering, 210, 153-168.

Jaeger, J. C., and N. W. G. Cook, 1979, Fundamentals of rock mechanics, 3rd ed.: Chapman & Hall.

Johnston, J. E., and N. I. Christensen, 1995, Seismic anisotropy of shales: J. Geophys. Res., 100, 5991–6003.

Karasinski D. R., 2006, Sedimentology and hydrocarbon potential of the Devonian Three Forks and Mississippian Bakken Formations, Sinclair Area, southeast Saskatchewan-southweat Manitoba: M.S. thesis, University of Manitoba (Canada).

Kimball, C. V., and T. L. Marzetta, 1984, Semblance processing of borehole acoustic array data, Geophysics, 49, 274–281.

Leaney, W. S., C. M. Sayers, and D. E. Miller, 1999, Analysis of multi-azimuthal VSP for anisotropy and AVO, Geophysics, 64, 1172-1180.

LeFever, J. A., 2008, Isopach of the Bakken Formation: North Dakota Geological Survey Geologic Investigations 59, Bakken Formation map series, scale 1:1,000,000.

LeFever, J. A., C. D. Martiniuk, E. F. R. Dancsok, and P. A. Mahnic, 1991, Petroleum potential of the middle member, Bakken Formation, Williston Basin, in J. E.

Lekhnitskii, S., 1981. Theory of elasticity of an anisotropic body. Moscow: Mir Publishers.

Li, X., Cui, L. and J. C. Rogegiers, 1998, Thermoporoelastic analyses of inclined borehole. SPE/ISRM, Eurock 98, Norway.

Maury, V., 1994, Rock failure mechanisms identification: a key for wellbore stability and reservoir behavior problem, SPE 28049 presented at the SPE/ISRM Rock Mechanics in Petroleum Engineering Conference held in Delft, The Netherlands, 29-31 August.

Mavko, G., Mukerji, T., and J. Dvorkin, 1998, The rock physics handbook, tools for seismic analysis in porous media: Cambridge University press, New York, 329 p.

McLean, M. R., 1987, Wellbore Stability Analysis. PhD Thesis, University of London. LTK.

Millitzer, H. and R. Stoll, 1973, EinigeBeitrageder geophysics zurprimadatenerfassungimbergbau, Neue Bergbautecknik, Lipzig 3, 21-25.

Mody, F. K. and A. H. Hale, 1993, A borehole stability model to coupled the mechanics and chemistry of drilling fluid shale interaction. 10th SPE Drilling Conference. Amsterdam.

Mouchet, J. and A. Mitchell, 1989, Abnormal pressure while drilling. Elf Acquitane Manuels Techniques 2, Boussens, France.

Mukerji, T., and M. Prasad, 2004, Analysis of microstructural textures and wave propagation characteristics in shales, http://www.osti.gov/bridge/servlets/purl/89053-yafcdC/890503.pdf, accessed 9 February 2010.

Mukerji, T., and M. Prasad, 2007, Image processing of acoustic microscopy data to estimate textural scales and anisotropy in shales: Acoustical Imaging, 28, 21 29.

Mueller, M. C., 1992, Using shear waves to predict lateral variability in vertical fracture intensity: The Leading Edge, 11, No. 2, 29-35.

Nordeng, S., 2010, A brief history of oil production from the Bakken formation in the Williston Basin: NDGS Newsletter, 37, 5-9.

Norris, A., and B. K. Sinha, 1993, weak elastic anisotropy and the tube wave, Geophysics, 58, 1091-1098.

Nye, J. F., 1985, Physical properties of crystals, Oxford University Press.

Odunlami, T., H. Soroush, P. Kalathingal and J. Somerville, 2011, Log based rock property evaluation - A new capability in a specialized log data management platform. In Proceedings SPE/DGS Saudi Arabia Technical symposium and Exhibition, Al khobar, 15-18 May, SPE 149050.

Okland, D. and J. M. Cook, 1998, Bedding Related Borehole Instability in High-Angle Wells", SPE 47285 presented at SPE/ISRM Conference on Rock Mechanics in Petroleum Engineering, Eurock' 98, Trondheim, Norway 7-10 July.

Ong, S. H. and J. C. Roegiers, 1993, Influence of anisotropies in borehole stability, Int. J. Rock Mech. Min. Sci. & Geomech. Abstr. Vol. 30.7: 1069-1075.

Papamichos, E. and I. Vardoulakis, 1995. Shear band formation in sand according to non-coaxial plasticity model. Geotechnique, 45(5): 649-661.

Pistre, V., T. Kinoshita, T. Endo, K. Schilling, J. Pabon, B. Sinha, T. Plona, T. Ikegamiand D. Johnson, 2005, A New modular wireline logging sonic tool for measurement of 3D (Azimuthal, radial and Axial) formation acoustic properties, In Proceedings of SPWLA 46th annual logging symposium, New Orleans, June 26-29.

Pitman, J., Price, L. and J. LeFever, 2001, Diagenesis and fracture development in Bakken Fm., Williston Basin: Implications for reservoir quality in the middle member, US Geological Survey professional paper, 1653.

Plona, T., Kane, M., B. Sinha, J. Walsh, and O. Viloria, 2000, Using acoustic anisotropy, SPWLA 41th annual logging symposium, June 4-7.

Plona, T., B. Sinha, M. Kane, R. Shenoy, S. Bose, J. Walsh, T. Endo, T. Ikegami, and O. Skelton, 2002, Mechanical damage detection and anisotropy evaluation using dipole sonic dispersion analysis, SPWLA 43th annual logging symposium, June 2-5.

Plumb, R. A., S. Edwards, G. Pidcock, D. Lee and B. Stace, 2000, The mechanical earth model and its application to high risk well construction projects. In Proceedings of IADC/SPE Drilling Conference, New Orleans, 23-25 February, IADC/SPE 59128.

Plumb, R., 1994. Influence of composition and texture on the failure properties of clastic rocks. In Proceeding Eurock SPE/ISRM Rock Mechanics in Petroleum Engineering Conference, Delft, 29-31 August, SPE 28022.

Plumb, R.A., P. Hooyman, D. Vineengen, N. Dutta, G. Ritchie and K. Bennaceur, 2004, A new geomechanics process reduces operational risks from exploration to production. In proceedings of the NARMS, Houston, 5-9 June, ARMA/NARMS 04-616.

Pollastro, R. M., T. M. Cook, L. N. R. Robert, C. J. Schenk, M. J. Lewan, L. O. Anna, S. B. Gaswirth, P. G. Lillis, T. R. Klett, and R. R. Charpentier, 2008, Assessment of undiscovered oil resources in the Devonian-Mississippian Bakken Formation, Williston Basin Province, Montana and North Dakota, 2008: U.S. Geological Survey Fact Sheet 2008-3021, http://pubs.usgs.gov/fs/2008/3021/, accessed 12 July 2008.

Prasad, M., and T. Mukerji, 2003, Analysis of Microstructural textures and wave propagation characteristics in shales: 73th Annual International Meeting, SEG, Expanded Abstracts, 1648-1651.

Price, L. and J. LeFever, 1994, Dysfunctionalism in Williston Basin: The Mid-Madison/Bakken petroleum system, Bulletin of Canadian Petroleum Geology, 42, 187-218.

Roegiers, J. C. and E. Detournay, 1998, Considerations on failures initiation in inclined boreholes, Proc. 29th U. S. Rock Symp. Balkema, Rotterdam.

Ruth, P. and R. Hillis, 2000, Estimating pore pressure in the Cooper Basin, South Australia: Sonic log method in an uplifted basin. J. Expl. Geophys. 31, 441-447.

Santareli, F. J. and E. T. Brown, 1987, Performance of deep boreholes in rock with a confining pressure dependent elastic modulus, Proc. 60 Int. Society of Rock Mech. Vol. 2: 1217-1222. Balkema, Rotterdam.

Sayers, C., 1994, The elastic anisotropy of shales, J. Geophys. Res.Solid Earth: 99, 767-774.

Sayers, C., C. Russel, M. Pelorosso, J. Adachi, J. Pastor, V. Singh, K. Tagbor and P. Hooyman, 2009, Determination of rock strength using advanced sonic log interpretation techniques. In Proceedings of the SPE ATCE, New Orleans, 4 – 7 October, SPE 124161.

Sayers, C., S. Kisra, K. Tagbor, A. D. Taleghani and J. Adachi, 2007, Calibrating the mechanical properties and in-situ stresses using acoustic radial profiles. In proceedings of the SPE ATCE, Anaheim, 11-14 November, SPE 110089.

Sayers, C., 2005, Seismic anisotropy of shales, Geophysics, 64, 93-98.

Sayers, C., 2006, An introduction to velocity-based pore pressure estimation. TLE December, 1496-1500.

Sherwood, J. D. and L. Bailey, 1994, Swelling of shale around a cylindrical wellbore. Proc. R. Soc. Land. p. 161-184.

Shoenberg, M., Muir, F. and C. Sayers, 1996, Introducing ANNIE: a simple three parameters anisotropic velocity model for shales, Journal of Seismic Exploration, 5, 34-49.

Sinha, B., B. Vissapragada, L. Renlie and E. Skomedal, 2006, Horizontal stress magnitude estimation using the three shear moduli - A Norwegian Sea case study, In Proceedings of SPE ATCE, San Antonio, 24-27 September, SPE 103079.

Sinha, B., B. Vissapragada, L. Renlie and S. Tysse, 2006, Radial profiling of the three formation shear moduli and its application to well completions. J Geophys.,71:6, E65-E77.

Sinha, B., Vissapragada, B., Wendt, A., Kongslien, M., Eser, H., Skomedal, E., Renile, L. and E. Pedersen, 2007, Estimation of formation stresses using radial variation of three shear moduli- a case study from a high-pressure, high-temperature reservoir in Norwegian continental shelf, In Proceedings of SPE ATCE, Anaheim, 11-14 November, SPE 109842.

Sinha, B. K. and S. Kostek, 1996, Stress-induced azimuthal anisotropy in borehole flexural waves, Geophysics 61, 1899–1907.

Sinha, B. K., J. Wang, S. Kisra, J. Li, V. Pistre, T. Bratton, M. Sanders and C. Jun, 2008, Estimation of borehole stresses using sonic data, 49th Annual Logging Symposium, May 25 - 28, Austin, Texas.

Smith, M. G., 1996, The Bakken Formation (Late Devonian-Early Mississippian): A black shale source rock in the Williston Basin: Ph.D. thesis, University of British Columbia.

Tatham, R. H., and M. D. McCormack, 1991, Multicomponent seismology in petroleum exploration: Society of Exploration Geophysicists.

Thiercelin, M. J. and R. A. Plumb, 1994. Core based predictions of lithologic stress contrasts in east Texas formations. J. SPE Formation Evaluation. 9: 14, 251-258.

Thomsen, L., 1986, Weak elastic anisotropy, Geophysics, 51, 1954-1966.

Traugott, B., 1997. Pore/Fracture determination in deep water. World Oil, 1997.

Tsuneyama F. and G. Mavko, 2005, Velocity anisotropy estimation for brine-saturated sandstone and shale: The Leading Edge, 24**,**882-888.

Tsvankin, I. 2005. Seismic signatures and analysis of reflection data in anisotropic media. 2nd ed. Elsevier Science.

Tsvankin, I., 1997, Reflection move-out and parameter estimation for horizontal transverse isotropy: Geophysics, 62, 614-629.

Tsvankin, I., and L. Thomsen, 1994, Nonhyperbolic reflection move-out in anisotropic media: Geophysics, 59, 1290-1304.

Van Oort, E., 2003, On the physical and chemical stability of shales, Journal of Petroleum Science & Engineering, 38 213-235.

Vernik L. and A. Nur, 1992, Petrophysical classification of siliciclastics for lithology and porosity prediction from seismic velocities: Bulletin of the American Association of Petroleum Geologists, 76, 1295-1309.

Vernik, L., and A. Nur, 1990, Ultrasonic velocity and anisotropy of hydrocarbon source rocks: Geophysics, 57, 727–735.

Vernik, L., and X. Liu, 1997, Velocity anisotropy in shales: A petrophysical study: Geophysics, 62, 521-532.

Walsh, J., Sinha, B., Plona, T., Miller, D. and D. Bently, 2007, Derivation of anisotropy parameters in a shale using borehole sonic data, SEG 77th annual meeting, expanded abstract.

Walsh, J., B. K. Sinha and A. Donald, 2006, Formation anisotropy parameters using borehole sonic data, SPWLA 74th annual logging symposium, June 4-7.

Wang Z., 2002, Seismic anisotropy in sedimentary rocks, part 1: A single-plug laboratory method: Geophysics, 67, 1415–1422.

Wang, Z., 2002, Seismic anisotropy in sedimentary rocks, part 2: Laboratory data: Geophysics, 67, 1423–1440.

Wang, Z., 2000, Dynamic vs. static properties of reservoir rocks. In Wang, Z., A. Nur and A. Eds, Seismic and acoustic velocities in reservoir rocks. Volume 3: Recent developments, Published by SEG.

Waters, G, R. Lewis and D. Bently, 2011, The effect of mechanical properties anisotropy in the generation of hydraulic fractures in organic shales. In Proceedings of SPE ATCE, Denver, 30 Oct- 2 Nov, SPE 146776.

Webster, R. L., 1982, Analysis of petroleum source rocks of the Bakken Formation (Devonian and Mississippian) in North Dakota: M.S. thesis, University of North Dakota.

Willson, S.M.; Last, N.C.; Zobach, M. D. and D. Moos, 1999, Drilling in South America: Stability approach for complex geologic conditions, SPE Latin American & Caribbean Petrol. Eng. Conf., Caracas, April, SPE 53940.

Winterstein, D. F., 1990, Velocity anisotropy terminology for geophysicists: Geophysics, 55, 1070-1088.

Wndt, A., M. Kongslien, B. Sinha, B. Vissapragada, A. Newton, E. Skomedal, L. Renlie and E. Pedersen, 2007, Enhanced mechanical earth modeling and wellbore stability calculations using advanced sonic measurements - A case study of HPHT Kvitebjon Field in the Norwegian North Sea. In Proceedings of SPE ATCE, Anaheim, 11-14 November, SPE 109662.

Yu, H. S., 2000, Cavity expansion methods in geomechanics, Kluwer Academic Publishers.

Zhang, J., 2005, The impact of shale properties on wellbore stability, PhD Thesis, University of Texas.

Zimmerman, R. W., J. Jeager, and N. Cook, 2007. Fundamentals of rock mechanics. 4th ed. Blackwell Publishing.

Zoback, M., 2007, Reservoir geomechanics, Cambridge University Press, First edition.